Finite Element Analysis Of Geodesically Stiffened Cylindrical Composite Shells Using A Layerwise Theory

by

Craig Steven Gerhard

Zafer Gürdal

Rakesh K. Kapania

Virginia Polytechnic Institute and State University

Blacksburg, VA 24061

Prepared for:

NASA Langley Research Center

Hampton, Virginia 23681-0001

Prepared under:

Grant NAG-1-1085

Finite Element Analysis Of Geodesically Stiffened Cylindrical Composite Shells Using A Layerwise Theory

by

Craig Steven Gerhard

Zafer Gürdal

Rakesh K. Kapania

(ABSTRACT)

Layerwise finite element analyses of geodesically stiffened cylindrical shells are presented. The layerwise laminate theory of Reddy (LWTR) is developed and adapted to circular cylindrical shells. The Ritz variational method is used to develop an analytical approach for studying the buckling of simply supported geodesically stiffened shells with discrete stiffeners. This method utilizes a Lagrange multiplier technique to attach the stiffeners to the shell. The development of the layerwise shells couples a one-dimensional finite element through the thickness with a Navier solution that satisfies the boundary conditions. The buckling results from the Ritz discrete analytical method are compared with smeared buckling results and with NASA Testbed finite element results. The development of layerwise shell and beam finite elements is presented and these elements are used to perform the displacement field, stress, and first-ply failure analyses. The layerwise shell elements are used to model the shell skin and the layerwise beam elements are used to model the stiffeners. This arrangement allows the beam stiffeners to be assembled directly into the global stiffness matrix. A series of analytical studies are made to compare the response of geodesically stiffened shells as a function of loading, shell geometry, shell radii, shell laminate thickness, stiffener height, and geometric nonlinearity. Comparisons of the structural response of geodesically stiffened shells, axial and ring stiffened shells, and unstiffened shells are provided. In addition, interlaminar stress results near the stiffener intersection are presented. First-ply failure analyses for geodesically stiffened shells utilizing the Tsai-Wu failure criterion are presented for a few selected cases.

Acknowledgements

This research is sponsored in part by NASA Grant NAG-1-1085 through the Aircraft Structures Branch at NASA-Langley Research Center. The authors would like to thank the NASA Technical Monitor Dr. James H. Starnes, Jr., for his advice and support. Also, recognition and thanks are given to Dr. J. N. Reddy who guided the first author through the first several years of his doctoral work and helped to initiate this research.

Table of Contents

Introduction 1

1.0 Background 1

1.2 Literature Review 5

1.2.1 Shell Theories and Finite Element Applications 5

1.2.2 Structural Analysis of Stiffened Shells 8

1.2.3 Failure Mechanisms 15

1.3 Present Work 18

Governing Equations 20

2.1 Introduction 20

2.2 Displacements and Strains for Laminated Shells 21

2.3 Displacements and Strains for Laminated Beams 24

2.4 Variational Formulation for Laminated Shells 28

2.5 Variational Formulation for Laminated Beams 37

2.6 Failure Equations 40

Ritz Buckling Method 42

3.1 Introduction 42

3.2 Euler-Bernoulli Beam Stiffeners 43

3.3 Lagrange Multiplier Method 45

3.4 Stiffened Shell System 47

3.5 Buckling Solutions and Equations 49
3.6 Constraint Equations 52
3.7 Shell/Stiffener Load Distribution 56
3.7.1 Introduction 56
3.7.2 Shell Constitutive Relations 57
3.7.3 Axial Stiffener Constitutive Relations 60
3.7.4 Ring Stiffener Constitutive Relations 63
3.7.5 Geodesic Stiffener Constitutive Relations 68
3.7.6 Skin/Stiffener System Constitutive Equations 73
3.7.7 Loading Conditions 76
3.7.7.1 Case 1 - Axial Compression (Applied Nx) 76
3.7.7.2 Case 2 - Pressure Loading (Applied Ny) 78
3.7.7.3 Case 3 - Shear Load (Applied Nxy) 80
3.7.7.4 Case 4 - Applied End Shortening 81
3.8 Governing Equations and Final Form 82

Finite Element Formulation 85
4.1 Introduction 85
4.2 Layerwise Shell Finite Element Formulation 86
4.3 Layerwise Beam Finite Element Formulation 89
4.4 Assembly and Nonlinear Analysis 92
4.5 Beam Element Stiffness Transformations 97
4.6 Interlaminar Stress Calculation 100
4.7 Finite Element Verification Analyses 102
4.7.1 Introduction 102
4.7.2 Unstiffened Plates and Shells 102

4.7.3 Beam Structures 111
4.7.4 Stiffened Structures 117

Results **128**
5.1 Ritz Buckling Results 128
5.2 LWTR/Testbed Finite Element Stress Analysis Comparison 158
5.3 Displacements and Interlaminar Stresses in Geodesically Stiffened Shells 168
5.4 Displacement Field in Geodesically Stiffened Shells 177
5.5 Detailed Stress Study 194
5.5.1 In-Plane Stress Study 195
5.5.2 Interlaminar Normal Stress Study 202
5.5.3 Interlaminar Shear Stress Study 216
5.6 First-Ply Failure Analysis 227

Conclusions and Recommendations **234**
6.1 Summary and Conclusions 234
6.2 Recommendations 238

References **241**

Nonlinear Variational Statement for Laminated Shells **255**
Nonlinear Variational Statement 256

Ritz Stiffness and Mass Terms **258**
Stiffness Terms 259
Mass Terms 262

Finite Element Stiffness Terms 263

C.1 Layerwise Shell Element Direct Stiffness Terms 264

C.2 Layerwise Shell Element Tangent Stiffness Terms 268

C.3 Layerwise Beam Element Direct Stiffness Terms 271

C.4 Layerwise Beam Element Tangent Stiffness Terms 272

C.5 Computation of Higher Order Derivatives 273

List of Illustrations

Figure 1. Geodesically stiffened circular cylindrical shell. 3

Figure 2. Cylindrical shell geometry and coordinate system. 25

Figure 3. Variables and interpolation functions for the shell layers. 26

Figure 4. Coordinate systems for the stiffeners: (a) axial stiffeners; (b) ring stiffeners; and (c) geodesic stiffeners. 29

Figure 5. Orthogonally stiffened circular cylindrical shell with axial and ring stiffeners. 30

Figure 6. Description of the radius of curvature for geodesic stiffeners. 31

Figure 7. Geodesically stiffened circular cylindrical shell showing the Lagrange constraint points. 50

Figure 8. Geometry of an N-layered shell laminate. 61

Figure 9. Axially stiffened cylindrical shell and unit cell for load distribution analysis: (a) stiffened cylindrical shell; b) unit axial cell. 64

Figure 10. Ring stiffened cylindrical shell and unit cell for load distribution analysis: (a) stiffened cylindrical shell; b) unit ring cell. 67

Figure 11. Geodesically stiffened cylindrical shell and unit cell for load distribution analysis: (a) stiffened cylindrical shell; b) unit geodesic cell. 74

Figure 12. Geometry of the finite element model: a) shell element; b) beam element. 87

Figure 13. Node numbering and coordinates for Linear, Serendipity, and Lagrange shell finite elements. 90

Figure 14. Node numbering and coordinates for Linear, Quadratic, and Cubic beam finite elements. 93

Figure 15. Newton-Raphson method of a one-dimensional problem with tangent stiffness matrix at each iteration. 96

Figure 16. Representation of the beam displacements (u', v', w') to shell transformation shell displacements (u, v, w). 99

Figure 17. A clamped cylindrical shell subjected to internal pressure. 103

Figure 18. An isotropic cylindrical shell roof under self-weight. 106

Figure 19. Axial deflection at the support of an isotropic cylindrical shell roof under self-weight. 107

Figure 20. Transverse deflection at the support of an isotropic cylindrical shell roof under self-weight. 108

Figure 21. Simply supported orthotropic cylindrical roof. 109

Figure 22. Simply supported [0/90] cylindrical roof. 110

Figure 23. Simply supported [0/90/0] square plate subjected to a uniformly distributed load. 112

Figure 24. Through-the-thickness distribution of the in-plane normal stress $\bar{\sigma}_{xx}$ for a simply supported, [0/90/0] laminated square plate under uniform load, (a/h = 10). 113

Figure 25. Through-the-thickness distribution of the transverse shear stress $\bar{\sigma}_{yz}$ for a simply supported, [0/90/0] laminated square plate under uniform load, (a/h = 10). 114

Figure 26. Through-the-thickness distribution of the transverse shear stress $\bar{\sigma}_{xz}$ for a simply supported, [0/90/0] laminated square plate under uniform load, (a/h = 10). 115

Figure 27. Through-the-thickness distribution of the transverse normal stress $\bar{\sigma}_{zz}$ for a simply supported, [0/90/0] laminated square plate under uniform load, (a/h = 10). 116

Figure 28. Cantilever beam subjected to two different loading conditions: a) applied end load; b) uniformly distributed load. 118

Figure 29. Large deflection of a cantilever beam under a uniform load (E = 1.2 x 10^4 psi, ν = 0.2, L = 10 in.). 120

Figure 30. Cantilever stiffened plate subjected to an end load. 122

Figure 31. Cantilever stiffened plate with symmetric stiffeners. 124

Figure 32. A square plate resting on elastic edge beams. 126

Figure 33. Geodesically stiffened panel for verification of the LWTR analysis: a) panel geometry; b) finite element mesh. 133

Figure 34. Axial buckling for a 24 axial stiffener shell model ($[-45/45/90/0]_S$ layup; R = 85", L = 100"; 1.0" x 0.2" stiffeners). 138

Figure 35. Buckling pressure for a 25 ring stiffener shell model ($[-45/45/90/0]_S$ layup; R = 85", L = 100"; 1.0" x 0.2" stiffeners). 141

Figure 36. Geodesically stiffened shell configurations. 143

Figure 37. Finite element mesh used for the geodesic buckling analysis (unit cell with 20x20 mesh). 144

Figure 38. Axial buckling results for a 2x12 geodesic shell model ([−45/45/90/0]s layup; R = 85″, L = 100″; 1.0″ x 0.2″ stiffeners). 149

Figure 39. Axial buckling for a 24 axial stiffener shell model ([0/90/90/0] layup; R = 85″, L = 100″; 1.0″ x 0.2″ stiffeners). 153

Figure 40. Buckling pressure for a 25 ring stiffener shell model ([0/90/90/0] layup; R = 85″, L = 100″; 1.0″ x 0.2″ stiffeners). 156

Figure 41. Axial buckling results for a 1x12 geodesic shell model ([0/90/90/0] layup; R = 85″, L = 100″; 1.0″ x 0.2″ stiffeners). 163

Figure 42. Unit cell finite element mesh and boundary conditions for the Testbed stress analysis (256 elements). 169

Figure 43. Unit cell finite element mesh and boundary conditions for the LWTR stress analysis (256 elements). 170

Figure 44. LWTR and Testbed 1x12 geodesic shell axial stresses for [0/90/0] laminate: a) bottom 0^0 ply; b) 90^0 ply; c) top 0^0 ply (x = L/2). 171

Figure 45. LWTR and Testbed 1x12 geodesic shell axial stresses for bottom layers of [45/ − 45/45/ − 45] laminate: a) bottom 45^0 ply; b) bottom -45^0 ply (x = L/2). 172

Figure 46. LWTR and Testbed 1x12 geodesic shell axial stresses for top layers of [45/ − 45/45/ − 45] laminate: a) top 45^0 ply; b) top -45^0 ply (x = L/2). 173

Figure 47. LWTR and Testbed 1x12 geodesic shell axial stresses for bottom layers of [60/ − 60/0/ − 60/60] laminate: a) bottom 60^0 ply; b) bottom -60^0 ply (x = L/2). 174

Figure 48. LWTR and Testbed 1x12 geodesic shell axial stresses for 0^0 layer of [60/ − 60/0/ − 60/60] laminate (x = L/2). 175

Figure 49. LWTR and Testbed 1x12 geodesic shell axial stresses for top layers of [60/ − 60/0/ − 60/60] laminate: a) top 60^0 ply; b) top -60^0 ply (x = L/2). 176

Figure 50. Nondimensional transverse displacements for a 1x12 geodesically stiffened shell as a function of the laminate stacking sequence under compressive loading (R = 85″, L = 100″). 179

Figure 51. Nondimensional transverse displacements for geodesically stiffened shells as a function of the stiffener orientation: a) changing cell geometry; b) changing cell length. 181

Figure 52. Nondimensional transverse displacements for geodesically stiffened shells as a function of the stiffener height: a) compressive loading; b) combined loading. 183

Figure 53. Nondimensional transverse displacements for geodesically stiffened shells as a function of the shell laminate thickness: a) compressive loading; b) combined loading. 185

Figure 54. Nondimensional transverse displacements for geodesically stiffened shells for linear and geometrically nonlinear analyses: a) compressive loading; b) combined loading. 186

Figure 55. Nondimensional transverse displacements for geodesically stiffened shells as a function of the shell radius: a) compressive loading; b) combined loading. 188

Figure 56. Nondimensional transverse displacements for geodesically stiffened, axial/ring stiffened, unstiffened shells: a) pure compressive; b) combined loading. 190

Figure 57. Unit cell finite element mesh and boundary conditions for the LWTR stress analysis of the axial and ring stiffened shell (256 elements). 191

Figure 58. Nondimensional transverse displacements for geodesically stiffened shells under combined loading: a) laminate thickness = 0.30″; b) laminate thickness = 0.15″ and 0.075″. 193

Figure 59. Surface plot of $\overline{\sigma}_{xx}$ for the inner layer of a [0/90/0] 1x12 geodesically stiffened shell under compressive loading. 197

Figure 60. Surface plot of $\overline{\sigma}_{xx}$ for the outer layer of a [0/90/0] 1x12 geodesically stiffened shell under compressive loading. 198

Figure 61. Surface plot of $\overline{\sigma}_{xx}$ for the inner layer of a [0/90/0] 1x12 geodesically stiffened shell under combined loading. 199

Figure 62. Surface plot of $\overline{\sigma}_{xx}$ for the outer layer of a [0/90/0] 1x12 geodesically stiffened shell under combined loading. 200

Figure 63. Surface plot of $\overline{\sigma}_{xy}$ for the inner layer of a [0/90/0] 1x12 geodesically stiffened shell under combined loading. 201

Figure 64. Surface plot of $\overline{\sigma}_{zz}$ for the outer layer of a [0/90/0] 1x12 geodesically stiffened shell under compressive loading. 203

Figure 65. Surface plot of $\overline{\sigma}_{zz}$ for the outer layer of a [0/90/0] 1x12 geodesically stiffened shell under combined loading. 204

Figure 66. Through-the-thickness distribution of $\overline{\sigma}_{zz}$ for G1x12 shell near the stiffener intersection for various shell laminates under combined loading. 206

Figure 67. Through-the-thickness distribution of $\bar{\sigma}_{zz}$ for G1x12 shell near the stiffener intersection for linear and geometrically nonlinear analyses under combined loading. 207

Figure 68. Through-the-thickness distribution of $\bar{\sigma}_{zz}$ for G1x12 shell near the stiffener intersection for varying stiffener heights under combined loading. 209

Figure 69. Through-the-thickness distribution of $\bar{\sigma}_{zz}$ for G1x12 shell near the stiffener intersection for varying the cell geometry under combined loading. 210

Figure 70. Through-the-thickness distribution of $\bar{\sigma}_{zz}$ for G1x12 shell near the stiffener intersection for increasing shell radii under combined loading. 212

Figure 71. Through-the-thickness distribution of $\bar{\sigma}_{zz}$ for G1x12 shell near the stiffener intersection for varying shell laminate thickness under combined loading. 213

Figure 72. Through-the-thickness distribution of $\bar{\sigma}_{zz}$ for G1x12 stiffened, axial/ring stiffened, and unstiffened shells under combined loading. 215

Figure 73. Surface plot of $\bar{\sigma}_{xz}$ for the outer layer of a [0/90/0] 1x12 geodesically stiffened shell under compressive loading. 218

Figure 74. Surface plot of $\bar{\sigma}_{xz}$ for the outer layer of a [0/90/0] 1x12 geodesically stiffened shell under combined loading. 219

Figure 75. Through-the-thickness distribution of $\bar{\sigma}_{xz}$ for G1x12 shell at the critical region for various shell laminates under combined loading. 220

Figure 76. Through-the-thickness distribution of $\bar{\sigma}_{xz}$ for G1x12 shell at the critical region for linear and geometrically nonlinear analyses under combined loading. 221

Figure 77. Through-the-thickness distribution of $\bar{\sigma}_{xz}$ for G1x12 shell at the critical region for changing cell geometry under combined loading. 223

Figure 78. Through-the-thickness distribution of $\bar{\sigma}_{xz}$ for G1x12 shell at the critical region for varying shell laminate thickness under combined loading. . . 224

Figure 79. Through-the-thickness distribution of $\bar{\sigma}_{xz}$ for G1x12 shell at the critical region for increasing shell radii under combined loading. 226

Figure 80. Through-the-thickness distribution of $\bar{\sigma}_{xz}$ for G1x12 stiffened, axial/ring stiffened, and unstiffened shells under combined loading. 228

Figure 81. Location of the first-ply failure in the layerwise finite element model. . 233

List of Tables

Table 1. Comparison of the Center Deflection of a Pressurized Clamped, Cylindrical Shell. 104

Table 2. Linear Results for a Clamped Beam Subjected to an Applied End Load and to a Uniformly Distributed Load (E = 1.2 x 10^4, ν = 0.2, L = 10 in.). 119

Table 3. Transverse Deflection of an Eccentrically Stiffened Plate. 123

Table 4. Transverse Deflection of a Cantilever Stiffened Plate with Symmetric Stiffeners. 125

Table 5. Transverse Deflection of an Elastically Supported Plate Subjected to a Uniformly Distributed Load. 127

Table 6. Unstiffened Buckling Results. 131

Table 7. Material Properties Used in the Stiffened Buckling and Finite Element Analyses. 132

Table 8. Analysis of $[-45/45/90/0]_S$ 0.2" Thick Plate with Geodesic Stiffeners Subjected to Axial Compression N_x (Lx = 80", Ly = 28", 12 Stiffeners). 134

Table 9. Analysis of $[-45/45/90/0]_S$ 0.2" Thick Circular Cylindrical Shell with Axial Stiffeners Subjected to Axial Compression (R = 85", L = 100") - Jones Smeared/LWTR Discrete. 136

Table 10. Analysis of $[-45/45/90/0]_S$ 0.2" Thick Circular Cylindrical Shell with Axial Stiffeners Subjected to Axial Compression (R = 85", L = 100") - Reddy Smeared/LWTR Discrete. 137

Table 11. Analysis of $[-45/45/90/0]_S$ 0.2" Thick Circular Cylindrical Shell with Ring Stiffeners Subjected to Lateral Pressure (R = 85", L = 100") - Jones Smeared/LWTR Discrete. 139

Table 12. Analysis of $[-45/45/90/0]_S$ 0.2" Thick Circular Cylindrical Shell with Ring Stiffeners Subjected to Lateral Pressure (R = 85", L = 100") - Reddy Smeared/LWTR Discrete. 140

Table 13. Analysis of $[-45/45/90/0]_S$ 0.2" Thick Circular Cylindrical Shell with Geodesic Stiffeners Subjected to Axial Compression (R = 85", L = 100", 1x12 Geodesic Shell Model). 145

Table 14. Analysis of $[-45/45/90/0]_S$ 0.2" Thick Circular Cylindrical Shell with Geodesic Stiffeners Subjected to Axial Compression (R = 85", L = 100", 1x16 Geodesic Shell Model). 146

Table 15. Analysis of $[-45/45/90/0]_S$ 0.2″ Thick Circular Cylindrical Shell with Geodesic Stiffeners Subjected to Axial Compression (R = 85″, L = 100″, 2x12 Geodesic Shell Model). 147

Table 16. Analysis of $[-45/45/90/0]_S$ 0.2″ Thick Circular Cylindrical Shell with Geodesic Stiffeners Subjected to Axial Compression (R = 85″, L = 100″, 2x16 Geodesic Shell Model). 148

Table 17. Analysis of [0/90/90/0] 0.2″ Thick Circular Cylindrical Shell with Axial Stiffeners Subjected to Axial Compression (R = 85″, L = 100″) - Jones Smeared/LWTR Discrete. 151

Table 18. Analysis of [0/90/90/0] 0.2″ Thick Circular Cylindrical Shell with Axial Stiffeners Subjected to Axial Compression (R = 85″, L = 100″) - Reddy Smeared/LWTR Discrete. 152

Table 19. Analysis of [0/90/90/0] 0.2″ Thick Circular Cylindrical Shell with Ring Stiffeners Subjected to Lateral Pressure (R = 85″, L = 100″) - Jones Smeared/LWTR Discrete. 154

Table 20. Analysis of [0/90/90/0] 0.2″ Thick Circular Cylindrical Shell with Ring Stiffeners Subjected to Lateral Pressure (R = 85″, L = 100″) - Reddy Smeared/LWTR Discrete. 155

Table 21. Analysis of [0/90/90/0] 0.2″ Thick Circular Cylindrical Shell with Geodesic Stiffeners Subjected to Axial Compression (R = 85″, L = 100″, 1x12 Geodesic Shell Model). 159

Table 22. Analysis of [0/90/90/0] 0.2″ Thick Circular Cylindrical Shell with Geodesic Stiffeners Subjected to Axial Compression (R = 85″, L = 100″, 1x16 Geodesic Shell Model). 160

Table 23. Analysis of [0/90/90/0] 0.2″ Thick Circular Cylindrical Shell with Geodesic Stiffeners Subjected to Axial Compression (R = 85″, L = 100″, 2x12 Geodesic Shell Model). 161

Table 24. Analysis of [0/90/90/0] 0.2″ Thick Circular Cylindrical Shell with Geodesic Stiffeners Subjected to Axial Compression (R = 85″, L = 100″, 2x16 Geodesic Shell Model). 162

Table 25. Analysis of [0/90/90/0] 0.2″ Thick Circular Cylindrical Shell with Geodesic Stiffeners Subjected to Lateral Pressure (R = 85″, L = 100″, 1x12 Geodesic Shell Model). 164

Table 26. Analysis of $[-45/45/90/0]_S$ 0.2″ Thick Circular Cylindrical Shell with Geodesic Stiffeners Subjected to Lateral Pressure (R = 85″, L = 100″, 1x12 Geodesic Shell Model). 165

Table 27. Comparison of First-Ply Failure and Buckling Loads for Geodesically Stiffened [0/90/0] Shells. 231

Table 28. First-Ply Failure Results for Geodesically Stiffened and Unstiffened 0.3" Thick Shells Subjected to High Pressures. 232

Chapter 1

Introduction

1.0 Background

Laminated composite shell structures have found varied applications in complicated aerospace structural systems. This is due primarily to the advantageous properties of composite materials such as high strength-to-weight and stiffness-to-weight ratios for weight sensitive applications. Additionally, composite structures have a high fatigue life, corrosion resistance, low fabrication cost, and are tailorable to the loading environment. Aerospace applications using composite structures are almost limitless, but often require the use of sophisticated analyses to determine the response behavior to external loads. This is because laminated composite materials consist of two or more layers that are bonded together to achieve desired structural properties. Material properties of laminated composites are discontinuous through the thickness because of the different material layers in the laminate. Thus, the analysis of composite structures is quite complicated due to material discontinuities across the laminate interfaces, bending-

stretching coupling in the laminate, and the geometrically nonlinear effects. Traditional analysis methods applied to isotropic materials cannot be applied directly to composite materials.

As new applications of composite structures evolve, so also the analytical techniques to study these applications must also evolve. Existing metal aircraft design methods permit the skin panels of some structural components to buckle under various loading conditions. Hence, these structures are designed to have postbuckling strength. Before composite structural components can be designed with similar buckling response, their strength limits and failure characteristics must be well understood [1,2]. Grid-stiffening concepts based on new, automated manufacturing methods such as filament winding where the co-curing of stiffeners and skin is achieved hold great potential for cost savings. Additional applications of stiffened shells may be found in aircraft fuselages, rocket motor cases, oil platform supports, grain silos, and submarine hulls.

Accurate design analysis of stiffened circular cylindrical composite shells is of great importance in the aerospace industry as it relates to aircraft fuselage design. The objective of this study will be to concentrate on the analysis of geodesically stiffened cylindrical composite shells subjected to compressive loads. The analysis will include a study of the stiffened shell buckling and stress analyses. See Figure 1 for a description of the geodesically stiffened shell system. Most previous analyses of stiffened composite shells have utilized either a smeared stiffener approach or a linear finite element analysis to determine the buckling loads. Although few, nonlinear analyses of stiffened shells are typically performed using the finite element method. Analysis of stiffened composite shells must include the failure characteristics of the shell structure including general instability, local stresses, interlaminar stresses, and failure analysis.

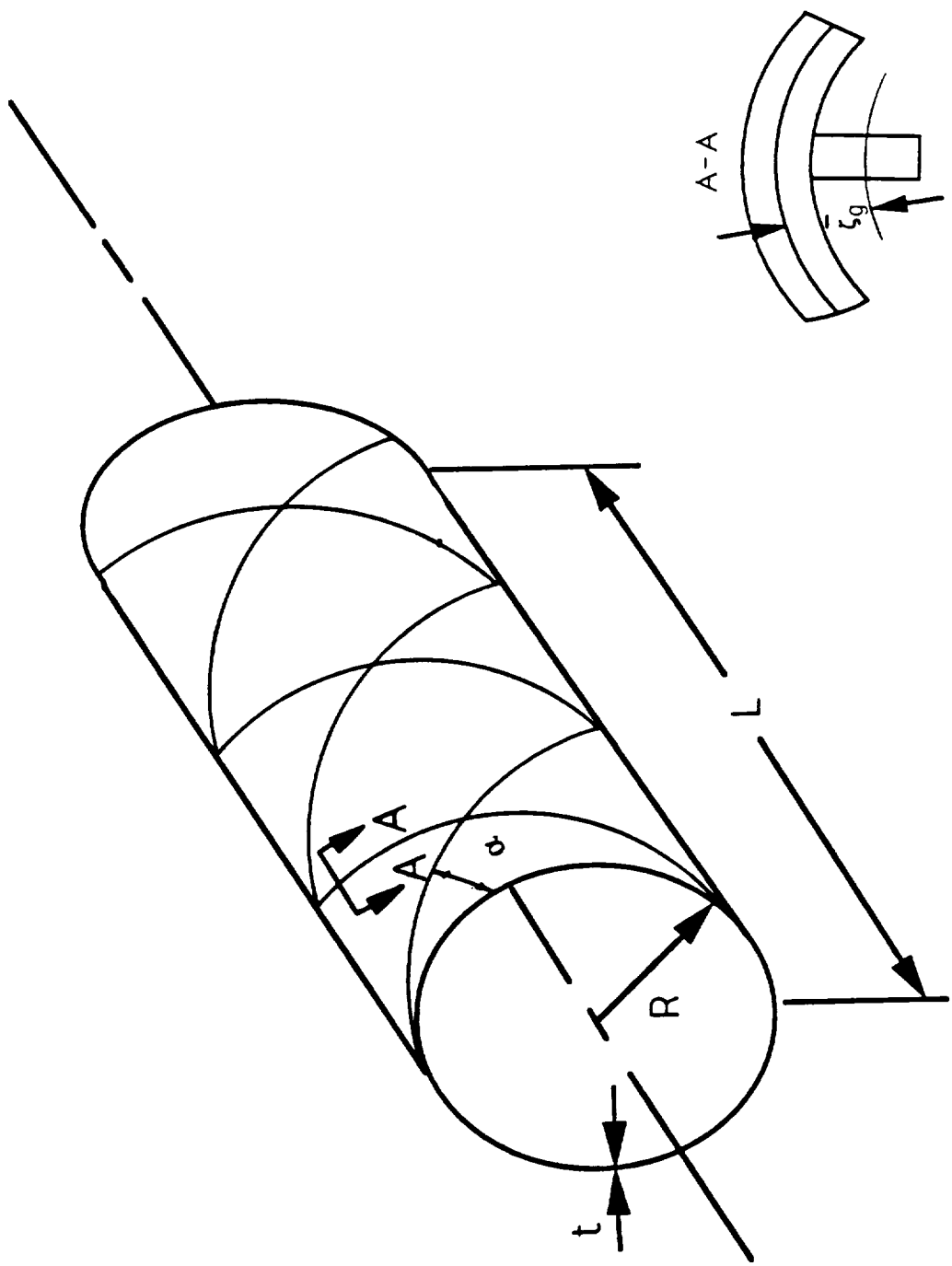

Figure 1. Geodesically stiffened circular cylindrical shell.

Traditionally, in order to capture the localized effects in laminated composite shells a three-dimensional (3-D) finite element analysis must be used. Further, a fully nonlinear 3-D finite element analysis must be performed to characterize the structural response in the postbuckling regime. Unfortunately, if a laminated composite shell is modeled with 3-D elements an excessively refined mesh must be used because the individual lamina thickness dictates the aspect ratio of the elements. The aspect ratio of the elements must be kept reasonable to avoid shear locking. Even in localized high stress regions a 3-D analysis will be computationally intensive and expensive.

The motivation of this research is to develop an accurate analytical methodology for the study of stiffened circular laminated composite shells without applying a costly nonlinear 3-D analysis. The analysis should be accurate in the nonlinear region and provide for any localized high stress regions. The interlaminar stresses near the stiffener intersections of stiffened structures is of interest to shell design engineers. Moreover, the effects of these interlaminar stresses on the structural integrity of stiffened shells has not been determined. The literature review in the next section provides a background for this study.

1.2 Literature Review

The purpose of this literature review is to present the current state of analysis of stiffened composite cylindrical shells. Also, included are discussions of shell theories, finite element methods, discrete stiffener approaches, and failure mechanisms in composite materials. This should provide sufficient background for the detailed theoretical and numerical work which follows.

1.2.1 Shell Theories and Finite Element Applications

The first classical theory of shells was proposed by Love [3] in 1888. The basic premise of Love's paper is the Kirchhoff-Love theory in which straight lines normal to the undeformed middle surface remain straight, inextensible, and normal to the deformed middle surface. As a result, the transverse normal strains are assumed to be zero and the transverse shear deformations are neglected. Love's theory can be applied to thin shells where the shell thickness is small compared to the least radius of curvature. An improvement to Love's work was made by Sanders [4] when he presented a theory to remove the strains for small rigid body rotations which are erroneously predicted by Love's theory. The thin shell approximations of Love requires that the thickness of the shell is small compared with the nominal radius of curvature. Donnell [5] removed the thin shell approximation of Love by developing a theory for shallow shells. Reissner [6] and Mindlin [7] each developed shear deformation theories for plates and Reissner [8,9,10] extended the theory to include transverse shear deformation in shells. Surveys

of classical linear elastic shell theories can be found in the works of Naghdi [11], Bert [12], Krauss [13], and Flügge [14].

The use of composite shell structures has forced the development of appropriate shell theories that can accurately account for the effects of bending-stretching coupling, shear deformations, and transverse normal strains. Ambartsumyan [15,16] developed the first analysis that incorporated bending-stretching coupling. Ambartsumyan's work dealt with orthotropic shells rather than anisotropic shells. Dong et al. [17] developed a theory for thin laminated anisotropic shells by applying Donnell type equations to Reissner's and Stavsky's [18] work for plates. Flügge's shell theory [14] was used by Cheng and Ho [19] in their buckling analysis of laminated anisotropic cylindrical shells. A first approximation theory for the unsymmetric deformation of nonhomogeneous, anisotropic, elastic cylindrical shells was derived by Widera et al. [20-22] by means of asymptotic integration of the three-dimensional elasticity equations. The laminated shell theories discussed thus far are based on the Kirchhoff-Love assumptions and therefore are only applicable to thin shells with mild material anisotropy. Application of such theories to layered anisotropic laminated composite shells could lead to as much as 30% or more errors in deflections, stresses, and frequencies according to Reddy [23].

The effects of transverse shear deformation in composite shells were introduced by Gulati and Essenburg [24], Hsu and Wang [25], Zukas and Vinson [26], and Dong and Tso [27]. The development presented in [24] is based upon the shell theory given by Naghdi [28,29] and assumes symmetry of the elastic properties with respect to the middle surface of the shell. The theory presented in [26] also includes the effects of transverse isotropy and thermal expansion through the shell thickness. The theories of references [25,27] are only applicable to orthotropic cylinders. Whitney and Sun [30,31] developed

a higher-order theory for laminated anisotropic cylindrical shells. The theory includes both transverse shear deformations and transverse normal strain. Reddy [23,32] extended Sanders theory for doubly curved shells to a shear deformation theory of laminated shells. The theory accounts for transverse shear strains and rotation about the normal to the shell midsurface. Reddy and Liu [33] proposed a higher-order shear deformation theory for laminated shells. The theory is based on a displacement field in which the displacements of the middle surface are expanded as cubic functions of the thickness coordinate, and the transverse displacement is assumed constant through the thickness. This displacement field leads to a parabolic distribution of the transverse shear stresses and therefore no shear correction factors are used. Librescu [34,35] developed a refined geometrically nonlinear theory of anisotropic symmetrically laminated composite shallow shells by incorporating transverse shear deformation and transverse normal stress effects. The theory was derived using a Lagrangian formulation in which the three-dimensional strain displacement relations were modified to include the nonlinear terms.

Recently, Reddy [36] developed a layerwise laminate theory which yields a layerwise smooth representation of displacements through the thickness. The layerwise laminate theory of Reddy (LWTR) reduces the 3-D elasticity theory to a quasi 3-D laminate theory by assuming an approximation of displacements through the thickness. Reddy [37] and Reddy and Barbero [38] extended the LWTR to the vibration of laminated cylindrical shells. Further study of laminated shell theories may be found in papers by Bert and Francis [39] and Kapania [40].

A large number of different finite elements have been formulated for the static and dynamic analysis of isotropic and anisotropic shells. One of three approaches are usually followed in shell finite element theoretical development. The first approach involves the

development of finite elements from an existing 2-D shell theory [41,42]. In the second approach, 3-D elements based on three-dimensional elasticity theory are used [43,44]. For the third method, 3-D degenerated elements are derived from the 3-D elasticity theory of shells [45-49]. One of the earliest uses of finite elements in layered composite shells was provided by Dong [50] on the analysis of statically loaded orthotropic shells of revolution. Other authors [51-54] continued the development of finite elements applicable to laminated composite shells. Nonlinear analysis is critical in the study of shell structures. The nonlinear response of shells under external loads was published in references [31, 47-49, 55-59] among others for laminated composite shells. A more detailed discussion of laminated shell finite elements may be found in [40].

1.2.2 Structural Analysis of Stiffened Shells

The circular cylindrical shell is used extensively as a primary load carrying structure in many applications and is therefore subjected to various loadings. Design limit loads often result from general or local instability due to the action or interaction of pressure, axial, torsional, and thermal loads. The elastic stability of monocoque isotropic cylinders is well documented in the open literature [5,14,60-67]. Developments on the buckling of unstiffened laminated composite circular cylinders may be found in references [68-77]. In 1947, Van der Neut [78] studied the effects of eccentric stiffeners on the buckling of circular cylindrical shells. The work presented in [78] showed a factor of three in the difference between the theoretical buckling loads for internally and externally stiffened shells under axial compression. Baruch and Singer [79] presented work on the general instability of a simply supported cylindrical shell under hydrostatic pressure that was

analyzed by considering the 'distributed stiffness' of the frames and stringers separately, taking into account their eccentricity. Additional theoretical work on the buckling of isotropic cylindrical shells with eccentric stiffeners may be found in the papers by Hedgepeth and Hall [80], Singer et al. [81,82], Block et al. [83], and McElman et al. [84]. Some of the first experimental work on the buckling of eccentrically stiffened cylinders was conducted by Card [85] and this work was compared to theoretical results by Card and Jones [86]. Many other papers on the theoretical and experimental buckling of eccentrically stiffened cylindrical shells are available in the open literature. The calculation of accurate buckling loads for stiffened composite cylinders is a formidable task because of material anisotropy, various loading and boundary conditions, skin-stiffener interaction, differing moduli in tension and compression, and nonlinear behavior.

Analysis of stiffened laminated cylindrical shells was first employed using the smeared stiffener approach. This type of analysis treats the eccentrically stiffened composite shell as an equivalent laminated cylindrical shell. A variational procedure is usually employed in order to obtain the results. The smeared approach was used by Simitses [87-89] and Jones [90,91] for the stability analysis of ring and stringer (axially) stiffened composite cylindrical shells. Simitses [87-89] considered the stiffened circular cylindrical shell as being orthotropic and reduced the strain-displacement relations to the Donnell type equations. Various loading conditions such as axial compression, lateral pressure, hydrostatic pressure, and torsion are considered for shells with clamped boundary conditions in references [87-89]. Jones' work [90,91] was presented for a circular cylindrical shell with multiple orthotropic layers and eccentric stiffeners under axial compression, lateral pressure, or a combination thereof. Classical stability theory which implies a membrane prebuckled state was used for the simply supported edge boundary condi-

tions. More recently, Reddy [37] has developed a smeared approach for axial and ring stiffened composite shells using the layerwise theory.

A new technology known as continuous filament grid stiffening has enabled the manufacture of complex stiffened cylindrical shells. This cost effective process reduces the number of parts and fasteners since the stiffeners are integrally wound as part of the shell. In this study, emphasis will be upon geodesically stiffened shells produced by the aforementioned manufacturing process. To date, published work on the subject of geodesically stiffened shells is sparse. Buckling analysis of orthotropic cylindrical shells with eccentric spiral-type stiffeners using the smeared technique was conducted by Soong [92] for simply supported shells subjected to one of the following loadings: axial compression, hydrostatic pressure, torsion, and bending. Soong concluded that based on equal stiffener weight or equal strength, the spirally stiffened cylinders are about equal to the ring and stringer cylinders for axial compression and pure bending loads, but are superior in resisting torsion hydrostatic pressure loads. Meyer [93] studied an isotropic geodesically stiffened shell have 45 ^{0} integrally milled out one sided stiffeners. This type of stiffener arrangement was used to exclude the buckling modes between hoop reinforcements. Meyer used a smeared approach for simply supported shells and concluded that no increases in axial critical loads were obtained for addition of internal pressure. Studies of isogrid composite cylindrical shells were conducted by Rehfield et al. [94] as well as Reddy et al. [95] extended the work to orthogrid stiffened composite shells. In both papers [94,95] a Donnell type theory was used for general instability, skin buckling, and stiffener buckling. Shaw and Simitses [96] used a smeared procedure in the nonlinear analysis of axially loaded laminated cylindrical shells with various in place transverse supports. The work in [96] includes the effects of geometric imperfections and lamina stacking sequence. Further work on geodesically type stiffened cylindrical shells

using a smeared approach may be found in references [97-99]. The smeared stiffener technique is effective if the cross sections of each stiffener is the same and the stiffener spacing is small. If the number of stiffeners is small or the spacing is large, the smeared stiffener analysis does not yield accurate results and usually overpredicts the buckling load.

A procedure other than the smeared technique must be used for the buckling analysis, vibration and/or stress analysis of sparsely stiffened shells. It is desirable to treat the stiffeners and skin as separate structural components to determine the most accurate buckling or vibration mode and the local peak stresses and strains. The discrete analysis procedure is the only alternative to a finite element analysis to study localized effects. Several authors [100-103] have studied the vibration analysis of discretely stiffened cylindrical shells. Because of the relatively simple geometry of ring stiffened cylindrical shells, treatment of the circumferential rings as discrete elements have been considered in several papers [104-107]. Wang et al. [108,109] first developed a discrete analysis for isotropic cylindrical shells with stiffeners and then later extended the same concepts to composite cylindrical shells with stiffeners [110]. In the discrete analysis of [110] separate equations are developed for the axial stiffeners, ring stiffeners, and skin. The equations are coupled through interacting normal and shear loads via the application of an Airy stress function to the compatibility relations. Pochtman and Tugai [111] used a discrete analysis to study the stability of composite cylindrical shells stiffened with cross ribs. The development was based on the principle of minimum potential energy where the strain energy of the skin and the stiffeners were treated as separate quantities. Chao et al. [112] also employed the principle of minimum potential energy in the analysis of stiffened orthotropic foam sandwich cylindrical shells. The authors in [112] included the effects of transverse shear deformation in their development. Birman [113] applied a discrete

analysis to the divergence instability of reinforced composite cylindrical shells. The development consisted of solving the equations of motion in terms of displacements. The Dirac delta function was applied to discretely include the stiffeners' extensional, bending, and torsional terms in the equations of motion. Additional references on buckling of discretely stiffened cylindrical shells may be found in [114-117].

Another method of constraining stiffeners to the skin is by the application of the Lagrange multiplier method. Several authors used the Lagrange multiplier method in plate stability problems in order to satisfy boundary conditions [118-121]. Al-Shareedah and Seireg [122] correctly predicted the transverse deflection of a pressure loaded rectangular isotropic plate with an oblique stiffener. Lagrange multipliers were used to enforce transverse displacement continuity between the plate and stiffener at a finite number of points. Phillips and Gürdal [123] applied the same technique to the stability of orthotropic plates with multiple orthotropic oblique stiffeners. The Lagrange multiplier method should be viable for stiffened composite circular cylindrical shells. Johnson and Rastogi [124] applied the Lagrange multiplier method to orthogonally stiffened composite cylindrical shells in order to determine the interacting loads between the stiffeners and the shell wall when the shells are subjected to internal pressure. No studies are presented in the open literature on the buckling of stiffened layerwise plates or shells having discrete stiffeners using an analytical method. The Lagrange multiplier method could easily be used to attach the stiffeners to the skin of a layerwise plate or shell.

Finite element analysis of stiffened structures has been divided into several categories. The simplest yet least accurate method is to use a coarse model with lumped stiffeners. In the lumped stiffener method each stiffener is lumped into the plate or shell on the nearest element boundary. The stiffeners are assumed to be connected along the nodes

of the plate or shell elements as bar elements. This model introduces inconsistencies. The lumped method is theoretically inaccurate, as the lumped stiffener indicates a coupling along the nodes to which it is connected whereas a stiffener placed within a plate or shell element indicates coupling of all the nodes of the element. Further, diagonal stiffening is difficult to achieve with this method. A second approach is to use orthotropic simulation (smeared technique) of stiffened structures. This method and its deficiencies was discussed previously for buckling analysis of stiffened cylindrical shells. Another approach is the development of a special bending element where the stiffener stiffnesses are incorporated into the bending element at the elemental level see references [125-130]. This method may work well for bending, but the effects of in-plane loadings are not documented. Also, obtaining the skin/stiffener interaction mechanisms is difficult to extract using this approach. The final method of modeling stiffened structures is by representing the stiffeners as beam, plate, or shell elements. This method provides the greatest accuracy, the most realistic model of skin/stiffener interaction, and consequently will be the method used in this work.

When employing the discretely stiffened finite element approach often curved beams are used as reinforcing members for shells. The beam elements must have a compatible displacement pattern with that of the shell. Kohnke et al. [131] analyzed an eccentrically stiffened cylindrical shell by using a beam finite element with displacements compatible with the cylindrical shell element. Venkatesh and Rao [132] developed a laminated anisotropic curved beam finite element to be used in conjunction with anisotropic shell elements [133-135]. Bhimaraddi et al. [136] used shear deformable laminated curved beam elements to study stiffened laminated shells. Ferguson and Clark [137] developed a variable thickness curved beam and shell stiffening element with transverse shear deformation for isotropic elements. Reddy and Liao [138,139] utilized degenerated 3-D beam

elements as stiffening members in their nonlinear analysis of composite shells. An alternative approach to stiffening shell structures with beams is to approximate the stiffeners with the same element type used for the shell [140]. Using this procedure results in the introduction of a substantial number of additional nodes and nodal displacements.

Work on postbuckling analysis of stiffened shells is sparse. Knight and Starnes et al. [1,2] have done some work on the postbuckling analysis of stiffened and unstiffened composite panels using a finite element analysis. Sandhu et al. [141] performed a finite element analysis of the torsional buckling and postbuckling of composite geodetic cylinders. This work concluded that joint flexibility is an important factor in the overall shell behavior. Hansen and Tennyson [142] presented an overview of the development of a computer model for analyzing the crash response of stiffened composite fuselage structures. A finite element formulation was presented that supposedly can treat laminated shell buckling, large deflections, nonlinear response, and element failure. However, no results were presented for this work.

The displacements, stresses, and failure analysis of shells is receiving more attention than in the past. Leissa and Qatu [143] applied the Ritz method to study the stresses and deflections in composite cantilevered shallow shells. Boitnott, Johnson, and Starnes [144] calculated the linear and nonlinear interlaminar stresses for pressurized composite cylindrical panels. The work in reference [144] also included a nonlinear failure analysis of pressurized composite panels. Failure was found to occur near the corners of the panels along the boundary of the panel. Research work on the stress distribution near the stiffener intersections is lacking. The layerwise theory could easily be adapted to the analysis of stresses near the stiffener intersections. Of particular interest may be the interlaminar stress at the stiffener intersections. Furthermore, the layerwise theory is a

quasi 3-D theory which overcomes the finite element aspect ratio problem of traditional 3-D elements.

1.2.3 Failure Mechanisms

Failure analysis of stiffened composite structures is a highly complex and sparsely researched area. The failure scenarios for stiffened composite structures include: general instability (global structural buckling), stiffener buckling (crippling), skin buckling, and material failure. If the structure is designed to have postbuckling strength, then failure will most likely be based upon ultimate rather than buckling strength. Spier [145] conducted a failure/column buckling analysis of graphite epoxy stiffened panels using a mechanics of materials approach. A comparison of skin buckling, stiffener crippling, and structural buckling was made. Reddy et al. [95] performed an analysis based on mechanics of materials in their study of isogrid and orthogrid stiffened composite circular shells. Their analysis considered general instability, rib (stiffener) crippling, and skin buckling.

In order to determine the failure load of a stiffened structure some type of failure criterion must be applied. Two approaches to failure may be used. The mechanistic (micromechanics) failure approach deals with the failure of a composite material at the constituent material (fiber, matrix) level. The micromechanics approach is difficult and often the results are intractable except for simplistic models. The phenomenological (macromechanics) failure prediction is developed by treating the composite as a homo-

geneous material where the effects of the constituent materials are detected only as averaged composite properties.

The mode of failure of laminated composites may be by fiber yielding, matrix yielding, fiber failure, delamination, or fracture. The first three failure modes depend on a constituent's strength properties. Delamination generally occurs in the form of cracks in the plane of the composite, resulting from manufacturing defects, low strength of resin rich regions, and high local stresses due to improper stacking sequence. Fracture is the result of preexisting voids or cracks in the constituent materials. Macroscopic failure criteria are based upon the tensile, compressive, and shear strengths of an individual lamina.

A myriad of literature exists concerning failure of composite materials. A survey of macroscopic failure criteria applied to composite materials is presented by Sandhu [146], Tsai [147], Tsai and Hahn [148], and Nahas [149]. Some of the more popular failure criteria include the maximum stress criterion, maximum strain criterion, and quadratic polynomial criteria such those proposed by Hill [150], Azzi-Tsai [151], Chamis [152], Hoffman [153], and Tsai-Wu [154]. The maximum stress criterion and maximum strain criterion are called independent mode failure criteria and thus there is no interaction between modes of failure. The quadratic polynomial failure theories are mathematical in nature and are basically empirical curve-fitting techniques. There exists considerable failure mode interaction with the polynomial failure theories. The Tsai-Wu criterion is a tensor failure theory which is invariant under rotation of coordinates and transforms via known tensor transformation laws. None of the aforementioned failure criteria can predict the mode of failure. Hashin [155] proposed a failure criterion which considers four distinct failure modes - tensile and compressive fiber and matrix modes.

Several authors have presented some relatively simple micromechanics failure approaches. Craddock and Zak [156] developed a theoretical model which accounts for large transverse stresses in the plies (laminae) and permits gradual plastic yielding of the matrix to failure. Sanders et al. [157] applied simple micromechanics failure models such as microbuckling, 'kink-band' failure, layer shear, and various interactive modes for application to composite aircraft design.

Initiation of failure is often determined via the first-ply failure analysis. Cope and Pipes [158] conducted finite element analyses of composite spar-wingskin joints and ultimate strength was predicted through application of Tsai-Wu, maximum stress, and maximum shear failure criterion. Reddy and Pandey [159] conducted first-ply failure analyses of composite laminates. The maximum stress, maximum strain, Hill, Tsai-Wu, and Hoffman failure criterion were used in their analyses. Kim and Soni [160,161] developed an analytical technique to predict the onset of delamination in laminated composites. Their work was extended by Brewer and Lagace [162] to develop a quadratic delamination criterion. This criterion is an average stress criterion which compares the calculated out-of-plane interlaminar stresses to their related strength parameters. The criterion showed excellent correlation with experimental delamination initiation stresses.

1.3 Present Work

The literature review presented in the previous sections indicates that analysis of stiffened composite shells is an area of extreme interest. The major emphasis of this research is to develop numerical techniques to study the buckling, linear, nonlinear, and failure behavior of geodesically stiffened circular cylindrical shells. The layerwise laminate theory of Reddy (LWTR) will be extended to stiffened circular cylindrical composite shells. Developments using the LWTR for shells will be applied using both a Ritz variational technique and a finite element approach. Application of appropriate failure criterion will be applied to the model in order to determine the appropriate failure scenario.

The present study was undertaken with the following objectives:

1. Develop a layerwise Ritz variational method with discrete stiffeners using the Lagrange multiplier constraint approach. Use this method to study the buckling of axially, ring, and geodesically stiffened cylindrical composite shells.

2. Develop and verify a layerwise finite element algorithm for accurate prediction of displacements and stresses in composite plates and shells. The stiffeners are to be modeled as layerwise beam elements. Linear and nonlinear strain displacement relations are to be considered.

3. Calculate the displacements, in-plane stresses, and interlaminar stresses in stiffened cylindrical shells with emphasis on geodesically stiffened shells when the shells are subjected to various loading conditions.

4. Apply failure criteria to study the first-ply failure of geodesically stiffened cylindrical composite shells.

The governing equations of stiffened laminated shells using a layerwise theory is presented in Chapter 2. Chapter 3 deals with the development of the Ritz variational method and the Lagrange multiplier constraint method. The finite element model, element types, numerical approach, and finite element verification problems are presented in Chapter 4. The results for several problems are described in Chapter 5. Conclusions and recommendations are presented in Chapter 6.

Chapter 2

Governing Equations

2.1 Introduction

The development of refined shell theories for laminated composite shells has been motivated by the shortcomings of the classical lamination theory. The classical lamination theory (CLT) as applied to shells is based upon the Kirchhoff-Love hypothesis in which the shear deformations are neglected. Consequently, first-order and higher order theories were developed to account for transverse stresses. These theories provide improved global response for deflections, natural frequencies, and buckling loads. However, these theories which are based upon a continuous and smooth displacement field do not yield good estimates of interlaminar stresses. Improved theories must be applied to model the local behavior near stiffener intersections of stiffened shells because laminate failure modes may depend upon the interlaminar stresses. The layerwise laminate theory of Reddy (LWTR), which has been shown to work well for plates, will be extended to circular cylindrical shells. The basic equations for circular cylindrical shells using the

LWTR will be presented in the next section. Also, included in the development will be governing equations for discrete stiffeners.

2.2 Displacements and Strains for Laminated Shells

The LWTR is a displacement based theory in which the three-dimensional elasticity theory is reduced to a quasi three-dimensional laminate theory by assuming an approximation of the displacements through the thickness. The displacement approximation is accomplished via a layerwise approximation through each individual lamina. A polynomial expansion with local support (finite element approximation) is used in this development. Consider a laminated circular cylindrical shell with N orthotropic lamina having the coordinate system described in Figure 2. The displacements u, v, w at a generic point (x, y, z) in the laminate are assumed to be of the form (see Reddy [37])

$$\begin{aligned} u(x,y,z) &= \sum_{j=1}^{N+1} u_j(x,y)\phi^j(z) = u_j\phi^j \\ v(x,y,z) &= \sum_{j=1}^{N+1} v_j(x,y)\phi^j(z) = v_j\phi^j \\ w(x,y,z) &= \sum_{j=1}^{N+1} w_j(x,y)\phi^j(z) = w_j\phi^j \end{aligned} \tag{2.1}$$

where N is the total number of layers (N+1 interfaces including the surfaces) and u_j, v_j, w_j are undetermined coefficients. The ϕ^j are any continuous functions that satisfy the condition through the entire thickness

$$\phi^j(0) = 0 \text{ for all } j = 1, 2, \ldots, (N+1) \tag{2.2}$$

In this development the summation convention will be used for repeated subscripts and superscripts.

The approximation in Eq. (2.1) can be viewed as the global semi-discrete finite element approximations [163] of u, v, and w through the thickness. The ϕ^j denote the global interpolation functions, and u_j, v_j, and w_j are the global nodal values of u, v, and w at the interface locations through the thickness of the laminate. A finite element approximation based on the Lagrangian interpolation through the thickness can be obtained from Eq. (2.1). In this study a linear interpolation will be assumed and thus

$$\begin{aligned} u_1 &= U_1^{(1)}, \quad u_2 = U_2^{(1)} = U_1^{(2)}, \ldots, u_k = U_2^{(k-1)} = U_1^{(k)} \\ v_1 &= V_1^{(1)}, \quad v_2 = V_2^{(1)} = V_1^{(2)}, \ldots, v_k = V_2^{(k-1)} = V_1^{(k)} \\ w_1 &= W_1^{(1)}, \quad w_2 = W_2^{(1)} = W_1^{(2)}, \ldots, w_k = W_2^{(k-1)} = W_1^{(k)} \end{aligned} \tag{2.3}$$

where $U_i^{(k)}$, $V_i^{(k)}$, $W_i^{(k)}$ represent the values of U, V, W at the i-th node of the k-th lamina as displayed in Figure 3.

The linear global interpolations are given by

$$\phi^k(z) = \begin{cases} \psi_2^{(k-1)}(z), & z_{k-1} \le z \le z_k \quad (k = 2, 3, \ldots, N+1) \\ \psi_1^{(k)}(z), & z_k \le z \le z_{k+1} \quad (k = 1, 2, \ldots, N) \end{cases} \tag{2.4}$$

where $\psi_i^{(k)}$ (i = 1, 2) is the local Lagrange interpolation function associated with the i-th node of the k-th layer as defined in Figure 3.

The theory presented in this study will be based upon the circular cylindrical shell analogue of the von Kármán large deflection theory. This theory was applied by Donnell [5] and assumes that the lateral displacement w is large enough that in plane forces and displacements must be considered in the nonlinear form. The strain displacement relations of the Donnell/von Kármán type [5,63] are

$$\begin{aligned}
\varepsilon_1 &= \frac{\partial u}{\partial x} + \frac{1}{2}\left(\frac{\partial w}{\partial x}\right)^2 \\
\varepsilon_2 &= \frac{\partial v}{\partial y} + \frac{w}{R} + \frac{1}{2}\left(\frac{\partial w}{\partial y}\right)^2 \\
\varepsilon_3 &= \frac{\partial w}{\partial z} \\
\varepsilon_4 &= \frac{\partial v}{\partial z} + \frac{\partial w}{\partial y} - \frac{v}{R} \\
\varepsilon_5 &= \frac{\partial u}{\partial z} + \frac{\partial w}{\partial x} \\
\varepsilon_6 &= \frac{\partial u}{\partial y} + \frac{\partial v}{\partial x} + \frac{\partial w}{\partial x}\frac{\partial w}{\partial y}
\end{aligned} \tag{2.5}$$

where R is the radius of the circular cylindrical shell. The coordinated system used in this analysis is defined in Figure 2. Upon substitution of Eq. (2.1) into Eq. (2.5) yields the following relationships

$$\begin{aligned}
\varepsilon_1 &= \frac{\partial u_I}{\partial x}\phi^I + \frac{1}{2}\left(\frac{\partial w_I}{\partial x}\phi^I\right)\cdot\left(\frac{\partial w_J}{\partial x}\phi^J\right) \\
\varepsilon_2 &= \left(\frac{\partial v_I}{\partial y} + \frac{1}{R}w_I\right)\phi^I + \frac{1}{2}\left(\frac{\partial w_I}{\partial y}\phi^I\right)\cdot\left(\frac{\partial w_J}{\partial y}\phi^J\right) \\
\varepsilon_3 &= w_I\frac{d\phi^I}{dz}
\end{aligned} \tag{cont.}$$

$$\varepsilon_4 = v_i \frac{d\phi^i}{dz} + \left(\frac{\partial w_i}{\partial y} - \frac{v_i}{R} \right) \phi^i$$

$$\varepsilon_5 = u_i \frac{d\phi^i}{dz} + \frac{\partial w_i}{\partial x} \phi^i \tag{2.6}$$

$$\varepsilon_6 = \left(\frac{\partial u_i}{\partial y} + \frac{\partial v_i}{\partial x} \right) \phi^i + \left(\frac{\partial w_i}{\partial y} \phi^i \right) \cdot \left(\frac{\partial w_j}{\partial x} \phi^j \right)$$

for all i,j = 1, 2, ..., N + 1.

2.3 Displacements and Strains for Laminated Beams

The layerwise theory is extended to beams in a procedure similar to laminated shells. Consider a laminated beam comprised of N orthotropic lamina having a coordinate system described in Figure 4c. The displacements u and w at a generic point (η, ξ, ζ) in the beam are assumed to be of the form

$$u(\eta, \zeta) = \sum_{j=1}^{N+1} u_j(\eta) \phi^j(\zeta) = u_j \phi^j$$

$$w(\eta, \zeta) = \sum_{j=1}^{N+1} w_j(\eta) \phi^j(\zeta) = w_j \phi^j \tag{2.7}$$

Here the u is the local displacement along the axis of the beam and w is the transverse displacement. In this research the out-of-plane stiffness and subsequently the out-of-plane displacement v is generated from the ratio of the out-of-plane beam bending moment of inertia to the in-plane beam bending moment of inertia. See section 4.5 for a description of the out-of-plane stiffness generation. Torsional stiffness of the layerwise beams is not inherently present in the layerwise elements, but this could be included if

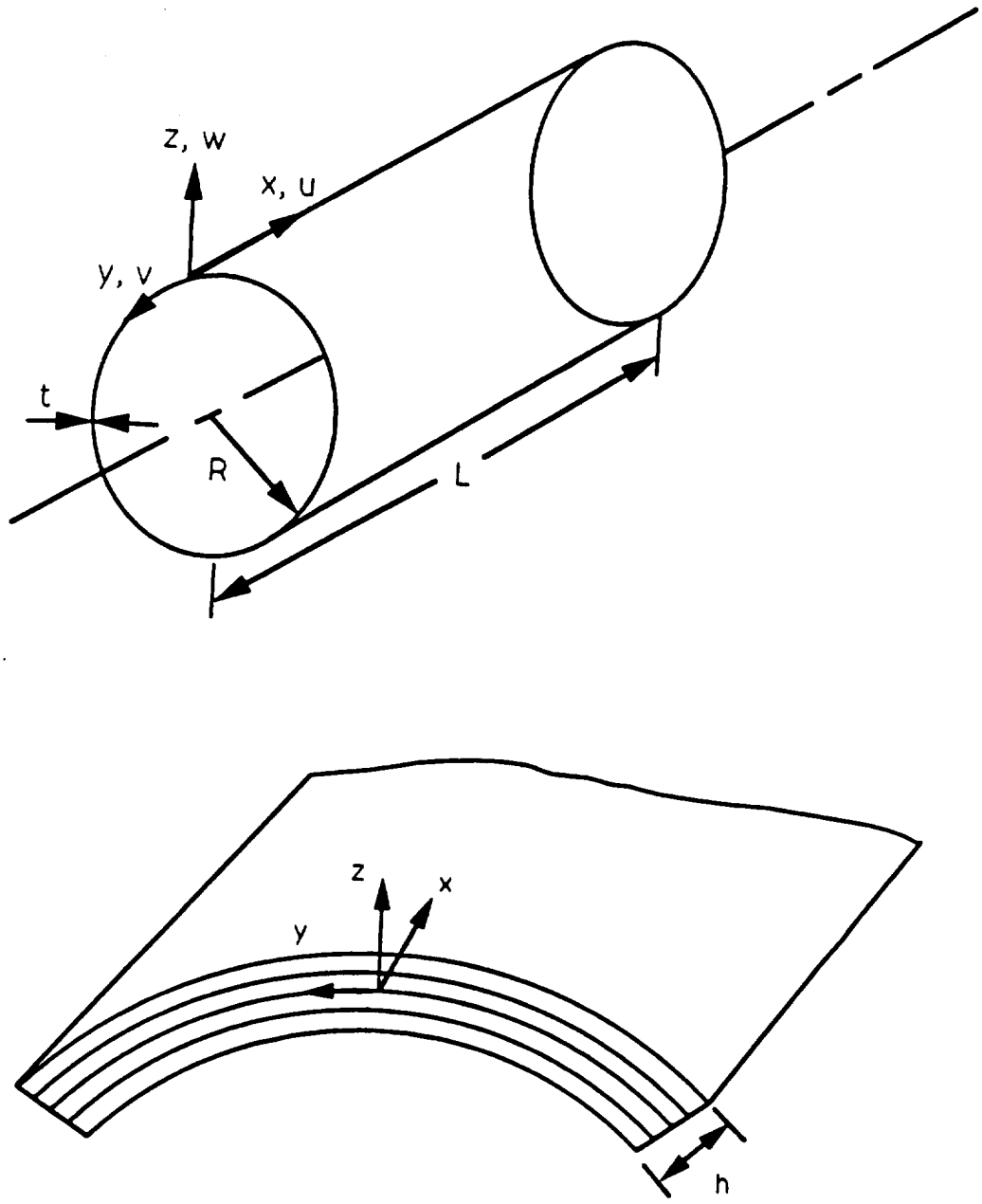

Figure 2. *Cylindrical shell geometry and coordinate system.*

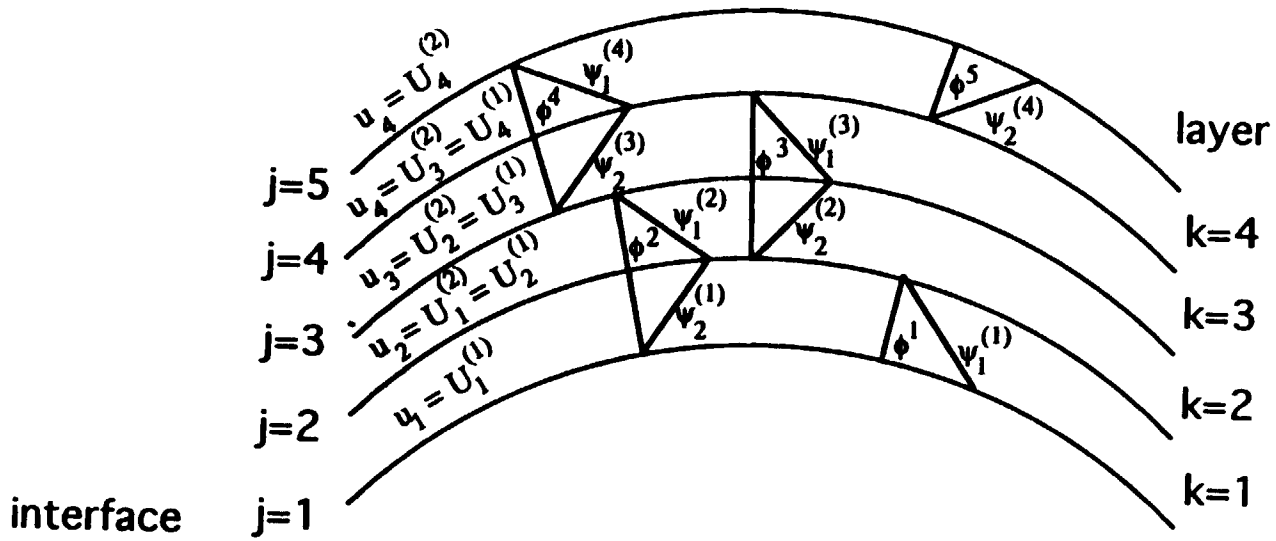

Figure 3. Variables and interpolation fuctions for the shell layers.

an assumed displacement distribution through the thickness of the stiffeners was made. Including torsional stiffness would involve significantly more development for the beam elements and is not included in this study. The importance of torsional stiffness in layerwise stiffeners needs further study and will be left for future work.

The strain relations for the stiffeners are developed in a procedure similar to that of the shell. The stiffeners are modeled as discrete structures and thus developments are made for individual stiffeners. A description of the stiffener coordinate systems is provided in Figure 4. Figures 1 and 5 contain illustrations of the geodesically stiffened and axial/ring stiffened shells respectively. The stiffeners are assumed to behave like beams. In addition, the displacement field is assumed to be similar to that of shells. See references [132-137,164,165] for similar curved beam developments. The stiffener strain displacement relations of the Donnell/von Kármán type are

$$\begin{aligned} \varepsilon_{\eta\eta} &= \frac{\partial u}{\partial \eta} + \frac{1}{2}\left(\frac{\partial w}{\partial \eta}\right)^2 + \frac{w}{R'} \\ \varepsilon_{\zeta\zeta} &= \frac{\partial w}{\partial \zeta} \\ \varepsilon_{\eta\zeta} &= \frac{\partial u}{\partial \zeta} + \frac{\partial w}{\partial \eta} - \frac{u}{R'} \end{aligned} \tag{2.8}$$

Here the radius of the stiffeners R', is developed from vector calculus and analytical geometry (see Figure 6) and is given by the following relation

$$R' = \frac{R^2 + b^2}{R} \tag{2.9}$$

where

$$\text{Stiffener pitch} = 2\pi b \tag{2.10}$$

Here b is the pitch parameter as shown in Figure 6. For ring stiffeners b = 0 and $R' = R$ and for axial stiffeners b = ∞ and thus $R' = \infty$.

Upon substitution of Eq. (2.7) into Eq. (2.8) yields the following layerwise following relations for the stiffeners

$$\begin{aligned}
\varepsilon_{\eta\eta} &= \frac{\partial u_i}{\partial \eta}\phi^i + \frac{1}{2}\left(\frac{\partial w_i}{\partial \eta}\phi^i\right)\cdot\left(\frac{\partial w_j}{\partial \eta}\phi^j\right) + \frac{w_i}{R'}\phi^i \\
\varepsilon_{\zeta\zeta} &= w_i\frac{d\phi^i}{d\zeta} \\
\varepsilon_{\eta\zeta} &= u_i\frac{d\phi^i}{d\zeta} + \frac{\partial w_i}{\partial \eta}\phi^i - \frac{u_i}{R'}\phi^i
\end{aligned} \tag{2.11}$$

for all i,j = 1, 2, ..., number of beam interfaces.

2.4 Variational Formulation for Laminated Shells

The principle of virtual displacements will be applied to the shell and stiffeners separately. For the shell, the principle of virtual displacements can be used to derive a consistent set of differential equations composed of N constant thickness lamina. The Principle of Minimum Potential Energy $\delta\Pi$ may be expressed in variational form as

$$\delta\Pi = \delta U + \delta V = 0 \tag{2.12}$$

Here δU is the virtual strain energy (virtual work done by the internal stresses) and δV represents the variation of the potential of the applied forces. The minimum potential energy statement for the shell in terms of stresses and virtual strains caused by virtual displacements may be expressed as

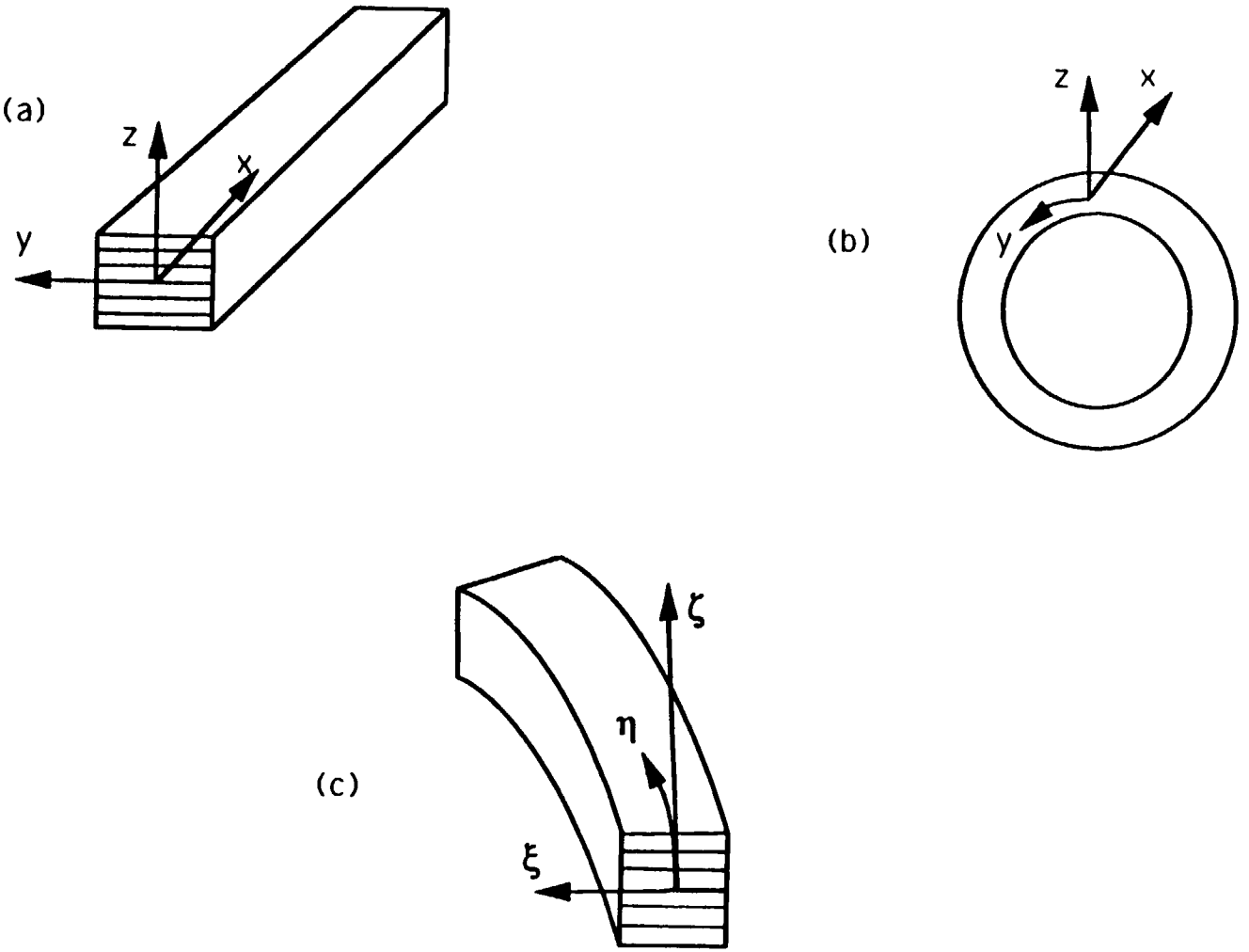

Figure 4. Coordinate systems for the stiffeners: (a) axial stiffeners; (b) ring stiffeners; and (c) geodesic stiffeners.

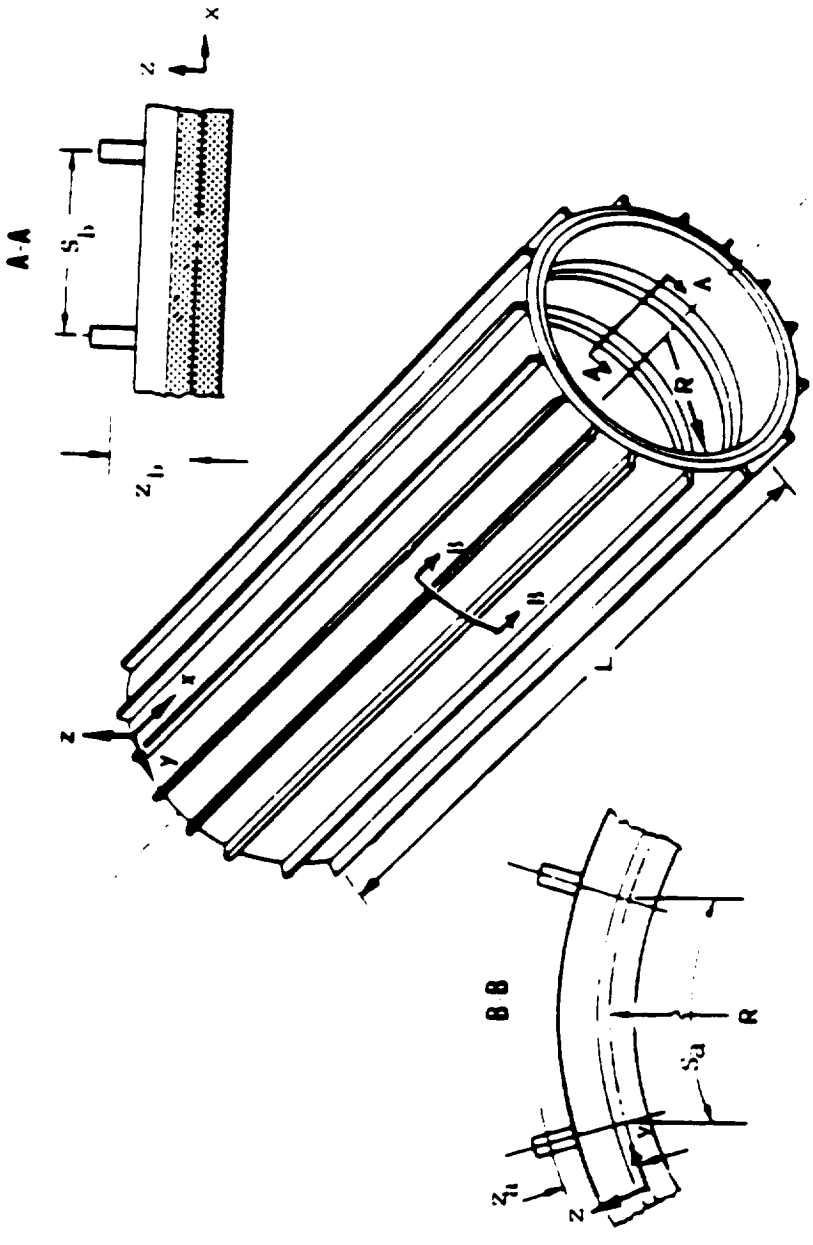

Figure 5. Orthogonally stiffened circular cylindrical shell with axial and ring stiffeners.

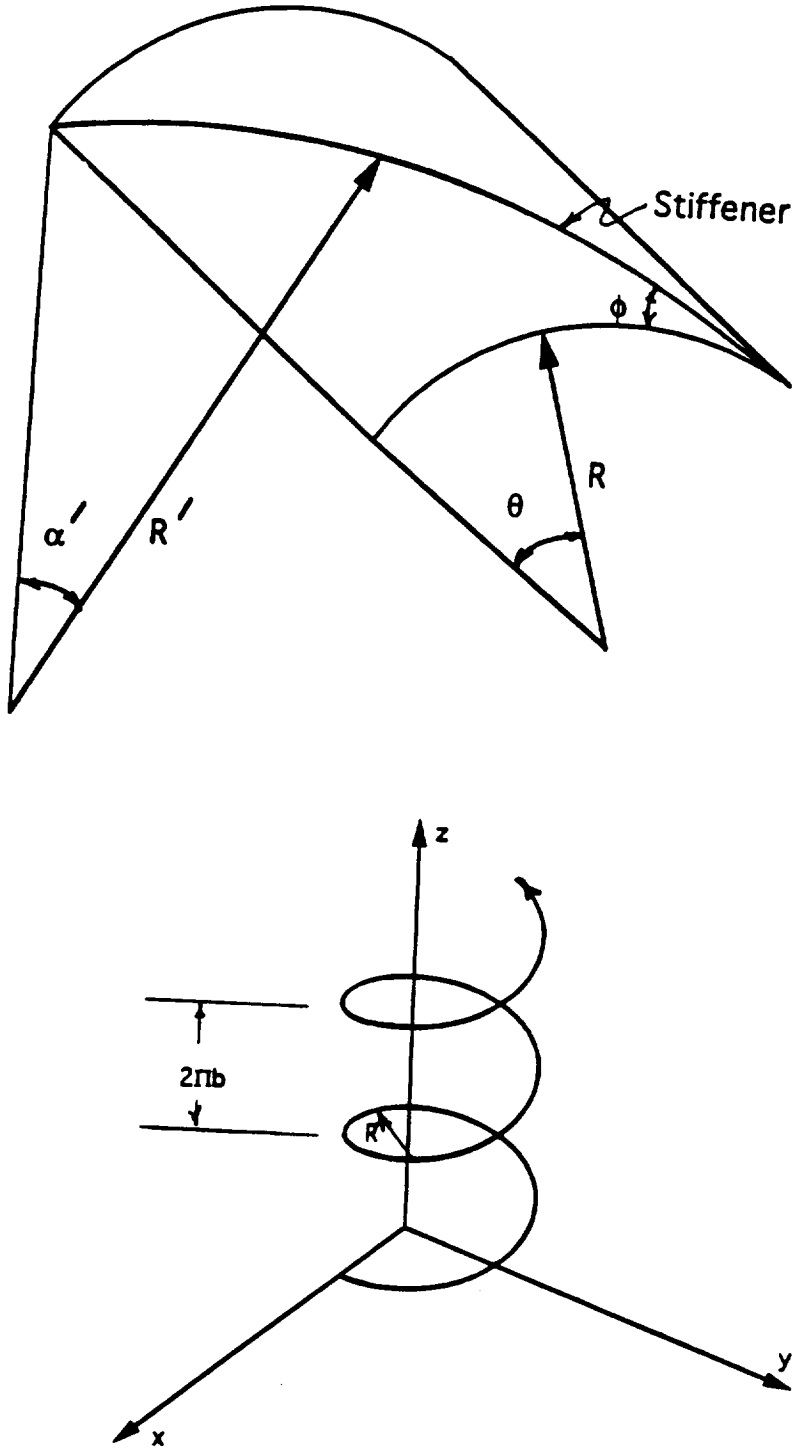

Figure 6. Description of the radius of curvature for geodesic stiffeners.

$$\delta\Pi = \int_{\Omega}\int_{\frac{-h}{2}}^{\frac{h}{2}} \{\sigma_1\delta\varepsilon_1 + \sigma_2\delta\varepsilon_2 + \sigma_3\delta\varepsilon_3 + \sigma_4\delta\varepsilon_4 + \sigma_5\delta\varepsilon_5 + \sigma_6\delta\varepsilon_6\}dzd\Omega + \delta V = 0 \quad (2.13)$$

where σ_1, σ_2, σ_3, σ_4, σ_5, and σ_6 are the shell stresses, $\delta\varepsilon_1$, $\delta\varepsilon_2$, $\delta\varepsilon_3$, $\delta\varepsilon_4$, $\delta\varepsilon_5$ and $\delta\varepsilon_6$ are the virtual strains in the shell coordinates, h is the total shell thickness, Ω denotes the total shell area at the midplane, and once again δV represents the variation of the potential of the applied forces. The variation of the total potential energy in terms of the stress resultants, displacements, and virtual displacements is obtained by substituting the strain displacement equations (2.6) and integrating through the shell thickness. The variation of the potential energy then takes the following form

$$\begin{aligned}\delta\Pi = \int_{\Omega}\Bigg[& M_1^i\frac{\partial\delta u_i}{\partial x} + M_2^i\left(\frac{\partial\delta v_i}{\partial y} + \frac{1}{R}\delta w_i\right) + M_6^i\left(\frac{\partial\delta u_i}{\partial y} + \frac{\partial\delta v_i}{\partial x}\right) \\ & + Q_1^i\delta u_i + Q_2^i\delta v_i + Q_3^i\delta w_i - \frac{1}{R}K_2^i\delta v_i \\ & + K_1^i\frac{\partial\delta w_i}{\partial x} + K_2^i\frac{\partial\delta w_i}{\partial y} + M_1^{ij}\frac{\partial\delta w_i}{\partial x}\frac{\partial w_j}{\partial x} \\ & + M_6^{ij}\left(\frac{\partial\delta w_i}{\partial x}\frac{\partial w_j}{\partial y} + \frac{\partial w_i}{\partial x}\frac{\partial\delta w_j}{\partial y}\right) + M_2^{ij}\frac{\partial w_i}{\partial y}\frac{\partial w_j}{\partial y}\Bigg]dxdy \\ & + \delta V\end{aligned} \quad (2.14)$$

where the stress resultants, M_a^i, M_a^{ij}, Q_1^i, Q_2^i, Q_3^i, K_1^i, and K_2^i, and the variation of the potential of the applied forces, δV, take the following form

$$M_\alpha^i = \int_{\frac{-h}{2}}^{\frac{h}{2}} \sigma_\alpha \phi^i dz\,, \qquad M_\alpha^{ij} = \int_{\frac{-h}{2}}^{\frac{h}{2}} \sigma_\alpha \phi^i \phi^j dz\,, \qquad (\alpha = 1, 2, 6)$$

$$(Q_1^i, Q_2^i, Q_3^i) = \int_{\frac{-h}{2}}^{\frac{h_1}{2}} (\sigma_5, \sigma_4, \sigma_3) \frac{d\phi^i}{dz} dz$$

$$(K_1^i, K_2^i) = \int_{\frac{-h}{2}}^{\frac{h}{2}} (\sigma_5, \sigma_4)\phi^i dz \tag{2.15a}$$

$$\delta V = -\int_\Omega p\delta w d\Omega - \int_\Omega \int_{\frac{-h}{2}}^{\frac{h}{2}} \left(\hat{N}_n \delta u_n + \hat{N}_s \delta u_s\right) dz d\Omega$$

$$- \int_\Omega \int_{\frac{-h}{2}}^{\frac{h}{2}} \left(\hat{M}_n \frac{\partial \delta w_n}{\partial n_n} + \hat{M}_s \frac{\partial \delta w_s}{\partial n_s} + \hat{Q}\delta w \right) dz d\Omega$$

for a linear prebuckling analysis δV reduces to

$$\delta V = \int_\Omega \left[\overline{N}_1 \frac{\partial \delta w_i}{\partial x} \frac{\partial w_j}{\partial x} + 2\overline{N}_6 \left(\frac{\partial \delta w_i}{\partial x} \frac{\partial w_j}{\partial y} + \frac{\partial w_j}{\partial x} \frac{\partial \delta w_i}{\partial y} \right) + \overline{N}_2 \frac{\partial \delta w_i}{\partial y} \frac{\partial w_j}{\partial y} \right] d\Omega \tag{2.15b}$$

For the potential energy of external loads p is the applied pressure, $\hat{N}_n$ and $\hat{N}_s$ are the applied in-plane normal and tangential forces respectively, and $\hat{M}_n$, $\hat{M}_s$, and $\hat{Q}$ are the applied edge normal moment, tangential moment, and shear force respectively. For a buckling analysis $\overline{N}_1$, $\overline{N}_2$, and $\overline{N}_6$ are the axial, lateral, and shear external forces respectively acting on the shell membrane.

The cylindrical shell is assumed to be laminated of orthotropic layers with the principal material coordinates of each layer oriented arbitrarily with respect to the shell axis. The layer constitutive equations referred to the shell coordinates are given as

$$\begin{Bmatrix} \sigma_1 \\ \sigma_2 \\ \sigma_3 \\ \sigma_6 \end{Bmatrix} = \begin{bmatrix} \overline{C}_{11} & \overline{C}_{12} & \overline{C}_{13} & \overline{C}_{16} \\ \overline{C}_{12} & \overline{C}_{22} & \overline{C}_{23} & \overline{C}_{26} \\ \overline{C}_{13} & \overline{C}_{23} & \overline{C}_{33} & \overline{C}_{36} \\ \overline{C}_{16} & \overline{C}_{26} & \overline{C}_{36} & \overline{C}_{66} \end{bmatrix} \begin{Bmatrix} \varepsilon_1 \\ \varepsilon_2 \\ \varepsilon_3 \\ \varepsilon_6 \end{Bmatrix} \tag{2.16a}$$

$$\begin{Bmatrix} \sigma_4 \\ \sigma_5 \end{Bmatrix} = \begin{bmatrix} \overline{C}_{44} & \overline{C}_{45} \\ \overline{C}_{45} & \overline{C}_{55} \end{bmatrix} \begin{Bmatrix} \varepsilon_4 \\ \varepsilon_5 \end{Bmatrix} \tag{2.16b}$$

where $\overline{C}_{ij}$ are the components of the orthotropic stiffness matrix. The stress resultants in terms of displacements is given by the following expression

$$M_1^l = \int_{\frac{-h}{2}}^{\frac{h}{2}} \sigma_1 \phi^l dz = \int_{\frac{-h}{2}}^{\frac{h}{2}} (\overline{C}_{1j}\varepsilon_j)\phi^l dz, \qquad (j = 1, 2, 3, 6)$$

$$\begin{aligned} M_1^l = \Bigg[& D_{11}^{lj} \frac{\partial u_j}{\partial x} + D_{12}^{lj}\left(\frac{\partial v_j}{\partial y} + \frac{w_j}{R} \right) + \overline{D}_{13}^{lj} w_j + D_{16}^{lj}\left(\frac{\partial u_j}{\partial y} + \frac{\partial v_j}{\partial x} \right) \\ & + \frac{1}{2} D_{11}^{ljk} \frac{\partial w_j}{\partial x}\frac{\partial w_k}{\partial x} + D_{16}^{ljk} \frac{\partial w_j}{\partial x}\frac{\partial w_k}{\partial y} + \frac{1}{2} D_{12}^{ljk} \frac{\partial w_j}{\partial y}\frac{\partial w_k}{\partial y} \Bigg] \end{aligned} \tag{2.17a}$$

$$\begin{aligned} M_2^l = \Bigg[& D_{12}^{lj} \frac{\partial u_j}{\partial x} + D_{22}^{lj}\left(\frac{\partial v_j}{\partial y} + \frac{w_j}{R} \right) + \overline{D}_{23}^{lj} w_j + D_{26}^{lj}\left(\frac{\partial u_j}{\partial y} + \frac{\partial v_j}{\partial x} \right) \\ & + \frac{1}{2} D_{12}^{ljk} \frac{\partial w_j}{\partial x}\frac{\partial w_k}{\partial x} + D_{26}^{ljk} \frac{\partial w_j}{\partial x}\frac{\partial w_k}{\partial y} + \frac{1}{2} D_{22}^{ljk} \frac{\partial w_j}{\partial y}\frac{\partial w_k}{\partial y} \Bigg] \end{aligned} \tag{2.17b}$$

$$\begin{aligned} M_6^l = \Bigg[& D_{16}^{lj} \frac{\partial u_j}{\partial x} + D_{26}^{lj}\left(\frac{\partial v_j}{\partial y} + \frac{w_j}{R} \right) + \overline{D}_{36}^{lj} w_j + D_{66}^{lj}\left(\frac{\partial u_j}{\partial y} + \frac{\partial v_j}{\partial x} \right) \\ & + \frac{1}{2} D_{16}^{ljk} \frac{\partial w_j}{\partial x}\frac{\partial w_k}{\partial x} + D_{66}^{ljk} \frac{\partial w_j}{\partial x}\frac{\partial w_k}{\partial y} + \frac{1}{2} D_{26}^{ljk} \frac{\partial w_j}{\partial y}\frac{\partial w_k}{\partial y} \Bigg] \end{aligned} \tag{2.17c}$$

$$Q_1^i = \int_{\frac{-h}{2}}^{\frac{h}{2}} \sigma_5 \frac{d\phi^i}{dz}\, dz = \int_{\frac{-h}{2}}^{\frac{h}{2}} (\overline{C}_{55}\varepsilon_5 + \overline{C}_{45}\varepsilon_4) \frac{d\phi^i}{dz}\, dz$$

$$Q_1^i = \left[\overline{\overline{D}}{}_{55}^{ij} u_j + \overline{D}_{55}^{ji} \frac{\partial w_j}{\partial x} + \overline{\overline{D}}{}_{45}^{ij} v_j + \overline{D}_{45}^{ji} \left(\frac{\partial w_j}{\partial y} - \frac{v_j}{R} \right) \right] \tag{2.17d}$$

$$Q_2^i = \left[\overline{\overline{D}}{}_{45}^{ij} u_j + \overline{D}_{45}^{ji} \frac{\partial w_j}{\partial x} + \overline{\overline{D}}{}_{44}^{ij} v_j + \overline{D}_{44}^{ji} \left(\frac{\partial w_j}{\partial y} - \frac{v_j}{R} \right) \right] \tag{2.17e}$$

$$Q_3^i = \int_{\frac{-h}{2}}^{\frac{h}{2}} \sigma_3 \frac{d\phi^i}{dz}\, dz = \int_{\frac{-h}{2}}^{\frac{h}{2}} (\overline{C}_{3j}\varepsilon_j) \frac{d\phi^i}{dz}\, dz\,, \qquad (j = 1, 2, 3, 6)$$

$$Q_3^i = \left[\overline{D}_{13}^{ji} \frac{\partial u_j}{\partial x} + \overline{D}_{23}^{ji} \left(\frac{\partial v_j}{\partial y} + \frac{w_j}{R} \right) + \overline{\overline{D}}{}_{33}^{ij} w_j + \overline{D}_{36}^{ji} \left(\frac{\partial u_j}{\partial y} + \frac{\partial v_j}{\partial x} \right) \right. \tag{2.17f}$$
$$\left. + \frac{1}{2} \overline{D}_{13}^{jkl} \frac{\partial w_j}{\partial x} \frac{\partial w_k}{\partial x} + \overline{D}_{36}^{jkl} \frac{\partial w_j}{\partial x} \frac{\partial w_k}{\partial y} + \frac{1}{2} \overline{D}_{23}^{jkl} \frac{\partial w_j}{\partial y} \frac{\partial w_k}{\partial y} \right]$$

$$K_1^i = \int_{\frac{-h}{2}}^{\frac{h}{2}} \sigma_5 \phi^i dz = \int_{\frac{-h}{2}}^{\frac{h}{2}} (\overline{C}_{55}\varepsilon_5 + \overline{C}_{45}\varepsilon_4)\phi^i dz$$

$$K_1^i = \left[\overline{D}_{55}^{ij} u_j + D_{55}^{ij} \frac{\partial w_j}{\partial x} + \overline{D}_{45}^{ij} v_j + D_{45}^{ij} \left(\frac{\partial w_j}{\partial y} - \frac{v_j}{R} \right) \right] \tag{2.17g}$$

$$K_2^i = \left[\overline{D}_{45}^{ij} u_j + D_{45}^{ij} \frac{\partial w_j}{\partial x} + \overline{D}_{44}^{ij} v_j + D_{44}^{ij} \left(\frac{\partial w_j}{\partial y} - \frac{v_j}{R} \right) \right] \tag{2.17h}$$

$$M_1^{ij} = \left[D_{11}^{ijk} \frac{\partial u_k}{\partial x} + D_{12}^{ijk} \left(\frac{\partial v_k}{\partial y} + \frac{w_k}{R} \right) + \overline{D}_{13}^{ijk} w_k + D_{16}^{ijk} \left(\frac{\partial u_k}{\partial y} + \frac{\partial v_k}{\partial x} \right) \right. \tag{2.17i}$$
$$\left. + \frac{1}{2} D_{11}^{ijkl} \frac{\partial w_k}{\partial x} \frac{\partial w_l}{\partial x} + D_{16}^{ijkl} \frac{\partial w_k}{\partial x} \frac{\partial w_l}{\partial y} + \frac{1}{2} D_{12}^{ijkl} \frac{\partial w_k}{\partial y} \frac{\partial w_l}{\partial y} \right]$$

$$M_2^{ij} = \left[D_{12}^{ijk} \frac{\partial u_k}{\partial x} + D_{22}^{ijk} \left(\frac{\partial v_k}{\partial y} + \frac{w_k}{R} \right) + \overline{D}_{23}^{ijk} w_k + D_{26}^{ijk} \left(\frac{\partial u_k}{\partial y} + \frac{\partial v_k}{\partial x} \right) + \frac{1}{2} D_{12}^{ijkl} \frac{\partial w_k}{\partial x} \frac{\partial w_l}{\partial x} + D_{26}^{ijkl} \frac{\partial w_k}{\partial x} \frac{\partial w_l}{\partial y} + \frac{1}{2} D_{22}^{ijkl} \frac{\partial w_k}{\partial y} \frac{\partial w_l}{\partial y} \right] \tag{2.17j}$$

$$M_6^{ij} = \left[D_{16}^{ijk} \frac{\partial u_k}{\partial x} + D_{26}^{ijk} \left(\frac{\partial v_k}{\partial y} + \frac{w_k}{R} \right) + \overline{D}_{36}^{ijk} w_k + D_{66}^{ijk} \left(\frac{\partial u_k}{\partial y} + \frac{\partial v_k}{\partial x} \right) + \frac{1}{2} D_{16}^{ijkl} \frac{\partial w_k}{\partial x} \frac{\partial w_l}{\partial x} + D_{66}^{ijkl} \frac{\partial w_k}{\partial x} \frac{\partial w_l}{\partial y} + \frac{1}{2} D_{26}^{ijkl} \frac{\partial w_k}{\partial y} \frac{\partial w_l}{\partial y} \right] \tag{2.17k}$$

for all i,j,k,l = 1, 2, ..., N + 1 and where

$$\begin{aligned}
D_{\alpha\beta}^{ij} &= \int_{\frac{-h}{2}}^{\frac{h}{2}} \overline{C}_{\alpha\beta} \phi^i \phi^j dz, \qquad D_{\alpha\beta}^{ijk} = \int_{\frac{-h}{2}}^{\frac{h}{2}} \overline{C}_{\alpha\beta} \phi^i \phi^j \phi^k dz \\
D_{\alpha\beta}^{ijkl} &= \int_{\frac{-h}{2}}^{\frac{h}{2}} \overline{C}_{\alpha\beta} \phi^i \phi^j \phi^k \phi^l dz, \qquad \overline{D}_{\alpha\beta}^{ij} = \int_{\frac{-h}{2}}^{\frac{h}{2}} \overline{C}_{\alpha\beta} \phi^i \frac{d\phi^j}{dz} dz \\
\overline{D}_{\alpha\beta}^{ijk} &= \int_{\frac{-h}{2}}^{\frac{h}{2}} \overline{C}_{\alpha\beta} \phi^i \phi^j \frac{d\phi^k}{dz} dz, \qquad \bar{\bar{D}}_{\alpha\beta}^{ij} = \int_{\frac{-h}{2}}^{\frac{h}{2}} \overline{C}_{\alpha\beta} \frac{d\phi^i}{dz} \frac{d\phi^j}{dz} dz
\end{aligned} \tag{2.18}$$

Note that $D_{\alpha\beta}^{ij}$, $\bar{D}_{\alpha\beta}^{ij}$, $D_{\alpha\beta}^{ijk}$, and $D_{\alpha\beta}^{ijkl}$ are symmetric in their subscripts and superscripts.

$$\begin{aligned}
D_{\alpha\beta}^{ij} &= D_{\alpha\beta}^{ji}, \quad D_{\alpha\beta}^{ij} = D_{\beta\alpha}^{ij} \\
D_{\alpha\beta}^{ijk} &= D_{\alpha\beta}^{jik} = D_{\alpha\beta}^{kji} = D_{\alpha\beta}^{kij} = D_{\alpha\beta}^{ikj}, \quad etc.
\end{aligned} \tag{2.19}$$

The coefficients with a single bar over them are not symmetric with respect to the superscripts. The variational statement in terms of displacements is provided in Appendix A.

2.5 Variational Formulation for Laminated Beams

The variation of the potential energy for the beam along the beam length, L_s, may be expressed in the following manner

$$\delta\Pi = \int_0^{L_s} \{\sigma_{\eta\eta}\delta\varepsilon_{\eta\eta} + \sigma_{\zeta\zeta}\delta\varepsilon_{\zeta\zeta} + \sigma_{\eta\zeta}\delta\varepsilon_{\eta\zeta}\}d\eta + \delta V \tag{2.20}$$

The three dimensional constitutive equations for an anisotropic body are reduced to that of a one-dimensional body by eliminating the normal stress $\sigma_{\xi\xi}$, the in-plane shear stress $\sigma_{\eta\xi}$, and the transverse shear stress $\sigma_{\xi\zeta}$. Similar procedures for the modeling of laminated composite beams were employed by Bhimaraddi and Chandrashekhara [164] and more recently by Kassegne [165]. The stresses $\sigma_{\xi\xi}$, $\sigma_{\eta\xi}$, and $\sigma_{\xi\zeta}$ are eliminated, but the strains $\varepsilon_{\xi\xi}$, $\varepsilon_{\eta\xi}$, and $\varepsilon_{\xi\zeta}$ are not eliminated. For a laminated beam the constitutive relations reduce to the following form

$$\begin{Bmatrix} \sigma_{\eta\eta} \\ \sigma_{\zeta\zeta} \\ \sigma_{\eta\zeta} \end{Bmatrix} = \begin{bmatrix} \overline{C}^S_{11} & \overline{C}^S_{13} & 0 \\ \overline{C}^S_{13} & \overline{C}^S_{33} & 0 \\ 0 & 0 & \overline{C}^S_{44} \end{bmatrix} \begin{Bmatrix} \varepsilon_{\eta\eta} \\ \varepsilon_{\zeta\zeta} \\ \varepsilon_{\eta\zeta} \end{Bmatrix} \tag{2.21}$$

where the components of the reduced orthotropic beam stiffness matrix, $\overline{C}^S_{ij}$, are expressed in terms of the original orthotropic stiffness terms, C_{ij}, and are expressed in the following form

$$
\begin{aligned}
\bar{C}_{11}^{S} &= \bar{C}_{11} + \left(\frac{\bar{C}_{16}\bar{C}_{26} - \bar{C}_{12}\bar{C}_{66}}{\bar{C}_{22}\bar{C}_{66} - \bar{C}_{26}^{2}} \right)\bar{C}_{12} + \left(\frac{\bar{C}_{12}\bar{C}_{26} - \bar{C}_{16}\bar{C}_{22}}{\bar{C}_{22}\bar{C}_{66} - \bar{C}_{26}^{2}} \right)\bar{C}_{16} \\
\bar{C}_{13}^{S} &= \bar{C}_{13} + \left(\frac{\bar{C}_{26}\bar{C}_{36} - \bar{C}_{23}\bar{C}_{66}}{\bar{C}_{22}\bar{C}_{66} - \bar{C}_{26}^{2}} \right)\bar{C}_{12} + \left(\frac{\bar{C}_{26}\bar{C}_{23} - \bar{C}_{36}\bar{C}_{22}}{\bar{C}_{22}\bar{C}_{66} - \bar{C}_{26}^{2}} \right)\bar{C}_{16} \\
\bar{C}_{33}^{S} &= \bar{C}_{33} + \left(\frac{\bar{C}_{26}\bar{C}_{36} - \bar{C}_{23}\bar{C}_{66}}{\bar{C}_{22}\bar{C}_{66} - \bar{C}_{26}^{2}} \right)\bar{C}_{23} + \left(\frac{\bar{C}_{26}\bar{C}_{23} - \bar{C}_{36}\bar{C}_{22}}{\bar{C}_{22}\bar{C}_{66} - \bar{C}_{26}^{2}} \right)\bar{C}_{36} \\
\bar{C}_{44}^{S} &= \bar{C}_{55} - \frac{\bar{C}_{45}^{2}}{\bar{C}_{44}}
\end{aligned}
\tag{2.22}
$$

Finally, the nonlinear variational statement for laminated beams in terms of displacements may be expressed as

$$
\begin{aligned}
\delta\Pi = \int_{\Omega} \Bigg\{ & \left[\bar{B}_{44}^{ij} u_j + \bar{B}_{44}^{jl} \frac{\partial w_j}{\partial \eta} - \bar{B}_{44}^{jl} \frac{u_j}{R'} - \bar{B}_{44}^{ij} \frac{u_j}{R'} - \frac{B_{44}^{ij}}{R'} \frac{\partial w_j}{\partial \eta} + \frac{B_{44}^{ij}}{R'} \frac{u_j}{R'} \right] (\delta u_i) \\
& + \left[\frac{B_{11}^{ij}}{R'} \frac{\partial u_j}{\partial \eta} + \frac{B_{11}^{ij}}{R'} \frac{w_j}{R'} + \frac{\bar{B}_{13}^{ij}}{R'} w_j + \bar{B}_{13}^{jl} \frac{\partial u_j}{\partial \eta} + \bar{B}_{13}^{jl} \frac{w_j}{R'} \right. \\
& \left. + \bar{B}_{33}^{ij} w_j + \frac{1}{2} \frac{B_{11}^{ijk}}{R'} \frac{\partial w_j}{\partial \eta} \frac{\partial w_k}{\partial \eta} + \frac{1}{2} \bar{B}_{13}^{jkl} \frac{\partial w_j}{\partial \eta} \frac{\partial w_k}{\partial \eta} \right] (\delta w_i) \\
& + \left[B_{11}^{ij} \frac{\partial u_j}{\partial \eta} + B_{11}^{ij} \frac{w_j}{R'} + \bar{B}_{13}^{ij} w_j + \frac{1}{2} B_{11}^{ijk} \frac{\partial w_j}{\partial \eta} \frac{\partial w_k}{\partial \eta} \right] \left(\frac{\partial \delta u_i}{\partial \eta} \right) \\
& + \left[B_{11}^{ijk} \frac{\partial u_k}{\partial \eta} \frac{\partial w_j}{\partial \eta} + B_{11}^{ijk} \frac{w_k}{R'} \frac{\partial w_j}{\partial \eta} + \bar{B}_{13}^{ijk} \frac{\partial w_j}{\partial \eta} w_k + \bar{B}_{44}^{ij} u_j + B_{44}^{ij} \frac{\partial w_j}{\partial \eta} \right. \\
& \left. - B_{44}^{ij} \frac{u_j}{R'} + \frac{1}{2} B_{11}^{ijkl} \frac{\partial w_j}{\partial \eta} \frac{\partial w_j}{\partial \eta} \frac{\partial w_l}{\partial \eta} \right] \left(\frac{\partial \delta w_i}{\partial \eta} \right) \Bigg\} d\Omega_b + \delta V
\end{aligned}
\tag{2.23}
$$

for all i,j,k,l = 1, 2, ..., number of beam interfaces.

Here Ω_b represents the in-plane area of the beam elements and where

$$B^{ij}_{\alpha\beta} = \int_{\frac{-h}{2}}^{\frac{h}{2}} \overline{C}^{S}_{\alpha\beta}\phi^{i}\phi^{j}dz\,, \qquad B^{ijk}_{\alpha\beta} = \int_{\frac{-h}{2}}^{\frac{h}{2}} \overline{C}^{S}_{\alpha\beta}\phi^{i}\phi^{j}\phi^{k}dz$$

$$B^{ijkl}_{\alpha\beta} = \int_{\frac{-h}{2}}^{\frac{h}{2}} \overline{C}^{S}_{\alpha\beta}\phi^{i}\phi^{j}\phi^{k}\phi^{l}dz\,, \qquad \overline{B}^{ij}_{\alpha\beta} = \int_{\frac{-h}{2}}^{\frac{h}{2}} \overline{C}^{S}_{\alpha\beta}\phi^{i}\frac{d\phi^{j}}{dz}dz \tag{2.24}$$

$$\overline{B}^{ijk}_{\alpha\beta} = \int_{\frac{-h}{2}}^{\frac{h}{2}} \overline{C}^{S}_{\alpha\beta}\phi^{i}\phi^{j}\frac{d\phi^{k}}{dz}dz\,, \qquad \overline{\overline{B}}^{ij}_{\alpha\beta} = \int_{\frac{-h}{2}}^{\frac{h}{2}} \overline{C}^{S}_{\alpha\beta}\frac{d\phi^{i}}{dz}\frac{d\phi^{j}}{dz}dz$$

Here h is the beam height and integration is made through the height of the beam dz.

Note that $B^{ij}_{\alpha\beta}$, $\overline{B}^{ij}_{\alpha\beta}$, $B^{ijk}_{\alpha\beta}$, and $B^{ijkl}_{\alpha\beta}$ are symmetric in their subscripts and superscripts.

$$B^{ij}_{\alpha\beta} = B^{ji}_{\alpha\beta}\,, \quad B^{ij}_{\alpha\beta} = B^{ij}_{\beta\alpha}$$
$$B^{ijk}_{\alpha\beta} = B^{jik}_{\alpha\beta} = B^{kjl}_{\alpha\beta} = B^{kij}_{\alpha\beta} = B^{ikj}_{\alpha\beta}\,, \quad etc. \tag{2.25}$$

The coefficients with a single bar over them are not symmetric with respect to the superscripts.

The potential of the external forces for a beam is given as

$$\delta V_s = \int_0^{L_s} \left\{ + \overline{F}_s \frac{\partial w_i}{\partial \eta}\frac{\partial \delta w_j}{\partial \eta} \right\} d\eta \tag{2.26}$$

for all i,j = 1, 2, ..., number of beam interfaces.

where L_s is the length of the beam and $\overline{F}_s$ is the force acting along the length of the stiffener.

2.6 Failure Equations

The various failure criteria were discussed in section 1.2.3. In this study, a macromechanics based first-ply failure analysis will be conducted for some select cases. As discussed previously there are many macromechanics based failure criteria. The failure analysis involves calculating the stresses and strains at a point in the structure and then applying the selected criterion. These criterion include the the experimentally determined macroscopic material strength data. In this research work, the Tsai-Wu failure theory is used as the working failure criterion. The Tsai-Wu criterion was selected because of its general character. The Tsai-Wu criterion has three distinct advantages: (1) invariance under coordinate rotation; (2) transformations are made via known tensor transformations; and (3) there exists symmetry of properties similar to those of the stiffnesses and compliances. Therefore, the Tsai-Wu criterion was selected for this work.

The Tsai-Wu criterion is given by the following expression

$$F_i\sigma_i + F_{ij}\sigma_i\sigma_j \geq 1 \quad i, j = 1, \ldots, 6 \tag{2.27}$$

Here σ_i are the stress components and F_i and F_{ij} are the strength terms. The strength tensor terms may be expressed as

$$F_1 = \frac{1}{X_T} - \frac{1}{X_C}$$
$$F_2 = \frac{1}{Y_T} - \frac{1}{Y_C} \qquad \text{(cont.)}$$
$$F_3 = \frac{1}{Z_T} - \frac{1}{Z_C}$$

$$
\begin{aligned}
F_{11} &= \frac{1}{X_T X_C} \\
F_{22} &= \frac{1}{Y_T Y_C} \\
F_{33} &= \frac{1}{R^2} \\
F_{44} &= \frac{1}{S^2} \\
F_{55} &= \frac{1}{T^2} \\
F_{66} &= \frac{1}{Z_T Z_C} \\
F_{12} &= -\frac{1}{2} \frac{1}{\sqrt{X_T X_C Y_T Y_C}} \\
F_{13} &= -\frac{1}{2} \frac{1}{\sqrt{X_T X_C Z_T Z_C}} \\
F_{23} &= -\frac{1}{2} \frac{1}{\sqrt{Y_T Y_C Z_T Z_C}}
\end{aligned}
\tag{2.28}
$$

All other strength tensor components are zero. Here σ_1, σ_2, σ_3 are the normal stress components, σ_4, σ_5, σ_6 are the shear stress components, $X_T\,(X_C)$, $Y_T\,(Y_C)$, $Z_T\,(Z_C)$ are the lamina normal tensile (compressive) strengths in the x, y, z directions respectively, and R, S, T are the shear strengths in the yz, xz, and xy planes respectively. The values for X_T, X_C, Y_T, Y_C, Z_T, Z_C, R, S, and T will be given later in this research work.

Chapter 3

Ritz Buckling Method

3.1 Introduction

In this chapter a method is developed to study the buckling of stiffened cylindrical composite shells with discrete stiffeners using a closed form analytical solution. The stiffeners are directly attached to the shell where the components of the displacements between the shell skin and the stiffeners is accomplished via the application of the Lagrange multiplier method. Many of the equations developed in Chapter 2 are applicable to the Ritz buckling method derived here, but some simplifications are also incorporated. In lieu of layerwise beams, the Euler-Bernoulli beam theory is used in developing the discrete stiffeners. The method developed in this chapter is applicable to cross-ply and some quasi-isotropic shell layups. In this study, simply supported edge boundary conditions will be assumed in order to apply the closed form solutions. Equations (2.1)-(2.6) and (2.12)-(2.19) are applicable for the layerwise shell used in this approach. The Euler-Bernoulli beam theory is presented in the next section.

3.2 Euler-Bernoulli Beam Stiffeners

The governing equations for the Euler-Bernoulli beams are developed in a procedure similar to that for layerwise beams of sections 2.3 and 2.5. The stiffeners are modeled as discrete structures and thus the development of a generic stiffening element may be applied to axial, ring, or geodesic stiffeners. The displacements for a stiffener using the Euler-Bernoulli beam theory are given by the following relation

$$\begin{aligned} u &= u_s^i - \zeta \frac{\partial w_s^i}{\partial \eta} \quad i = 1, 2, \ldots, T \\ w &= w_s^i \end{aligned} \tag{3.1}$$

where u_s^i and w_s^i are the displacements for each of the T stiffeners. Here u is the local displacement of the stiffeners. For ring stiffeners the u's are replaced by v's. A description of the stiffener coordinate system is provided in Figure 4.

The Euler-Bernoulli strains for the stiffeners are developed from the displacements and are given as

$$\varepsilon_1 = \varepsilon_s^i = \frac{\partial u_s^i}{\partial \eta} + \frac{1}{2}\left(\frac{\partial w_s^i}{\partial \eta}\right)^2 + \frac{w_s^i}{R'} - \zeta \frac{\partial^2 w_s^i}{\partial \eta^2} \quad i = 1, 2, \ldots, T \tag{3.2}$$

The definition of R' was developed in section 2.3. Here ζ is the distance from the stiffener centroid to the reference surface. The uniaxial stress-strain equation for the stiffeners is

$$\sigma_s^i = E_s^i \varepsilon_s^i \quad i = 1, 2, \ldots, T \tag{3.3}$$

where σ_s^i is the stress in an individual stiffener, E_s^i is the modulus of the stiffener, and ε_s^i is the strain in an individual stiffener.

The variation of the potential energy for the stiffeners may be expressed as

$$\delta\Pi = \delta U_s^i + \delta V_s^i \quad i = 1, 2, \ldots, T \tag{3.4}$$

The variation of the strain energy δU_s^i for an individual stiffener may be expressed as

$$\begin{aligned}
\delta U_s^i &= \int_0^{L_s^i} \left\{ \int_{A_s^i} \sigma_s^i \delta\varepsilon_s^i dA_s^i \right\} d\eta \\
&= \int_0^{L_s^i} \left\{ E_s^i A_s^i \left[\frac{\partial u_s^i}{\partial \eta} + \frac{w_s^i}{R'} + \frac{1}{2}\left(\frac{\partial w_s^i}{\partial \eta} \right)^2 \right] \right. \\
&\quad \cdot \left[\frac{\partial \delta u_s^i}{\partial \eta} + \frac{\delta w_s^i}{R'} + \frac{\partial w_s^i}{\partial \eta}\frac{\partial \delta w_s^i}{\partial \eta} \right] + E_s^i I_s^i \frac{\partial^2 w_s^i}{\partial \eta^2}\frac{\partial^2 \delta w_s^i}{\partial \eta^2} \\
&\quad - \bar{\zeta}_s^i A_s^i E_s^i \frac{\partial^2 w_s^i}{\partial \eta^2}\left[\frac{\partial \delta u_s^i}{\partial \eta} + \frac{\delta w_s^i}{R'} + \frac{\partial w_s^i}{\partial \eta}\frac{\partial \delta w_s^i}{\partial \eta} \right] \\
&\quad \left. - \bar{\zeta}_s^i A_s^i E_s^i \frac{\partial^2 \delta w_s^i}{\partial \eta^2}\left[\frac{\partial u_s^i}{\partial \eta} + \frac{w_s^i}{R'} + \frac{1}{2}\left(\frac{\partial w_s^i}{\partial \eta} \right)^2 \right] \right\} d\eta
\end{aligned} \tag{3.5}$$

for i = 1, 2, ..., T.

where

- I_s^i = moment of inertia of an individual stiffener about the reference surface (ie., $\bar{\zeta}$ = 0) and thus $I_s^i = \hat{I}_{xc}^i + (\bar{\zeta}_s^i)^2 A_s^i$.

- $\bar{\zeta}_s^i$ = distance from the stiffener centroid to the reference surface.

- L_s^i = length of an individual stiffener.

The variation of the external forces for the Euler-Bernoulli beam stiffeners is developed from the potential energy statement and is expressed as

$$\delta V_s^i = \int_0^{L_s^i} \left\{ + \bar{F}_s \frac{\partial w_s^i}{\partial \eta} \frac{\partial \delta w_s^i}{\partial \eta} \right\} d\eta \quad i = 1, 2, \ldots, T \tag{3.6}$$

where $\bar{F}_s^i$ is the force acting along the length of the stiffener.

3.3 Lagrange Multiplier Method

The procedure used in applying the fundamental mathematical principles of Lagrange multipliers is described briefly in this section. The Lagrange multiplier method will be used to constrain the discrete stiffeners to the shell surface. Proof of the validity of the Lagrange multiplier method is provided in references [118, 119]. Al-Shareedah and Seireg [120-122] successfully applied the Lagrange multiplier method to stiffened plates. Phillips and Gürdal [123] applied this method in the stability analysis of orthotropic plates with multiple orthotropic geodesic stiffeners under in-plane loadings. A description of the Lagrange multiplier method follows.

Let it be required to minimize a function of I variables $x_1, x_2, \ldots, x_I$

$$f(x_1, x_2, \ldots, x_I) \tag{3.7}$$

where the x's are not independent but are bound together by J independent constraint functions h_J such that

$$\begin{aligned} h_1(x_1, x_2, \ldots, x_I) &= 0 \\ h_2(x_1, x_2, \ldots, x_I) &= 0 \\ &\vdots \\ h_J(x_1, x_2, \ldots, x_I) &= 0 \end{aligned} \tag{3.8}$$

Lagrange's method of simultaneously minimizing f and satisfying the constraint functions is to minimize a composite function L called the Lagrangian defined as

$$\begin{aligned} L(\bar{x}, \bar{\alpha}) &= f(\bar{x}) + \alpha_1 h_1(\bar{x}) + \alpha_2 h_2(\bar{x}) + \cdots + \alpha_J h_J(\bar{x}) \\ &= f(\bar{x}) + \sum_{j=1}^{J} \alpha_j h_j(\bar{x}) \end{aligned} \tag{3.9}$$

where $\bar{x}$ denotes the vector of variables $x_1, x_2, \ldots, x_I$ and $\bar{\alpha}$ is the vector of undetermined Lagrange multipliers $\alpha_1, \alpha_2, \ldots, \alpha_J$ The necessary conditions for $f(\bar{x})$ to be a minimum while simultaneously satisfying the constraints $\bar{\alpha}$ are

$$\begin{aligned} \frac{\partial L(\bar{x}, \bar{\alpha})}{\partial x_i} &= 0 \qquad i = 1, 2, \ldots, I \\ \frac{\partial L(\bar{x}, \bar{\alpha})}{\partial \alpha_j} &= 0 \qquad i = 1, 2, \ldots, J \end{aligned} \tag{3.10}$$

Differentiation of Eq. (3.9) results in the following set of equations

$$\begin{aligned} &\frac{\partial f(\bar{x})}{\partial x_i} + \sum_{j=1}^{J} \alpha_j \frac{\partial h_j(\bar{x})}{\partial x_i} = 0 \qquad i = 1, 2, \ldots, I \\ &h_j(\bar{x}) = 0 \qquad\qquad\qquad\qquad\qquad\quad j = 1, 2, \ldots, J \end{aligned} \tag{3.11}$$

Equation (3.11) is a set of (I + J) simultaneous equations for (I + J) unknowns $\bar{x}$ and $\bar{\alpha}$ The Lagrange multipliers may be used for variational type problems where the variational statement is considered a functional similar to $f(\bar{x})$. The Lagrange multipliers may be used to constrain the displacements and or rotations of a discretely stiffened structure.

3.4 Stiffened Shell System

In this study, the stiffeners are treated as discrete structures and are attached to the skin using the Lagrange multiplier constraint technique discussed in the previous section. See Figure 7 for a representation of a discretely stiffened shell showing the constraint points. The variation of the total potential energy for the stiffened cylindrical shell may be expressed as

$$\delta\Pi = \delta U_{\text{SHELL}} + \delta U_{\text{STIFF}} + \delta V_{\text{SHELL}} + \delta V_{\text{STIFF}} \tag{3.12}$$

The virtual work for the shell was derived and is shown in Eqs. (2.12)-(2.19) and in Appendix A. The Euler-Bernoulli beam strain energy and potential energy was shown in Eqs. (3.5) and (3.6) respectively. For the buckling analysis used here only the linear portion of the virtual work statement is applicable and thus is given as

$$\begin{aligned}\delta\Pi = \int_\Omega \Bigg[& M_1^l \frac{\partial \delta u_l}{\partial x} + M_2^l\left(\frac{\partial \delta v_l}{\partial y} + \frac{1}{R}\delta w_l\right) + M_6^l\left(\frac{\partial \delta u_l}{\partial y} + \frac{\partial \delta v_l}{\partial x}\right) \\ & + Q_1^l \delta u_l + Q_2^l \delta v_l + Q_3^l \delta w_l - \frac{1}{R} K_2^l \delta v_l + K_1^l \frac{\partial \delta w_l}{\partial x} + K_2^l \frac{\partial \delta w_l}{\partial y} \\ & + \overline{N}_1 \frac{\partial \delta w_l}{\partial x}\frac{\partial w_J}{\partial x} + 2\overline{N}_6\left(\frac{\partial \delta w_l}{\partial x}\frac{\partial w_J}{\partial y} + \frac{\partial w_J}{\partial x}\frac{\partial \delta w_l}{\partial y}\right) + \overline{N}_2 \frac{\partial \delta w_l}{\partial y}\frac{\partial w_J}{\partial y} \Bigg\} \, d\Omega\end{aligned}$$

$$+\sum_{k=1}^{T}\int_0^{L_s^k}\left\{E_s^kA_s^k\left(\frac{\partial u_s^k}{\partial\eta}+\frac{w_s^k}{R'}\right)\left(\frac{\partial\delta u_s^k}{\partial\eta}+\frac{\delta w_s^k}{R'}\right)+E_s^kI_s^k\frac{\partial^2 w_s^k}{\partial\eta^2}\frac{\partial^2\delta w_s^k}{\partial\eta^2}\right.$$
$$-\bar{\zeta}_s^kA_s^kE_s^k\frac{\partial^2 w_s^k}{\partial\eta^2}\left(\frac{\partial\delta u_s^k}{\partial\eta}+\frac{\delta w_s^k}{R'}\right)-\bar{\zeta}_s^kA_s^kE_s^k\frac{\partial^2\delta w_s^k}{\partial\eta^2}\left(\frac{\partial u_s^k}{\partial\eta}+\frac{w_s^k}{R'}\right) \quad (3.13)$$
$$\left.+\bar{F}_s^k\frac{\partial w_s^k}{\partial\eta}\frac{\partial\delta w_s^k}{\partial\eta}\right\}d\eta$$

for i,j = 1, 2, ..., N + 1 and for k = 1, 2, ..., T (number of stiffeners).

The definitions of M_1^i, M_2^i, M_6^i, Q_1^i, Q_2^i, Q_3^i, K_1^i, K_2^i, $\overline{N}_1$, $\overline{N}_2$, and $\overline{N}_6$ are provided in Eqs. (2.15) and (2.17). The development presented here is for specially orthotropic cylinders where $\overline{C}_{16} = \overline{C}_{26} = \overline{C}_{36} = \overline{C}_{45} = 0$. However, when the values of $\overline{C}_{16}$, $\overline{C}_{26}$, $\overline{C}_{36}$, and $\overline{C}_{45}$ are small such as the case for certain quasi-isotropic materials then the layerwise Ritz method should provide reasonable results. This is demonstrated in the results presented in Chapter 5.

For a buckling analysis we have

$$\begin{aligned}\overline{N}_1 &= \lambda\hat{N}_1\\ \overline{N}_2 &= \lambda\hat{N}_2\\ \overline{N}_6 &= \lambda\hat{N}_6\\ \overline{F}_s^k &= \lambda\hat{F}_s^k\end{aligned} \quad (3.14)$$

where λ is the minimum buckling eigenvalue.

We have

- $\hat{N}_1 = -1$, $\hat{N}_2 = 0$, $\hat{N}_6 = 0$, buckling under axial compressive load.

- $\hat{N}_1 = 0,\ \hat{N}_2 = -1,\ \hat{N}_6 = 0$, buckling under lateral pressure.

3.5 Buckling Solutions and Equations

The Ritz method will be employed for this buckling analysis. The results may be compared to other solution procedures like those described by Jones [90,91], Reddy [37], and linear finite element methods. The global buckling solution of stiffened circular cylindrical shells consists of solving Eq. (3.12) such that

$$\delta\Pi = 0 \tag{3.15}$$

In order to solve the equations using a Ritz variational approach, a solution must be assumed. In this study, simply supported edge conditions will be studied. The edge boundary conditions for the shell skin and the individual stiffeners are (see Figure 2)

$$w = v = 0 \text{ at } x = 0,\ L \tag{3.16}$$

The following solutions of the Navier form which satisfy the boundary conditions are assumed:

Shell Skin

$$\begin{aligned} u_i &= U_i^{mn} \cos(\alpha_m x) \cos(\beta_n y) \quad i = 1, 2, \ldots, (N+1) \\ v_i &= V_i^{mn} \sin(\alpha_m x) \sin(\beta_n y) \ ; \ \alpha_m = \frac{m\pi}{L}, \quad \beta_n = \frac{n}{R} \\ w_i &= W_i^{mn} \sin(\alpha_m x) \cos(\beta_n y) \end{aligned} \tag{3.17}$$

where U_i^{mn}, V_i^{mn}, and W_i^{mn} amplitudes are to be determined for each mode (m, n).

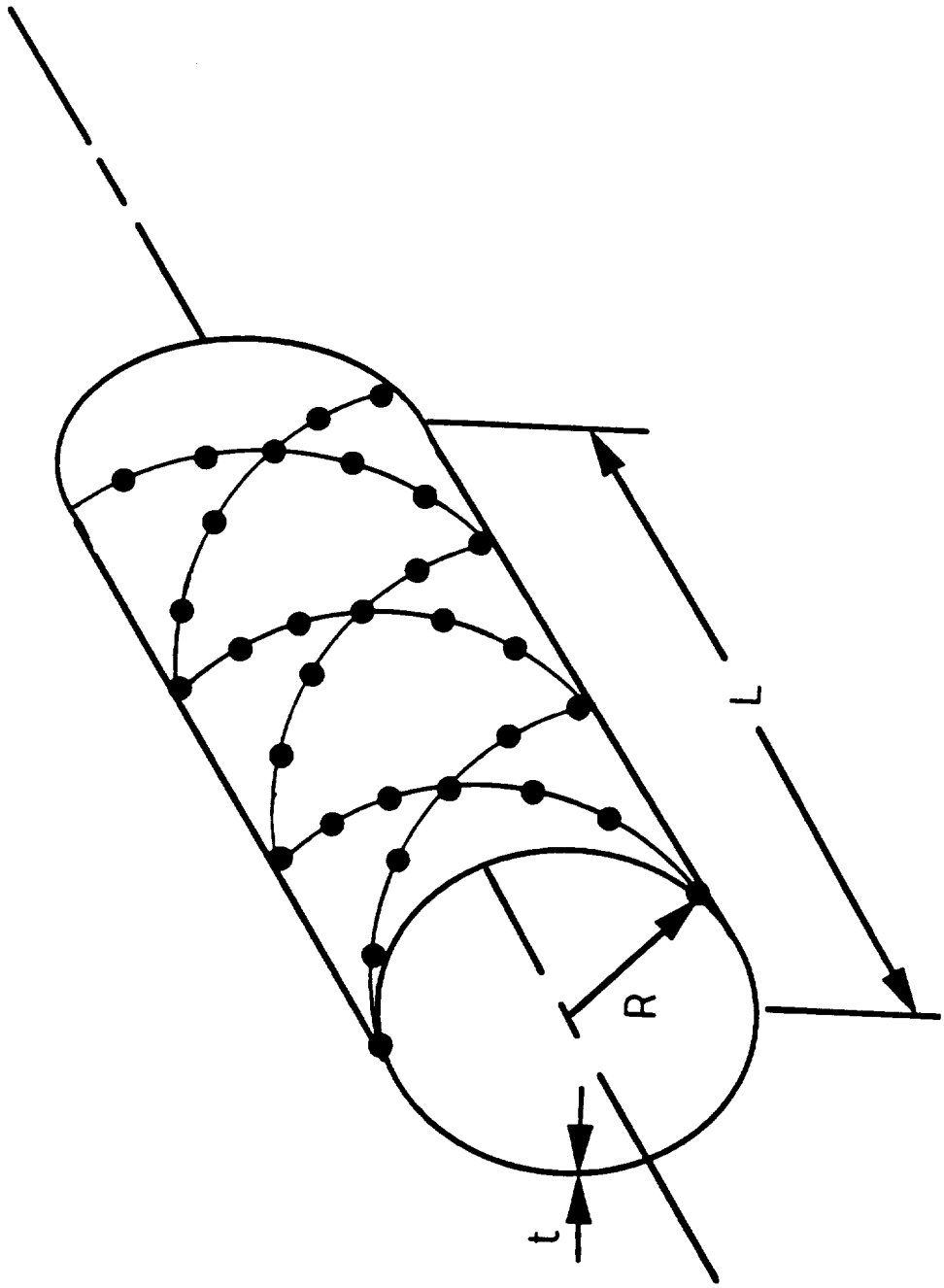

Figure 7. Geodesically stiffened cylindrical shell showing the Lagrange constraint points.

Axial and Geodesic Stiffeners

$$u_s^i = U_s^{ik}\cos(\alpha_k x) \;\; ; \;\; \alpha_k = \frac{k\pi}{L_s^i}, \quad i = 1, 2, \ldots, T$$
$$w_s^i = W_s^{ik}\sin(\alpha_k x) \tag{3.18}$$

Ring Stiffeners

$$v_s^l = V_s^{il}\sin(\beta_l y) \;\; ; \;\; \beta_l = \frac{l}{R}, \quad i = 1, 2, \ldots, T$$
$$w_s^l = W_s^{il}\cos(\beta_l y) \tag{3.19}$$

where U_s^{ik} (V_s^{il}) and W_s^{ik} (W_s^{il}) amplitudes are to be determined for each stiffener mode k (l). For axial stiffeners the η axis is along the x direction and for ring stiffeners the η axis is along the y direction.

Substituting Eqs. (3.17)-(3.19) into the buckling expression, Eq. (3.13), and integrating over the regions ($L_c = 2\pi R$) below

$$\begin{aligned}\delta\Pi &= \int_\Omega (\delta U_{\text{SHELL}} + \delta V_{\text{SHELL}})\, d\Omega + \int_0^{L_\eta} (\delta U_{\text{STIFF}} + \delta V_{\text{STIFF}})\, d\eta \\ &= \int_0^{L_c}\int_0^{L} (\delta U_{\text{SHELL}} + \delta V_{\text{SHELL}})\, dx\, dy + \int_0^{L_\eta} (\delta U_{\text{STIFF}} + \delta V_{\text{STIFF}})\, d\eta\end{aligned} \tag{3.20}$$

yields the following expression

$$
\begin{aligned}
0 = \delta\Pi = \frac{LL_c}{4}\Big\{&\Big(D_{11}^{ij}\alpha_m{}^2 + D_{66}^{ij}\beta_n{}^2 + \bar{\bar{D}}_{55}^{ij}\Big)U_j^{mn} - \alpha_m\beta_n\big(D_{12}^{ij} + D_{66}^{ij}\big)V_j^{mn} \\
&- \alpha_m\Big(\frac{1}{R}D_{12}^{ij} + \bar{D}_{13}^{ij} - \bar{D}_{55}^{jl}\Big)\Big\}\delta U_i^{mn} + \frac{LL_c}{4}\Big\{-\alpha_m\beta_n\big(D_{12}^{ij} + D_{66}^{ij}\big)U_j^{mn} \\
&+ \Big(D_{66}^{ij}\alpha_m{}^2 + D_{22}^{ij}\beta_n{}^2 + \bar{\bar{D}}_{44}^{ij} - \frac{1}{R}\big(\bar{D}_{44}^{ij} + \bar{D}_{44}^{jl}\big) + \frac{1}{R^2}D_{44}^{ij}\Big)V_j^{mn} \\
&+ \beta_n\Big(\frac{1}{R}D_{22}^{ij} + \frac{1}{R}D_{44}^{ij} + \bar{D}_{23}^{ij} - \bar{D}_{44}^{jl}\Big)W_j^{mn}\Big\}\delta V_i^{mn} + \frac{LL_c}{4}\Big\{-\alpha_m\big(\bar{D}_{13}^{jl} \\
&- \bar{D}_{55}^{ij} + \frac{1}{R}D_{12}^{ij}\Big)U_j^{mn} + \beta_n\Big(\frac{1}{R}D_{22}^{ij} + \frac{1}{R}D_{44}^{ij} + \bar{D}_{23}^{jl} - \bar{D}_{44}^{ij}\Big)V_j^{mn} \\
&+ \Big(D_{55}^{ij}\alpha_m{}^2 + D_{44}^{ij}\beta_n{}^2 + \frac{1}{R^2}D_{22}^{ij} + \frac{1}{R}\bar{D}_{23}^{ij} + \frac{1}{R}\bar{D}_{23}^{jl} + \bar{\bar{D}}_{33}^{jl}\Big)W_j^{mn} \\
&+ \lambda\big(\hat{N}_1\alpha_m{}^2 + \hat{N}_2\beta_n{}^2\big)W_j^{mn}\Big\}\delta W_i^{mn} \\
&+ \sum_{i=1}^{T}\frac{L_s^i}{2}\Big\{E_s^iA_s^i\Big(\alpha_k{}^2U_s^{ik} - \alpha_k\frac{W_s^{ik}}{R'} - \bar{\zeta}_s^i\alpha_k{}^3W_s^{ik}\Big)\delta U_s^{jk} \\
&+ \Big[E_s^iI_s^i\alpha_k{}^4W_s^{ik} - E_s^iA_s^i\bar{\zeta}_s^i\Big(\alpha_k{}^3U_s^{ik} - \frac{2}{R'}\alpha_k{}^2W_s^{ik}\Big) \\
&+ \frac{E_s^iA_s^i}{R'}\Big(-\alpha_kU_s^{ik} + \frac{W_s^{ik}}{R'}\Big) + \lambda\hat{F}_s^i\alpha_k{}^2W_s^{ik}\Big]\delta W_s^{jk}\Big\}
\end{aligned}
\tag{3.21}
$$

For ring stiffeners replace U_s^{ik} by V_s^{il}, W_s^{ik} by W_s^{il}, and α_k by $(-\beta_l)$.

3.6 Constraint Equations

In this part of the study the displacements u and w of the shell and stiffeners will be constrained (v and w for ring stiffeners) to attach the stiffeners to the shell skin. The compatibility of displacements is imposed at a finite number of points along each

stiffener (see Figure 7). The compatibility of displacement equations may be expressed as

Axial and Geodesic Stiffener Constraint Equations

$$
\begin{aligned}
e_{jp} &= u_i - u_s^j = U_i^{mn}\cos(\alpha_m x_{jp})\cos(\beta_n y_{jp}) - U_s^{jk}\cos(\alpha_k \eta_{jp}) = 0 \\
f_{jp} &= w_i - w_s^j = W_i^{mn}\sin(\alpha_m x_{jp})\cos(\beta_n y_{jp}) - W_s^{jk}\sin(\alpha_k \eta_{jp}) = 0 \\
& \qquad\qquad i = 1, 2, \ldots, (N+1) \\
& \qquad\qquad j = 1, 2, \ldots, T \\
& \qquad\qquad p = 1, 2, \ldots, P
\end{aligned}
\tag{3.22}
$$

Ring Stiffener Constraint Equations

$$
\begin{aligned}
g_{jp} &= v_i - v_s^j = V_i^{mn}\sin(\alpha_m x_{jp})\sin(\beta_n y_{jp}) - V_s^{jl}\sin(\beta_l \eta_{jp}) = 0 \\
h_{jp} &= w_i - w_s^j = W_i^{mn}\sin(\alpha_m x_{jp})\cos(\beta_n y_{jp}) - W_s^{jl}\cos(\beta_l \eta_{jp}) = 0 \\
& \qquad\qquad i = 1, 2, \ldots, (N+1) \\
& \qquad\qquad j = 1, 2, \ldots, T \\
& \qquad\qquad p = 1, 2, \ldots, P
\end{aligned}
\tag{3.23}
$$

Here the subscript p represents the number of constraint points for P total constraint points along the stiffeners. A set of Lagrange multipliers may be developed where one multiplier is required for each constraint condition. The equations take the form

$$L = \gamma_{jp} e_{jp} + \mu_{jp} f_{jp} + \phi_{jp} g_{jp} + \psi_{jp} h_{jp} \tag{3.24}$$

where γ_{jp}, μ_{jp}, ϕ_{jp}, and ψ_{jp} are the Lagrange multipliers and L is the set of Lagrange multiplier equations. The system of Lagrange multipliers L may be added to the potential energy Π to form a variational functional I such that

$$I = \Pi + L \tag{3.25}$$

In order to minimize the functional, the variation of I may be set equal to 0 so that

$$\delta I = \delta \Pi + \delta L = 0 \tag{3.26}$$

The minimum potential energy $\delta\Pi$ has been defined previously. The variation of the set of Lagrange multipliers is

$$\begin{aligned}
\delta L = {} & \delta\gamma_{jp} e_{jp} + \gamma_{jp}\delta U_i^{mn} \cos(\alpha_m x_{jp}) \cos(\beta_n y_{jp}) - \gamma_{jp}\delta U_s^{jk} \cos(\alpha_k \eta_{jp}) \\
& + \delta\mu_{jp} f_{jp} + \mu_{jp}\delta W_i^{mn} \sin(\alpha_m x_{jp}) \cos(\beta_n y_{jp}) - \mu_{jp}\delta W_s^{jk} \sin(\alpha_k \eta_{jp}) \\
& + \delta\phi_{jp} g_{jp} + \phi_{jp}\delta V_i^{mn} \sin(\alpha_m x_{jp}) \sin(\beta_n y_{jp}) - \phi_{jp}\delta V_s^{jl} \sin(\beta_n \eta_{jp}) \\
& + \delta\psi_{jp} h_{jp} + \psi_{jp}\delta W_i^{mn} \sin(\alpha_m x_{jp}) \cos(\beta_n y_{jp}) - \psi_{jp}\delta W_s^{jl} \sin(\beta_n \eta_{jp})
\end{aligned} \tag{3.27}$$

From Eq. (3.26) $\delta I = 0$ so the individual components must therefore be 0 and hence

$$\begin{aligned}
\delta U_i^{mn} &= 0 & \delta\gamma_{jp} &= 0 \\
\delta V_i^{mn} &= 0 & \delta\mu_{jp} &= 0 \\
\delta W_i^{mn} &= 0 & \delta\phi_{jp} &= 0 \\
\delta U_s^{jk} &= 0 & \delta\psi_{jp} &= 0 \\
\delta W_s^{jk} &= 0 & & \\
\delta V_s^{jl} &= 0 & & \\
\delta W_s^{jl} &= 0 & &
\end{aligned} \tag{3.28}$$

Eq. (3.28) yields 11 sets of equations which may be solved. If no ring stiffeners are present then 9 sets of equations must be solved. Similarly, if no axial or geodesic stiffeners are present then 9 sets of equations must be solved. Carrying out the operations of Eq. (3.28) yields the following sets of equations.

$$\delta U_i^{mn}\colon \frac{LL_c}{4}\left\{\left(D_{11}^{ij}\alpha_m{}^2 + D_{66}^{ij}\beta_n{}^2 + \bar{\bar{D}}_{55}^{ij}\right)U_j^{mn} - \alpha_m\beta_n\left(D_{12}^{ij} + D_{66}^{ij}\right)V_j^{mn}\right.$$
$$\left. - \alpha_m\left(\frac{1}{R}D_{12}^{ij} + \bar{D}_{13}^{ij} - \bar{D}_{55}^{ij}\right)W_j^{mn}\right\} + \gamma_{jp}\cos(\alpha_m x_{jp})\cos(\beta_n y_{jp}) = 0 \tag{3.29a}$$

$$\delta V_i^{mn}\colon \frac{LL_c}{4}\left\{-\alpha_m\beta_n\left(D_{12}^{ij} + D_{66}^{ij}\right)U_j^{mn} + \left(D_{66}^{ij}\alpha_m{}^2 + D_{22}^{ij}\beta_n{}^2 + \bar{\bar{D}}_{44}^{ij} - \frac{1}{R}\left(\bar{D}_{44}^{ij}\right.\right.\right.$$
$$\left.\left.\left. + \bar{D}_{44}^{ji}\right) + \frac{1}{R^2}D_{44}^{ij}\right)V_j^{mn} + \beta_n\left(D_{22}^{ij} + \frac{1}{R}D_{44}^{ij} + \bar{D}_{23}^{ij} - \bar{D}_{44}^{ji}\right)W_j^{mn}\right\} \tag{3.29b}$$
$$+ \phi_{jp}\sin(\alpha_m x_{jp})\sin(\beta_n y_{jp}) = 0$$

$$\delta W_i^{mn}\colon \frac{LL_c}{4}\left\{-\alpha_m\left(\frac{1}{R}D_{12}^{ij} + \bar{D}_{13}^{ji} - \bar{D}_{55}^{ij}\right)U_j^{mn}\right.$$
$$+ \beta_n\left(\frac{1}{R}D_{22}^{ij} + \frac{1}{R}D_{44}^{ij} + \bar{D}_{23}^{ji} - \bar{D}_{44}^{ij}\right)V_j^{mn}$$
$$+ \left(D_{55}^{ij}\alpha_m{}^2 + D_{44}^{ij}\alpha_m{}^2 + D_{44}^{ij}\beta_n{}^2 + \frac{1}{R^2}D_{22}^{ij} + \frac{1}{R}\bar{D}_{23}^{ij}\right. \tag{3.29c}$$
$$\left.\left. + \frac{1}{R}\bar{D}_{23}^{ji} + \bar{\bar{D}}_{33}^{ij}\right)W_j^{mn} + \lambda\left(\hat{N}_1\alpha_m{}^2 + \hat{N}_2\beta_n{}^2\right)W_j^{mn}\right\}$$
$$+ \mu_{jp}\sin(\alpha_m x_{jp})\cos(\beta_n y_{jp}) + \psi_{jp}\sin(\alpha_m x_{jp})\cos(\beta_n y_{jp}) = 0$$

$$\delta U_s^{jk}\colon \frac{L_s^j}{2}\left\{E_s^j A_s^j\left(\alpha_k{}^2 U_s^{jk} - \alpha_k\frac{W_s^{jk}}{R'} - \bar{\zeta}_s^j\alpha_k{}^3 W_s^{jk}\right)\right\} - \gamma_{jp}\cos(\alpha_k\eta_{jp}) = 0 \tag{3.29d}$$

$$\delta W_s^{jk}\colon \frac{L_s^j}{2}\left\{E_s^j I_s^j\alpha_k{}^4 W_s^{jk} - E_s^j A_s^j\bar{\zeta}_s^j\left(\alpha_k{}^3 U_s^{jk} - \frac{2}{R'}\alpha_k{}^2 W_s^{jk}\right)\right.$$
$$\left. + \frac{E_s^j A_s^j}{R'}\left(\alpha_k U_s^{jk} + \frac{W_s^{jk}}{R'}\right) + \lambda\hat{F}_s^j\alpha_k{}^2 W_s^{jk}\right\} - \mu_{jp}\sin(\alpha_k\eta_{jp}) = 0 \tag{3.29e}$$

$$\delta V_s^{jl}\colon \frac{L_s^j}{2}\left\{E_s^j A_s^j\left(\beta_l{}^2 V_s^{jl} + \beta_l\frac{W_s^{jl}}{R'} + \bar{\zeta}_s^j\beta_l{}^3 W_s^{jl}\right)\right\} - \phi_{jp}\sin(\beta_l\eta_{jp}) = 0 \tag{3.29f}$$

$$\delta W_s^{jl}\colon \frac{L_s^i}{2}\left\{E_s^i I_s^i \beta_l^4 W_s^{il} + E_s^i A_s^i \bar{r}_s^i\left(\beta_l^3 V_s^{il} + \frac{2}{R'}\beta_l^2 W_s^{il}\right) + \frac{E_s^i A_s^i}{R'}\left(\beta_l V_s^{il} + \frac{W_s^{il}}{R'}\right) + \lambda \hat{F}_s^i \beta_l^2 W_s^{il}\right\} - \psi_{jp}\cos(\beta_l \eta_{jp}) = 0 \tag{3.29g}$$

$$\delta \gamma_{jp}\colon U_l^{mn}\cos(\alpha_m x_{jp})\cos(\beta_n y_{jp}) - U_s^{jk}\cos(\alpha_k \eta_{jp}) = 0 \tag{3.29h}$$

$$\delta \mu_{jp}\colon W_l^{mn}\sin(\alpha_m x_{jp})\cos(\beta_n y_{jp}) - W_s^{jk}\sin(\alpha_k \eta_{jp}) = 0 \tag{3.29i}$$

$$\delta \phi_{jp}\colon V_l^{mn}\sin(\alpha_m x_{jp})\sin(\beta_n y_{jp}) - V_s^{jl}\sin(\beta_l \eta_{jp}) = 0 \tag{3.29j}$$

$$\delta \psi_{jp}\colon W_l^{mn}\sin(\alpha_m x_{jp})\cos(\beta_n y_{jp}) - W_s^{jl}\cos(\beta_l \eta_{jp}) = 0 \tag{3.29k}$$

3.7 Shell/Stiffener Load Distribution

3.7.1 Introduction

The appropriate prebuckling load distribtion as applied to the shell (skin) and the stiffeners is essential for proper analysis of the stiffened shell structure. In the smeared buckling analyses the skin and stiffener properties are averaged to form and equivalent structure and therefore no prebuckling load distribution is necessary. However, for discrete structures the proper distribution of loads applied to the skin and the individual stiffeners must be obtained. The approach taken here for the prebuckling load distribution involves using classical lamination theory (CLT) and a smeared load distribution whereby the stiffeners are considered to be smeared for the sake of calculating the appropriate prebuckling load distributions only similar to the approach used by Phillips

and Gürdal [123] in their study of stiffened plates. The stiffeners will be assumed to carry only forces along the length of the stiffener. The development of the constitutive equations presented here follows the approach of Jones [166].

3.7.2 Shell Constitutive Relations

Using CLT for the shell/skin, the stress strain relations in the principal material coordinates for a 2D laminate are

$$\begin{Bmatrix} \sigma_1 \\ \sigma_2 \\ \sigma_{12} \end{Bmatrix} = \begin{bmatrix} Q_{11} & Q_{12} & 0 \\ Q_{12} & Q_{22} & 0 \\ 0 & 0 & Q_{66} \end{bmatrix} \begin{Bmatrix} \varepsilon_1 \\ \varepsilon_2 \\ \gamma_{12} \end{Bmatrix} \tag{3.30}$$

Here the Q_{ij} are the reduced stiffnesses. If the coordinate system is transformed then the stress-strain relations are given by

$$\begin{Bmatrix} \sigma_x \\ \sigma_y \\ \sigma_{xy} \end{Bmatrix} = \begin{bmatrix} \overline{Q}_{11} & \overline{Q}_{12} & \overline{Q}_{16} \\ \overline{Q}_{12} & \overline{Q}_{22} & \overline{Q}_{26} \\ \overline{Q}_{16} & \overline{Q}_{26} & \overline{Q}_{66} \end{bmatrix} \begin{Bmatrix} \varepsilon_x \\ \varepsilon_y \\ \gamma_{xy} \end{Bmatrix} \tag{3.31}$$

The $\overline{Q}_{ij}$ are the transformed reduced stiffness terms. Using the Kirchhoff-Love hypothesis the displacements u and v within a laminate may be expressed as

$$\begin{aligned} u &= u^o - z\frac{\partial w^o}{\partial x} \\ v &= v^o - z\frac{\partial w^o}{\partial y} \end{aligned} \tag{3.32}$$

Here u^o, v^o, w^o are the displacements at the midsurface of the shell. The subsequent strains may be expressed as

$$\begin{aligned}
\varepsilon_x &= \frac{\partial u}{\partial x} = \frac{\partial u^o}{\partial x} - z\frac{\partial^2 w^o}{\partial x^2} \\
\varepsilon_y &= \frac{\partial v}{\partial y} = \frac{\partial v^o}{\partial y} + \frac{w^o}{R'} - z\frac{\partial^2 w^o}{\partial y^2} \\
\gamma_{xy} &= \frac{\partial u}{\partial y} + \frac{\partial v}{\partial x} = \frac{\partial u^o}{\partial y} + \frac{\partial v^o}{\partial x} - 2z\frac{\partial^2 w^o}{\partial x \partial y}
\end{aligned} \tag{3.33}$$

or

$$\begin{Bmatrix} \varepsilon_x \\ \varepsilon_y \\ \gamma_{xy} \end{Bmatrix} = \begin{Bmatrix} \varepsilon_x^o \\ \varepsilon_y^o \\ \gamma_{xy}^o \end{Bmatrix} + z \begin{Bmatrix} \kappa_x \\ \kappa_y \\ \kappa_{xy} \end{Bmatrix} \tag{3.34}$$

where the middle surface strains are

$$\begin{Bmatrix} \varepsilon_x^o \\ \varepsilon_y^o \\ \gamma_{xy}^o \end{Bmatrix} = \begin{Bmatrix} \dfrac{\partial u^o}{\partial x} \\ \dfrac{\partial v^o}{\partial y} + \dfrac{w^o}{R} + \dfrac{\partial v^o}{\partial x} \\ \dfrac{\partial u^o}{\partial y} \end{Bmatrix} \tag{3.35}$$

and the middle surface curvatures

$$\begin{Bmatrix} \kappa_x \\ \kappa_y \\ \kappa_{xy} \end{Bmatrix} = - \begin{Bmatrix} \dfrac{\partial^2 w^o}{\partial x^2} \\ \dfrac{\partial^2 w^o}{\partial y^2} \\ 2\dfrac{\partial^2 w^o}{\partial x \partial y} \end{Bmatrix} \tag{3.36}$$

Substituting the strain relations (3.34) into the stress-strain relations (3.31) the stresses in the k^{th} layer of the shell may be expressed as

$$\begin{Bmatrix} \sigma_x \\ \sigma_y \\ \sigma_{xy} \end{Bmatrix}_k = \begin{bmatrix} \overline{Q}_{11} & \overline{Q}_{12} & \overline{Q}_{16} \\ \overline{Q}_{12} & \overline{Q}_{22} & \overline{Q}_{26} \\ \overline{Q}_{16} & \overline{Q}_{26} & \overline{Q}_{66} \end{bmatrix}_k \begin{Bmatrix} \varepsilon_x^o \\ \varepsilon_y^o \\ \gamma_{xy}^o \end{Bmatrix} + z \begin{Bmatrix} \kappa_x \\ \kappa_y \\ \kappa_{xy} \end{Bmatrix} \tag{3.37}$$

The resultant forces and moments acting on the shell laminate may be obtained by integration of the stresses in each layer (lamina) through the laminate thickness. The resulting expressions are

$$\begin{Bmatrix} N_x^s \\ N_y^s \\ N_{xy}^s \end{Bmatrix} = \int_{\frac{-h}{2}}^{\frac{h}{2}} \begin{Bmatrix} \sigma_x \\ \sigma_y \\ \sigma_{xy} \end{Bmatrix} dz = \sum_{k=1}^{N} \int_{z_{k-1}}^{z_k} \begin{Bmatrix} \sigma_x \\ \sigma_y \\ \sigma_{xy} \end{Bmatrix}_k dz \tag{3.38}$$

$$\begin{Bmatrix} M_x^s \\ M_y^s \\ M_{xy}^s \end{Bmatrix} = \int_{\frac{-h}{2}}^{\frac{h}{2}} \begin{Bmatrix} \sigma_x \\ \sigma_y \\ \sigma_{xy} \end{Bmatrix} z\, dz = \sum_{k=1}^{N} \int_{z_{k-1}}^{z_k} \begin{Bmatrix} \sigma_x \\ \sigma_y \\ \sigma_{xy} \end{Bmatrix}_k z\, dz \tag{3.39}$$

where z_k and z_{k-1} are defined in Figure 8. Upon integration through the laminate the following expressions result

$$\begin{Bmatrix} N_x^s \\ N_y^s \\ N_{xy}^s \end{Bmatrix} = \begin{bmatrix} A_{11}^s & A_{12}^s & A_{16}^s \\ A_{12}^s & A_{22}^s & A_{26}^s \\ A_{16}^s & A_{26}^s & A_{66}^s \end{bmatrix} \begin{Bmatrix} \varepsilon_x \\ \varepsilon_y \\ \gamma_{xy} \end{Bmatrix} + \begin{bmatrix} B_{11}^s & B_{12}^s & B_{16}^s \\ B_{12}^s & B_{22}^s & B_{26}^s \\ B_{16}^s & B_{26}^s & B_{66}^s \end{bmatrix} \begin{Bmatrix} \kappa_x \\ \kappa_y \\ \kappa_{xy} \end{Bmatrix}$$

$$\begin{Bmatrix} M_x^s \\ M_y^s \\ M_{xy}^s \end{Bmatrix} = \begin{bmatrix} B_{11}^s & B_{12}^s & B_{16}^s \\ B_{12}^s & B_{22}^s & B_{26}^s \\ B_{16}^s & B_{26}^s & B_{66}^s \end{bmatrix} \begin{Bmatrix} \varepsilon_x \\ \varepsilon_y \\ \gamma_{xy} \end{Bmatrix} + \begin{bmatrix} D_{11}^s & D_{12}^s & D_{16}^s \\ D_{12}^s & D_{22}^s & D_{26}^s \\ D_{16}^s & D_{26}^s & D_{66}^s \end{bmatrix} \begin{Bmatrix} \kappa_x \\ \kappa_y \\ \kappa_{xy} \end{Bmatrix} \tag{3.40}$$

where

$$(A_{ij}^s, B_{ij}^s, D_{ij}^s) = \int_{\frac{-h}{2}}^{\frac{h}{2}} (\bar{Q}_{ij})_k (1, z, z^2) \tag{3.41}$$

The superscript s denotes that these are shell(skin) constitutive relations.

3.7.3 Axial Stiffener Constitutive Relations

The effective stiffener spacing l_x over which the influence a particular axial stiffener has upon the structure is described in Figure 9 and is given by the expression

$$l_x = \frac{2\pi R}{N_a} \tag{3.42}$$

where N_a is the total number of axial stiffeners. The linear strain displacement relationship for axial stiffeners is

$$\varepsilon_x^a = \frac{\partial u^a}{\partial x} - z\frac{\partial^2 w^a}{\partial x^2} \tag{3.43}$$

where ε_x^a is the smeared axial stiffener strain and u^a and w^a are the respective displacements of the axial stiffeners. The stress strain relationship is given as

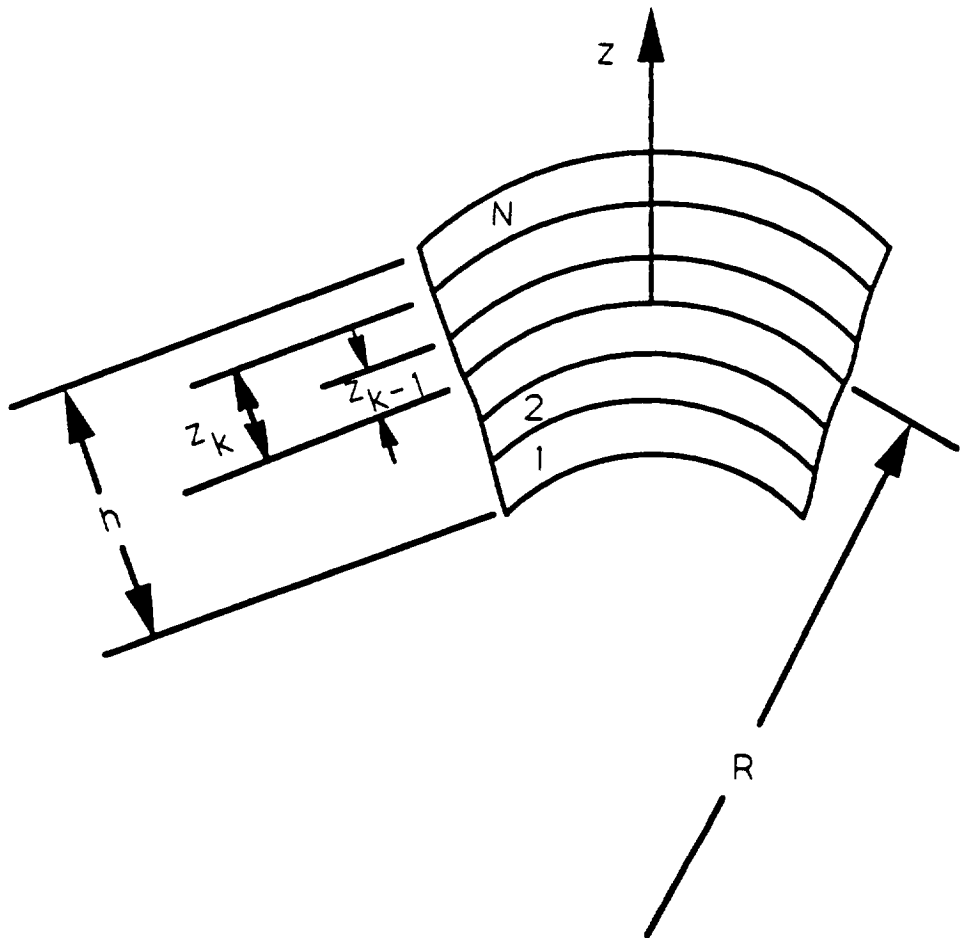

Figure 8. Geometry of an N-layered shell laminate.

$$\sigma_x^a = E_a \varepsilon_x^a = E_a \left[\frac{\partial u^a}{\partial x} - z \frac{\partial^2 w^a}{\partial x^2} \right] \tag{3.44}$$

where σ_x^a is the smeared axial stiffener stress and E_a is the modulus of the axial stiffeners. The total force in the stiffener is calculated by integrating the stress distribution in the stiffener over the area, A_a, and is expressed as

$$\begin{aligned} F_x^a &= \int_{A_a} \sigma_x^a dA_a = \int_{A_a} E_a \left[\frac{\partial u^a}{\partial x} - z \frac{\partial^2 w^a}{\partial x^2} \right] dA_a \\ &= E_a A_a \varepsilon_x^a + E_a A_a \bar{z}_a \kappa_x \end{aligned} \tag{3.45}$$

The force resultant, N_x, is then calculated by distributing the total stiffener force F_x^a over the stiffener spacing l_x and is written as

$$\begin{aligned} N_x^a = \frac{F_x^a}{l_x} &= \frac{E_a A_a}{l_x} \frac{\partial u^a}{\partial x} + \frac{E_a A_a \bar{z}_a}{l_x} \left[- \frac{\partial^2 w^a}{\partial x^2} \right] \\ &= \frac{E_a A_a}{l_x} \varepsilon_x^o + \frac{E_a A_a \bar{z}_a}{l_x} \kappa_x \end{aligned} \tag{3.46}$$

The moment resultant M_x^a, is calculated by multiplying the force resultant N_x^a, by the distance $\bar{z}_a$ from the neutral axis to the centroid of the stiffener at which the force acts. Here it is assumed that the forces act at the centroid of the stiffeners. The moment resultant is then

$$M_x^a = \frac{F_x^a \bar{z}_a}{l_x} = \frac{E_a A_a \bar{z}_a}{l_x} \varepsilon_x^o + \frac{E_a I_a}{l_x} \kappa_x \tag{3.47}$$

where the moment of inertia I_a is

$$I_a = I_{xc}^a + \bar{z}_a^{\,2} A_a \tag{3.48}$$

The set of constitutive relations for the axial stiffeners becomes

$$\begin{aligned} N_x^a &= A_{11}^a \varepsilon_x^o + B_{11}^a \kappa_x \\ M_x^a &= B_{11}^a \varepsilon_x^o + D_{11}^a \kappa_x \end{aligned} \tag{3.49}$$

where

$$\begin{aligned} A_{11}^a &= \frac{E_a A_a}{l_x} \\ B_{11}^a &= \frac{E_a A_a \bar{z}_a}{l_x} \\ D_{11}^a &= \frac{E_a\left(I_{xc}^a + \bar{z}_a^{\,2} A_a\right)}{l_x} = \frac{E_a I_a}{l_x} \end{aligned} \tag{3.50}$$

3.7.4 Ring Stiffener Constitutive Relations

The effective stiffener spacing l_y over which the influence a particular ring stiffener has upon the structure is described in Figure 10 and is defined by the relation

$$l_y = \frac{L}{N_c} \tag{3.51}$$

where L is the length of the cylinder and N_c is the number of ring stiffeners. The linear strain displacement relationship for ring stiffeners is

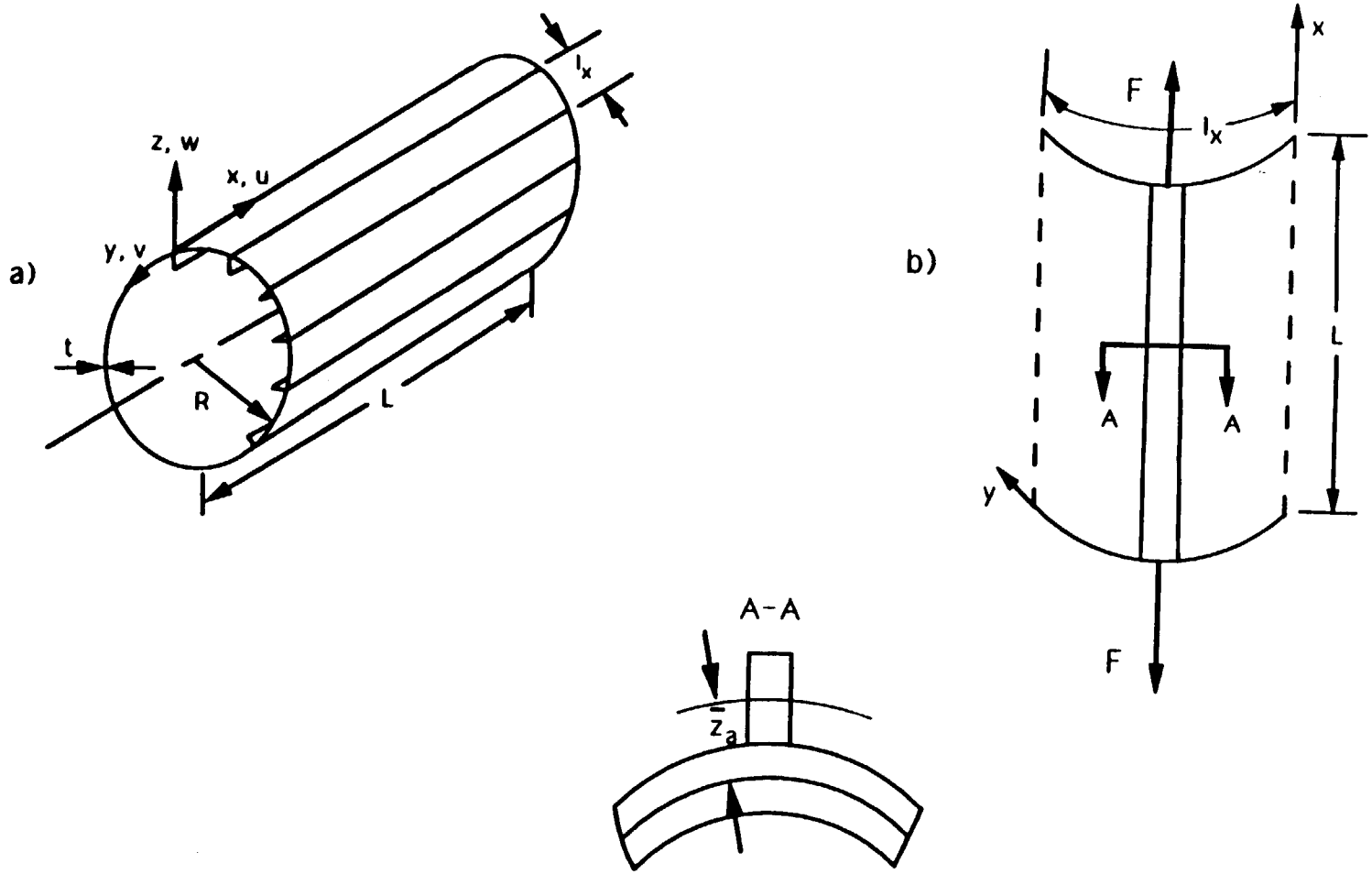

Figure 9. Axially stiffened cylindrical shell and unit cell for load distribution analysis: (a) stiffened cylindrical shell; (b) unit axial cell.

$$\varepsilon_y^c = \frac{\partial v^c}{\partial y} + \frac{w^c}{R} - z\frac{\partial^2 w^c}{\partial y^2} \tag{3.52}$$

where ε_y^c is the smeared ring stiffener strain and v^c and w^c are the respective displacements of the ring stiffeners. The stress strain relationship is the given as

$$\sigma_y^c = E_c\varepsilon_y^c = E_c\left[\frac{\partial v^c}{\partial y} + \frac{w^c}{R} - z\frac{\partial^2 w^c}{\partial y^2}\right] \tag{3.53}$$

where σ_y^c is the smeared ring stiffener stress and E_c is the ring stiffener modulus. The total force in the stiffener is calculated by integrating the stress distribution in the stiffener over the area, A_c, and is expressed as

$$\begin{aligned} F_y^c = \int_{A_c} \sigma_y^c dA_c &= \int_{A_c} E_c\left[\frac{\partial v^c}{\partial y} + \frac{w^c}{R} - z\frac{\partial^2 w^c}{\partial y^2}\right] dA_c \\ &= E_c A_c \varepsilon_y^c + E_c A_c \bar{z}_c \kappa_y \end{aligned} \tag{3.54}$$

The force resultant, N_y, is then calculated by distributing the total stiffener force F_y^c over the stiffener spacing l_y and is written as

$$\begin{aligned} N_y^c = \frac{F_y^c}{l_y} &= \frac{E_c A_c}{l_y}\left[\frac{\partial v^c}{\partial y} + \frac{w^c}{R}\right] + \frac{E_c A_c \bar{z}_c}{l_y}\left[-\frac{\partial^2 w^c}{\partial y^2}\right] \\ &= \frac{E_c A_c}{l_y}\varepsilon_y^o + \frac{E_c A_c \bar{z}_c}{l_y}\kappa_y \end{aligned} \tag{3.55}$$

The moment resultant M_y^c, is calculated by multiplying the force resultant N_y^c, by the distance $\bar{z}_c$ from the neutral axis to the centroid of the stiffener at which the force acts.

Here it is assumed that the forces act at the centroid of the stiffeners. The moment resultant is then

$$M_y^c = \frac{F_y^c \bar{z}_c}{l_y} = \frac{E_c A_c \bar{z}_c}{l_y} \varepsilon_y^o + \frac{E_c I_c}{l_y} \kappa_y \tag{3.56}$$

where the moment of inertia I_c is

$$I_c = I_{yc}^c + \bar{z}_c^{\,2} A_c \tag{3.57}$$

The set of constitutive relations for the axial stiffeners becomes

$$\begin{aligned} N_y^c &= A_{22}^c \varepsilon_y^o + B_{22}^c \kappa_y \\ M_y^c &= B_{22}^c \varepsilon_y^o + D_{22}^c \kappa_y \end{aligned} \tag{3.58}$$

where

$$\begin{aligned} A_{22}^c &= \frac{E_c A_c}{l_y} \\ B_{22}^c &= \frac{E_c A_c \bar{z}_c}{l_y} \\ D_{22}^c &= \frac{E_c I_c}{l_y} \end{aligned} \tag{3.59}$$

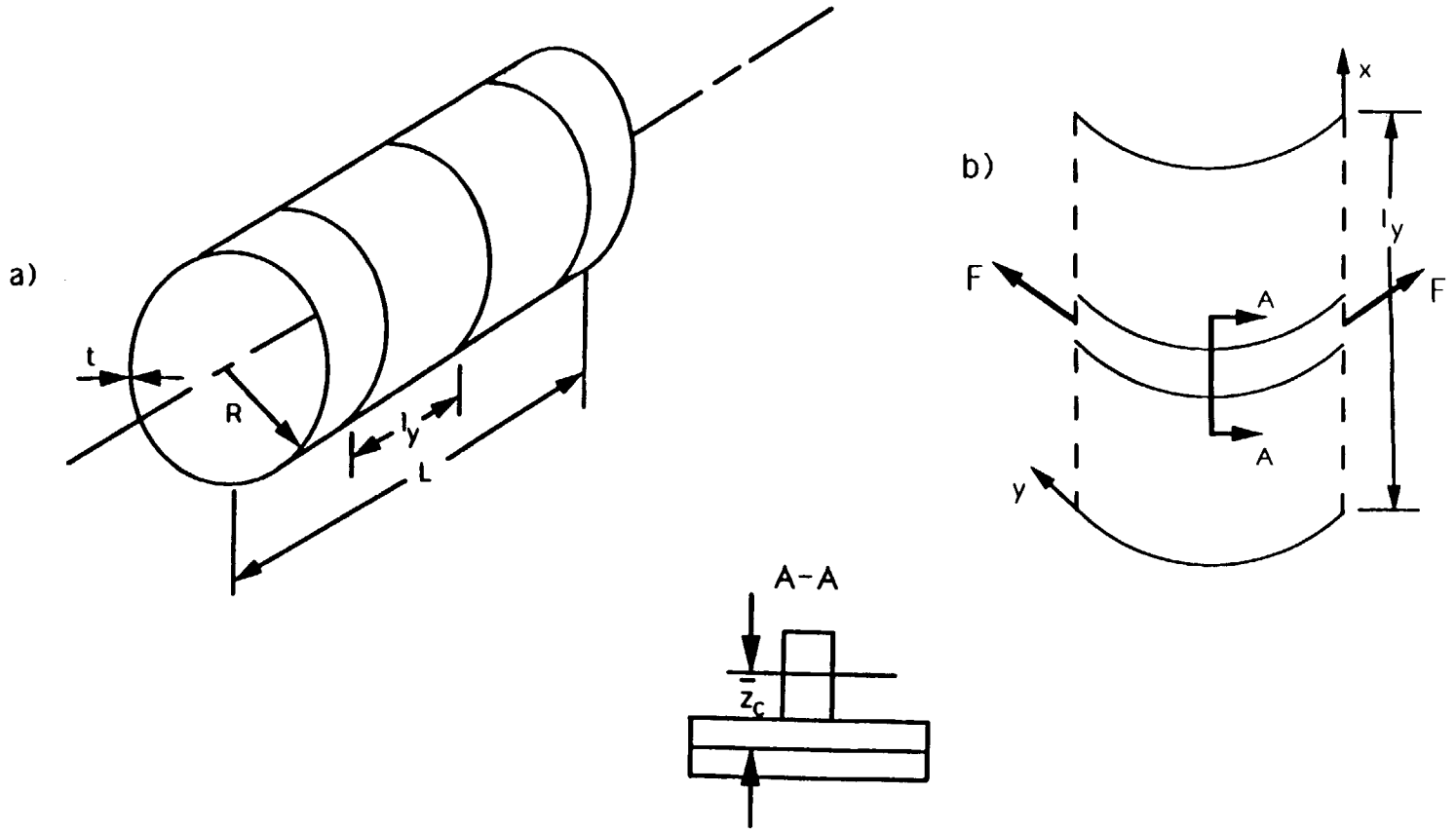

Figure 10. Ring stiffened cylindrical shell and unit cell for load distribution analysis: (a) stiffened cylindrical shell; (b) unit ring cell.

3.7.5 Geodesic Stiffener Constitutive Relations

Described in Figure 11 is the coordinate system for the geodesically stiffened shell and the definition of a single geodesic cell. The effective circumferential length l_g is the circumference divided by the number of cells per shell circumference such that

$$l_g = \frac{2\pi R}{N_g} \tag{3.60}$$

where N_g is the number of geodesic cells. The cell length is given by L_g. The strains in stiffener coordinates are

$$\begin{aligned} \varepsilon_\eta &= \frac{\partial u^g}{\partial \eta} + \frac{w^g}{R} - \bar{z}_g \frac{\partial^2 w^g}{\partial \eta^2} \\ \varepsilon_\xi &= \frac{\partial v^g}{\partial \xi} - \bar{z}_g \frac{\partial^2 w^g}{\partial \xi^2} \\ \gamma_{\eta\xi} &= \frac{\partial u^g}{\partial \xi} + \frac{\partial v^g}{\partial \eta} \end{aligned} \tag{3.61}$$

where ε_η is strain along the stiffener axis, ε_ξ is strain transverse to the stiffener axis, $\gamma_{\eta\xi}$ is the shear strain, and u^g and w^g are the geodesic stiffener displacements. See Figure 4 for the stiffener coordinate system.

The stiffeners 1 and 2 of Figure 11 are oriented at angles ϕ and $-\phi$ respectively from the y axis of the shell. Since the stiffeners are not aligned with the shell coordinate system, the values in the local coordinate system aligned with the stiffener axes must be transformed to the shell coordinates. The strains in the local coordinate system aligned with the stiffener can be determined using the strain transformation relations by Jones [166]. These are

$$\begin{Bmatrix} \varepsilon_\eta \\ \varepsilon_\xi \\ \gamma_{\eta\xi} \end{Bmatrix} = \begin{bmatrix} s^2\phi & c^2\phi & s\phi c\phi \\ c^2\phi & s^2\phi & -s\phi c\phi \\ -2s\phi c\phi & 2s\phi c\phi & c^2\phi - s^2\phi \end{bmatrix} \begin{Bmatrix} \varepsilon_x \\ \varepsilon_y \\ \gamma_{xy} \end{Bmatrix} \tag{3.62}$$

where

$$\begin{aligned} s\phi &= \sin\phi \\ c\phi &= \cos\phi \end{aligned} \tag{3.63}$$

The axial strain component for stiffener #1 of the unit cell at angle $+\phi$ yields

$$\begin{aligned} \varepsilon_1 &= \sin^2\phi\varepsilon_x + \cos^2\phi\varepsilon_y + \sin\phi\cos\phi\gamma_{xy} \\ &= s^2\phi\varepsilon_x + c^2\phi\varepsilon_y + s\phi c\phi\gamma_{xy} \end{aligned} \tag{3.64}$$

The axial strain component for stiffener #2 of the unit cell at angle $-\phi$ yields

$$\begin{aligned} \varepsilon_2 &= \sin^2(-\phi)\varepsilon_x + \cos^2(-\phi)\varepsilon_y + \sin(-\phi)\cos(-\phi)\gamma_{xy} \\ &= s^2\phi\varepsilon_x + c^2\phi\varepsilon_y - s\phi c\phi\gamma_{xy} \end{aligned} \tag{3.65}$$

The stiffener axial forces F_1 and F_2 may be found by multiplying the strains ε_1 and ε_2 by the stiffener elastic modulus E_s and integrating over the area of an individual stiffener area A_s. This results in the following expressions

$$\begin{aligned} F_1 &= E_s\int_{A_s}(s^2\phi\varepsilon_x + c^2\phi\varepsilon_y + s\phi c\phi\gamma_{xy})dA_s \\ F_2 &= E_s\int_{A_s}(s^2\phi\varepsilon_x + c^2\phi\varepsilon_y - s\phi c\phi\gamma_{xy})dA_s \end{aligned} \tag{3.66}$$

Solving for the force F_x along the circumferential edge involves resolving F_1 and F_2 into components along the x direction as indicated in Figure 11.

$$\begin{aligned} F_x^g &= F_1 \sin\phi + F_2 \sin\phi \\ &= E_g\Bigg[\int_{A_g} (s^3\phi\varepsilon_x + c^2\phi s\phi\varepsilon_y + s^2\phi c\phi\gamma_{xy})dA_g \\ &\quad + \int_{A_g} (s^3\phi\varepsilon_x + c^2\phi s\phi\varepsilon_y - s^2\phi c\phi\gamma_{xy})dA_g\Bigg] \\ &= 2E_g\int_{A_g} (s^3\phi\varepsilon_x + c^2\phi s\phi\varepsilon_y)dA_g \end{aligned} \tag{3.67}$$

The force resultant, N_x^g, distributed over the circumferential length is calculated by distributing the force F_x over the length l_g. Distributing the force F_x^g over l_g and carrying out the integration of Eq. (3.67) yields (constant cross sectional area)

$$\begin{aligned} N_x^g = &\frac{2E_gA_g}{l_g} s^3\phi\varepsilon_x + \frac{2E_gA_g}{l_g} c^2\phi s\phi\varepsilon_y \\ &+ \frac{2E_gA_g\bar{z}_g}{l_g} s^3\phi\kappa_x + \frac{2E_gA_g\bar{z}_g}{l_g} c^2\phi s\phi\kappa_y \end{aligned} \tag{3.68}$$

where for a constant cross sectional area

$$\bar{z}_g = \int_{A_g} z dA_g \tag{3.69}$$

A similar procedure is used to calculate the force resultant N_y^g along the lengthwise edge and produces the following result

$$N_y^g = \frac{2E_gA_g}{L_g} s^2\phi c\phi\varepsilon_x + \frac{2E_gA_g}{L_g} c^3\phi\varepsilon_y + \frac{2E_gA_g\bar{z}_g}{L_g} s^2\phi c\phi\kappa_x + \frac{2E_gA_g\bar{z}_g}{L_g} c^3\phi\kappa_y \tag{3.70}$$

To determine the shear force resultant, the forces tangential to either the circumferential or lengthwise edges will produce eigenvalue results. The tangential force components along the edge are $F_1 \cos\phi$ in the positive y direction and $F_2 \cos\phi$ in the negative y direction. Substituting for F_1 and F_2 of Eq. (3.66) yields

$$\begin{aligned} F_{xy}^g &= F_1 \cos\phi - F_2 \cos\phi \\ &= E_g\left[\int_{A_g} (s^2\phi c\phi\varepsilon_x + c^3\phi\varepsilon_y + s\phi c^2\phi\gamma_{xy})dA_g \right. \\ &\quad \left. - \int_{A_g} (s^2\phi c\phi\varepsilon_x + c^3\phi\varepsilon_y - s\phi c^2\phi\gamma_{xy})dA_g\right] \\ &= 2E_g\int_{A_g} (c^2\phi s\phi\gamma_{xy})dA_g \end{aligned} \tag{3.71}$$

Distributing the force F_{xy} over the length l_g and integrating Eq. (3.71) yields the shear force resultant

$$N_{xy}^g = \frac{2E_gA_g}{l_g} c^2\phi s\phi\gamma_{xy} + \frac{2E_gA_g\bar{z}_g}{l_g} c^2\phi s\phi\kappa_{xy} \tag{3.72}$$

The loads acting upon the stiffeners are offset by an amount $\bar{z}_g$. Thus, moment resultants are introduced into the problem. The resultant moment M_x^g may be calculated by multiplying Eq. (3.67) by z and distributing over l_g which yields

$$M_x^g = \frac{zF_x^g}{l_g} = \frac{2E_g}{l_g}\int A_g\left[s^3\phi\varepsilon_x + c^2\phi s\phi\varepsilon_y\right]zdA_g$$
$$= \frac{2E_gA_g\bar{z}_g}{l_g}s^3\phi\varepsilon_x + \frac{2E_gA_g\bar{z}_g}{l_g}c^2\phi s\phi\varepsilon_y \qquad (3.73)$$
$$+\frac{2E_gI_g}{l_g}s^3\phi\kappa_x + \frac{2E_gI_g}{l_g}c^2\phi s\phi\kappa_y$$

where

$$I_g = \int_{A_g} z^2dA_g = I_c^g + \bar{z}_g{}^2A_g \qquad (3.74)$$

Similar procedures will produce the moment resultants M_β and $M_{\xi y}$. These moment resultants are

$$M_y^g = \frac{2E_gA_g\bar{z}_g}{L_g}s^2\phi c\phi\varepsilon_x + \frac{2E_gA_g\bar{z}_g}{L_g}c^3\phi\varepsilon_y$$
$$+\frac{2E_gI_g}{L_g}s^2\phi c\phi\kappa_x + \frac{2E_gI_g}{L_g}c^3\phi\kappa_y \qquad (3.75)$$

$$M_{xy}^g = \frac{2E_gA_g\bar{z}_g}{l_g}c^2\phi s\phi\gamma_{xy} + \frac{2E_gA_g\bar{z}_g}{l_g}c^2\phi s\phi\varepsilon_y \qquad (3.76)$$

The constitutive equations for geodesic stiffeners are given as

$$\begin{Bmatrix} N_x^g \\ N_y^g \\ N_{xy}^g \end{Bmatrix} = \begin{bmatrix} A_{11}^g & A_{12}^g & 0 \\ A_{21}^g & A_{22}^g & 0 \\ 0 & 0 & A_{66}^g \end{bmatrix}\begin{Bmatrix} \varepsilon_x^o \\ \varepsilon_y^o \\ \gamma_{xy}^o \end{Bmatrix} + \begin{bmatrix} B_{11}^g & B_{12}^g & 0 \\ B_{21}^g & B_{22}^g & 0 \\ 0 & 0 & B_{66}^g \end{bmatrix}\begin{Bmatrix} \kappa_x \\ \kappa_y \\ \kappa_{xy} \end{Bmatrix}$$

$$\begin{Bmatrix} M_x^g \\ M_y^g \\ M_{xy}^g \end{Bmatrix} = \begin{bmatrix} B_{11}^g & B_{12}^g & 0 \\ B_{21}^g & B_{22}^g & 0 \\ 0 & 0 & B_{66}^g \end{bmatrix} \begin{Bmatrix} \varepsilon_x^o \\ \varepsilon_y^o \\ \gamma_{xy}^o \end{Bmatrix} + \begin{bmatrix} D_{11}^g & D_{12}^g & 0 \\ D_{21}^g & D_{22}^g & 0 \\ 0 & 0 & D_{66}^g \end{bmatrix} \begin{Bmatrix} \kappa_x \\ \kappa_y \\ \kappa_{xy} \end{Bmatrix} \tag{3.77}$$

where

$$\begin{aligned}
A_{11}^g &= \frac{2E_gA_g}{l_g}s^3\phi & B_{21}^g &= \frac{2E_gA_g\bar{z}_g}{L_g}s^2\phi c\phi \\
A_{12}^g &= \frac{2E_gA_g}{l_g}c^2\phi s\phi & B_{22}^g &= \frac{2E_gA_g\bar{z}_g}{L_g}c^3\phi \\
A_{21}^g &= \frac{2E_gA_g}{L_g}s^2\phi c\phi & B_{66}^g &= \frac{2E_gA_g\bar{z}_g}{l_g}c^2\phi s\phi \\
A_{22}^g &= \frac{2E_gA_g}{L_g}c^3\phi & D_{11}^g &= \frac{2E_gI_g}{l_g}s^3\phi \\
A_{66}^g &= \frac{2E_gA_g}{l_g}c^2\phi s\phi & D_{12}^g &= \frac{2E_gI_g}{l_g}c^2\phi s\phi \\
B_{11}^g &= \frac{2E_gA_g\bar{z}_g}{l_g}s^3\phi & D_{21}^g &= \frac{2E_gI_g}{l_g}s^2\phi c\phi \\
B_{12}^g &= \frac{2E_gA_g\bar{z}_g}{l_g}c^2\phi s\phi & D_{22}^g &= \frac{2E_gI_g}{l_g}c^3\phi \\
D_{66}^g &= \frac{2E_gI_g}{l_g}c^2\phi s\phi
\end{aligned} \tag{3.78}$$

3.7.6 Skin/Stiffener System Constitutive Equations

Using the principle of superposition the force and moment resultants for the stiffened structure are

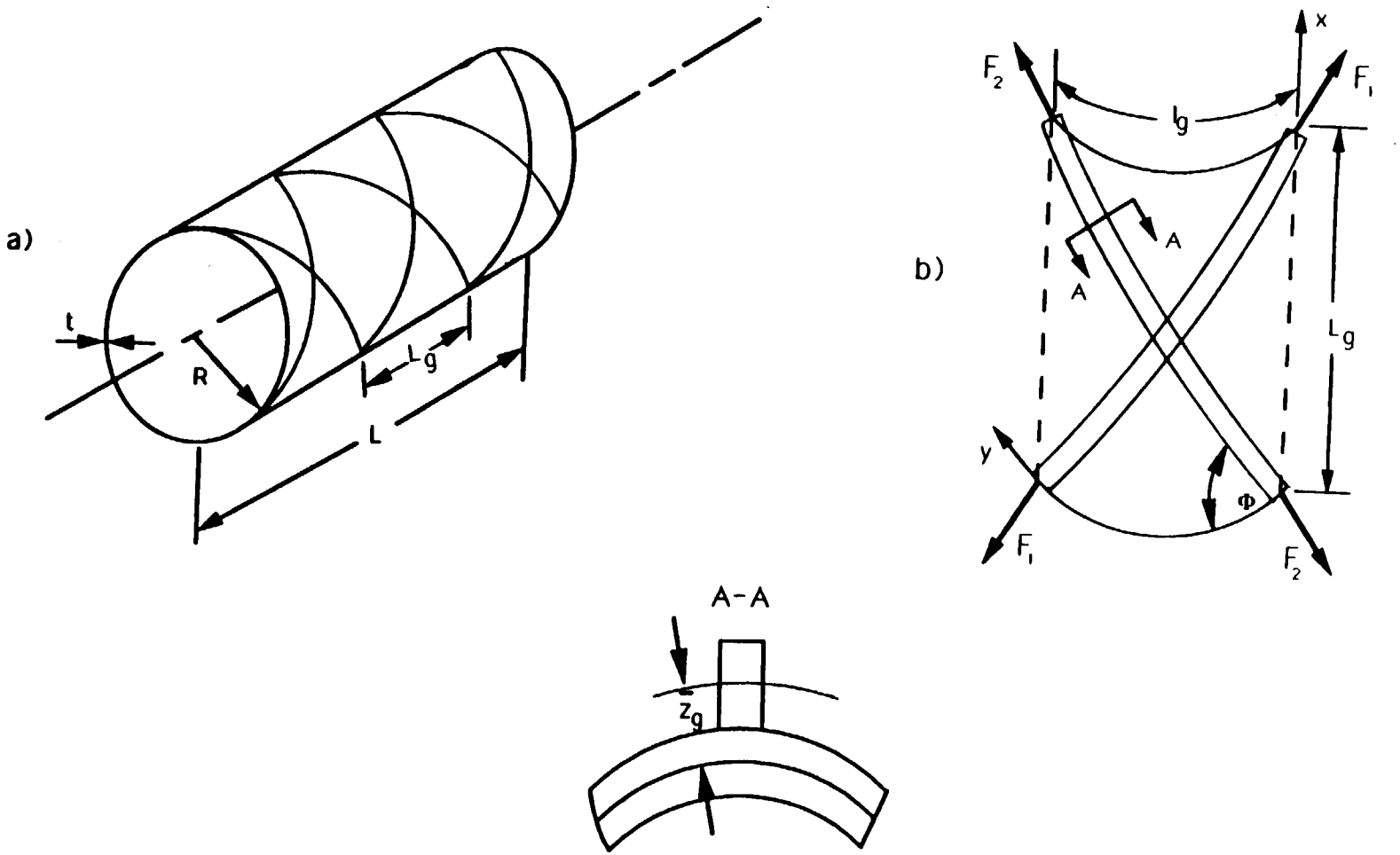

Figure 11. Geodesically stiffened cylindrical shell and unit cell for load distribution analysis: (a) stiffened cylindrical shell; (b) unit geodesic cell.

$$
\begin{aligned}
N_x &= N_x^s + N_x^a + N_x^g & M_x &= M_x^s + M_x^a + M_x^g \\
N_y &= N_y^s + N_y^c + N_y^g & M_y &= M_y^s + M_y^c + M_y^g \\
N_{xy} &= N_{xy}^s + N_{xy}^g & M_{xy} &= M_{xy}^s + M_{xy}^g
\end{aligned} \tag{3.79}
$$

The stiffness terms (A, B, D) are then

$$
\begin{aligned}
A_{11} &= A_{11}^s + A_{11}^a + A_{11}^g & B_{26} &= B_{26}^s \\
A_{12} &= A_{12}^s + A_{12}^g & B_{22} &= B_{22}^s + B_{22}^c + B_{22}^g \\
A_{16} &= A_{16}^s & B_{66} &= B_{66}^s + B_{66}^g \\
A_{26} &= A_{26}^s & D_{11} &= D_{11}^s + D_{11}^a + D_{11}^g \\
A_{22} &= A_{22}^s + A_{22}^c + A_{22}^g & D_{12} &= D_{12}^s + D_{12}^g \\
A_{66} &= A_{66}^s + A_{66}^g & D_{16} &= D_{16}^s \\
B_{11} &= B_{11}^s + B_{11}^a + B_{11}^g & D_{26} &= D_{26}^s \\
B_{12} &= B_{12}^s + B_{12}^g & D_{22} &= D_{22}^s + D_{22}^c + D_{22}^g \\
B_{16} &= B_{16}^s & D_{66} &= D_{66}^s + D_{66}^g
\end{aligned} \tag{3.80}
$$

It is assumed that the skin and stiffeners have identical strains. The constitutive equations for the shell (skin)/ stiffeners are:

$$
\begin{Bmatrix} N_x \\ N_y \\ N_{xy} \end{Bmatrix} = \begin{bmatrix} A_{11} & A_{12} & A_{16} \\ A_{12} & A_{22} & A_{26} \\ A_{16} & A_{26} & A_{66} \end{bmatrix} \begin{Bmatrix} \varepsilon_x^o \\ \varepsilon_y^o \\ \gamma_{xy}^o \end{Bmatrix} + \begin{bmatrix} B_{11} & B_{12} & B_{16} \\ B_{12} & B_{22} & B_{26} \\ B_{16} & B_{26} & B_{66} \end{bmatrix} \begin{Bmatrix} \kappa_x \\ \kappa_y \\ \kappa_{xy} \end{Bmatrix}
$$

$$
\begin{Bmatrix} M_x \\ M_y \\ M_{xy} \end{Bmatrix} = \begin{bmatrix} B_{11} & B_{12} & B_{16} \\ B_{12} & B_{22} & B_{26} \\ B_{16} & B_{26} & B_{66} \end{bmatrix} \begin{Bmatrix} \varepsilon_x^o \\ \varepsilon_y^o \\ \gamma_{xy}^o \end{Bmatrix} + \begin{bmatrix} D_{11} & D_{12} & D_{16} \\ D_{21} & D_{22} & D_{26} \\ D_{16} & D_{26} & D_{66} \end{bmatrix} \begin{Bmatrix} \kappa_x \\ \kappa_y \\ \kappa_{xy} \end{Bmatrix} \tag{3.81}
$$

3.7.7 Loading Conditions

Four different loading conditions will be considered for the solution of shell/stiffener prebuckling load distributions; axial compression, pressure loading, applied shear (torsion), and applied end shortenings. In this study only buckling due to axial compression and/or pressure loading will be considered. The other two loading conditions, torsion and applied end shortening, are included for completeness and can be included in future work including calculating the prebuckling load distributions for a finite element analysis. Load distributions for combinations of the above loading conditions such as for example axial compression and pressure loading may be obtained via the superposition of two or more load conditions.

3.7.7.1 Case 1 - Axial Compression (Applied Nx)

For this case it will be assumed that the prebuckling $N_y = N_{xy} = 0$. Further, due to the offset loads acting at the stiffeners' centroid, a resultant moment is developed. An applied N_x may be reacted by either axial or geodesic stiffeners. Thus, the resulting moment is

$$M_x = \bar{z}_a N_x^a + \bar{z}_g N_x^g \tag{3.82}$$

The resulting offset moment in terms of strains is

$$M_x = \bar{z}_a(A_{11}^a \varepsilon_x^o + B_{11}^a \kappa_x) + \bar{z}_g(A_{11}^g \varepsilon_x^o + A_{12}^g \varepsilon_y^o + B_{11}^g \kappa_x + B_{12}^g \kappa_y) \tag{3.83}$$

Substituting Eq. (3.83) into Eq. (3.81) reduces the constitutive equations to

$$\begin{Bmatrix} N_x \\ 0 \\ 0 \end{Bmatrix} = \begin{bmatrix} A_{11} & A_{12} & A_{16} \\ A_{12} & A_{22} & A_{26} \\ A_{16} & A_{26} & A_{66} \end{bmatrix} \begin{Bmatrix} \varepsilon_x^o \\ \varepsilon_y^o \\ \gamma_{xy}^o \end{Bmatrix} + \begin{bmatrix} B_{11} & B_{12} & B_{16} \\ B_{12} & B_{22} & B_{26} \\ B_{16} & B_{26} & B_{66} \end{bmatrix} \begin{Bmatrix} \kappa_x \\ \kappa_y \\ \kappa_{xy} \end{Bmatrix}$$

$$\begin{Bmatrix} M_x \\ 0 \\ 0 \end{Bmatrix} = \begin{bmatrix} B_{11} & B_{12} & B_{16} \\ B_{12} & B_{22} & B_{26} \\ B_{16} & B_{26} & B_{66} \end{bmatrix} \begin{Bmatrix} \varepsilon_x^o \\ \varepsilon_y^o \\ \gamma_{xy}^o \end{Bmatrix} + \begin{bmatrix} D_{11} & D_{12} & D_{16} \\ D_{12} & D_{22} & D_{26} \\ D_{16} & D_{26} & D_{66} \end{bmatrix} \begin{Bmatrix} \kappa_x \\ \kappa_y \\ \kappa_{xy} \end{Bmatrix} \tag{3.84}$$

The set of equations, (3.84), will be solved using a Gauss elimination procedure for ε_x^o, ε_y^o, γ_{xy}^o, κ_x, κ_y, κ_{xy}. The solution for the skin force resultants is then

$$\begin{aligned} N_x^s &= A_{11}^s\varepsilon_x^o + A_{12}^s\varepsilon_y^o + A_{16}^s\gamma_{xy}^o + B_{11}^s\kappa_x + B_{12}^s\kappa_y + B_{16}^s\kappa_y \\ N_y^s &= A_{12}^s\varepsilon_x^o + A_{22}^s\varepsilon_y^o + A_{26}^s\gamma_{xy}^o + B_{12}^s\kappa_x + B_{22}^s\kappa_y + B_{26}^s\kappa_y \\ N_{xy}^s &= A_{16}^s\varepsilon_x^o + A_{26}^s\varepsilon_y^o + A_{66}^s\gamma_{xy}^o + B_{16}^s\kappa_x + B_{26}^s\kappa_y + + B_{66}\kappa_{xy} \end{aligned} \tag{3.85}$$

The resultant force in the axial stiffener is

$$N_x^a = A_{11}^a\varepsilon_x^o + B_{11}^a\kappa_x \tag{3.86}$$

and the force in each axial stiffener is

$$F_x^a = l_x N_x^a \tag{3.87}$$

The resultant force in the geodesic stiffeners is

$$N_x^g = A_{11}^g\varepsilon_x^o + A_{12}^g\varepsilon_y^o + B_{11}^g\kappa_x + B_{12}^g\kappa_y \tag{3.88}$$

and the force on the the geodesic stiffeners is then

$$F_1 = F_2 = \frac{F_x^g}{2s\phi} = \frac{l_g N_x^g}{2s\phi} \tag{3.89}$$

It is assumed that the ring stiffeners do not carry any loads when the shell is subjected to axial compression so $F_y^c = 0$.

3.7.7.2 Case 2 - Pressure Loading (Applied Ny)

For pressure analysis the value of $N_y = -pR$ where p is the external pressure. If internal pressure is applied then $N_y = pR$. For this case it will be assumed that the prebuckling $N_x = N_{xy} = 0$. Due to the offset loads applied to the stiffeners this results in an applied moment resultant. This moment resultant is created because of the offset force resultants acting on the ring or geodesic stiffeners acting at the centroid and may be expressed as

$$M_y = \bar{z}_c N_y^c + \bar{z}_g N_y^g \tag{3.90}$$

The resulting offset moment in terms of strains is

$$M_y = \bar{z}_c(A_{22}^c \varepsilon_y^o + B_{22}^c \kappa_y) + \bar{z}_g(A_{21}^g \varepsilon_x^o + A_{22}^g \varepsilon_y^o + B_{21}^g \kappa_x + B_{22}^g \kappa_y) \tag{3.91}$$

Substituting Eq. (3.91) into Eq. (3.81) reduces the constitutive equations to

$$\begin{Bmatrix} 0 \\ N_y \\ 0 \end{Bmatrix} = \begin{bmatrix} A_{11} & A_{12} & A_{16} \\ A_{12} & A_{22} & A_{26} \\ A_{16} & A_{26} & A_{66} \end{bmatrix} \begin{Bmatrix} \varepsilon_x^o \\ \varepsilon_y^o \\ y_{xy}^o \end{Bmatrix} + \begin{bmatrix} B_{11} & B_{12} & B_{16} \\ B_{12} & B_{22} & B_{26} \\ B_{16} & B_{26} & B_{66} \end{bmatrix} \begin{Bmatrix} \kappa_x \\ \kappa_y \\ \kappa_{xy} \end{Bmatrix}$$

$$\begin{Bmatrix} 0 \\ M_y \\ 0 \end{Bmatrix} = \begin{bmatrix} B_{11} & B_{12} & B_{16} \\ B_{12} & B_{22} & B_{26} \\ B_{16} & B_{26} & B_{66} \end{bmatrix} \begin{Bmatrix} \varepsilon_x^o \\ \varepsilon_y^o \\ \gamma_{xy}^o \end{Bmatrix} + \begin{bmatrix} D_{11} & D_{12} & D_{16} \\ D_{12} & D_{22} & D_{26} \\ D_{16} & D_{26} & D_{66} \end{bmatrix} \begin{Bmatrix} \kappa_x \\ \kappa_y \\ \kappa_{xy} \end{Bmatrix} \tag{3.92}$$

The set of equations, (3.92), will be solved using a Gauss elimination procedure for ε_x^o, ε_y^o, γ_{xy}^o, κ_x, κ_y, κ_{xy}. The solution for the skin force resultants may be found from Eq. (3.85). The resultant force in the ring stiffener is

$$N_y^c = A_{22}^c \varepsilon_y^o + B_{22}^c \kappa_y \tag{3.93}$$

and the force in the ring stiffeners acting at the ring stiffener centroid

$$F_y^c = l_y N_y^c = l_y (A_{22}^c \varepsilon_y^o + B_{22}^c \kappa_y) \tag{3.94}$$

The resultant force in the geodesic stiffeners is

$$N_y^g = A_{21}^g \varepsilon_x^o + A_{22}^g \varepsilon_y^o + B_{21}^g \kappa_x + B_{22}^g \kappa_y \tag{3.95}$$

and the force on the the geodesic stiffeners is then

$$F_1 = F_2 = \frac{F_y^g}{2c\phi} = \frac{L_g N_y^g}{2c\phi} \tag{3.96}$$

The axial stiffeners carry no circumferential load and hence $F_x^g = 0$.

3.7.7.3 Case 3 - Shear Load (Applied Nxy)

In this case a state of applied shear loading, N_{xy}, exists. For this case it will be assumed that the prebuckling $N_x = N_y = 0$. The applied offset moment resisted by the geodesic stiffeners is then

$$M_{xy} = \bar{z}_g N_y^c \tag{3.97}$$

The resulting offset moment in terms of strains is

$$M_{xy} = \bar{z}_g (A_{66}^g \gamma_{xy}^o + B_{66}^g \kappa_{xy}) \tag{3.98}$$

Substituting Eq. (3.98) into Eq. (3.81) reduces the constitutive equations to

$$\begin{Bmatrix} 0 \\ 0 \\ N_{xy} \end{Bmatrix} = \begin{bmatrix} A_{11} & A_{12} & A_{16} \\ A_{12} & A_{22} & A_{26} \\ A_{16} & A_{26} & A_{66} \end{bmatrix} \begin{Bmatrix} \varepsilon_x^o \\ \varepsilon_y^o \\ \gamma_{xy}^o \end{Bmatrix} + \begin{bmatrix} B_{11} & B_{12} & B_{16} \\ B_{12} & B_{22} & B_{26} \\ B_{16} & B_{26} & B_{66} \end{bmatrix} \begin{Bmatrix} \kappa_x \\ \kappa_y \\ \kappa_{xy} \end{Bmatrix}$$

$$\begin{Bmatrix} 0 \\ 0 \\ M_{xy} \end{Bmatrix} = \begin{bmatrix} B_{11} & B_{12} & B_{16} \\ B_{12} & B_{22} & B_{26} \\ B_{16} & B_{26} & B_{66} \end{bmatrix} \begin{Bmatrix} \varepsilon_x^o \\ \varepsilon_y^o \\ \gamma_{xy}^o \end{Bmatrix} + \begin{bmatrix} D_{11} & D_{12} & D_{16} \\ D_{12} & D_{22} & D_{26} \\ D_{16} & D_{26} & D_{66} \end{bmatrix} \begin{Bmatrix} \kappa_x \\ \kappa_y \\ \kappa_{xy} \end{Bmatrix} \tag{3.99}$$

The solutions of Eq. (3.99) for ε_x^o, ε_y^o, γ_{xy}^o, κ_x, κ_y, and κ_{xy} may be substituted into Eq. (3.85) to find the skin resultant forces. The solution for the skin force resultants may be found from Eq. (3.85). The load distribution in the geodesic stiffeners may be found from the following expressions

$$F_{xy}^g = l_g N_{xy}^g = l_g (A_{66}^g \gamma_{xy}^o + B_{66}^g \kappa_{xy}) \tag{3.100}$$

$$F_1 = -F_2 = \frac{F^g_{xy}}{2c\phi} \tag{3.101}$$

The axial and ring stiffeners carry no shear loads and hence $F^a_x = 0$ and $F^c_y = 0$.

3.7.7.4 Case 4 - Applied End Shortening

In this case the strain, ε^o_x, must be calculated from the applied end displacements Δ such that

$$\varepsilon^o_x = \frac{\Delta}{L} \tag{3.102}$$

The solution will involve solving for N_x as an unknown rather than ε^o_x. It is assumed that in the prebuckling state N_y, N_{xy}, M_y, and M_{xy} are all zero. The offset moment will be given by Eq. (3.83). Substituting Eq. (3.83) into Eq. (3.81) and rearranging to solve for N_x as an unknown with ε^o_x known yields the following equation

$$\begin{Bmatrix} -A_{11}\varepsilon^o_x \\ -A_{12}\varepsilon^o_x \\ -A_{16}\varepsilon^o_x \end{Bmatrix} = \begin{bmatrix} -1 & A_{12} & A_{16} \\ 0 & A_{22} & A_{26} \\ 0 & A_{26} & A_{66} \end{bmatrix} \begin{Bmatrix} N_x \\ \varepsilon^o_y \\ \gamma^o_{xy} \end{Bmatrix} + \begin{bmatrix} B_{11} & B_{12} & B_{16} \\ B_{12} & B_{22} & B_{26} \\ B_{16} & B_{26} & B_{66} \end{bmatrix} \begin{Bmatrix} \kappa_x \\ \kappa_y \\ \kappa_{xy} \end{Bmatrix}$$

$$\begin{Bmatrix} -(B_{11} + \bar{z}_a A^g_{11} + \bar{z}_g A^g_{11})\varepsilon^o_x \\ -B_{21}\varepsilon^o_x \\ -B_{16}\varepsilon^o_x \end{Bmatrix} = \begin{bmatrix} 0 & (B_{12} - \bar{z}_g A^g_{12}) & B_{16} \\ 0 & B_{22} & B_{26} \\ 0 & B_{26} & B_{66} \end{bmatrix} \begin{Bmatrix} \varepsilon^o_x \\ \varepsilon^o_y \\ \gamma^o_{xy} \end{Bmatrix}$$

$$+\begin{bmatrix} (D_{11}-\bar{z}_a B_{11}^a-\bar{z}_g B_{11}^g) & (D_{12}-\bar{z}_g B_{12}^g) & D_{16} \\ D_{21} & D_{22} & D_{26} \\ D_{16} & D_{26} & D_{66} \end{bmatrix} \begin{Bmatrix} \kappa_x \\ \kappa_y \\ \kappa_{xy} \end{Bmatrix} \tag{3.103}$$

The set of equations, (3.103) will be yield ε_x^o, ε_y^o, γ_{xy}^o, κ_x, κ_y, κ_{xy}. The solutions and the known ε_x^o may be substituted into Eqs. (3.85)-(3.89) to calculate the appropriate forces in the skin and stiffeners.

3.8 Governing Equations and Final Form

The set equations of 3.29 represent 11 sets of equations which may be written in matrix form as

$$[K_{11x11}]\{\Delta\} = \lambda[M_{11x11}] \tag{3.104}$$

The nonzero elements of the stiffness and mass matrices of Eq. (3.104) are provided in Appendix B. The stiffness matrix of Eq. (3.104) is sparse and thus in this study the eigenvalue problem will be solved in terms of the shell (skin) displacements U, V, and W. The Lagrange multipliers, γ_{jp}, μ_{jp}, ϕ_{jp}, and ψ_{jp}, are eliminated from the problem by expressing these terms as functions of U, V, and W. After reducing the 11 x 11 set of equations the following eigenvalue problem results

$$\begin{bmatrix} [S_{11}] & [S_{12}] & [S_{13}] \\ [S_{12}] & [S_{22}] & [S_{23}] \\ [S_{13}] & [S_{23}] & [S_{33}] \end{bmatrix} \begin{Bmatrix} \{U\} \\ \{V\} \\ \{W\} \end{Bmatrix} = \lambda \begin{bmatrix} [0] & [0] & [0] \\ [0] & [0] & [0] \\ [0] & [0] & [\overline{M}_{33}] \end{bmatrix} \begin{Bmatrix} \{U\} \\ \{V\} \\ \{W\} \end{Bmatrix} \tag{3.105}$$

where

$$[S_{11}] = [K_{11}] + [K_{1,8}][K_{4,8}]^{-1}[K_{44}][K_{8,4}]^{-1}[K_{8,1}]$$

$$[S_{12}] = [K_{12}]$$

$$[S_{13}] = [K_{13}] + [K_{1,8}][K_{4,8}]^{-1}[K_{45}][K_{9,5}]^{-1}[K_{9,3}]$$

$$[S_{21}] = [K_{21}]$$

$$[S_{22}] = [K_{22}] + [K_{2,10}][K_{6,10}]^{-1}[K_{66}][K_{10,6}]^{-1}[K_{10,2}]$$

$$[S_{23}] = [K_{23}] + [K_{2,10}][K_{6,10}]^{-1}[K_{67}][K_{11,7}]^{-1}[K_{11,3}]$$

$$[S_{31}] = [K_{31}] + [K_{3,9}][K_{5,9}]^{-1}[K_{54}][K_{8,4}]^{-1}[K_{8,1}]$$

$$[S_{32}] = [K_{32}] + [K_{3,11}][K_{7,11}]^{-1}[K_{76}][K_{10,6}]^{-1}[K_{10,2}]$$

$$\begin{aligned}[S_{33}] = {} & [K_{33}] + [K_{3,9}][K_{5,9}]^{-1}[K_{55}][K_{9,5}]^{-1}[K_{9,3}] \\ & + [K_{3,11}][K_{7,11}]^{-1}[K_{77}][K_{11,7}]^{-1}[K_{11,3}]\end{aligned}$$

$$\begin{aligned}[\overline{M}_{33}] = {} & [M_{33}] + [M_{3,9}][M_{5,9}]^{-1}[M_{55}][M_{9,5}]^{-1}[M_{9,3}] \\ & + [M_{3,11}][M_{7,11}]^{-1}[M_{77}][M_{11,7}]^{-1}[M_{11,3}]\end{aligned} \tag{3.106}$$

The solutions of Eq. (3.105) yields the eigenvalues λ_{mn} for each mode M, N and the minimum eigenvalue is the critical buckling load.

In this development the out-of-plane and torsional stiffnesses of the beams were neglected. However, both the transverse and the in-plane displacements were constrained between the shell skin and the stiffeners. In many similar analyses only the transverse

displacements were constrained [118-123] and reasonable results were achieved. Moreover, this development is just an initial study of the buckling of stiffened shells using the layerwise theory and an analytical approach. The results shown in Chapter 5 reveal that this method does work well. Hence, including the out-of-plane and torsional stiffness of the stiffeners may in fact overstiffen the structure as developed in this chapter. This could yield poor results when compared with other analyses. The majority of this research involves the development and the use of the layerwise finite element method described in Chapter 4. Consequently, it was decided to concentrate more upon the finite element method and analyses rather then to include every minute detail into the analytical buckling approach. Including the out-of-plane and torsional stiffnesses of the stiffeners can be included in the future.

Chapter 4

Finite Element Formulation

4.1 Introduction

Displacement based finite element models developed from the governing equations presented in Chapter 2 are derived for both layerwise shell and beam elements. The layerwise theory reduces the equations of three-dimensional elasticity to a quasi three-dimensional laminate theory by assuming a layerwise approximation of the displacements through the thickness. Consequently, the strains are different in different layers. The interlaminar stresses (σ_{xz}, σ_{yz}, σ_{zz}) will be calculated using information from the in-plane stresses calculated from the finite element solution and by using an approximate technique to integrate the equilibrium equations. The variational statements of Appendix A and Eq. (2.23) are used in the development of the finite element models. In addition, the derivation of the direct stiffness and tangent stiffness matrices are presented. The finite element method for plates and shells is discussed in Refs. [32, 41-59, 125-142,

163, 167-170]. Several example problems are included in this chapter to verify the finite element program.

4.2 Layerwise Shell Finite Element Formulation

The generalized displacements (u_j, v_j, w_j) for the shell elements are expressed over each element as a linear combination of the two-dimensional interpolation functions ψ^n and the nodal values (u_j^n, v_j^n, w_j^n) as follows

$$(u_j, v_j, w_j) = \sum_{n=1}^{NDS} (u_j^n, v_j^n, w_j^n)\psi^n \tag{4.1}$$

where NDS is the total number of nodes per element. Substituting Eq. (4.1) into the variational statement of Appendix A yields the shell finite element model. A geometric description of the finite element shell model is shown in Figure 12a. The elemental finite model for layerwise shells may be expressed as

$$\begin{bmatrix} K_{11}^{mn} & K_{12}^{mn} & K_{13}^{mn} \\ K_{21}^{mn} & K_{22}^{mn} & K_{23}^{mn} \\ K_{31}^{mn} & K_{32}^{mn} & K_{33}^{mn} \end{bmatrix} \begin{Bmatrix} \{U\} \\ \{V\} \\ \{W\} \end{Bmatrix} = \begin{Bmatrix} \{F_x\} \\ \{F_y\} \\ \{F_z\} \end{Bmatrix} \tag{4.2}$$

where K_{11}^{mn}, K_{12}^{mn}, etc. are the element submatrices provided in Appendix C, {U}, {V}, and {W} are the column vectors of nodal displacements, $\{F_x\}$, $\{F_y\}$, and $\{F_z\}$ are the column vectors containing the boundary and force contributions.

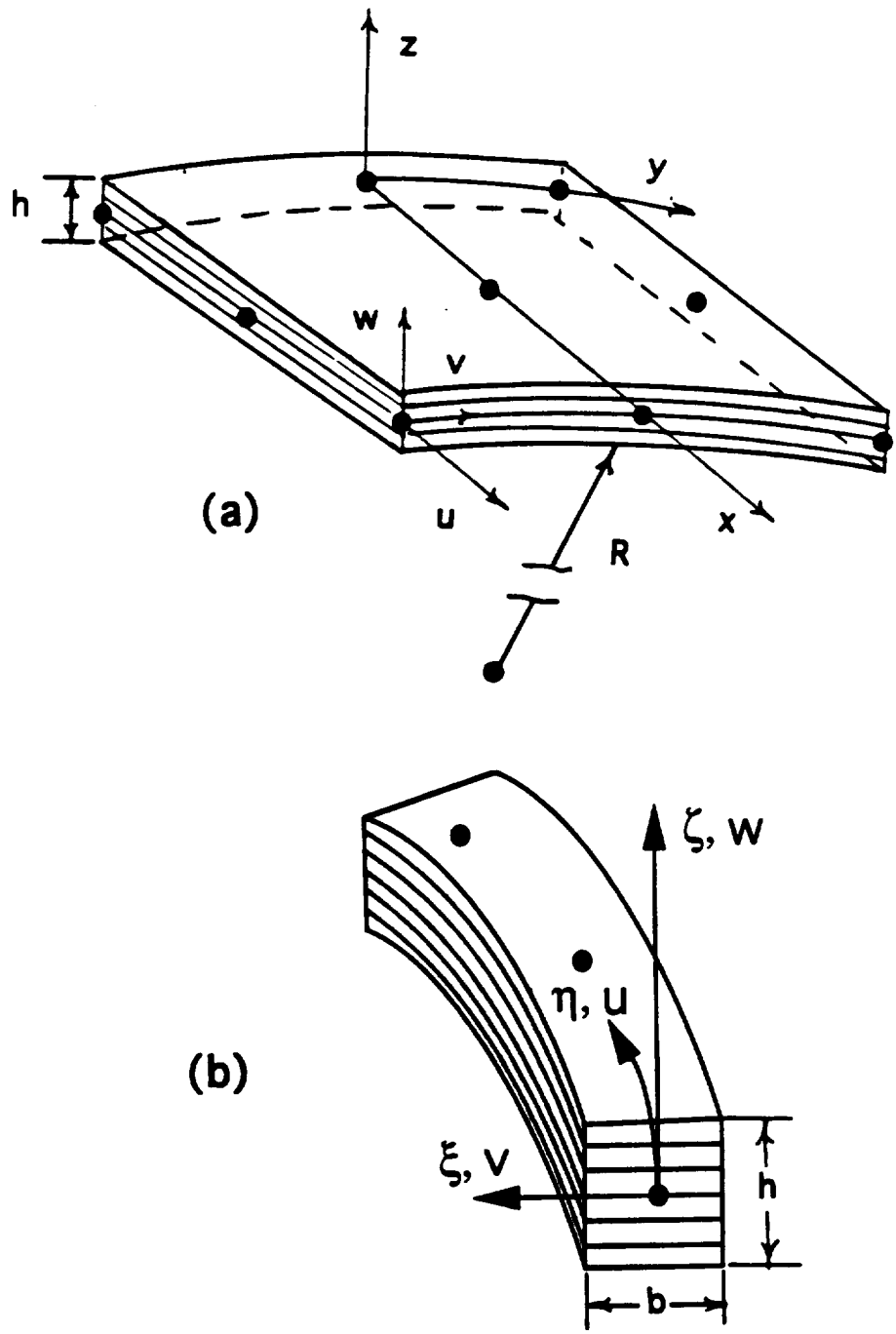

Figure 12. Geometry of the finite element model: a) shell element; b) beam element.

Three types of finite elements are developed in the finite element program. These are linear (4 nodes), Serendipity (8 nodes), and Lagrange (9 nodes) elements. Figure 13 shows these three types of finite elements. In this study the isoparametric rectangular master elements are used. The interpolation functions for these elements are listed below.

Linear Element (NDS = 4)

$$\begin{aligned}
\psi^1(\xi, \eta) &= \frac{1}{4}(1 - \xi)(1 - \eta) \\
\psi^2(\xi, \eta) &= \frac{1}{4}(1 + \xi)(1 - \eta) \\
\psi^3(\xi, \eta) &= \frac{1}{4}(1 + \xi)(1 + \eta) \\
\psi^4(\xi, \eta) &= \frac{1}{4}(1 - \xi)(1 + \eta)
\end{aligned} \tag{4.3}$$

Serendipity Element (NDS = 8)

$$\begin{aligned}
\psi^1(\xi, \eta) &= \frac{1}{4}(1 - \xi)(1 - \eta)(-1 - \xi - \eta) \\
\psi^2(\xi, \eta) &= \frac{1}{4}(1 + \xi)(1 - \eta)(-1 + \xi - \eta) \\
\psi^3(\xi, \eta) &= \frac{1}{4}(1 + \xi)(1 + \eta)(-1 + \xi + \eta) \\
\psi^4(\xi, \eta) &= \frac{1}{4}(1 - \xi)(1 + \eta)(-1 - \xi + \eta) \\
\psi^5(\xi, \eta) &= \frac{1}{2}(1 - \xi^2)(1 - \eta) \\
\psi^6(\xi, \eta) &= \frac{1}{2}(1 + \xi)(1 - \eta^2) \\
\psi^7(\xi, \eta) &= \frac{1}{2}(1 - \xi^2)(1 + \eta) \\
\psi^8(\xi, \eta) &= \frac{1}{2}(1 - \xi)(1 - \eta^2)
\end{aligned} \tag{4.4}$$

Lagrange Element (NDS = 9)

$$
\begin{aligned}
\psi^1(\xi, \eta) &= \frac{1}{4}(\xi^2 - \xi)(\eta^2 - \eta) \\
\psi^2(\xi, \eta) &= \frac{1}{4}(\xi^2 + \xi)(\eta^2 - \eta) \\
\psi^3(\xi, \eta) &= \frac{1}{4}(\xi^2 + \xi)(\eta^2 + \eta) \\
\psi^4(\xi, \eta) &= \frac{1}{4}(\xi^2 - \xi)(\eta^2 + \eta) \\
\psi^5(\xi, \eta) &= \frac{1}{2}(1 - \xi^2)(\eta^2 - \eta) \\
\psi^6(\xi, \eta) &= \frac{1}{2}(\xi^2 + \xi)(1 - \eta^2) \\
\psi^7(\xi, \eta) &= \frac{1}{2}(1 - \xi^2)(\eta^2 + \eta) \\
\psi^8(\xi, \eta) &= \frac{1}{2}(\xi^2 - \xi)(1 - \eta^2) \\
\psi^9(\xi, \eta) &= (1 - \xi^2)(1 - \eta^2)
\end{aligned}
\tag{4.5}
$$

4.3 Layerwise Beam Finite Element Formulation

The generalized displacements (u_j, w_j) for the beam elements are expressed over each element as a linear combination of the one-dimensional interpolation functions ψ^n and the nodal values (u_j^n, w_j^n) as follows

$$
(u_j, w_j) = \sum_{n=1}^{NDS} (u_j^n, w_j^n)\psi^n \tag{4.6}
$$

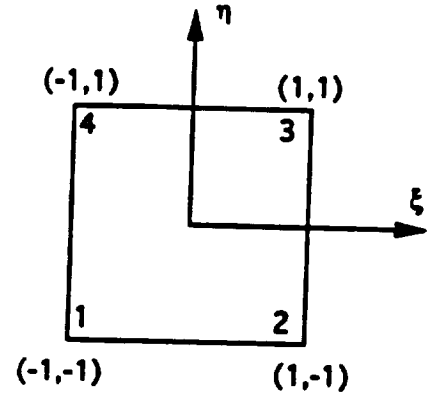

LINEAR ELEMENT

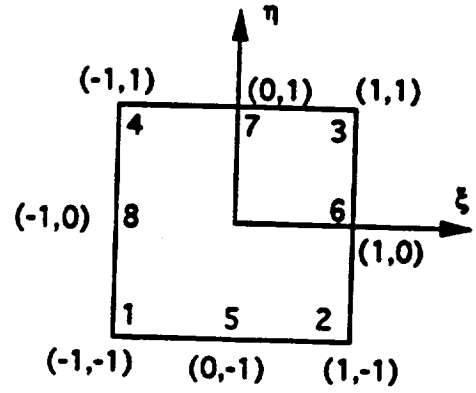

SERENDIPITY ELEMENT

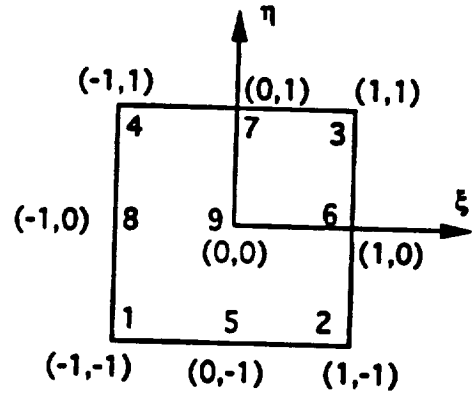

LAGRANGE ELEMENT

Figure 13. Node numbering and coordinates for Linear, Serendipity, and Lagrange shell finite elements.

where NDS is the total number of nodes per element. Substituting Eq. (4.6) into the variational statement of Eq. (2.23) yields the shell finite element model. The elemental finite model for layerwise shells may be expressed as

$$\begin{bmatrix} \overset{s}{K}{}^{mn}_{11} & \overset{s}{K}{}^{mn}_{12} \\ \overset{s}{K}{}^{mn}_{21} & \overset{s}{K}{}^{mn}_{22} \end{bmatrix} \begin{Bmatrix} \{U\} \\ \{W\} \end{Bmatrix} = \begin{Bmatrix} \{F_\eta\} \\ \{F_\zeta\} \end{Bmatrix} \tag{4.7}$$

where $\overset{s}{K}{}^{mn}_{\eta\eta}$, $\overset{s}{K}{}^{mn}_{\eta\gamma}$, etc. are the element submatrices provided in Appendix C, {U} and {W} are the column vectors of nodal displacements, $\{F_\eta\}$ and $\{F_\zeta\}$ are the column vectors containing the boundary and force contributions. See Figure 12b for a description of the layerwise beam element geometry.

Three types of finite elements are developed in the finite element program. These are linear (2 nodes), quadratic (3 nodes), and cubic (4 nodes) elements. Figure 14 shows these three types of finite elements. In this study the Lagrange family of master elements are used. The interpolation functions for these elements are listed below.

Linear Element (NDS = 2)

$$\begin{aligned} \psi^1 &= \frac{1}{2}(1 - \xi) \\ \psi^2 &= \frac{1}{2}(1 + \xi) \end{aligned} \tag{4.8}$$

Quadratic Element (NDS = 3)

$$\begin{aligned} \psi^1 &= -\frac{1}{2}\xi(1-\xi) \\ \psi^2 &= (1+\xi)(1-\xi) \\ \psi^3 &= \frac{1}{2}\xi(1+\xi) \end{aligned} \tag{4.9}$$

Cubic Element (NDS = 4)

$$\begin{aligned} \psi^1 &= -\frac{9}{16}(1-\xi)(\frac{1}{3}+\xi)(\frac{1}{3}-\xi) \\ \psi^2 &= \frac{27}{16}(1+\xi)(1-\xi)(\frac{1}{3}-\xi) \\ \psi^3 &= \frac{27}{16}(1+\xi)(1-\xi)(\frac{1}{3}+\xi) \\ \psi^4 &= -\frac{9}{16}(\frac{1}{3}+\xi)(\frac{1}{3}-\xi)(1+\xi) \end{aligned} \tag{4.10}$$

4.4 Assembly and Nonlinear Analysis

The layerwise shell and beam elements are assembled directly into the global stiffness matrix which yields the following sets of equations

$$[K(\Delta)]\{\Delta\} = \{F\} \tag{4.11}$$

such that

$$[K(\Delta)] = ([K_L] + [K_{NL}(\Delta)]) \tag{4.12}$$

where $[K(\Delta)]$ is the assembled global stiffness matrix, $[K_L]$ and $[K_{NL}(\Delta)]$ are the linear and geometrically nonlinear parts of the global stiffness matrix respectively, $\{\Delta\}$ is the

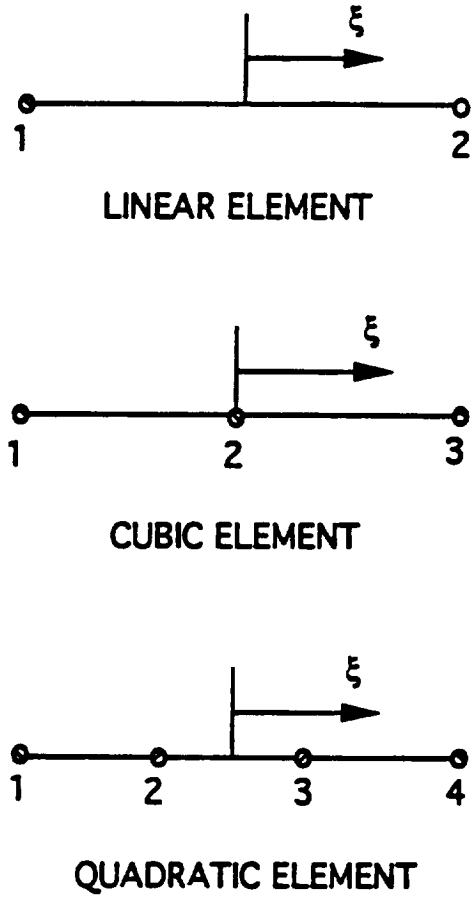

Figure 14. Node numbering and coordinates for Linear, Quadratic, and Cubic beam finite elements.

column vector of nodal displacements, and $\{F\}$ is the column vector of boundary or applied force conditions. The system of equations represented by Eq. (4.11) can be solved directly for linear problems. However, for geometrically nonlinear problems the stiffness matrix is a nonlinear function of the unknown solution and must be solved iteratively.

The method selected here for solving geometrically nonlinear problems of stiffened plates and shells is the Newton-Raphson method. In the Newton-Raphson iteration method, the basic equations for the residual vector $\{R\}$ is given by the expression

$$\{R\} \equiv [K(\Delta)]\{\Delta\} - \{F\} = 0 \tag{4.13}$$

Assuming that the solution is known at the r^{th} iteration, the residual vector $\{R\}$ is expanded in a Taylor series about $\{\Delta^r\}$,

$$\begin{aligned} 0 &= \{R\}_r + \frac{\partial\{R\}}{\partial\{\Delta\}}\{\delta\Delta\}_r + \cdots \\ &= ([K(\Delta^r)]\{\Delta^r\} - \{F\}) + [K^T(\Delta^r)]\{\delta\Delta^r\} \end{aligned} \tag{4.14}$$

where the tangent stiffness matrix $[K^T]$ is given by

$$[K^T(\Delta^r)] = \left[\frac{\partial\{R\}}{\partial\{\Delta^r\}}\right] \tag{4.15}$$

The tangent stiffness matrices for layerwise shell and beam elements are presented in Appendix C. The final equation to be solved for the increment of the solution $\{\delta\Delta^r\}$ is

$$[K^T(\Delta^r)]\{\delta\Delta^r\} = \{R\} \tag{4.16}$$

The total displacement at the $(r+1)^{th}$ iteration is given by

$$\{\Delta^{r+1}\} = \{\Delta^r\} + \{\delta\Delta^r\} \tag{4.17}$$

The convergence criteria used to determine when the iterative solution stops is

$$\sqrt{\frac{\sum_{i=1}^{NDS} |\Delta_i^{r+1} - \Delta_i^r|^2}{\sum_{i=1}^{N} |\Delta_i^r|^2}} \leq EPS \tag{4.18}$$

If applied displacements rather than applied forces are specified for a particular problem then the total loads at the $(r+1)^{th}$ iteration is given by

$$\{F^{r+1}\} = \{F^r\} + \{\delta F^r\} \tag{4.19}$$

The subsequent convergence criteria is then

$$\sqrt{\frac{\sum_{i=1}^{I} |F_i^{r+1} - F_i^r|^2}{\sum_{i=1}^{I} |F_i^r|^2}} \leq EPS \tag{4.20}$$

where I is the number of nodes at which the applied displacements are not specified.

A geometric explanation of the Newton-Raphson technique for a one-dimensional problem is provided in Figure 15.

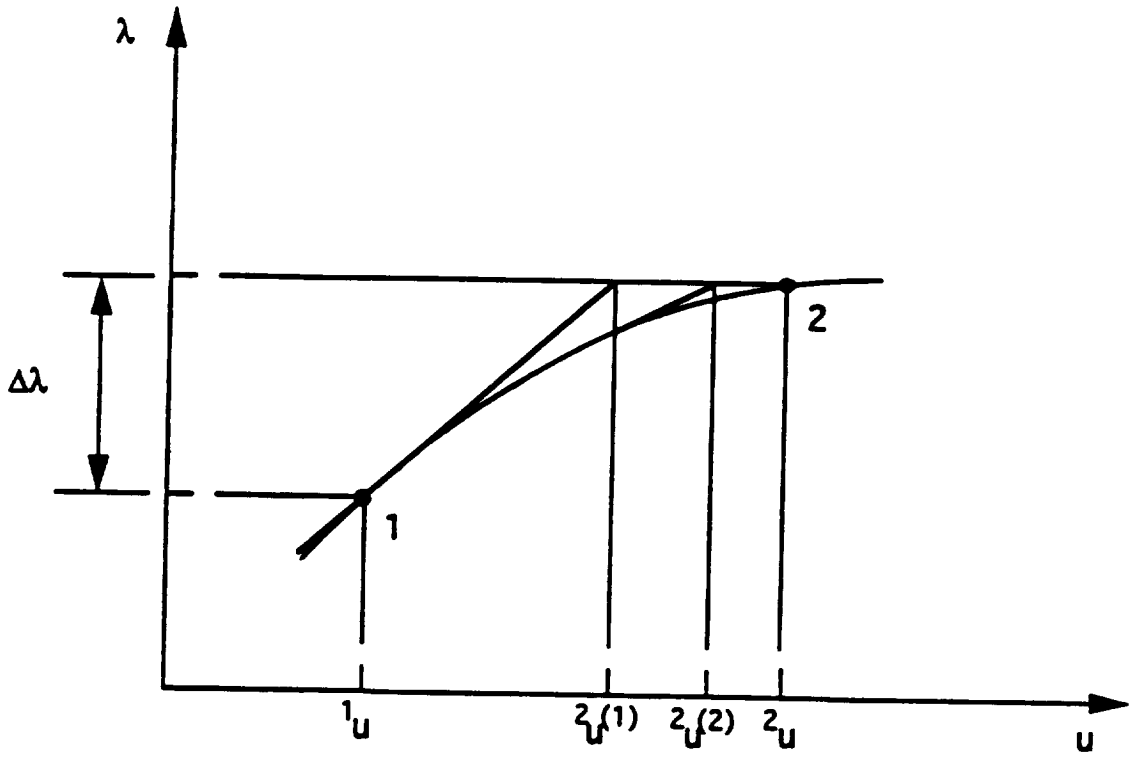

Figure 15. Newton-Raphson method of a one-dimensional problem with tangent stiffness matrix at each iteration.

4.5 Beam Element Stiffness Transformations

Beam elements may be oriented at any arbitrary angle α from the x axis of the shell as shown in Figure 16. The translational degrees of freedom of the beam u' and w' are related to the displacements in the shell coordinates u, v, and w by the following vector relationships

$$\begin{aligned} u' &= u\cos\alpha + v\sin\alpha \\ v' &= -u\sin\alpha + v\cos\alpha \\ w' &= w \end{aligned} \tag{4.21}$$

The stiffness transformation relation may be expressed as (see Cook [170])

$$[K_s] = [T]^T[K'_s][T] \tag{4.22}$$

where $[K_s]$ is the transformed beam stiffness matrix, $[T]$ is the transformation matrix, and $[K'_s]$ is the stiffness matrix to be transformed. For example, the beam node local to global coordinate transformation matrix is

$$[T_{(3x3)}] = \begin{bmatrix} c\alpha & s\alpha & 0 \\ -s\alpha & c\alpha & 0 \\ 0 & 0 & 1 \end{bmatrix} \tag{4.23}$$

where

$$\begin{aligned} s\alpha &= \sin\alpha \\ c\alpha &= \cos\alpha \end{aligned} \tag{4.24}$$

The stiffness matrix to be transformed is

$$[K'_{s\,(3x3)}] = \begin{bmatrix} K'_{11} & 0 & K'_{12} \\ 0 & \hat{K}'_{11} & 0 \\ K'_{21} & 0 & K'_{22} \end{bmatrix} \tag{4.25}$$

where K'_{11} represents the in-plane stiffness, K'_{12} and K'_{21} are the shear stiffnesses, K'_{22} is the transverse stiffness, and $\hat{K}'_{11}$ is the out-of-plane stiffness.

In this research the stiffeners are thin (0.2") and an approximation of the out-of-plane stiffness is made based upon the ratios of the out-of-plane moment of inertia, I_η, with the in-plane moment of inertia, I_ξ. See Figure 12b for a description of the beam element and the geometry. The out-of-plane stiffness is then developed as

$$\begin{aligned} \hat{K}'_{11} &= \frac{I_\eta}{I_\xi} K'_{11} \\ \hat{K}'_{11} &= \frac{b^2}{h^2} K'_{11} \end{aligned} \tag{4.26}$$

where $I_\xi = \frac{bh^3}{12}$ and $I_\eta = \frac{hb^3}{12}$.

Carrying out the matrix multiplications as defined by Eq. (4.22) yields the following transformed stiffness matrix

$$[K_{s\,(3x3)}] = \begin{bmatrix} (K'_{11}c^2\alpha + \hat{K}'_{11}s^2\alpha) & (K'_{11}c\alpha s\alpha - \hat{K}'_{11}c\alpha s\alpha) & K'_{12}c\alpha \\ (K'_{11}c\alpha s\alpha - \hat{K}'_{11}c\alpha s\alpha) & (K'_{11}s^2\alpha + \hat{K}'_{11}c^2\alpha) & K'_{12}s\alpha \\ K'_{21}c\alpha & K'_{21}s\alpha & K'_{22} \end{bmatrix} \tag{4.27}$$

Each node in the beam will transfer in the same manner as that presented in Eqs. (4.21-4.27).

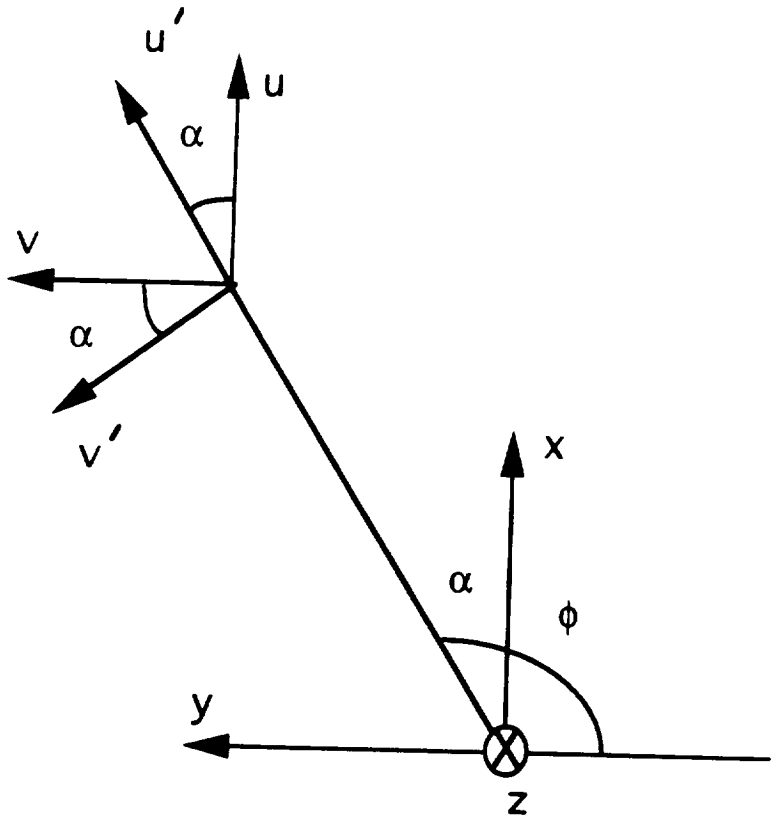

$$u' = u \cos \alpha + v \sin \alpha$$

$$v' = -u \sin \alpha + v \cos \alpha$$

$$w' = w$$

Figure 16. Representation of the beam displacements (u', v', w') to shell transformation shell displacements (u, v, w).

4.6 Interlaminar Stress Calculation

In this study an approximate technique is used to integrate the equilibrium equations by using the in-plane stress information provided by the finite element solution. The technique presented by Chaudhuri and Seide [171] is extended here to quadrilateral isoparametric elements. The work of Reference [171] is derived for interlaminar shear stresses and was also adopted in the work by Barbero and Reddy [172]. The authors of [172] obtained the transverse shear stresses using derivatives of in-plane stresses that were calculated by differentiating the interpolation functions of a finite element approximation based on a generalized laminated plate theory. The work presented in [171,172] will be extended to both transverse shear stresses (σ_{xz}, σ_{yz}) and the transverse normal stresses σ_{zz} for layerwise shell elements. Additional references on calculating interlaminar stresses may be found in [173-175].

In this study the interlaminar stress distribution through each layer is approximated with a quadratic function requiring 3N equations for each of the interlaminar stresses (σ_{xz}, σ_{yz}, σ_{zz}) where N is the number of layers; N equations are used to satisfy the N average shear stresses on each layer. Two equations are used either to impose vanishing shear stresses at the top and bottom surfaces of the shell or for the interlaminar normal stress $\sigma_{zz} = p_o$ on the surfaces. If there is no applied p_o on one or both surfaces then $\sigma_{zz} = 0$. Then, (N - 1) equations are employed to satisfy continuity of the stresses as the interfaces between layers. The remaining (N - 1) equations are used to compute the jump in $\frac{\partial \sigma_{xz}}{\partial z}$, $\frac{\partial \sigma_{yz}}{\partial z}$, or $\frac{\partial \sigma_{zz}}{\partial z}$ at each interface.

The average stresses on each layer are computed from the constitutive equations and the displacement field obtained in the finite element analysis.

The equilibrium equations for a cylindrical shell are

$$
\begin{aligned}
&\frac{\partial \sigma_{xx}}{\partial x} + \frac{1}{R}\frac{\partial \sigma_{xy}}{\partial y} + \frac{\partial \sigma_{xz}}{\partial z} = 0 \\
&\frac{1}{R}\frac{\partial \sigma_{yy}}{\partial y} + \frac{\partial \sigma_{xy}}{\partial x} + \frac{\partial \sigma_{yz}}{\partial z} = 0 \\
&\frac{\partial}{\partial x}\left(\sigma_{xx}\frac{\partial w}{\partial x}\right) - \frac{\sigma_{yy}}{R} + \frac{1}{R}\frac{\partial}{\partial y}\left(\frac{\sigma_{yy}}{R}\frac{\partial w}{\partial y}\right) \\
&+ \frac{1}{R}\frac{\partial \sigma_{yz}}{\partial y} + \frac{\partial \sigma_{xz}}{\partial x} + \frac{1}{R}\frac{\partial}{\partial y}\left(\sigma_{xy}\frac{\partial w}{\partial x}\right) \\
&+ \frac{\partial}{\partial x}\left(\frac{\sigma_{xy}}{R}\frac{\partial w}{\partial y}\right) + \frac{\partial \sigma_{zz}}{\partial z} + p_o = 0
\end{aligned}
\tag{4.28}
$$

The equilibrium equations for a flat plate reduce to

$$
\begin{aligned}
&\frac{\partial \sigma_{xx}}{\partial x} + \frac{\partial \sigma_{xy}}{\partial y} + \frac{\partial \sigma_{xz}}{\partial z} = 0 \\
&\frac{\partial \sigma_{yy}}{\partial y} + \frac{\partial \sigma_{xy}}{\partial x} + \frac{\partial \sigma_{yz}}{\partial z} = 0 \\
&\frac{\partial \sigma_{xz}}{\partial x} + \frac{\partial \sigma_{yz}}{\partial y} + \frac{\partial \sigma_{zz}}{\partial z} + p_o = 0
\end{aligned}
\tag{4.29}
$$

Here the equilibrium equations are used to compute $\frac{\partial \sigma_{xz}}{\partial z}$, $\frac{\partial \sigma_{yz}}{\partial z}$, and $\frac{\partial \sigma_{zz}}{\partial z}$ directly from the finite element approximation. The components of the stresses and their derivatives are computed from the constitutive equations for each layer. The procedure requires computation of the second derivatives of the displacements (u_j, v_j, w_j) are presented in Appendix D.

4.7 Finite Element Verification Analyses

4.7.1 Introduction

Several representative problems are analyzed using the previously derived layerwise elements and solution procedures. Some of the problems have analytical solutions or the analysis has been presented in the open literature by using different finite element models. Comparisons of the present results with published solutions, where available, provide a check for the accuracy and applicability of the layerwise elements developed for this research work. Although additional analyses were performed only a selected group of representative sample problems are presented here.

4.7.2 Unstiffened Plates and Shells

1. Orthotropic Clamped Cylindrical Shell

A comparison of the center deflection of an orthotropic clamped cylindrical shell subjected to internal pressure as shown in Figure 17 is presented in Table 1. A comparison is made with the finite element solutions presented by Reddy [167] and Rao [176] and the analytical solution presented by Timoshenko and Woinowsky-Krieger [61]. A 2x2 mesh of 9 node layerwise shell elements was used for this analysis. The layerwise finite element results yield a good correlation with the published solutions.

2. Cylindrical Shell Roof Under the Action of Self-Weight

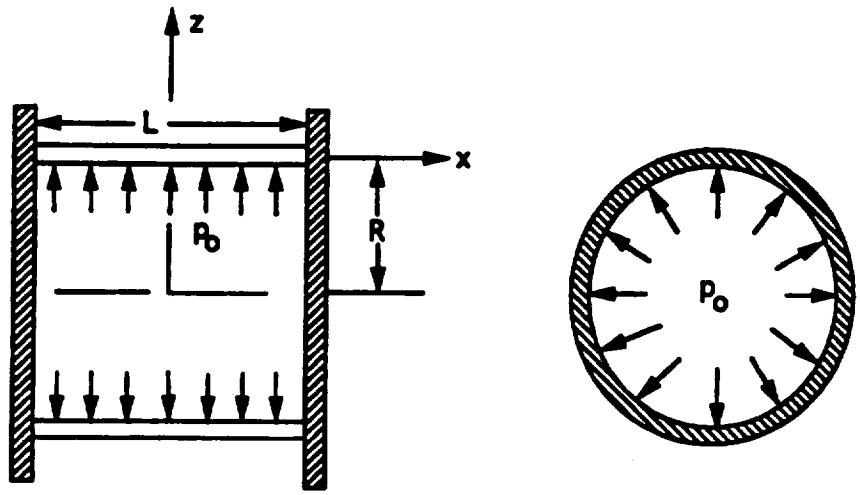

R = 20 inches

L = 20 inches

$p_o = 6.4/\pi$ psi

Figure 17. A clamped cylindrical shell subjected to internal pressure.

Table 1. Comparison of the Center Deflection of a Pressurized Clamped, Cylindrical Shell.

Lamination Scheme	Reddy		LWTR (FEA)	K. P. Rao	Analytical
	4L	2Q9	2Q9	1978	
0^0	0.0003754	0.0003727	0.0003746	0.0003666	0.000367
$0^0/90^0$	0.0001870	0.0001803	0.0001838	———	———

Material Properties

$E_1 = 7.5 \times 10^6$ psi

$E_2 = 2.0 \times 10^6$ psi

$G_{12} = 1.25 \times 10$ psi

$G_{12} = G_{13} = G_{23}$

$\nu_{12} = \nu_{13} = 0.25$

This problem as shown in Figure 18 was solved using conventional techniques by Scordelis and Lo [177]. This particular cylindrical shell problem has been used frequently to assess shell finite element performance [45, 178-181]. The shell is supported on rigid diaphrams and is loaded by its own weight. This is a test case of the application of the full process to a shell in which bending action is severe due to the supports restraining deflection at the ends. In Reference [178], the authors showed that using fully reduced integration yields more rapid convergence and better accuracy than selectively reduced integration on the transverse shear terms only. The results presented in Figures 19 and 20 are for layerwise shell elements with fully reduced integration and using 1x1, 2x2, and 3x3 meshes 9 node elements. The layerwise elements produce excellent correlation with the analytical solution of Reference [177].

3. Center Deflection of a Simply Supported Orthotropic Cylindrical Roof

The geometry, boundary conditions, material properties, and results for the simply supported orthotropic cylindrical roof is shown in Figure 21. The nonlinear results were developed from the Newton-Raphson procedure discussed in Section 4.5. The results are in good agreement with the results presented by Palmerio [182].

4. Center Deflection of a Simply Supported 0/90 Cylindrical Roof

The geometry, boundary conditions, material properties, and results for this problem are found in Figure 22. The Newton-Raphson technique was employed to acquire the nonlinear results. The results agree well with the work by Palmerio [182].

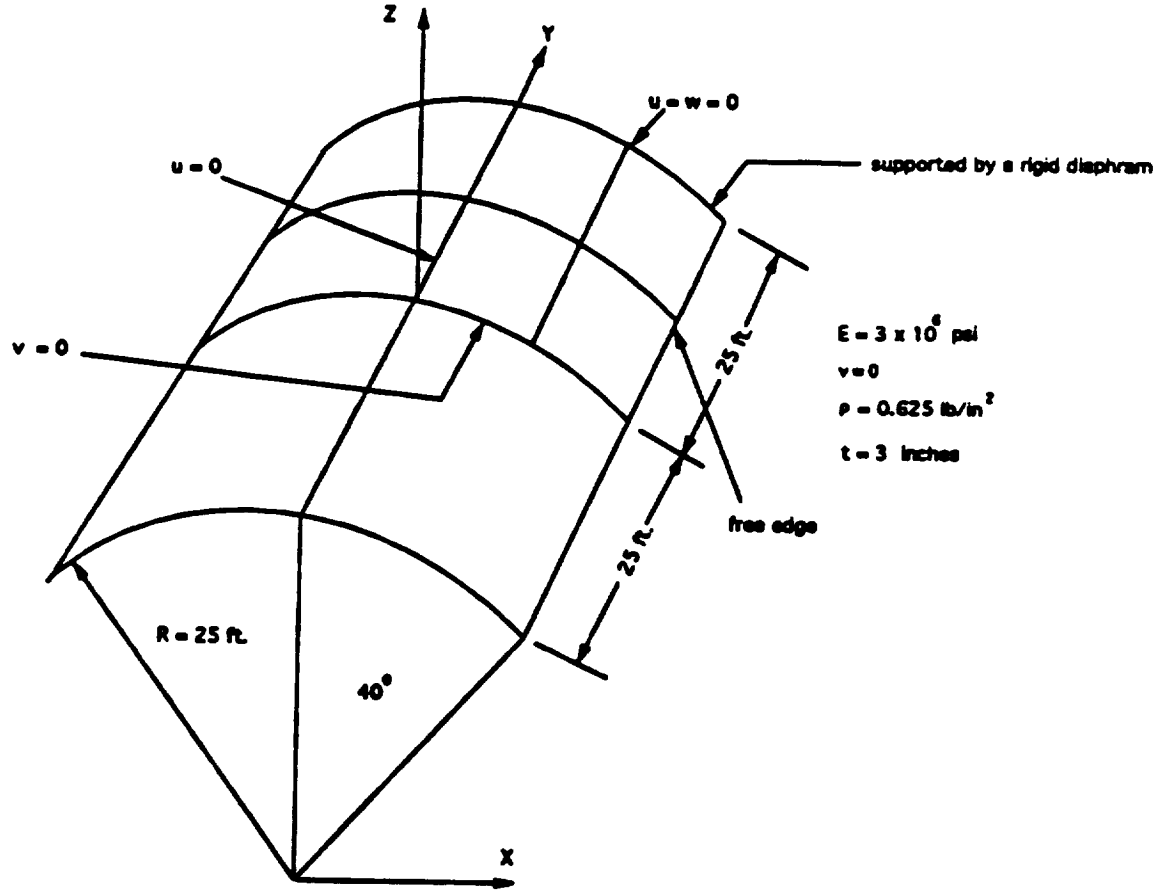

Figure 18. An isotropic cylindrical shell roof under self-weight.

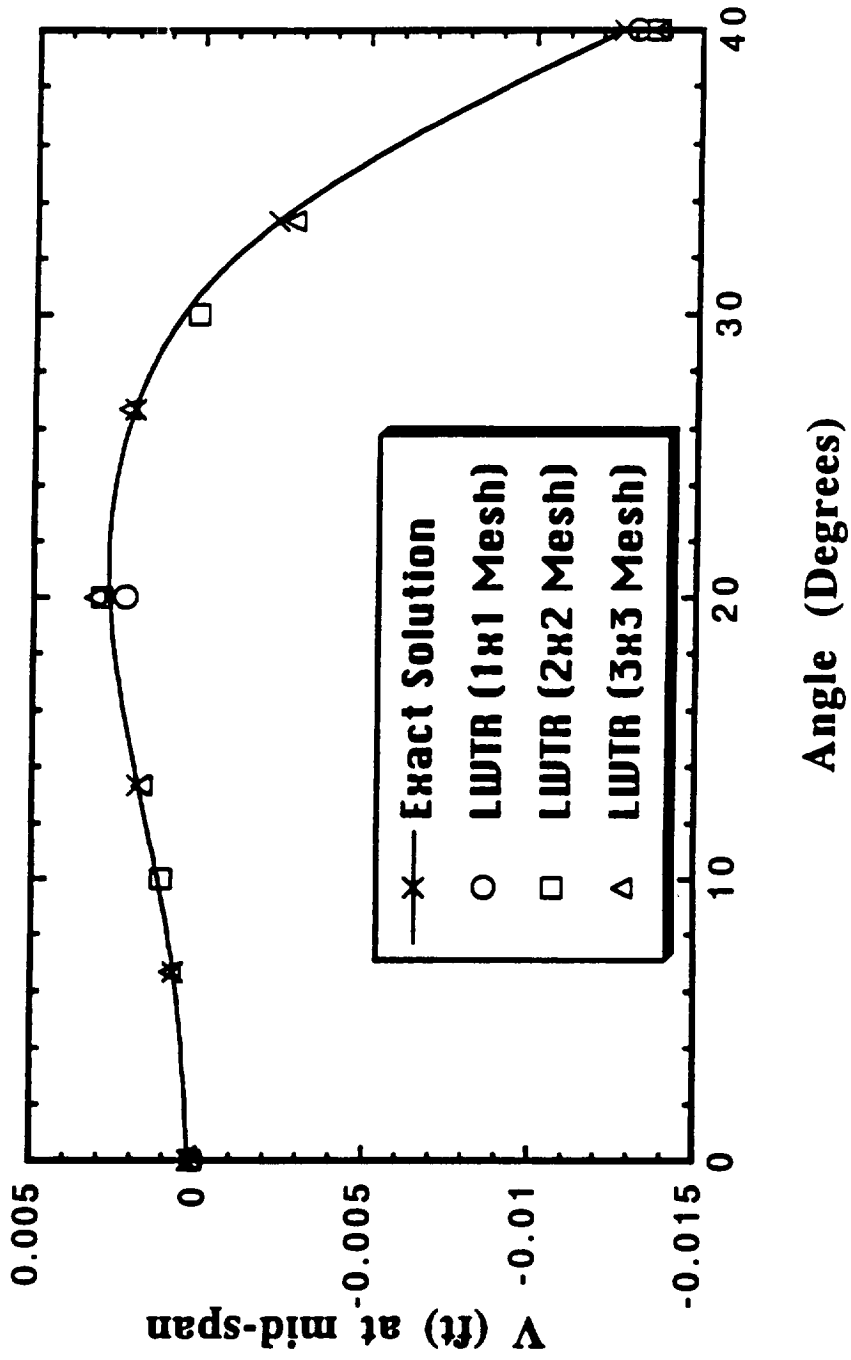

Figure 19. Axial deflection at the support of an isotropic cylindrical shell roof under self-weight.

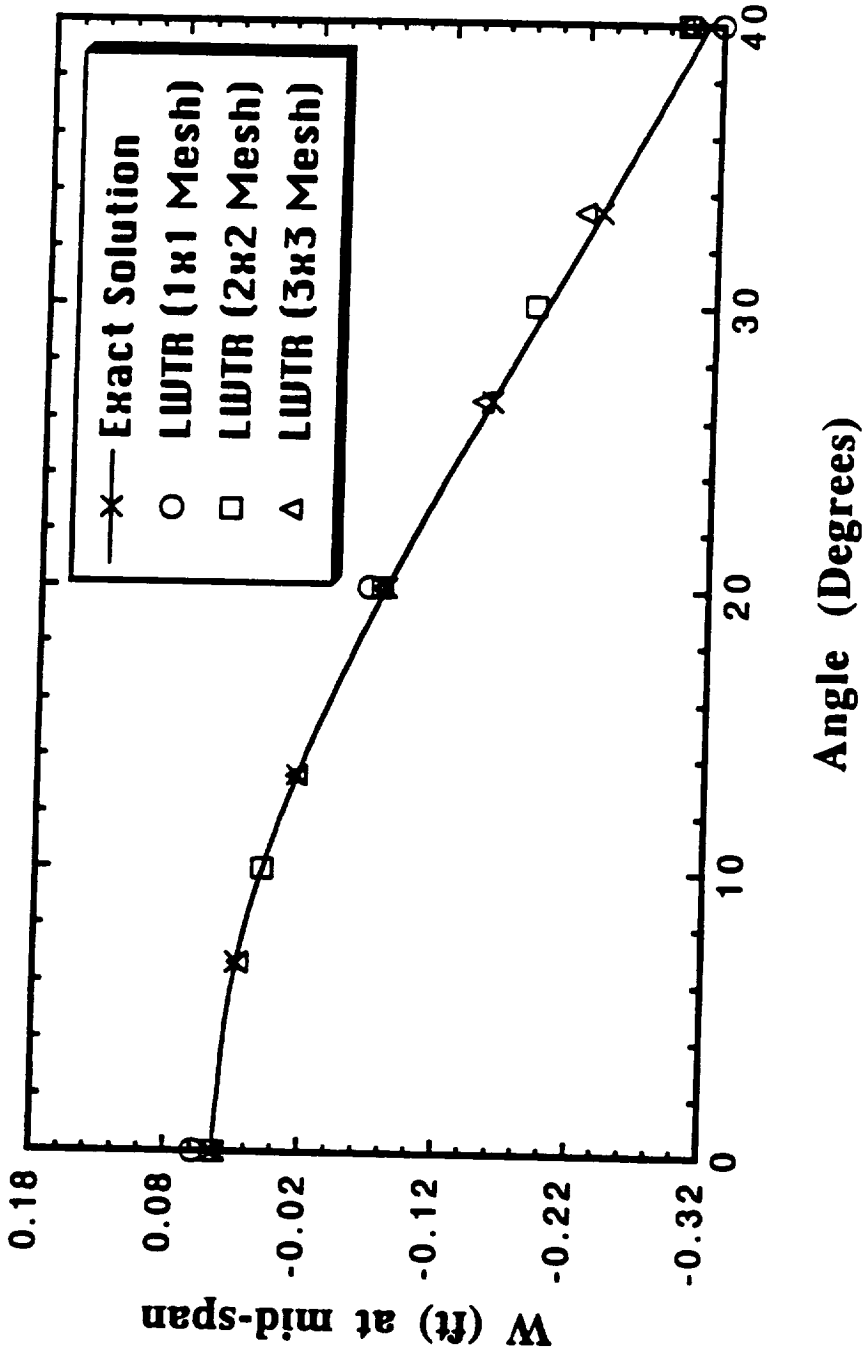

Figure 20. Transverse deflection at the support of an isotropic cylindrical shell roof under self-weight.

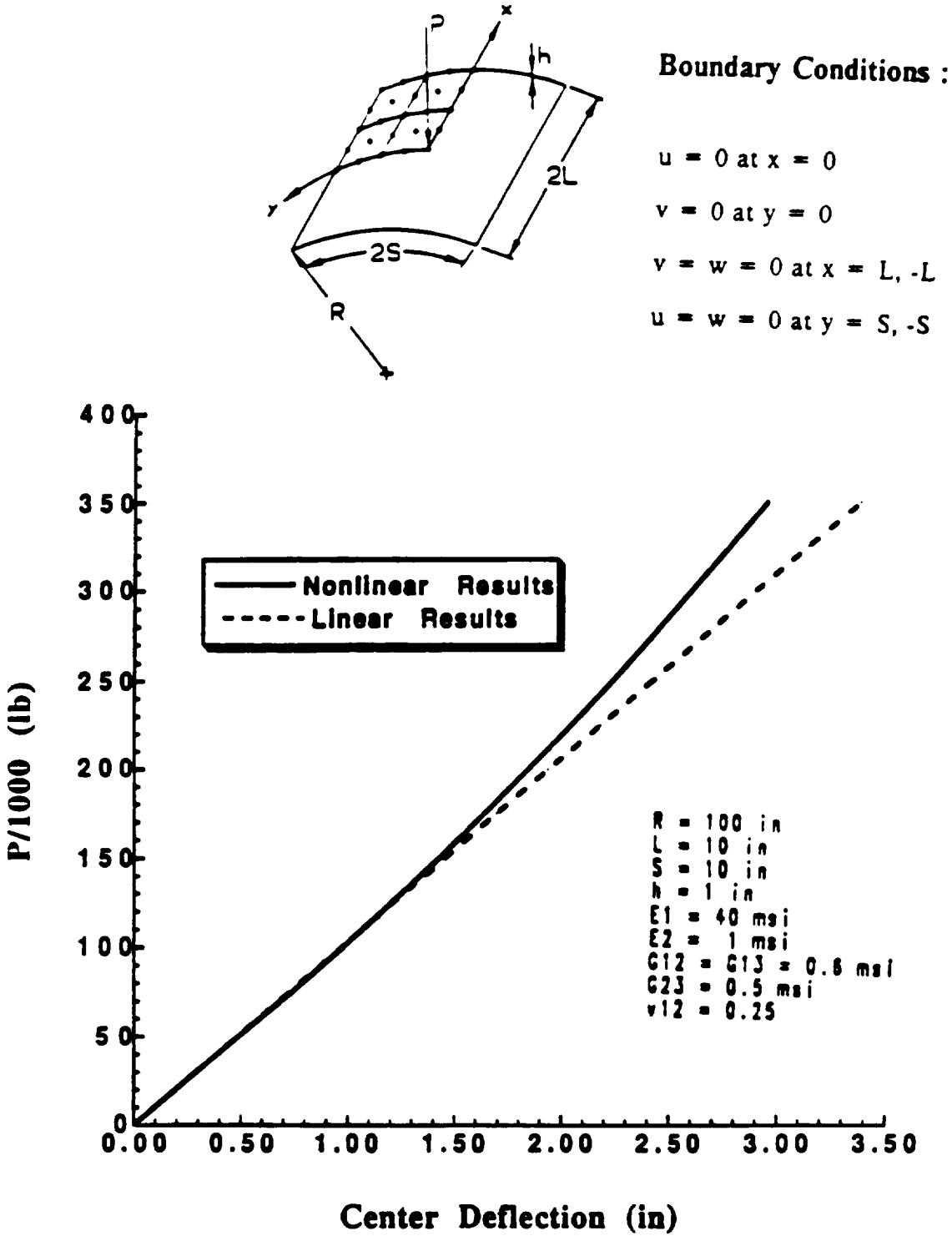

Figure 21. Simply supported orthotropic cylindrical roof.

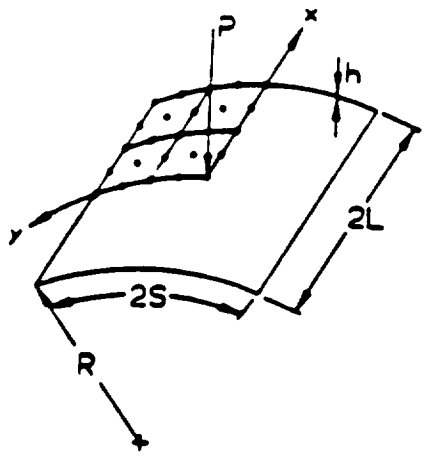

Boundary Conditions :

u = 0 at x = 0

v = 0 at y = 0

v = w = 0 at x = L, -L

u = w = 0 at y = S, -S

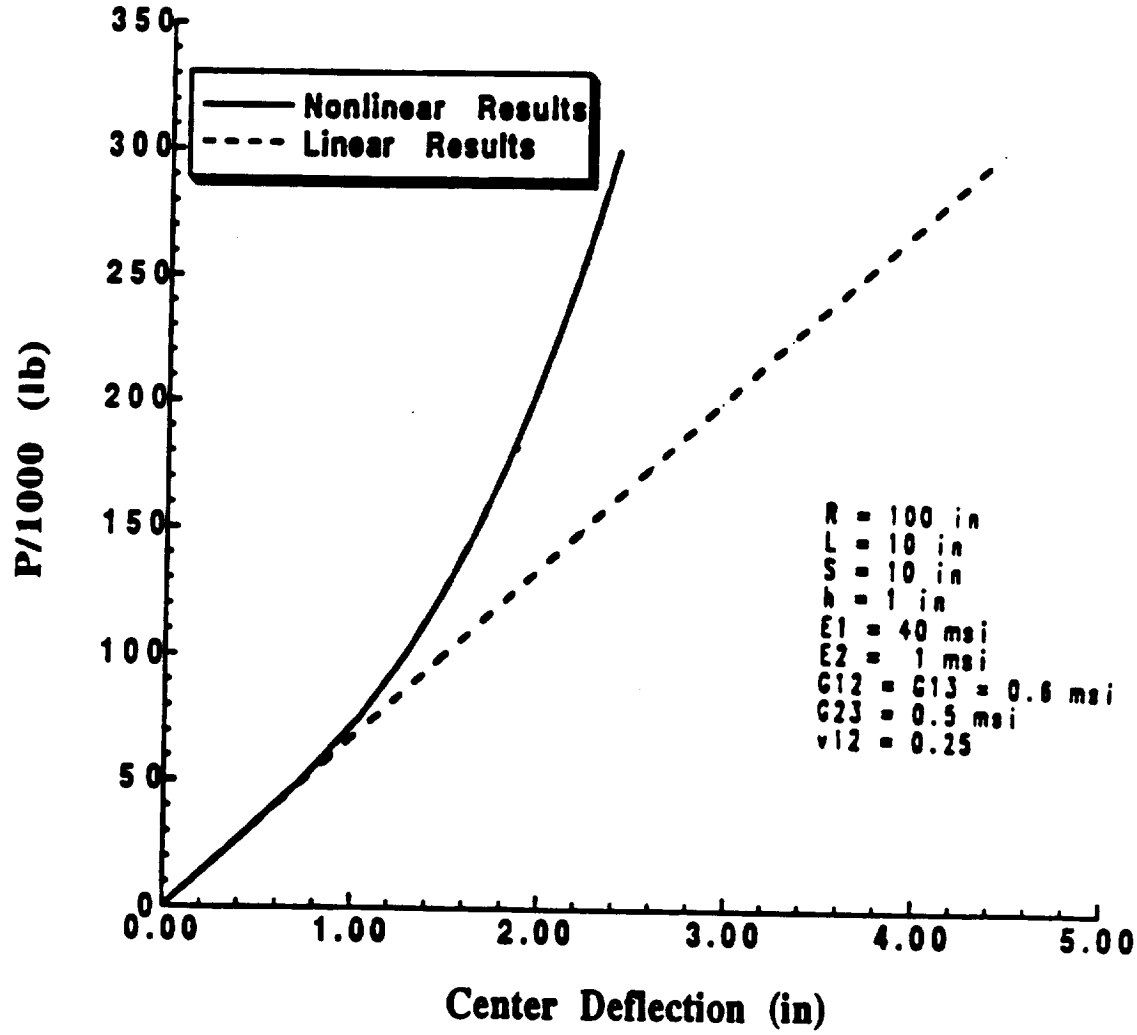

Figure 22. Simply supported [0/90] cylindrical roof.

5. Stress Analysis of a Simply Supported [0/90/0] Plate

The plate being studied is loaded with a uniformly distributed transverse load. The plate boundary conditions and material properties are described in Figure 23. The plate is simply supported on all four sides and due to symmetry only a quarter of the plate is modeled. A 4x4 mesh of 9 node elements are used in this analysis. The through the thickness distribution of the inplane normal stress, $\bar{\sigma}_{xx}$, for an aspect ratio of a/h = 10, is shown in Figure 24. The stresses were computed at the Gauss point x = y = 0.0528a. Figures 25 and 26 contain similar plots of the interlaminar shear stresses $\bar{\sigma}_{yz}$ and $\bar{\sigma}_{xz}$, respectively. In Figure 25, $\bar{\sigma}_{yz}$ is computed at the point x = 0.0528a and y = 0.9472a. In Figure 26, $\bar{\sigma}_{xz}$ is computed at the point x = 0.9472a and y = 0.0528a. In these plots, dashed lines represent stresses obtained from the constitutive equations, while the smooth solid line represents the stress distribution obtained using the equilibrium equations as developed in Section 4.6. Stresses obtained using the LWTR, the FSDT (first order shear deformation theory) are also compared in these plots. The transverse normal stress, $\bar{\sigma}_{zz}$ obtained from both the constitutive and equilibrium equations is shown in Figure 27. The transverse normal stress is obtained at the Gauss point x = y = 0.0528a. Modeling each layer in the composite plate as several layers may serve to increase the agreement between the LWTR equilibrium and the LWTR constitutive results.

4.7.3 Beam Structures

1. Cantilever Beam Subjected to an End Load

The beam dimensions and properties used in this analysis are found in Figure 28. The

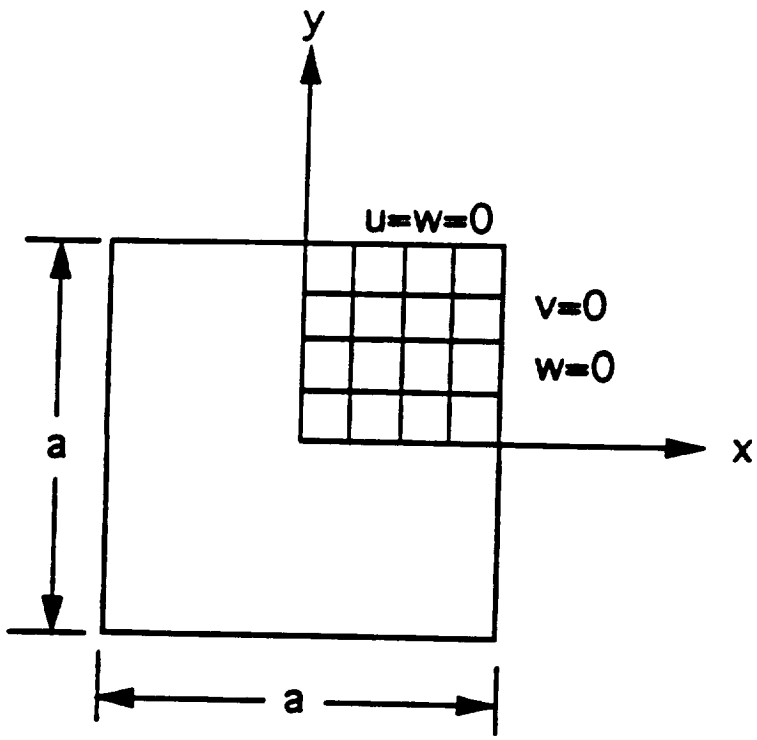

[0/90/0] Simply Supported Plate

$E_1 = 18.5 \times 10^6$ psi

$E_2 = E_3 = 1.64 \times 10^6$ psi

$G_{12} = G_{13} = 0.87 \times 10^6$ psi

$G_{23} = 0.54 \times 10^6$ psi

$\nu_{12} = \nu_{13} = 0.30$

$\nu_{23} = 0.49$

Figure 23. Simply supported [0/90/0] square plate subjected to a uniformly distributed load.

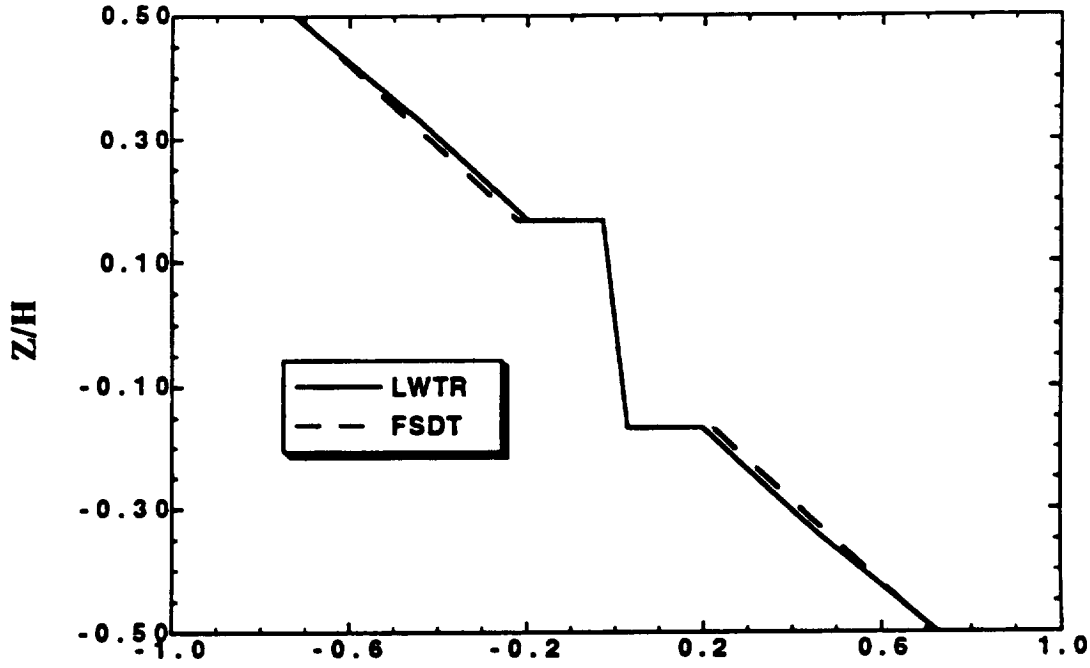

$$\bar{\sigma}_{xx} = \frac{\sigma_{xx}}{q\left(\frac{a}{h}\right)}$$

Figure 24. Through-the-thickness distribution of the in-plane normal stress $\bar{\sigma}_{xx}$ for a simply supported, [0/90/0] laminated square plate under uniform load, (a/h = 10).

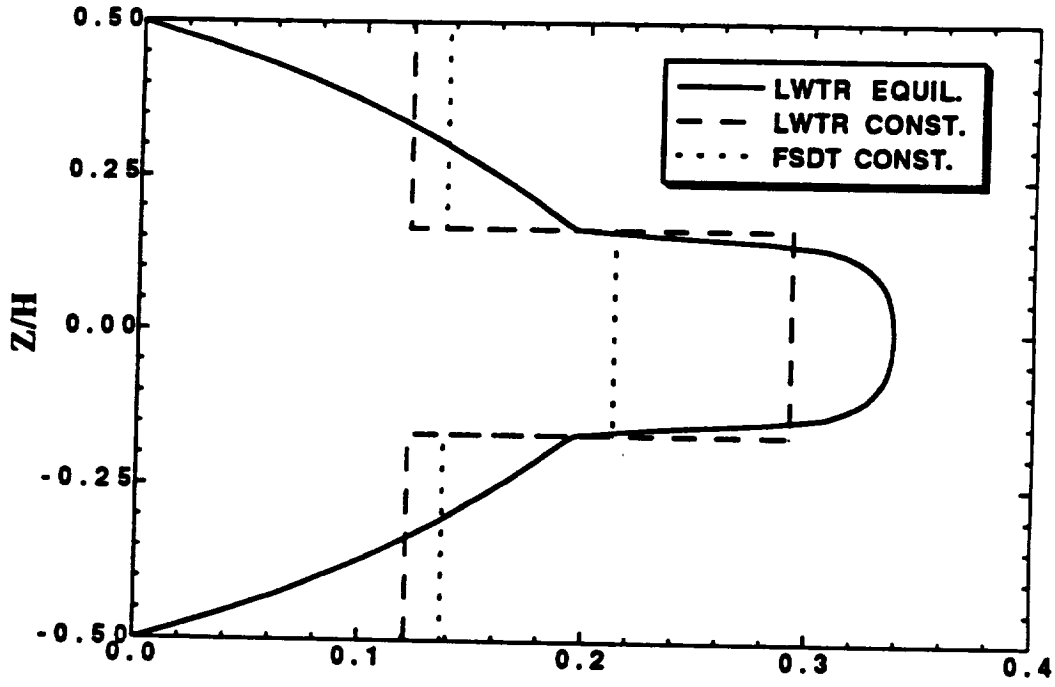

Figure 25. Through-the-thickness distribution of the transverse shear stress $\bar{\sigma}_{yz}$ for a simply supported, [0/90/0] laminated square plate under uniform load, (a/h = 10).

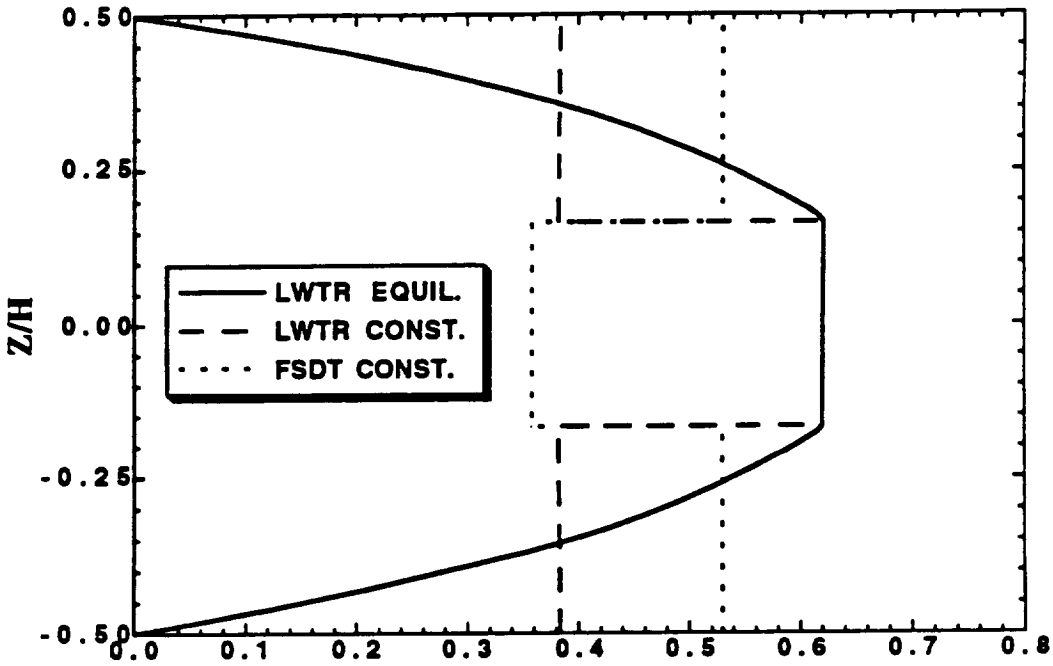

$$\bar{\sigma}_{xz} = \frac{\sigma_{xz}}{q\left(\frac{a}{h}\right)^2}$$

Figure 26. Through-the-thickness distribution of the transverse shear stress $\bar{\sigma}_{xz}$ for a simply supported, [0/90/0] laminated square plate under uniform load, (a/h = 10).

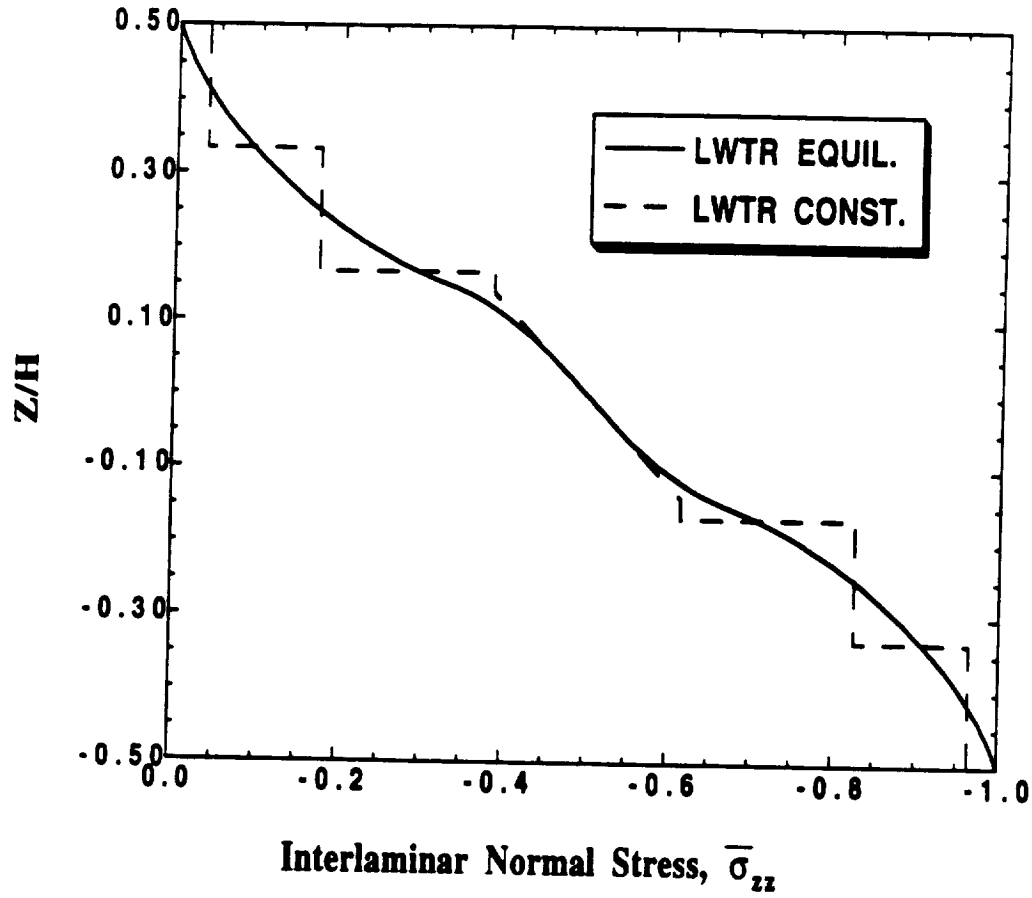

$$\bar{\sigma}_{zz} = \frac{\sigma_{zz}}{q}$$

Figure 27. Through-the-thickness distribution of the transverse normal stress $\bar{\sigma}_{zz}$ for a simply supported, [0/90/0] laminated square plate under uniform load, (a/h = 10).

linear results for this analysis are presented in Table 2 and good correlation exists between the finite element and the classical solutions.

2. Cantilever Beam Subjected to a Uniform Load

The beam dimensions and properties used for this example problem are shown in Figure 28. The linear results for this analysis are presented in Table 2. The linear finite element results compare well with the results from classical beam theory. The large deflection analysis of the cantilever beam subjected to a uniform load is presented in Figure 29. These results compare well with the results presented by Liao [183].

4.7.4 Stiffened Structures

1. Analysis of a Stiffened Plate with Eccentric Stiffeners

This problem shown in Figure 30 was analyzed by Liao [183]. Analyses were made using both 2 and 4 layers for the plate and 2 beam layers. Reduced integration was used for the transverse shear stiffness terms. The results of this problem are shown in Table 3. The LWTR finite element results compare well with the finite element results presented by Liao and with classical beam theory.

2. Cantilever Plate with Symmetric Stiffeners

The geometry, material properties, and loading condition of the cantilever stiffened plate are shown in Figure 31. The results obtained are compared with the finite element re-

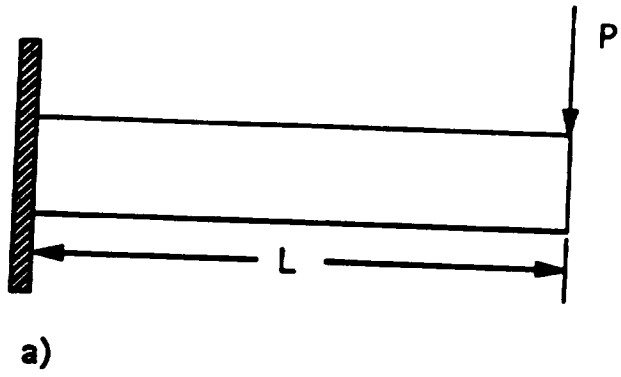

a)

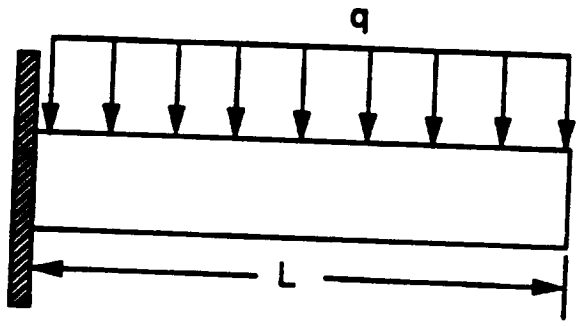

b)

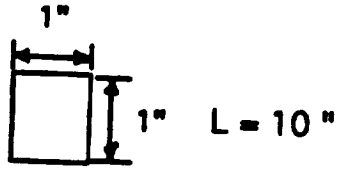

$E = 1.2 \times 10^{4}$ psi

$\nu = 0.2$

Figure 28. Cantilever beam subjected to two different loading conditions: a) applied end load; b) uniformly distributed load.

Table 2. Linear Results for a Clamped Beam Subjected to an Applied End Load and to a Uniformly Distributed Load ($E = 1.2 \times 10^4$, $\nu = 0.2$, $L = 10$ in.)

Loading Condition	Load	LWTR (FEA) (inches)	Classical Beam Theory (inches)
End Load	P = 1 lb.	-0.334694	-0.333333
Distibuted Load	q = 1 lb./in.	-0.125691	-0.125000

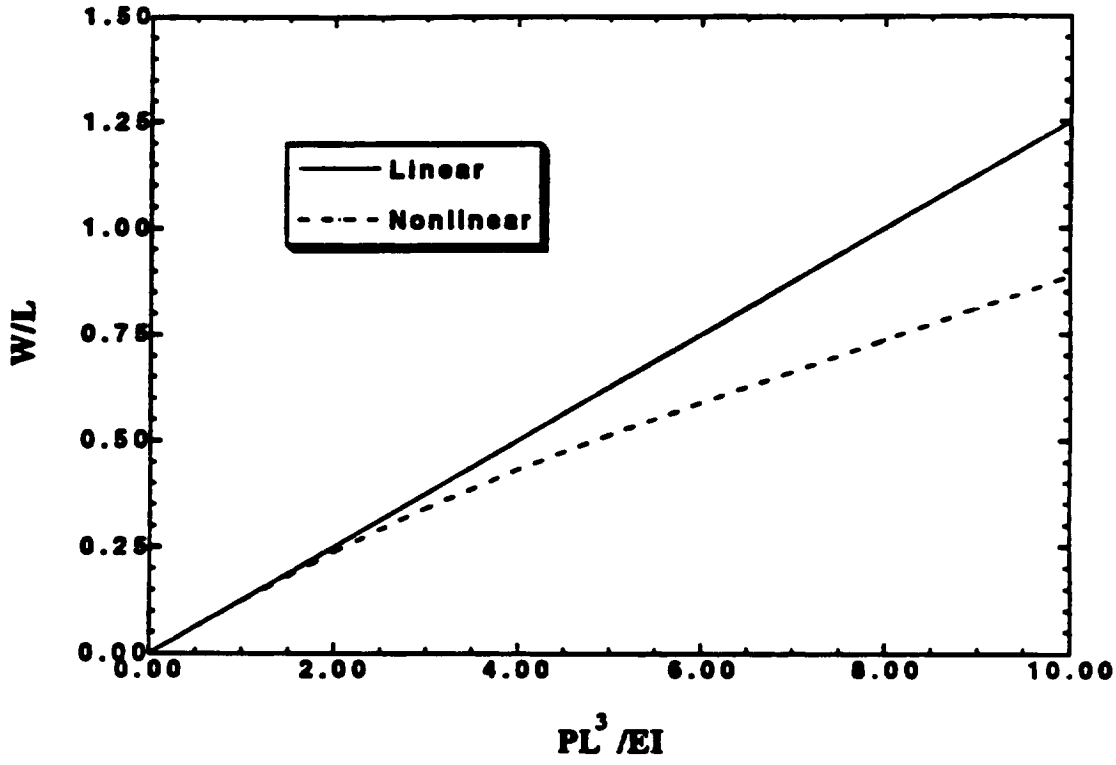

Figure 29. Large deflection of a cantilever beam under a uniform load (E = 1.2 x 10^4 psi, ν = 0.2, L = 10 in.).

sults obtained by Liao [183] and are provided in Table 4. A good comparison exists between the two finite element solutions.

3. A Square Plate Resting on Elastic Edge Beams and Supported at the Corners, Subjected to a Uniformly Distributed Load

Figure 32 shows the plate geometry and material properties. The same problem was solved by Timoshenko [61] who assumed that the elastic edge beams are of zero torsional rigidity. Liao [183] also solved this problem using a finite element technique. The results are obtained with a 2x2 mesh of 9-node shell elements and four 3-node elements are displayed in Table 5. Results compare favorably with those of Liao.

This concludes the finite element verification analyses. The next chapter deals with the buckling and stress analysis of stiffened composite shells, with emphasis on geodesically stiffened cylindrical composite shells.

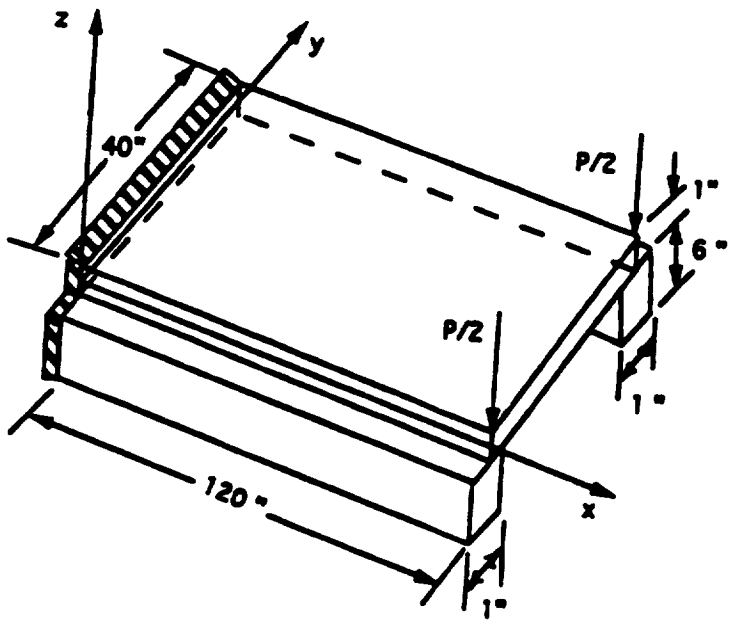

Figure 30. Cantilever stiffened plate subjected to an end load.

Table 3. Transverse Deflection of an Eccentrically Stiffened Plate.

Mesh	Liao (1987) (inches)	LWTR (FEA) (inches)	Classical Beam Theory (inches)
One 9 Node Shell Element Four 2 Node Beam Elements	-0.25447×10^{-3}	-0.25235×10^{-3} (2 layers) -0.25860×10^{-3} (4 layers)	-0.25195×10^{-3}
Two 9 Node Shell Elements Eight 2 Node Beam Elements	-0.25533×10^{-3}	-0.26104×10^{-3} (2 layers) -0.26393×10^{-3} (4 layers)	-0.25195×10^{-3}

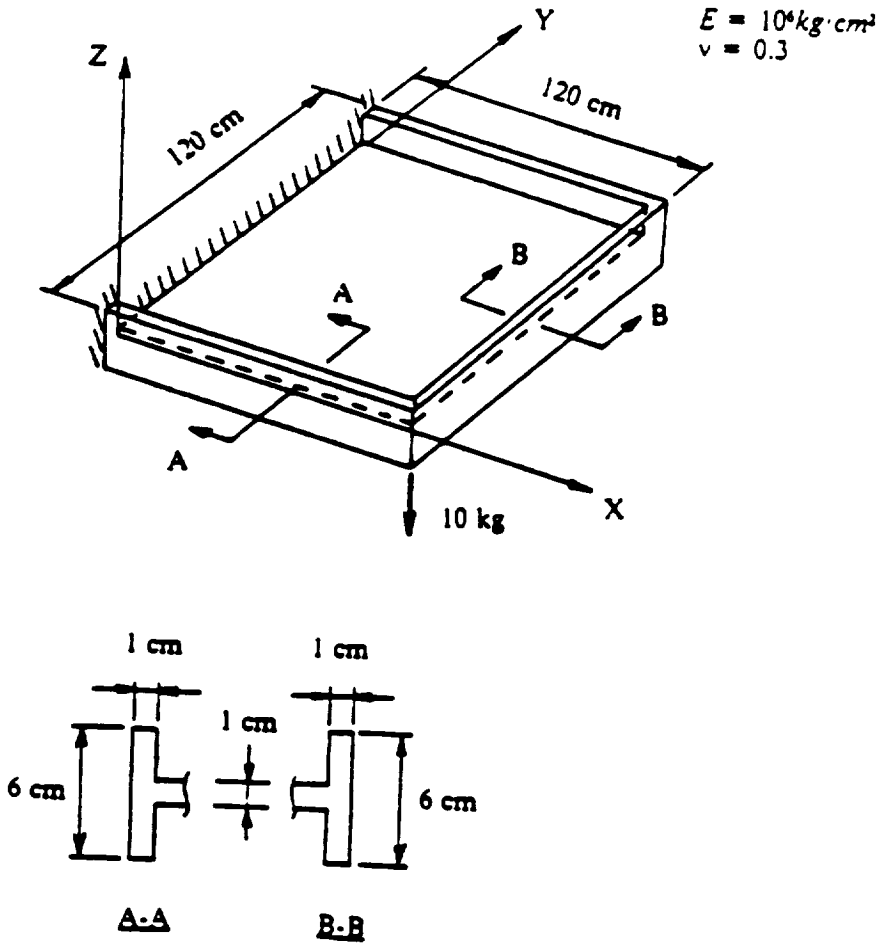

Figure 31. Cantilever stiffened plate with symmetric stiffeners.

Table 4. Transverse Deflection of a Cantilever Stiffened Plate with Symmetric Stiffeners.

Mesh	Liao (1987)* (cm)	LWTR (FEA)* (cm)
4x4 Shell 12 Beam	-0.18103	-0.18482 (2 layers)

* Transverse Deflection at the Loaded Point

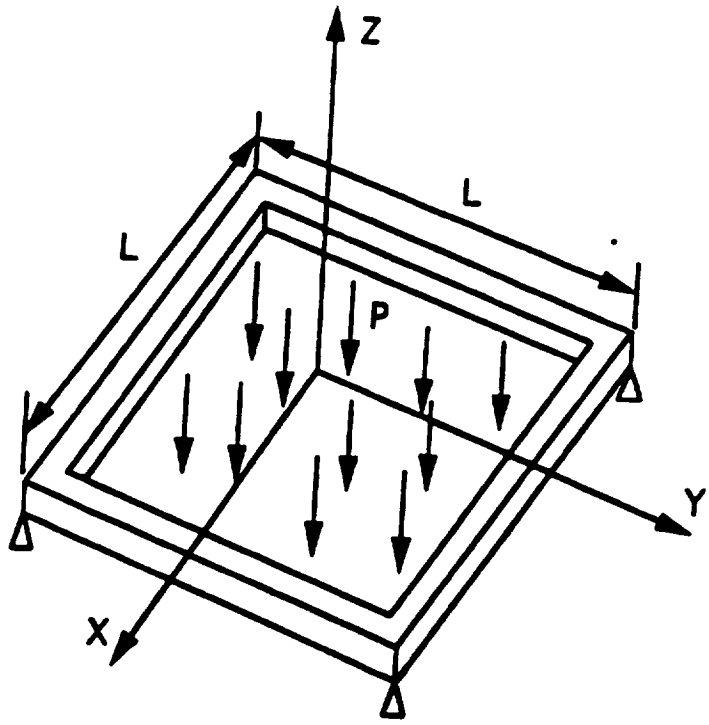

Plate: 19.53" x 19.53" x 0.2"
Edge beams : 0.5" width, 1" depth
$E = 10^7$ psi, $\nu = 0.25$
P = 1 psi

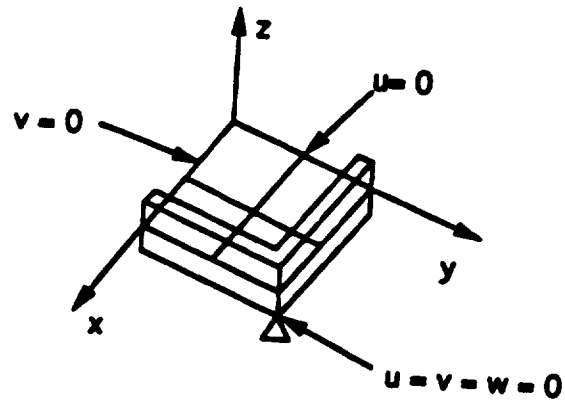

Figure 32. A square plate resting on elastic edge beams.

Table 5. Transverse Deflection of an Elastically Supported Plate Subjected to a Uniformly Distributed Load.

Mesh	Liao (1987) (inches)	LWTR (FEA) (inches)	Timoshenko (inches)
2x2 Shell 8 Beam	-0.095957	-0.097258 (2 layers) -0.102152 (4 layers)	-0.120290

Chapter 5

Results

5.1 Ritz Buckling Results

In order to validate the LWTR for discretely stiffened shells, some numerical results are needed. Before the LWTR is used to generate results for discretely stiffened shells, numerical results for certain known configurations are generated and compared with the published solutions. A comparison of buckling results for unstiffened circular cylindrical shells with simply supported boundary conditions are presented in Table 6. The results of the LWTR are compared with an analytical solution first for an isotropic aluminum circular cylinder subjected to axial compression. Also, in Table 6 a comparison of the nondimensional buckling load for the LWTR, first-order shear deformation theory (FSDT), third-order shear deformation theory (HSDT), and classical lamination theory (CLT) for various cross-ply circular cylinders is presented. Results for the FSDT, HSDT, and CLT are from the paper by Khdeir, Reddy, and Frederick [185]. Results for

the LWTR analysis compare well for isotropic and cross-ply unstiffened circular cylindrical shells as can be observed from Table 1.

Next, a study of a geodesically stiffened quasi-isotropic $[-45/45/90/0]_S$ plate subjected to axial compression was made. The geodesically stiffened plate was presented in the work by Phillips and Gürdal [123]. They used a Lagrange multiplier approach to discretely attach beam-like orthotropic (isotropic) stiffeners to the plate and classical lamination theory to model the plate skin. Also, they conducted a finite element analysis of the plate using 9-node combined membrane and quadrilateral elements for both the skin and stiffeners. The stiffened plate was comprised of symmetric stiffeners with stiffener heights of 0.5", 0.75", 1.0", and 1.25". A description of the plate geometry and the applied loads is shown in Figure 33. The boundary conditions were chosen so that

$$\begin{aligned} &u = w = 0 \text{ at } y = 0,\ L_y \\ &v = w = 0 \text{ at } x = 0,\ L_x \\ &(L_x = 80\text{in.}, \quad L_y = 28\text{in.}) \end{aligned} \tag{5.1}$$

The Ritz solutions which satisfy these boundary conditions are

Plate

$$\begin{aligned} u_i &= U_i^{mn} \cos(\alpha_m x) \sin(\beta_n y) \quad i = 1, 2, \ldots, (N+1) \\ v_i &= V_i^{mn} \sin(\alpha_m x) \cos(\beta_n y) \ ; \ \alpha_m = \frac{m\pi}{L_y}, \quad \beta_n = \frac{n\pi}{L_x} \\ w_i &= W_i^{mn} \sin(\alpha_m x) \sin(\beta_n y) \end{aligned} \tag{5.2}$$

where U_i^{mn}, V_i^{mn}, and W_i^{mn} amplitudes are to be determined for each mode (m, n).

Geodesic Stiffeners

$$u_s^i = U_s^{ik}\cos(\alpha_k x) \;\; ; \;\; \alpha_k = \frac{k\pi}{L_s^i}, \quad i = 1, 2, \ldots, T$$
$$w_s^i = W_s^{ik}\sin(\alpha_k x) \tag{5.3}$$

The procedure used to develop the buckling equations is exactly the same as that described for shells. Material properties for the plate and stiffeners are presented in Table 7. Using the same geometry and loading a comparison of the buckling results is presented in [123] and the LWTR for discretely stiffened plates is shown in Table 8. The LWTR compares well with the finite element method, and seems to produce better results than the Lagrange Multiplier Method (LMM) of Phillips and Gürdal, especially at lower stiffener heights. One reason for the difference between the buckling loads obtained from the finite element method and the LWTR discrete method could be that for smaller stiffener heights the finite element (plate) stiffeners have more of an effect on the skin than does the LWTR. This results in higher finite element buckling loads at lower stiffener heights.

Next, buckling analyses of quasi-isotropic $[-45/45/90/0]_S$ circular cylindrical shells with eccentric axial, ring, and geodesic stiffeners were conducted. The material properties used for these analyses are the same as those found in Table 7. A nominal shell radius of 85" and a shell length of 100" were selected. A shell thickness of 0.2" and a stiffener thickness of 0.2" were used. These same dimensions were use by Gürdal and Gendron [186] in their design optimization analysis of geodesically stiffened shells. Comparisons of the discrete LWTR approach with the smeared CLT method proposed by Jones [90,91] and the smeared LWTR method of Reddy [37] were made for axial and ring stiffeners.

Table 6. Unstiffened Buckling Results.

Buckling of a Simply Supported Unstiffened Aluminum Circular Cylinder
Subjected to Axial Compression

Buckling Load Roark [184] (lbs./inch)	Buckling Load LWTR (lbs./inch)	Error
6408.29	6106.10	-4.95%

$E = 10 \times 10^6$ psi

$\nu = 0.30$

thickness = 0.30 "

Buckling of Unstiffened Composite Cylinders
Comparison of Layerwise Laminate Theory of Reddy (LWTR) with Theories of Ref. [185]

$(L/R = 1,\ R/h=10),\qquad \bar{N} = \dfrac{\bar{N} L^2}{100\, h^3 E_2}$

Lamination	Theory	$\bar{N}$ Simply Supported
$0^0/90^0$	LWTR	0.1523
	HSDT	0.1687
	FSDT	0.1670
	CLT	0.1817
$0^0/90^0/0^0$	LWTR	0.2814
	HSDT	0.2794
	FSDT	0.2813
	CLT	0.4186
$0^0/90^0/$ ...	LWTR	0.2728
10 layers	HSDT	0.2896
	FSDT	0.2898
	CLT	0.3395

HSDT - Higher Order Shear Deformation Theory (third-order)

FSDT - First-order Shear Deformation Theory

CLT - Classical Lamination Theory

$E_1/E_2 = 40,\ G_{12} = G_{13} = 0.6E_2,\ G_{23} = 0.5E_2,\ \nu_{12} = 0.25$

Table 7. Material Properties Used in the Stiffened Buckling and Finite Element Analyses.

Properties	Values
E_1	18.5×10^6psi
E_2	1.64×10^6psi
E_3	1.64×10^6psi
G_{12}	0.87×10^6psi
G_{13}	0.87×10^6psi
G_{23}	0.54×10^6psi
ν_{12}	0.30
ν_{13}	0.30
ν_{23}	0.49
X_T	182.8×10^3psi
X_C	210.5×10^3psi
$Y_T = Z_T$	27.2×10^3psi
$Y_C = Z_C$	17.6×10^3psi
R	13.5×10^3psi
S = T	21.75×10^3psi
ply thickness	0.005 in./ply
E_{STIFF}	18.5×10^6psi
stiffener thickness	0.20 in.

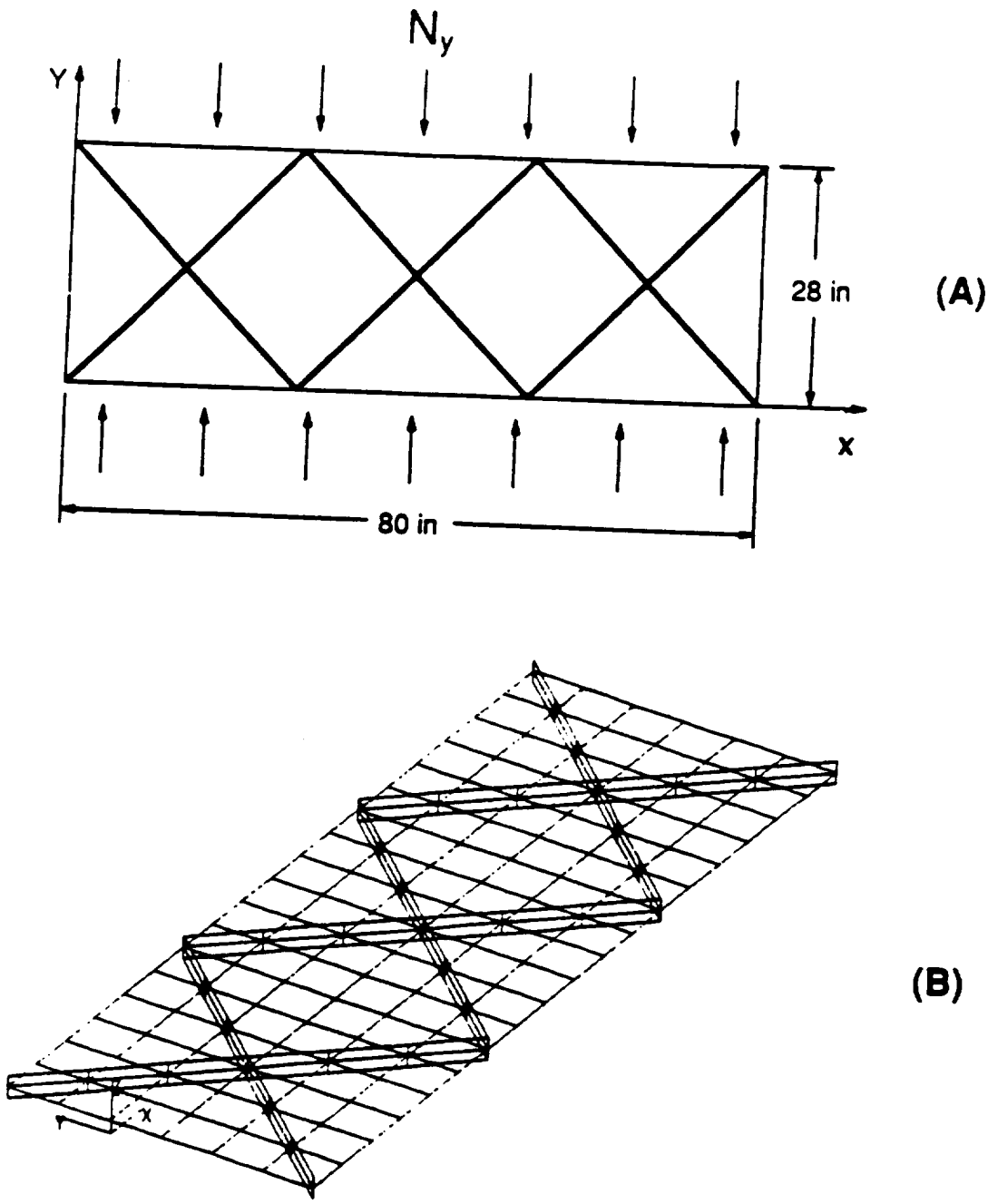

Figure 33. *Geodesically stiffened panel for verification of the LWTR analysis: a) panel geometry; b) finite element mesh.*

Table 8. Analysis of $[-45/45/90/0]_S$ 0.2″ Thick Plate with Geodesic Stiffeners Subjected to Axial Compression N_x (Lx = 80″, Ly = 28″, 12 Stiffeners).

Stiffener Height (inches)	Testbed FEA N_{FEM} (lbs./inch)	N_{LAM} (lbs./inch)	N_{LWTRD} (lbs./inch)	$\frac{N_{LAM}}{N_{FEM}}$	$\frac{N_{LWTRD}}{N_{FEM}}$
0.5	573	342	512	0.596	0.894
0.75	705	613	656	0.870	0.930
1.0	748	708	713	0.946	0.953
1.25	783	743	784	0.949	1.001

N_{FEM} — Finite Element Buckling Load

N_{LAM} — CLT Lagrange Multiplier Buckling Load

N_{LWTRD} — LWTR Discrete Buckling Load

Results for quasi-isotropic $[-45/45/90/0]_S$ shells with external (eccentric) axial stiffeners subjected to axial compression are shown in Tables 9 and 10 and in Figure 34. The results in Tables 9 and 10 are for composite shells having 4, 8, 16, and 24 axial stiffeners with various stiffener heights (1.0", 2.0", 3.0"). The plot of Figure 34 is a comparison of the buckling load for a shell having 24 axial stiffeners as a function of stiffener height for the various theories used in this study. The results indicate that the discrete LWTR yields more conservative (lower) buckling results than the smeared approaches. Moreover, as the stiffener height increases the difference between the discrete and the smeared approaches increase. In addition, as the number of stiffeners increases the difference between the discrete and smeared approaches increases. This could be due to some localized stiffener buckling which occurs in the discrete stiffener analyses, but cannot be accounted for when using a smeared approach. At this time this localized buckling cannot be predicted directly by the discrete method.

Results for quasi-isotropic $[-45/45/90/0]_S$ shells with internal (eccentric) ring stiffeners subjected to external pressure are presented in Tables 11 and 12 and in Figure 35. The results in Tables 6 and 7 are for composite shells having 5, 10, and 25 ring stiffeners subjected to external pressure for various stiffener heights (0.5", 1.0", 1.5"). The plot in Figure 35 is for buckling pressure versus stiffener height for a cylindrical composite shell having 25 ring stiffeners. As can be seen by the results in Tables 11 and 12 and in Figure 35 the discrete LWTR yields more conservative buckling results than the smeared approach. The difference becomes more pronounced as the number of stiffeners increases and as the stiffener height increases. As mentioned previously this is probably due in part to some localized stiffener buckling that is accounted for only in the discrete analysis.

Table 9. Analysis of $[-45/45/90/0]_s$ 0.2" Thick Circular Cylindrical Shell with Axial Stiffeners Subjected to Axial Compression (R = 85", L = 100") - Jones Smeared/LWTR Discrete.

No. of Stiffeners / Stiffener Height (inches)	Smeared/ Jones Approach (lbs./inch)	LWTR Discrete (lbs./inch)	Error	Lowest Analysis
Unstiffened	1799 M=15, N=1	1793 M=15, N=1	-0.33%	LWTRD
4 / (1.0")	2192 M=1, N=10	2181 M=1, N=10	-0.50%	LWTRD
8 / (1.0")	2255 M=1, N=10	2221 M=1, N=10	-1.53%	LWTRD
16 / (1.0")	2381 M=1, N=10	2334 M=1, N=10	-2.01%	LWTRD
24 / (1.0")	2506 M=1, N=10	2446 M=1, N=10	-2.45%	LWTRD
4 / (2.0")	2423 M=1, N=10	2423 M=1, N=9	0.0%	LWTRD
8 / (2.0")	2716 M=1, N=10	2543 M=1, N=10	-6.37%	LWTRD
16 / (2.0")	3296 M=1, N=10	3010 M=1, N=10	-9.50%	LWTRD
24 / (2.0")	3867 M=1, N=10	3411 M=1, N=11	-13.36%	LWTRD
4 / (3.0")	2940 M=1, N=10	2769 M=1, N=11	-6.18%	LWTRD
8 / (3.0")	3743 M=1, N=10	3178 M=1, N=11	-17.78%	LWTRD
16 / (3.0")	5328 M=1, N=10	4238 M=1, N=11	-25.72%	LWTRD
24 / (3.0")	6882 M=1, N=10	5219 M=1, N=11	-31.86%	LWTRD

M = number of axial halfwaves
N = number of circumferential halfwaves
LWTRD - Layer-wise Laminate Theory of Reddy with Discrete Stiffeners

Results

Table 10. Analysis of $[-45/45/90/0]_S$ 0.2" Thick Circular Cylindrical Shell with Axial Stiffeners Subjected to Axial Compression (R = 85", L = 100") - Reddy Smeared/LWTR Discrete.

No. of Stiffeners / Stiffener Height (inches)	Smeared/ Reddy Approach (lbs./inch)	LWTR Discrete (lbs./inch)	Error	Lowest Analysis
Unstiffened	1793 M=15, N=1	1793 M=15, N=1	0.0%	Same
4 / (1.0")	2177 M=1, N=10	2181 M=1, N=10	+0.18%	Reddy
8 / (1.0")	2247 M=1, N=10	2221 M=1, N=10	-1.17%	LWTRD
16 / (1.0")	2388 M=1, N=10	2334 M=1, N=10	-2.31%	LWTRD
24 / (1.0")	2528 M=1, N=10	2446 M=1, N=10	-3.24%	LWTRD
4 / (2.0")	2422 M=1, N=10	2423 M=1, N=9	+0.04%	Reddy
8 / (2.0")	2734 M=1, N=10	2543 M=1, N=10	-7.51%	LWTRD
16 / (2.0")	3354 M=1, N=10	3010 M=1, N=10	-11.43%	LWTRD
24 / (2.0")	3964 M=1, N=10	3411 M=1, N=11	-16.21%	LWTRD
4 / (3.0")	2956 M=1, N=10	2769 M=1, N=11	-6.75%	LWTRD
8 / (3.0")	3797 M=1, N=10	3178 M=1, N=11	-19.48%	LWTRD
16 / (3.0")	5456 M=1, N=10	4238 M=1, N=11	-28.74%	LWTRD
24 / (3.0")	7081 M=1, N=10	5219 M=1, N=11	-35.68%	LWTRD

M = number of axial halfwaves
N = number of circumferential halfwaves
LWTRD - Layer-wise Laminate Theory of Reddy with Discrete Stiffeners

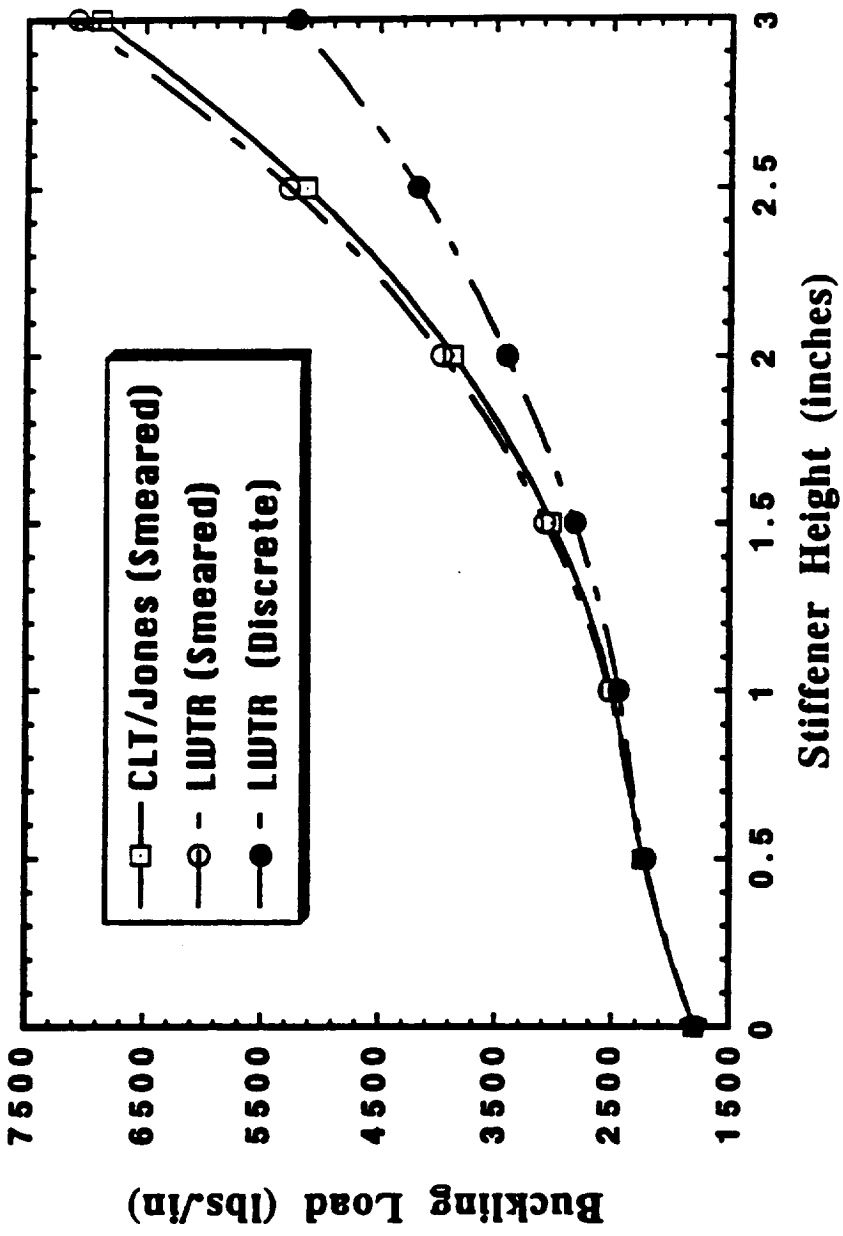

Figure 34. Axial buckling for a 24 axial stiffener shell model ([−45/45/90/0]$_s$ layup; R = 85", L = 100"; 1.0" x 0.2" stiffeners).

Table 11. Analysis of $[-45/45/90/0]_s$ 0.2" Thick Circular Cylindrical Shell with Ring Stiffeners Subjected to Lateral Pressure (R = 85", L = 100") - Jones Smeared/LWTR Discrete.

No. of Stiffeners / Stiffener Height (inches)	Smeared/ Jones Approach Buckling Press. (psi)	(LWTR) Discrete Buckling Press. (psi)	Error	Lowest Analysis
Unstiffened	1.63 M=1, N=11	1.61 M=1, N=11	-1.1%	LWTRD
5/(0.5")	5.57 M=1, N=9	5.00 M=1, N=9	-11.4%	LWTRD
10/(0.5")	8.62 M=1, N=8	7.49 M=1, N=9	-15.2%	LWTRD
25/(0.5")	15.53 M=1, N=8	12.68 M=1, N=8	-22.5%	LWTRD
5/(1.0")	18.14 M=1, N=7	14.02 M=1, N=8	-29.4%	LWTRD
10/(1.0")	28.91 M=1, N=7	21.42 M=1, N=6	-35.0%	LWTRD
25/(1.0")	51.38 M=1, N=6	36.29 M=1, N=5	-41.6%	LWTRD
5/(1.5")	39.36 M=1, N=6	28.46 M=1, N=7	-38.3%	LWTRD
10/(1.5")	62.06 M=1, N=6	28.46 M=1, N=7	-44.9%	LWTRD
25/(1.5")	108.19 M=1, N=6	70.00 M=1, N=6	-54.6%	LWTRD

M = number of axial halfwaves

N = number of circumferential halfwaves

LWTRD - Layer-wise Laminate Theory of Reddy with Discrete Stiffeners

Table 12. Analysis of $[-45/45/90/0]_S$ 0.2" Thick Circular Cylindrical Shell with Ring Stiffeners Subjected to Lateral Pressure (R = 85", L = 100") - Reddy Smeared/LWTR Discrete.

No. of Stiffeners / Stiffener Height (inches)	Smeared/ Reddy Approach Buckling Press. (psi)	(LWTR) Discrete Buckling Press. (psi)	Error	Lowest Analysis
Unstiffened	1.61 M=1, N=11	1.61 M=1, N=11	0.0%	LWTRD
5/(0.5")	6.50 M=1, N=9	5.00 M=1, N=9	-29.9%	LWTRD
10/(0.5")	10.03 M=1, N=8	7.49 M=1, N=9	-34.0%	LWTRD
25/(0.5")	18.10 M=1, N=7	12.68 M=1, N=8	-42.7%	LWTRD
5/(1.0")	19.85 M=1, N=7	14.02 M=1, N=8	-41.6%	LWTRD
10/(1.0")	32.00 M=1, N=7	21.42 M=1, N=6	-49.4%	LWTRD
25/(1.0")	55.71 M=1, N=6	36.29 M=1, N=5	-53.5%	LWTRD
5/(1.5")	41.83 M=1, N=6	28.46 M=1, N=7	-47.0%	LWTRD
10/(1.5")	66.35 M=1, N=6	28.46 M=1, N=7	-54.9%	LWTRD
25/(1.5")	113.27 M=1, N=6	70.00 M=1, N=6	-61.8%	LWTRD

M = number of axial halfwaves

N = number of circumferential halfwaves

LWTRD - Layer-wise Laminate Theory of Reddy with Discrete Stiffeners

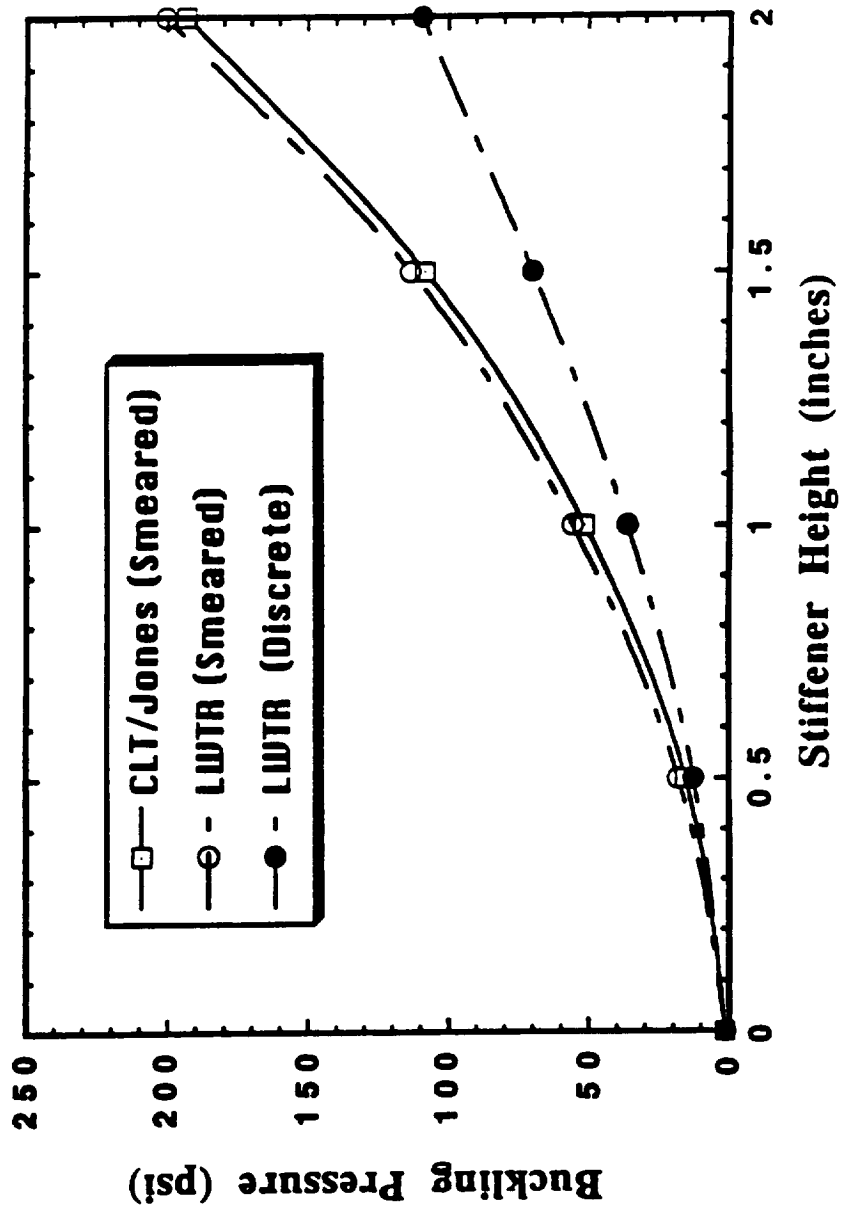

Figure 35. Buckling pressure for a 25 ring stiffener shell model ([−45/45/90/0]$_3$ layup; R = 85", L = 100"; 1.0" x 0.2" stiffeners).

Analyses of quasi-isotropic $[-45/45/90/0]_S$ shells with eccentric, internal stiffeners was conducted next to compare the discrete LWTR with a finite element solution. The finite element program CSM Testbed [187,188] was used to analyze the geodesic cylindrical shells. Nine-node assumed-natural-coordinate strain (ANS) C^o (transverse-shear deformable) shell elements were used to model both the shell and the stiffeners. In these buckling analyses and in the finite element analyses to follow, geodesically stiffened shells having 1x12, 1x16, 2x12, and 2x16 unit cells as described in Figure 36 are studied. The finite element model will be made of a unit cell of one of the aforementioned geodesic cylinders. A typical finite element model of a unit cell is shown in Figure 37. The cylinders were subjected to axial compression and stiffener heights of 0.5", 1.0", 1.5.", and 2.0" were used for these analyses. The results of this study are presented in Tables 13-16. The 2x12 geodesic shell model yields the closest agreement between the two analytical methods and the results for this model are plotted in Figure 38. The LWTR discrete results and the Testbed finite element results show good agreement. The LWTR discrete method yields more conservative buckling loads than the finite element method except for the 2x16 shell and the 0.5" and 2.0" stiffener heights in the 1x12 shell. The maximum difference in the buckling loads is for the 1x16 shell where the LWTR discrete results are 9.3% more conservative for the 1.0" and 1.5" stiffener heights than the finite element method. The difference between the LWTR discrete method and the finite element method can be attributed to the fact that the LWTR method neglects the out-of-plane and the torsional stiffnesses of the stiffeners. Also, the shell is comprised of a quasi-isotropic laminate and although small, the orthotropic stiffnesses, $\overline{C}_{16}$, $\overline{C}_{26}$, $\overline{C}_{36}$, $\overline{C}_{45}$, are present. The LWTR discrete approach assumes these values are zero and this may result in a slight change in the buckling load. Nevertheless, a good correlation of the discrete and finite element buckling results does exist.

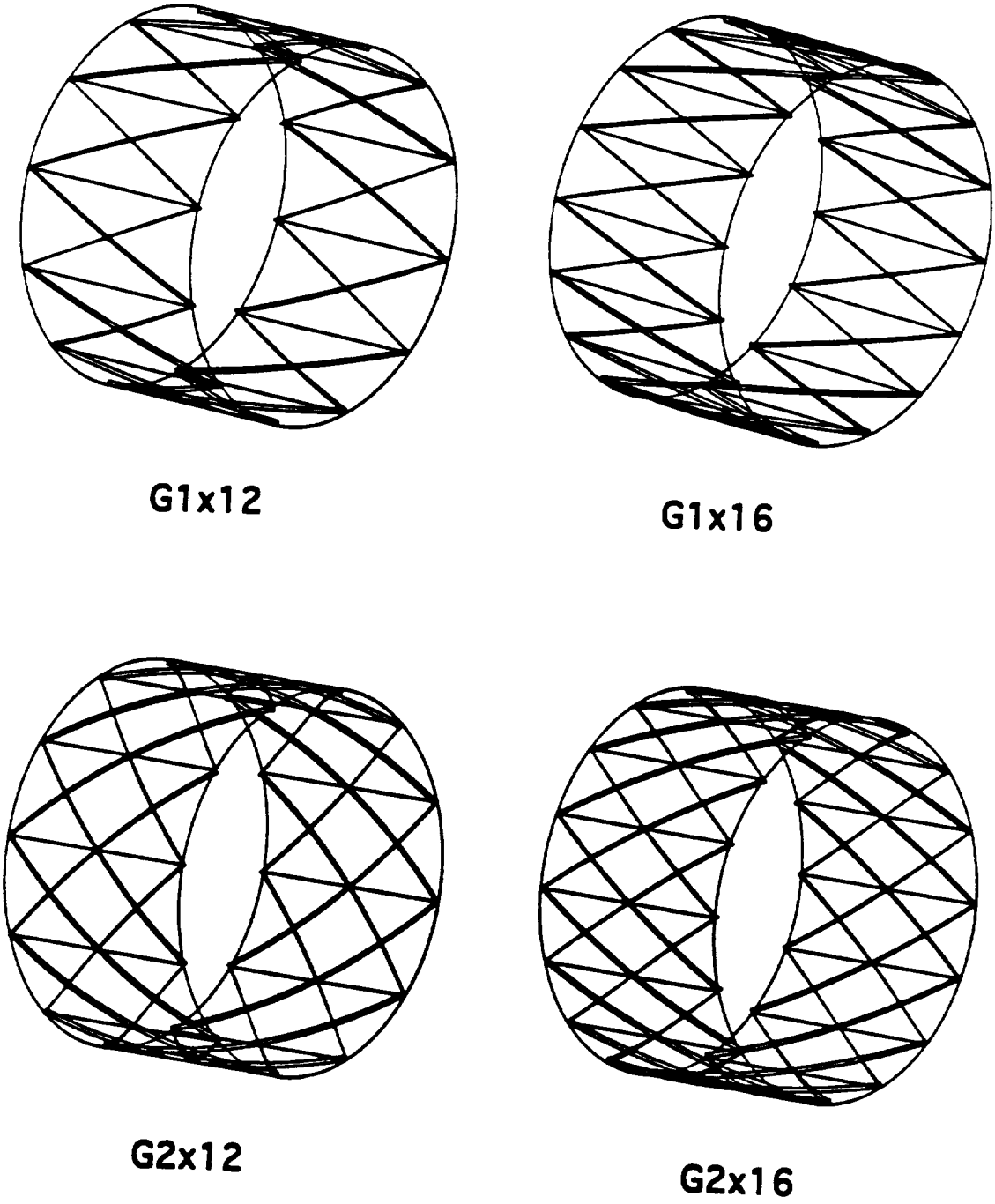

Figure 36. Geodesically stiffened shell configurations.

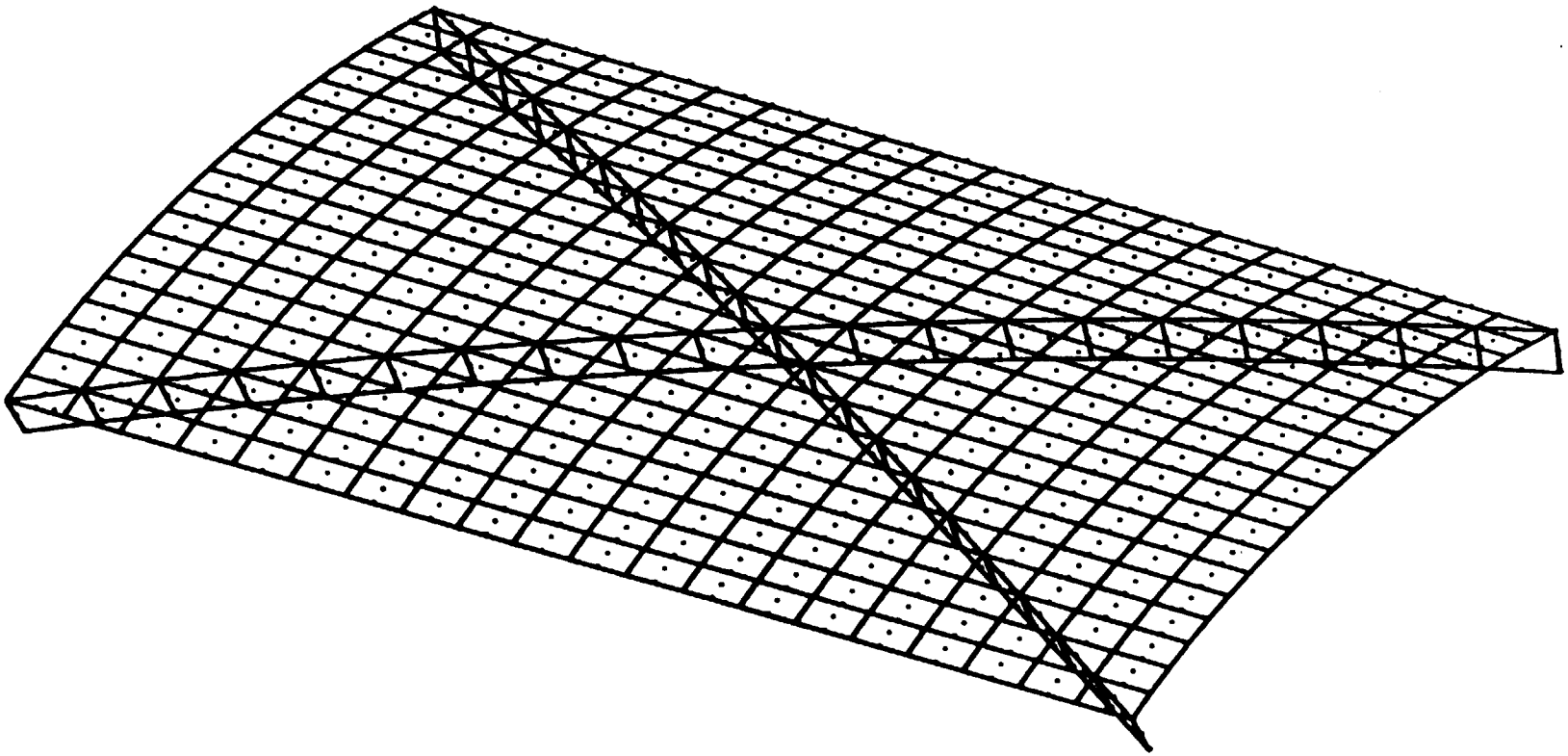

Figure 37. Finite element mesh used for the geodesic buckling analysis (unit cell with 20x20 mesh).

Table 13. Analysis of $[-45/45/90/0]_S$ 0.2" Thick Circular Cylindrical Shell with Geodesic Stiffeners Subjected to Axial Compression (R = 85", L = 100", 1x12 Geodesic Shell Model).

Stiffener Height (inches)	Testbed FEA (lbs./inch)	LWTR Discrete (lbs./inch)	Error	Lowest Analysis
Unstiffened	1759	1793 M=15, N=1	+1.9%	FEA
0.5	2105	2119	+0.7%	FEA
1.0	2172	2139	-1.5%	LWTRD
1.5	2232	2211	-0.9%	LWTRD
2.0	2284	2382	+4.3%	FEA

M = 1, N= 10 for all LWTRD Results

1x12 Geodesic Model
α = 23.99 Degrees

M = number of axial halfwaves

N = number of circumferential halfwaves

LWTRD - Layerwise Laminate Theory of Reddy with Discrete Stiffeners

Table 14. Analysis of $[-45/45/90/0]_S$ 0.2" Thick Circular Cylindrical Shell with Geodesic Stiffeners Subjected to Axial Compression (R = 85", L = 100", 1x16 Geodesic Shell Model).

Stiffener Height (inches)	Testbed FEA (lbs./inch)	LWTR Discrete (lbs./inch)	Error	Lowest Analysis
Unstiffened	1759	1793 M=15, N=1	+1.9%	FEA
0.5	2225	2121	-4.3%	LWTRD
1.0	2368	2148	-9.3%	LWTRD
1.5	2488	2257	-9.3%	LWTRD
2.0	2595	2494	-3.9%	LWTRD

M = 1, N = 10 for all LWTRD Results

1x16 Geodesic Model

α = 18.46 Degrees

M = number of axial halfwaves

N = number of circumferential halfwaves

LWTRD - Layerwise Laminate Theory of Reddy with Discrete Stiffeners

Table 15. Analysis of $[-45/45/90/0]_S$ 0.2" Thick Circular Cylindrical Shell with Geodesic Stiffeners Subjected to Axial Compression (R = 85", L = 100", 2x12 Geodesic Shell Model).

Stiffener Height (inches)	Testbed FEA (lbs./inch)	LWTR Discrete (lbs./inch)	Error	Lowest Analysis
Unstiffened	1759	1793 M=15, N=1	+1.9%	FEA
0.5	2156	2129	-1.2%	LWTRD
1.0	2193	2146	-1.8%	LWTRD
1.5	2250	2189	-2.7%	LWTRD
2.0	2289	2286	-0.1%	LWTRD

M = 1, N = 10 for all LWTRD Results
2x12 Geodesic Model
α = 41.67 Degrees

M = number of axial halfwaves
N = number of circumferential halfwaves
LWTRD - Layerwise Laminate Theory of Reddy with Discrete Stiffeners

Table 16. Analysis of $[-45/45/90/0]_S$ 0.2" Thick Circular Cylindrical Shell with Geodesic Stiffeners Subjected to Axial Compression (R = 85", L = 100", 2x16 Geodesic Shell Model).

Stiffener Height (inches)	Testbed FEA (lbs./inch)	LWTR Discrete (lbs./inch)	Error	Lowest Analysis
Unstiffened	1759	1793 M=15, N=1	+1.9%	FEA
0.5	2049	2130	+4.0%	FEA
1.0	2078	2146	+3.3%	FEA
1.5	2122	2189	+3.2%	FEA
2.0	2192	2286	+4.3%	FEA

M = 1, N = 10 for all LWTRD Results
2x16 Geodesic Model
α = 33.73 Degrees

M = number of axial halfwaves
N = number of circumferential halfwaves

LWTRD - Layerwise Laminate Theory of Reddy with Discrete Stiffeners

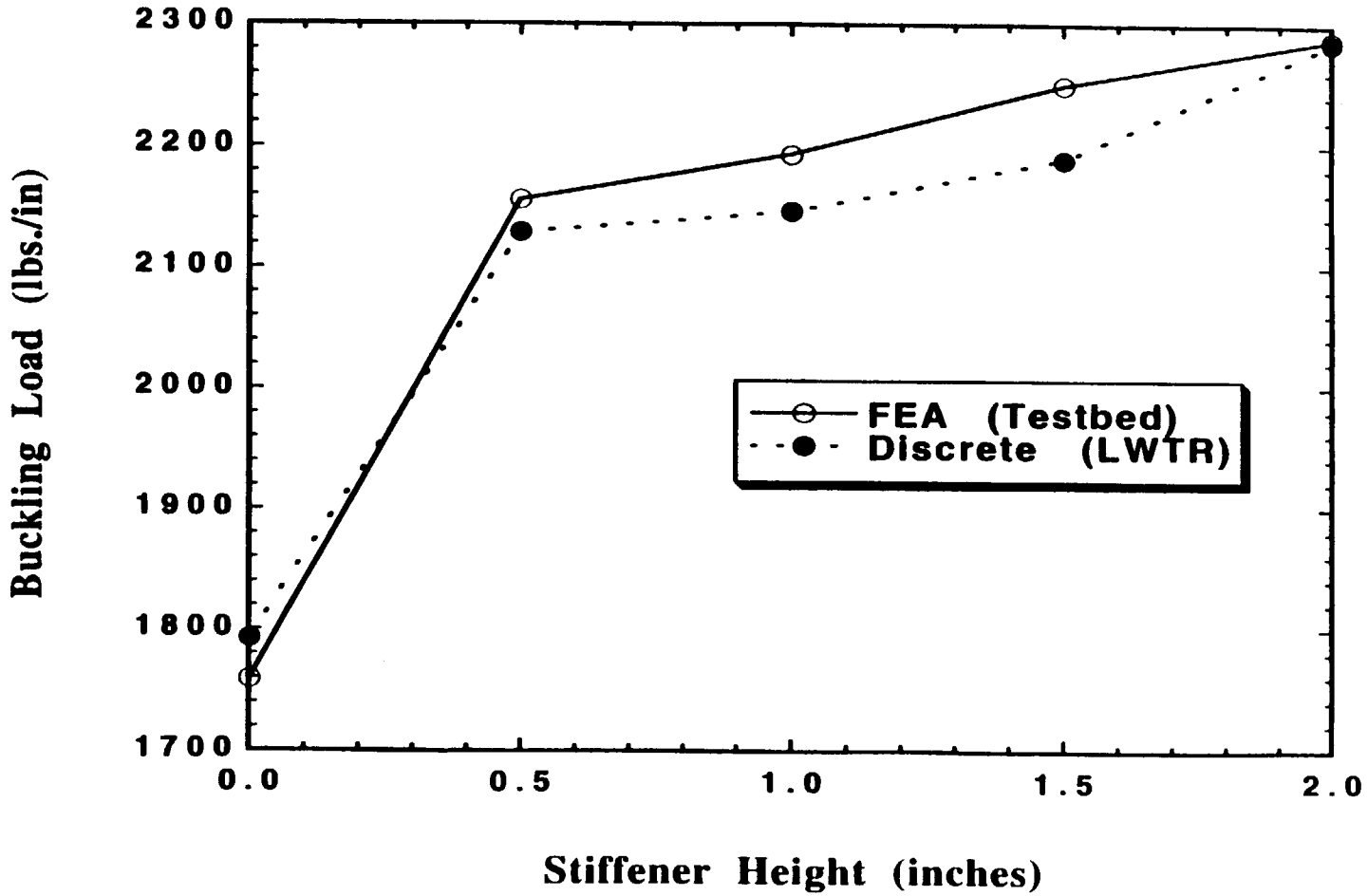

Figure 38. Axial buckling results for a 2x12 geodesic shell model ($[-45/45/90/0]_S$ layup; R = 85", L = 100"; 1.0" x 0.2" stiffeners).

Analysis of cross-ply [0/90/90/0] circular cylindrical shells with eccentric axial, ring, and geodesic stiffeners was also performed. The same material properties, shell thickness, stiffener thickness, and geometries as those of the quasi-isotropic case were used.

Results for the cross-ply shells with external, eccentric axial stiffeners subjected to axial compression are shown in Tables 17 and 18 and in Figure 39. Once again the discrete approach yields more conservative buckling results than the smeared approach. As the stiffener height increases the difference between the LWTR discrete and the smeared approaches becomes larger as expected. The results plotted in Figure 40 are for 24 axial stiffeners at various stiffener heights for the smeared and discrete approaches.

The results for internally ring stiffened cross-ply cylinders subjected to external pressure are provided in Tables 19 and 20 and in Figure 40. The buckling pressure predicted by the LWTR discrete approach is much lower than that predicted by the smeared approaches. The difference is more pronounced as the stiffener height increases. The plot shown in Figure 40 is for a cylinder having 25 internal ring stiffeners.

Analyses of cross-ply shells with internal geodesic stiffeners was performed to compare the LWTR discrete and the CSM Testbed finite element results. The same models and geometries used in the quasi-isotropic analysis were also used for the geodesic cross-ply analyses (see Figures 36 and 37). The results are for axial compression and are presented in Tables 21-24. The 1x12 geodesic shell model yields the closest agreement between the two solutions and a plot of the buckling results for this shell is shown in Figure 41. The maximum difference in the buckling loads is for the 1x16 shell where the LWTR discrete results are 13.4% more conservative for the 1.5" stiffener height than the finite element results. As seen from Tables 21 and 23 the results begin to diverge at the 2.0" stiffener heights. The difference between the LWTR discrete method and the finite element

Table 17. Analysis of [0/90/90/0] 0.2" Thick Circular Cylindrical Shell with Axial Stiffeners Subjected to Axial Compression (R = 85", L = 100") - Jones Smeared/LWTR Discrete.

No. of Stiffeners / Stiffener Height (inches)	Smeared/ Jones Approach (lbs./inch)	LWTR Discrete (lbs./inch)	Error	Lowest Analysis
Unstiffened	1033 M=4, N=17	1030 M=4,N=17	-0.3%	LWTRD
4 / (1.0")	1376 M=1, N=10	1381 M=1, N=10	+0.4%	Jones
8 / (1.0")	1424 M=1, N=10	1399 M=1, N=10	-1.8%	LWTRD
16 / (1.0")	1515 M=1, N=10	1475 M=1, N=10	-2.7%	LWTRD
24 / (1.0")	1605 M=1, N=10	1550 M=1, N=10	-3.5%	LWTRD
4 / (2.0")	1530 M=1, N=10	1511 M=1, N=11	-1.3%	LWTRD
8 / (2.0")	1726 M=1, N=10	1654 M=1, N=10	-4.4%	LWTRD
16 / (2.0")	2109 M=1, N=10	1972 M=1, N=10	-6.9%	LWTRD
24 / (2.0")	2481 M=1, N=10	2266 M=1, N=11	-9.5%	LWTRD
4 / (3.0")	2046 M=1, N=10	1755 M=1, N=10	-15.3%	LWTRD
8 / (3.0")	2749 M=1, N=10	2187 M=1, N=10	-25.7%	LWTRD
16 / (3.0")	4120 M=1, N=10	2978 M=1, N=11	-38.3%	LWTRD
24 / (3.0")	5450 M=1, N=10	3729 M=1, N=11	-46.2%	LWTRD

M = number of axial halfwaves
N = number of circumferential halfwaves
LWTRD - Layer-wise Laminate Theory of Reddy with Discrete Stiffeners

Table 18. Analysis of [0/90/90/0] 0.2" Thick Circular Cylindrical Shell with Axial Stiffeners Subjected to Axial Compression (R = 85", L = 100") - Reddy Smeared/LWTR Discrete.

No. of Stiffeners / Stiffener Height (inches)	Smeared/ Reddy Approach (lbs./inch)	LWTR Discrete (lbs./inch)	Error	Lowest Analysis
Unstiffened	1030 M=4, N=17	1030 M=4,N=17	0.0%	LWTRD
4 / (1.0")	1374 M=1, N=10	1381 M=1, N=10	+0.5%	Reddy
8 / (1.0")	1427 M=1, N=10	1399 M=1, N=10	-2.0%	LWTRD
16 / (1.0")	1530 M=1, N=10	1475 M=1, N=10	-3.7%	LWTRD
24 / (1.0")	1631 M=1, N=10	1550 M=1, N=10	-5.2%	LWTRD
4 / (2.0")	1585 M=1, N=10	1511 M=1, N=11	-4.9%	LWTRD
8 / (2.0")	1846 M=1, N=10	1654 M=1, N=10	-11.6%	LWTRD
16 / (2.0")	2356 M=1, N=10	1972 M=1, N=10	-19.5%	LWTRD
24 / (2.0")	2853 M=1, N=10	2266 M=1, N=11	-25.9%	LWTRD
4 / (3.0")	2071 M=1, N=10	1755 M=1, N=10	-16.7%	LWTRD
8 / (3.0")	2807 M=1, N=10	2187 M=1, N=10	-28.3%	LWTRD
16 / (3.0")	4240 M=1, N=10	2978 M=1, N=11	-42.4%	LWTRD
24 / (3.0")	5627 M=1, N=10	3729 M=1, N=11	-50.9%	LWTRD

M = number of axial halfwaves
N = number of circumferential halfwaves
LWTRD - Layer-wise Laminate Theory of Reddy with Discrete Stiffeners

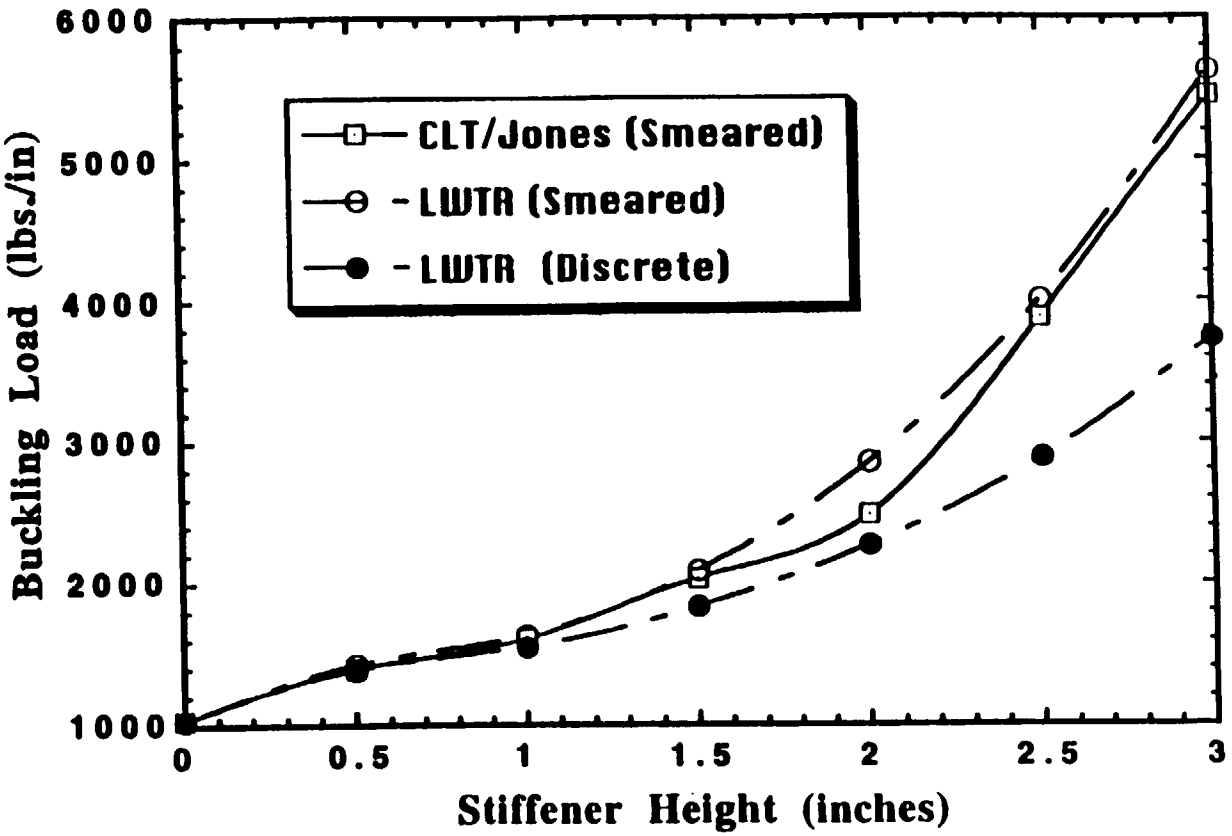

Figure 39. Axial buckling for a 24 axial stiffener shell model ([0/90/90/0] layup; R = 85", L = 100"; 1.0" x 0.2" stiffeners).

Table 19. Analysis of [0/90/90/0] 0.2" Thick Circular Cylindrical Shell with Ring Stiffeners Subjected to Lateral Pressure (R = 85", L = 100") - Jones Smeared/LWTR Discrete.

No. of Stiffeners / Stiffener Height (inches)	Smeared/ Jones Approach Buckling Press. (psi)	(LWTR) Discrete Buckling Press. (psi)	Error	Lowest Analysis
Unstiffened	0.89 M=1, N=12	0.88 M=1, N=12	-0.9%	LWTRD
5/(0.5")	4.67 M=1, N=9	4.08 M=1, N=9	-14.4%	LWTRD
10/(0.5")	7.21 M=1, N=8	6.21 M=1, N=9	-16.0%	LWTRD
25/(0.5")	12.87 M=1, N=7	10.63 M=1, N=7	-21.0%	LWTRD
5/(1.0")	15.36 M=1, N=7	11.73 M=1, N=7	-30.9%	LWTRD
10/(1.0")	23.83 M=1, N=6	18.25 M=1, N=6	-30.6%	LWTRD
25/(1.0")	42.49 M=1, N=5	29.69 M=1, N=6	-43.1%	LWTRD
5/(1.5")	32.73 M=1, N=6	23.414 M=1, N=6	-39.8%	LWTRD
10/(1.5")	49.92 M=1, N=5	36.19 M=1, N=6	-37.9%	LWTRD
25/(1.5")	90.72 M=1, N=4	55.75 M=1, N=5	-62.7%	LWTRD

M = number of axial halfwaves

N = number of circumferential halfwaves

LWTRD - Layer-wise Laminate Theory of Reddy with Discrete Stiffeners

Table 20. Analysis of [0/90/90/0] 0.2" Thick Circular Cylindrical Shell with Ring Stiffeners Subjected to Lateral Pressure (R = 85", L = 100") - Reddy Smeared/LWTR Discrete.

No. of Stiffeners / Stiffener Height (inches)	Smeared/ Reddy Approach Buckling Press. (psi)	(LWTR) Discrete Buckling Press. (psi)	Error	Lowest Analysis
Unstiffened	0.88 M=1, N=12	0.88 M=1, N=12	0.0%	LWTRD
5/(0.5")	5.52 M=1, N=8	4.08 M=1, N=9	-35.1%	LWTRD
10/(0.5")	8.57 M=1, N=8	6.21 M=1, N=8	-38.0%	LWTRD
25/(0.5")	15.15 M=1, N=7	10.63 M=1, N=7	-42.5%	LWTRD
5/(1.0")	17.03 M=1, N=7	11.73 M=1, N=8	-45.1%	LWTRD
10/(1.0")	26.02 M=1, N=6	18.25 M=1, N=6	-42.6%	LWTRD
25/(1.0")	45.35 M=1 N=5	29.69 M=1, N=6	-52.7%	LWTRD
5/(1.5")	35.17 M=1, N=6	23.41 M=1, N=6	-50.2%	LWTRD
10/(1.5")	52.80 M=1, N=5	36.19 M=1, N=6	-45.9%	LWTRD
25/(1.5")	93.76 M=1, N=4	55.75 M=1, N=5	-68.2%	LWTRD

M = number of axial halfwaves

N = number of circumferential halfwaves

LWTRD - Layer-wise Laminate Theory of Reddy with Discrete Stiffeners

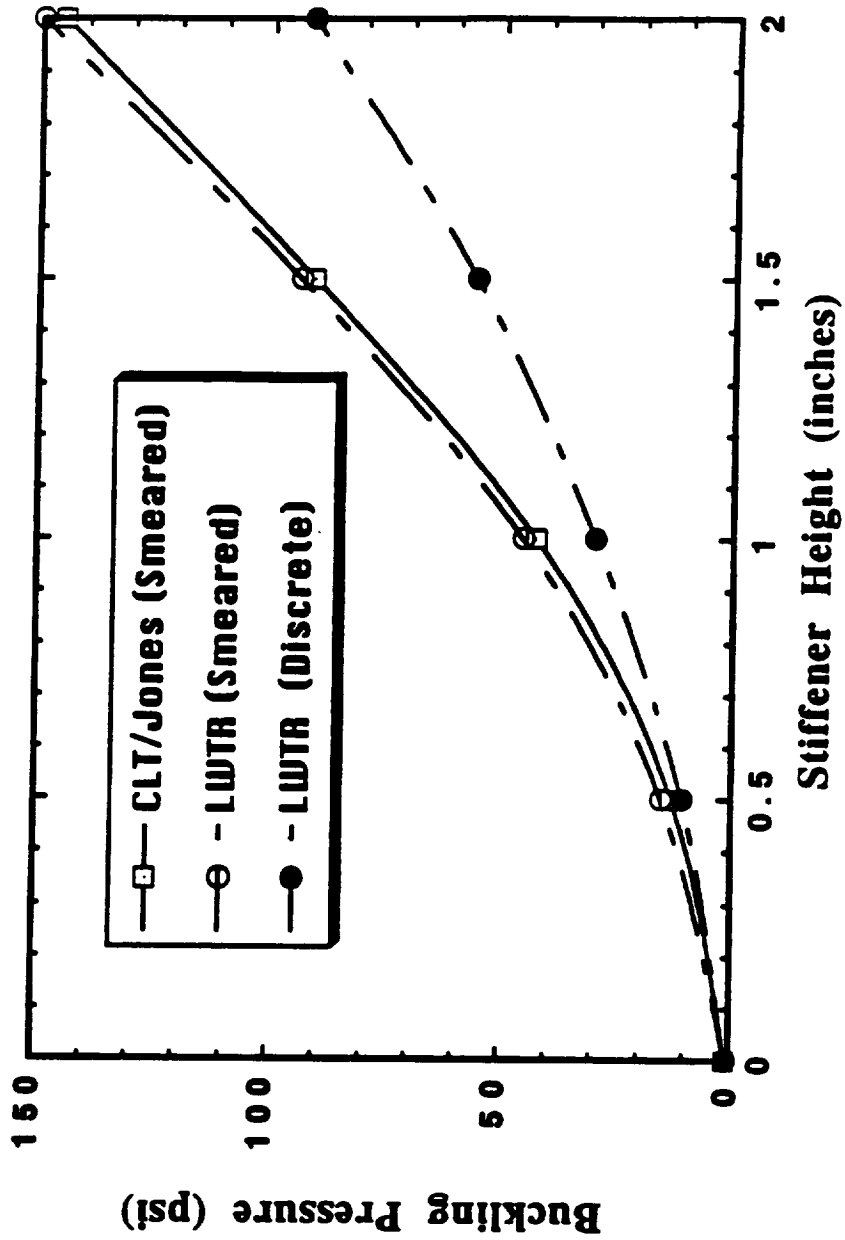

Figure 40. Buckling pressure for a 25 ring stiffener shell model ([0/90/90/0] layup; R = 85", L = 100"; 1.0" x 0.2" stiffeners).

method can be attributed to the fact that the LWTR method neglects the out-of-plane and the torsional stiffnesses of the stiffeners. The difference starts to become more pronounced as the stiffener heights increase. This is due to the fact that as the stiffener height increases the effects of the out-of-plane and the torsional stiffnesses on the global buckling results increase. Except for the 1x16 geodesic shell model there appears to be a good correlation of the buckling results, especially for the 1.0″ and 1.5″ stiffener heights.

Finally, a study of the buckling of geodesically stiffened cylinders subjected to external pressure was conducted. A 1x12 geodesic shell model was selected which has the same geometry and dimensions as used for the axial compression analyses. A comparison between the LWTR discrete method and the finite element method (CSM Testbed) was made for both the cross-ply case, [0/90/90/0], and the quasi-isotropic case, $[-45/45/90/0]_S$. The results for the cross-ply [0/90/90/0] shell is found in Table 25. The LWTR results correlate fairly well with the finite element solutions especially for the unstiffened case and for lower stiffener heights. The quasi-isotropic results are presented in Table 26. The results indicate that at lower stiffener heights the buckling pressures for both analytical methods are reasonably close, but as the stiffener height increases the buckling pressures tend to diverge. Neglecting the orthotropic stiffnesses, $\overline{C}_{16}$, $\overline{C}_{26}$, $\overline{C}_{36}$, $\overline{C}_{45}$, definitely must have a major impact on the stiffness of the layerwise quasi-isotropic laminates when the shells are sbjected to external pressures. Another difference between the LWTR discrete method and the finite element method can be attributed to the fact that the LWTR method neglects the out-of-plane and the torsional stiffnesses of the stiffeners. The difference becomes larger as the stiffener height increases because as the stiffener height increases the effects of the out-of-plane and the torsional stiffnesses on the global buckling results become more prominent.

The typical CPU time for the Testbed finite element buckling analyses is 620 seconds. The CPU time for the layerwise discrete method for one buckling mode (m, n) is 410 seconds. Consequently, the CPU times for the layerwise discrete method can become large, perhaps 8-10 hours or more, if a sweep of a large number of buckling modes (m, n) is made in order to determine the minimum eigenvalue.

5.2 LWTR/Testbed Finite Element Stress Analysis Comparison

A stress analysis comparison of the LWTR and CSM Testbed finite element codes was made for geodesically stiffened shells. A 1x12 geodesically stiffened shell as shown in Figure 36 with 1.0" high by 0.2" thick internal stiffeners was selected as the comparison model. The shell geometry consists of a radius of 85" and length of 100". In lieu of modeling the entire cylinder, symmetry conditions were employed and an analysis of a unit cell was made, see Figures 42 and 43. The loadings were employed via the application of uniformly applied end displacements. Three laminate layups were studied in this analysis: [0/90/0]; [45/ – 45/45/ – 45]; and [60/ – 60/0/ – 60/60]. The material properties used are given in Table 7. The ply thickness used in these analyses is 0.100". Analyses were performed with 0^0 orthotropic stiffeners. Applied end displacements of 0.01" were used to generate the compressive loads.

The CSM Testbed elements described in section 5.1 were used for this analysis. The finite element model shown in Figure 42 describes the finite element mesh and the boundary conditions used for this analysis. The Testbed finite element model uses 256 nine-node assumed-natural-coordinate strain (ANS) shear deformable shell elements to model the the shell and 32 nine-node plate elements to model the stiffeners.

Table 21. Analysis of [0/90/90/0] 0.2" Thick Circular Cylindrical Shell with Geodesic Stiffeners Subjected to Axial Compression (R = 85", L = 100", 1x12 Geodesic Shell Model).

Stiffener Height (inches)	Testbed FEA (lbs./inch)	LWTR Discrete (lbs./inch)	Error	Lowest Analysis
Unstiffened	1053	1030 M=15, N=1	-2.2%	LWTRD
0.5	1347	1326	-1.6%	LWTRD
1.0	1570	1549	-1.3%	LWTRD
1.5	1664	1702	+2.2%	FEA
2.0	1743	1953	+10.8%	FEA

M = 1, N= 10 for all LWTRD Results

1x12 Geodesic Model
α = 23.99 Degrees

M = number of axial halfwaves

N = number of circumferential halfwaves

LWTRD - Layerwise Laminate Theory of Reddy with Discrete Stiffeners

Table 22. Analysis of [0/90/90/0] 0.2" Thick Circular Cylindrical Shell with Geodesic Stiffeners Subjected to Axial Compression (R = 85", L = 100", 1x16 Geodesic Shell Model).

Stiffener Height (inches)	Testbed FEA (lbs./inch)	LWTR Discrete (lbs./inch)	Error	Lowest Analysis
Unstiffened	1053	1030 M=15, N=1	-2.2%	LWTRD
0.5	1357	1327	-2.2%	LWTRD
1.0	1768	1537	-13.1%	LWTRD
1.5	1980	1715	-13.4%	LWTRD
2.0	2150	2016	-6.2%	LWTRD

M = 1, N= 10 for all LWTRD Results

1x16 Geodesic Model

α = 18.46 Degrees

M = number of axial halfwaves

N = number of circumferential halfwaves

LWTRD - Layerwise Laminate Theory of Reddy with Discrete Stiffeners

Table 23. Analysis of [0/90/90/0] 0.2" Thick Circular Cylindrical Shell with Geodesic Stiffeners Subjected to Axial Compression (R = 85", L = 100", 2x12 Geodesic Shell Model).

Stiffener Height (inches)	Testbed FEA (lbs./inch)	LWTR Discrete (lbs./inch)	Error	Lowest Analysis
Unstiffened	1053	1030 M=15, N=1	-2.2%	LWTRD
0.5	1505	1588	+5.2%	FEA
1.0	1724	1764	+2.3%	FEA
1.5	1802	1908	+5.6%	FEA
2.0	1838	2052	+10.4%	FEA

M = 1, N= 10 for all LWTRD Results

2x12 Geodesic Model

α = 41.67 Degrees

M = number of axial halfwaves

N = number of circumferential halfwaves

LWTRD - Layerwise Laminate Theory of Reddy with Discrete Stiffeners

Table 24. Analysis of [0/90/90/0] 0.2" Thick Circular Cylindrical Shell with Geodesic Stiffeners Subjected to Axial Compression (R = 85", L = 100", 2x16 Geodesic Shell Model).

Stiffener Height (inches)	Testbed FEA (lbs./inch)	LWTR Discrete (lbs./inch)	Error	Lowest Analysis
Unstiffened	1053	1030 M=15, N=1	-2.2%	LWTRD
0.5	1658	1574	-5.2%	LWTRD
1.0	1937	1763	-9.0%	LWTRD
1.5	2052	1957	-4.6%	LWTRD
2.0	2180	2206	+1.2%	FEA

M = 1, N= 10 for all LWTRD Results

2x16 Geodesic Model

α = 33.73 Degrees

M = number of axial halfwaves

N = number of circumferential halfwaves

LWTRD - Layerwise Laminate Theory of Reddy with Discrete Stiffeners

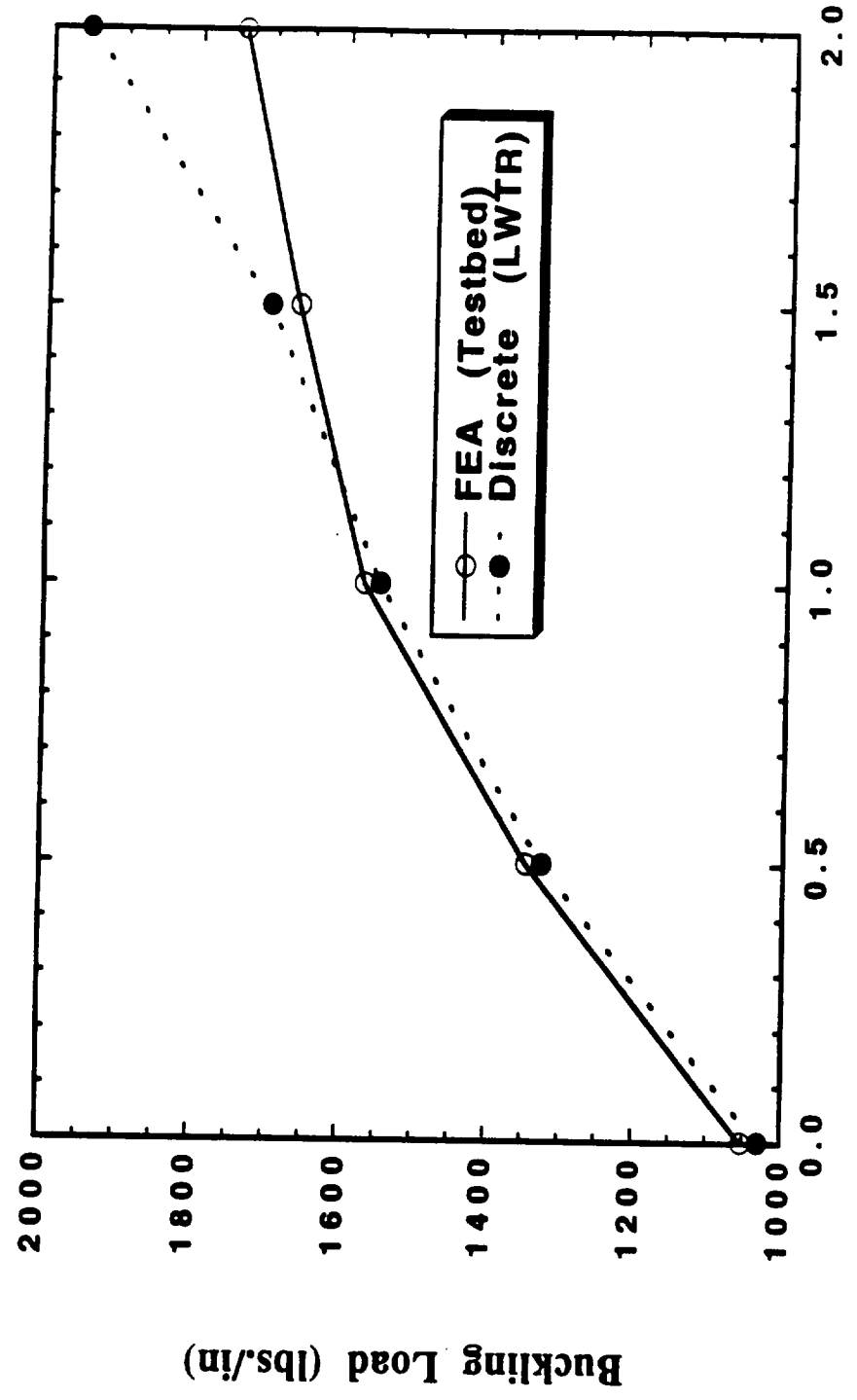

Figure 41. Axial buckling results for a 1x12 geodesic shell model ([0/90/90/0] layup; R = 85", L = 100"; 1.0" x 0.2" stiffeners).

Table 25. Analysis of [0/90/90/0] 0.2" Thick Circular Cylindrical Shell with Geodesic Stiffeners Subjected to Lateral Pressure (R = 85", L = 100", 1x12 Geodesic Shell Model).

Stiffener Height (inches)	Testbed FEA (psi)	LWTR Discrete (psi)	Error	Lowest Analysis
Unstiffened	0.89	0.88 M=1, N=11	-1.1%	LWTRD
0.5	1.22	1.17	-4.0%	LWTRD
1.0	1.88	1.67	-11.2%	LWTRD
1.5	2.40	2.17	-9.6%	LWTRD
2.0	2.65	2.33	-12.1%	LWTRD

M = 1, N = 11 for all LWTRD Results

1x12 Geodesic Model

α = 23.99 Degrees

M = number of axial halfwaves

N = number of circumferential halfwaves

LWTRD - Layerwise Laminate Theory of Reddy with Discrete Stiffeners

Table 26. Analysis of $[-45/45/90/0]_S$ 0.2" Thick Circular Cylindrical Shell with Geodesic Stiffeners Subjected to Lateral Pressure (R = 85", L = 100", 1x12 Geodesic Shell Model).

Stiffener Height (inches)	Testbed FEA (psi)	LWTR Discrete (psi)	Error	Lowest Analysis
Unstiffened	1.63	1.61 M=1, N=11	-1.2%	LWTRD
0.5	2.09	1.90	-9.1%	LWTRD
1.0	2.79	2.09	-25.1%	LWTRD
1.5	3.80	2.20	-42.1%	LWTRD

M = 1, N = 11 for all LWTRD Results

1x12 Geodesic Model

α = 23.99 Degrees

M = number of axial halfwaves
N = number of circumferential halfwaves

LWTRD - Layerwise Laminate Theory of Reddy with Discrete Stiffeners

The LWTR finite element model described in Figure 43 shows the finite element mesh and the boundary conditions used for this analysis. A more refined mesh is used in critical regions such as the stiffener intersection. The model employs 256 four-node LWTR shell elements to model the shell and 32 two-node LWTR beam elements to model the stiffeners.

The first analysis considered here is for a [0/90/0] shell with orthotropic (0^0) stiffeners. The plot in Figure 44 shows the axial stress, σ_{xx}, for all layers at $x = \frac{L}{2}$ plotted along the nondimensional circumference of the unit cell, $\frac{Y}{L_y}$. The stresses calculated from the two analyses are in good agreement away from the point of the stiffener intersection. Near the stiffener intersection i.e. $\frac{Y}{L_y} = \frac{1}{2}$, the LWTR stresses are less compressive than the stresses calculated by the Testbed analysis. For the bottom 0^0 layer the axial compressive stress is 3.2% (120 psi) less compressive than the Testbed axial stress. This small difference is within reason and some of the difference can be attributed to the fact that a different type of element is used for the stiffeners in each of the models and a small difference in the behavior of the stiffener intersection intersection is being observed. The axial stresses in the 90^0 layer as shown in Figure 44 are in good agreement except at the location of the stiffener intersection where the LWTR stress, σ_{xx}, is 10.6% (30 psi) less compressive than the Testbed axial stress at that location. The LWTR axial stress at the stiffener intersection in the top 0^0 layer is 3.0% (104 psi) less compressive than the Testbed axial stress. It is apparent from this analysis that the stiffener intersection is slightly more compliant (less stiff) for the LWTR method when compared with the results generated from the Testbed analysis.

The second analysis considered here is that of an angle ply laminate, [45/ – 45/45/ – 45], with orthotropic stiffeners. The axial stresses for the individual

layers are presented in Figures 45 and 46. The axial compressive stresses in the individual layers are in fairly close agreement. The largest difference in stresses occurs at the stiffener intersection location for the top -45^0 layer shown in Figure 46 where the LWTR are 10.5% (40 psi) less compressive than those calculated from the Testbed method. This difference in stresses at the stiffener intersection can be attributed to the difference in the stiffener intersection stiffness of the two analytical methods.

The final analysis is that of a symmetric 5 layer quasi-isotropic shell laminate, [60/ – 60/0/ – 60/60], with orthotropic stiffeners. The results of this analysis are presented in Figures 47-49. There is good agreement of the axial stresses for all layers. The axial stresses in the 60^0 and -60^0 layers are 5-6% (20-25 psi) smaller in the LWTR along the circumference of the shell. The largest percentage difference in compressive stress occurs at the location of the stiffener intersection in the top 60^0 layer where the LWTR axial stress is 10.4% (35 psi) smaller than the Testbed stress, see Figure 49. In the 0^0 layer the Testbed results are an average of 2.5% (80-100 psi) smaller than the LWTR results. Thus, for the LWTR analysis the 0^0 layer is carrying slightly more compressive load and the 60^0 and -60^0 layers do not carry quite as much compressive load when compared with the Testbed results. Overall there is good agreement of the axial stresses for all layers.

The stress analysis comparison here was conducted to help verify the stress analysis capabilities of the LWTR finite element program. Several lamination schemes were considered to accomplish this task. A good correlation exists between the LWTR analyses and the Testbed analyses. Small differences in stresses do occur at the siffener intersection. These differences are not major and are due to the difference in stiffener intersection response measured by the two analysis methods.

The CPU time for the Testbed finite element stress analysis is 125 seconds. Run times for the layerwise theory vary depending upon the number of shell laminate layers, number of nodes in the mesh, and the type of elements used (4 or 9 nodes). A three layered shell, [0/90/0], model (289 nodes) with one layered beams has 3567 active degrees of freedom. A mesh of 256 four node layerwise shell elements and 32 two node layerwise beam elements will have a half-bandwidth of 285. The CPU times for this model are 139 seconds for a linear analysis and 730 seconds for a geometrically nonlinear analysis (4 iterations to converge). If the mesh is changed to 64 nine node layerwise shell elements and 16 three node layerwise beam elements with a half-bandwidth of 555, the CPU times increase to 736 seconds for a linear analysis and 4251 seconds for a nonlinear analysis (5 iterations to converge). A six layered shell, $[45/90/0]_S$, with 289 nodes using one layered beams has 6168 active degrees of freedom. A mesh of 256 four node layerwise shell elements and 32 two node layerwise beam elements will have a half-bandwidth of 456. The CPU times for this model are 752 seconds for a linear analysis and 3261 seconds for a geometrically nonlinear analysis (4 iterations to converge). Increasing the bandwidth has a large influence on the CPU time necessary to run the layerwise finite element analyses. Furthermore, layerwise elements are not practical elements to use if a postbuckling analysis must be conducted due to the large run times.

5.3 Displacements and Interlaminar Stresses in Geodesically Stiffened Shells

In this study it was desired to conduct analyses of geodesically stiffened shells using the LWTR in order to determine the trends that have major effects on the transverse displacements and the interlaminar stresses. Variables such as the laminate layup and thickness, stiffener height, stiffener orientation, stiffener angle, cell geometry, cell length,

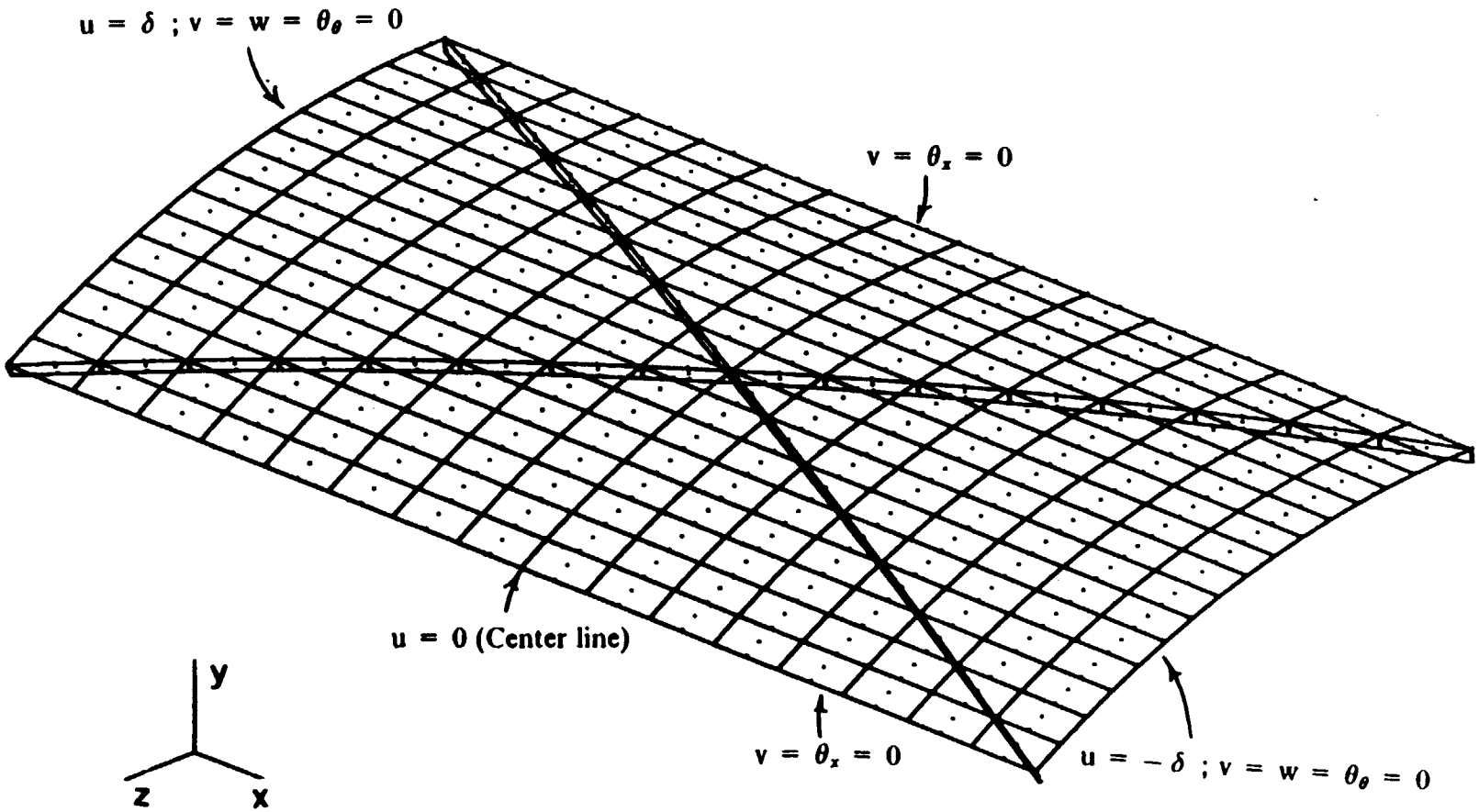

Figure 42. Unit cell finite element mesh and boundary conditions for the Testbed stress analysis (256 elements).

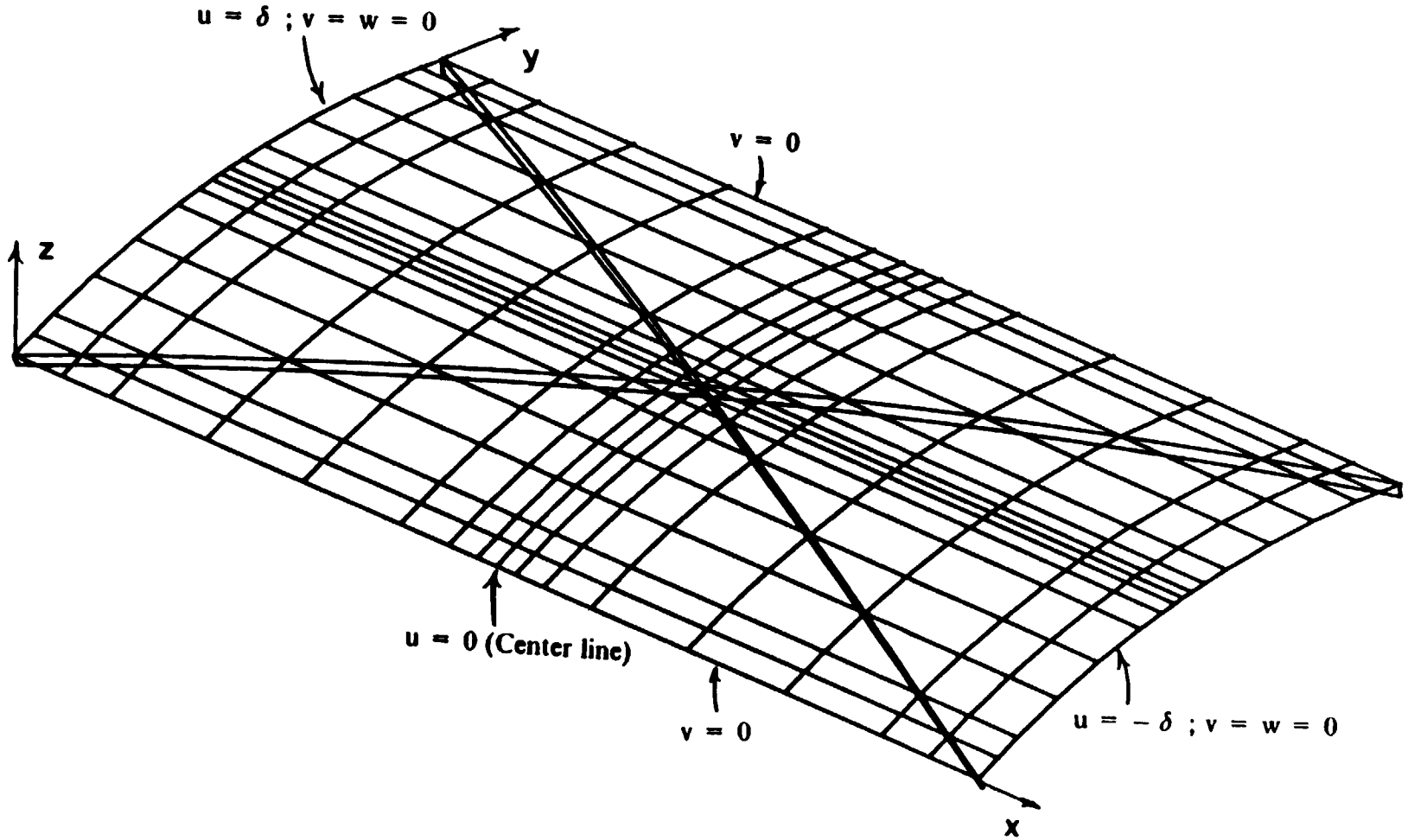

Figure 43. Unit cell finite element mesh and boundary conditions for the LWIR stress analysis (256 elements).

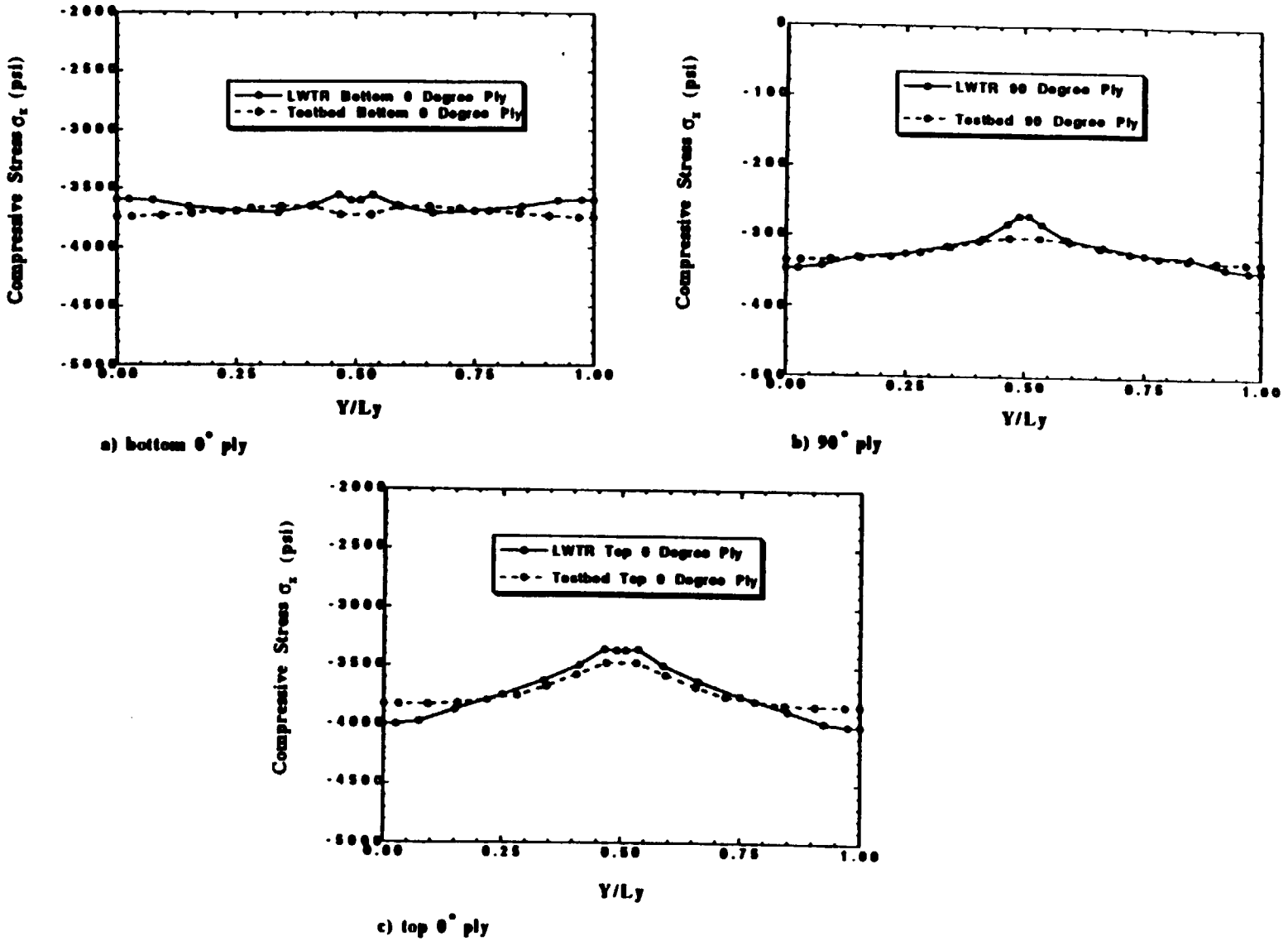

Figure 44. LWTR and Testbed 1x12 geodesic shell axial stresse for [0/90/0] laminate: a) bottom 0° ply; b) 90° ply; c) top 0° ply (x = 1/2).

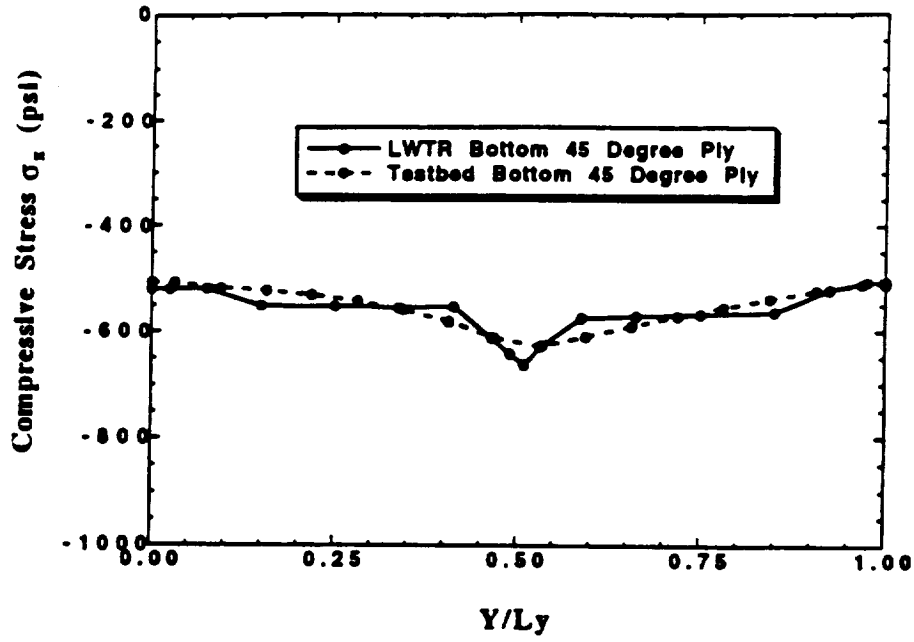

a)bottom 45° ply

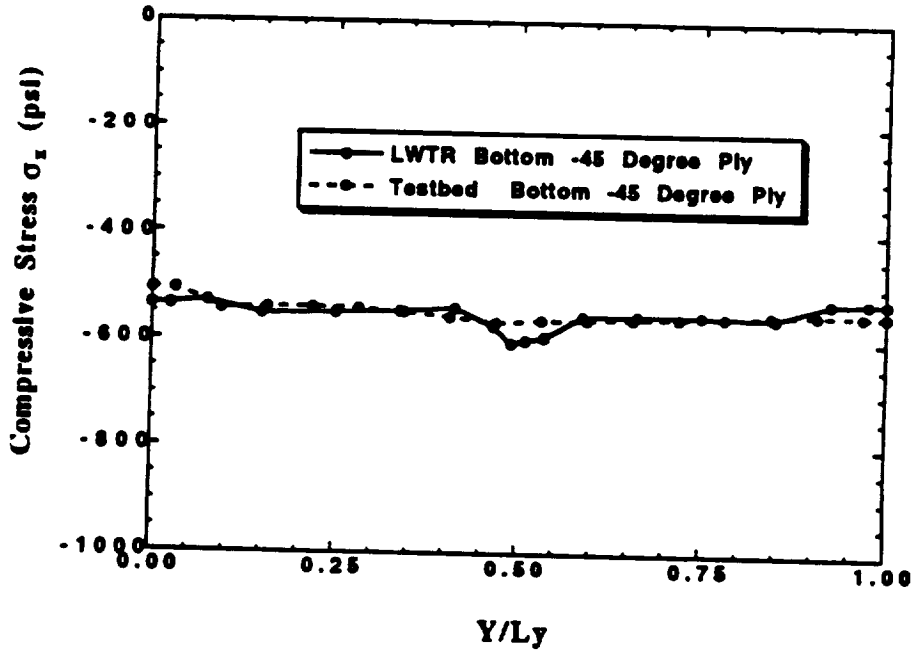

b) bottom -45° ply

Figure 45. LWTR and Testbed 1x12 geodesic shell axial stresses for bottom layers of [45/ – 45/45/ – 45] laminate: a) bottom 45° ply; b) bottom –45° ply (x = L/2).

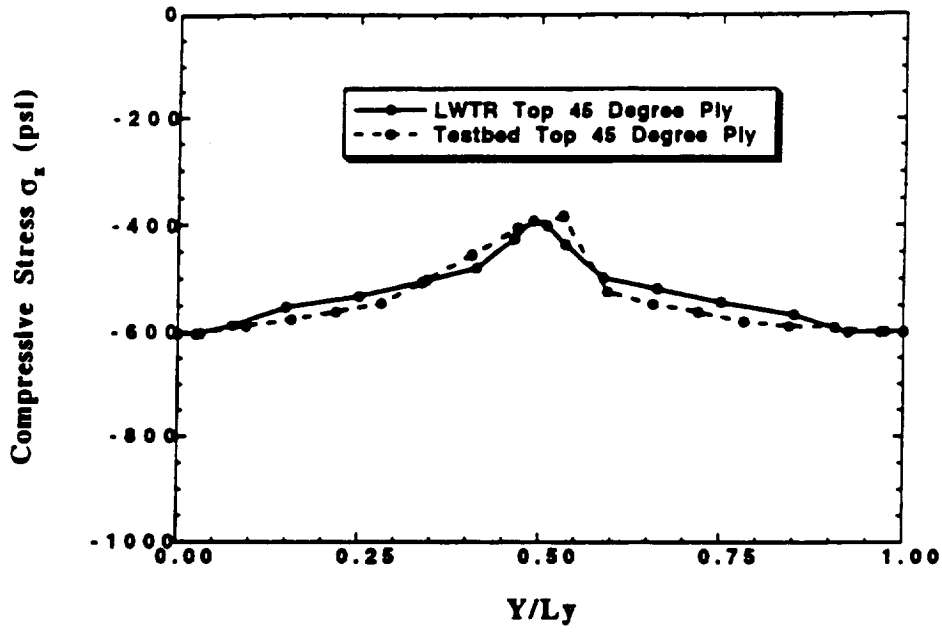

a) top 45° ply

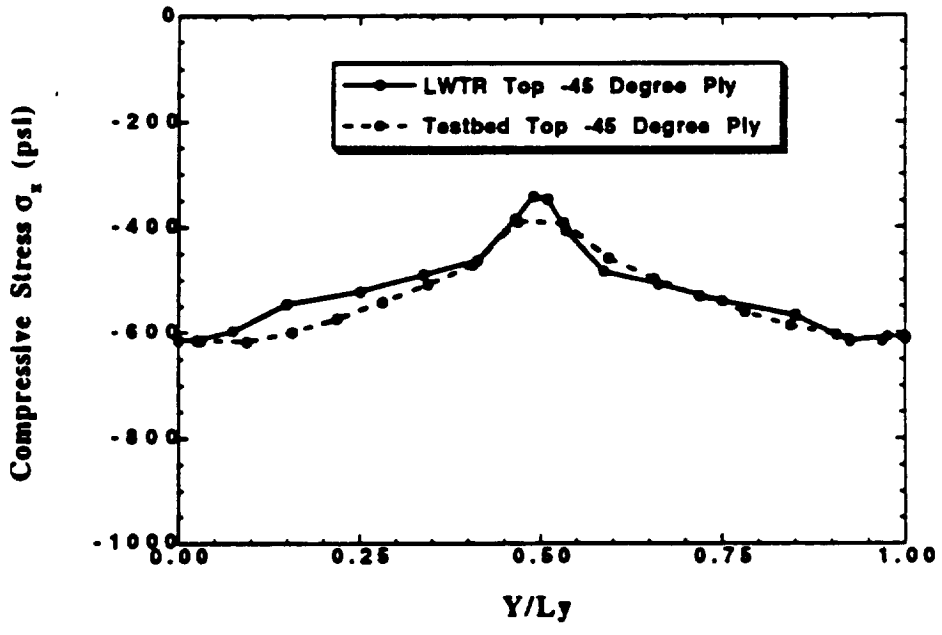

b) top -45° ply

Figure 46. LWTR and Testbed 1x12 geodesic shell axial stresses for top layers of [45/ – 45/45/ – 45] laminate: a) top 45° ply; b) top –45° ply (x = L/2).

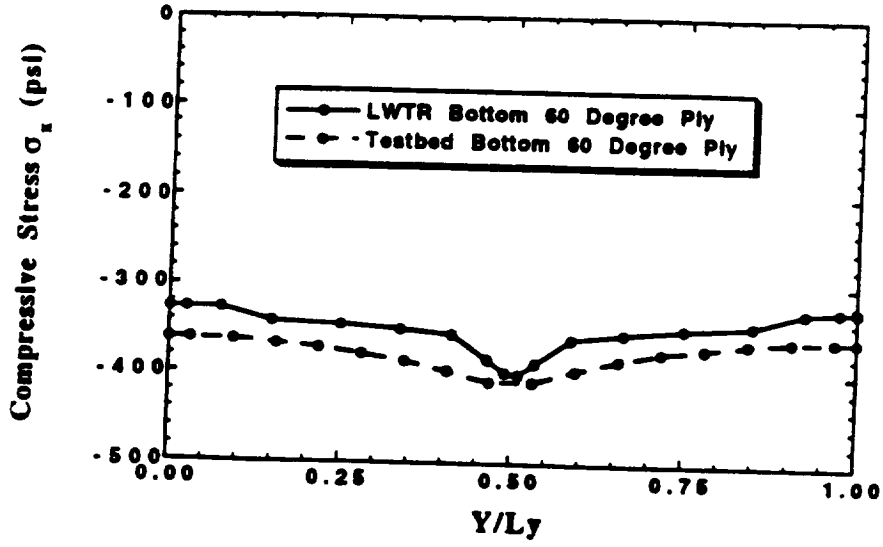

a) bottom 60° ply

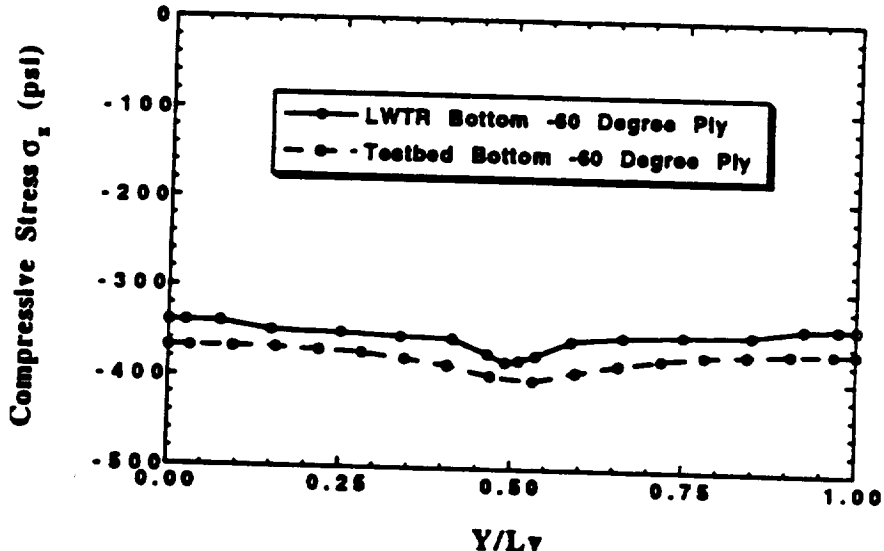

b) bottom -60° ply

Figure 47. LWTR and Testbed 1x12 geodesic shell axial stresses for bottom layers of [60/ – 60/0/ – 60/60] laminate: a) bottom 60° ply; b) bottom –60° ply (x = L/2).

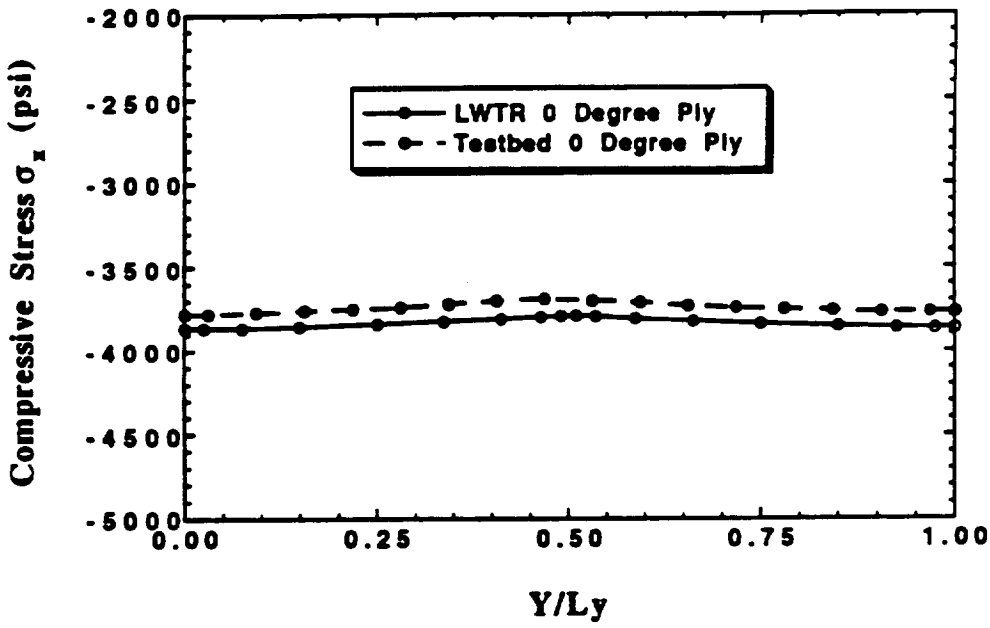

Figure 48. LWTR and Testbed 1x12 geodesic shell axial stresses for 0° layer of [60/ – 60/0/ – 60/60] laminate (x = L/2).

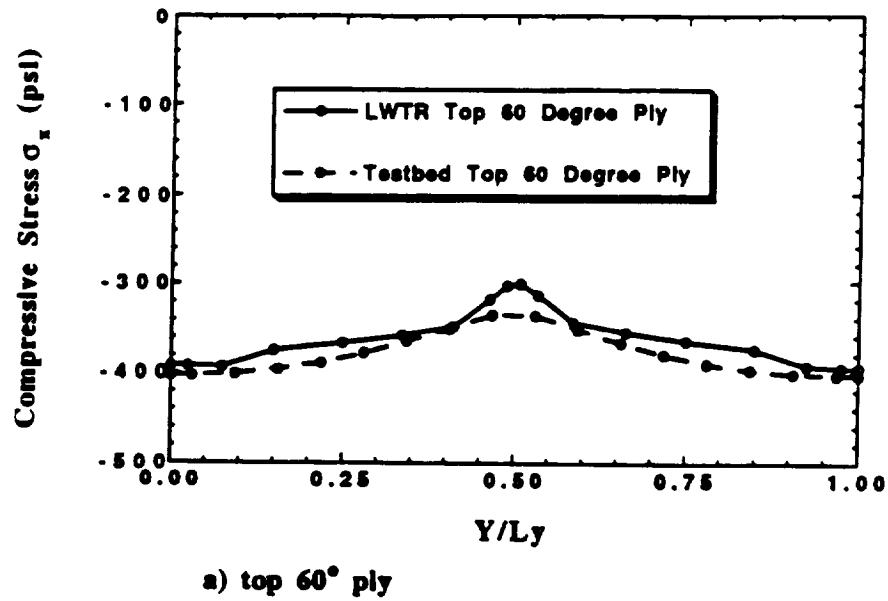

a) top 60° ply

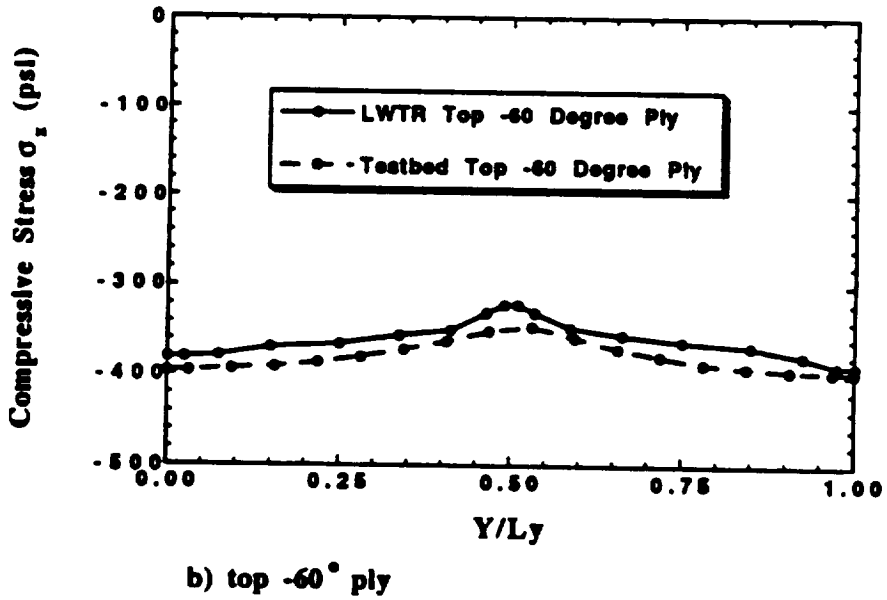

b) top -60° ply

Figure 49. LWTR and Testbed 1x12 geodesic shell axial stresses for top layers of [60/ – 60/0/ – 60/60] laminate: a) top 60° ply; b) top –60° ply (x = L/2).

were varied when performing this study. Concentration here is placed upon the action of the shells under pure compressive loads and combined loads generated with the addition of internal pressure. In addition, a geometrically nonlinear analysis was performed to determine the effects on the displacement and stress fields. A base line design using a 1x12 geodesically stiffened shell with a nominal radius of 85″, shell length of 100″, 1.0″ high by 0.2″ thick orthotropic internal stiffeners, and a [0/90/0] shell laminate was used for a large number of the analyses. A simple shell laminate, [0/90/0], was used to perform many of the comparison studies in order to keep the number of degrees of freedom manageable and in particular to keep the bandwidth of the global stiffness matrix from becoming excessively large. The bandwidth can become extremely large when analyzing a large number of nodes and laminate layers using the layerwise theory. The LWTR finite element model used in these analyses was described previously in Figure 36. The model consists of 289 nodes, 256 four-node layerwise shell elements, and 32 two-node beam elements.

5.4 Displacement Field in Geodesically Stiffened Shells

A study of the transverse displacement field along the circumference of the unit cell at $x = \frac{L}{2}$ was performed for various shell parameters. The transverse displacements are the largest and most interesting displacements for the structures being analyzed in this research. The shells are subjected to compressive loading via the application of applied end displacements of 0.01″ and to a combined loading consisting of applied end displacements of 0.01″ and an internal pressure of 10 psi. The transverse displacements presented in this study are nondimensionalized using the following expression:

$$\overline{w} = \frac{wE_1h^2}{\overline{N}_xRL} \times 100 \tag{5.4}$$

Here $\overline{w}$ is the nondimensional transverse displacement, w is the transverse displacement, h is the total laminate thickness, E_1 is the modulus in the 1 direction, $\overline{N}_x$ is the applied load, R is the shell radius, and L is the shell length. The first study considered here is the effect of changing the laminate layup when the shell is subjected to compressive loading. The nondimensional displacement results presented in Figure 50 are for six different laminate layups: [0/90/0], [45/ – 45/45/ – 45], [60/ – 60/0/ – 60/60], $[45/90/0]_S$, $[-45/45/90/0]_S$, and [30/ – 30/0/ – 30/30]. The [0/90/0], $[-45/45/90/0]_S$, and [30/ – 30/0/ – 30/30] laminates show the largest variations in nondimensional transverse displacement 234%, 155%, and 113% respectively from the edge of the unit cell to the stiffener intersection at $\frac{Y}{L_y} = 0.5$. The [45/ – 45/45/ – 45], [60/ – 60/0/ – 60/60], $[45/90/0]_S$ yield respective changes in nondimensional transverse displacement along the circumference of the shell of 45%, 52%, 100%. The [45/ – 45/45/ – 45] and [30/ – 30/0/ – 30/30] laminates yield the maximum nondimensional transverse displacement along the circumference of 1.484 and 1.305 respectively for the given geometry and loading conditions. Thus, in order to avoid the largest transverse displacements and variations in transverse displacements in geodesically stiffened composite shells it is best to avoid designs containing cross-ply laminates, angle ply laminates, and laminates containing $+30^0$ or -30^0 plys.

The next study concentrates on the effects of changing the geodesically stiffened shell geometry and the stiffener orientation angle on the transverse displacement field. A [0/90/0] 1x12 geodesically stiffened shell is used in this analysis. The shells are subjected to uniform compressive loading via applied end displacements of 0.01". The stiffener

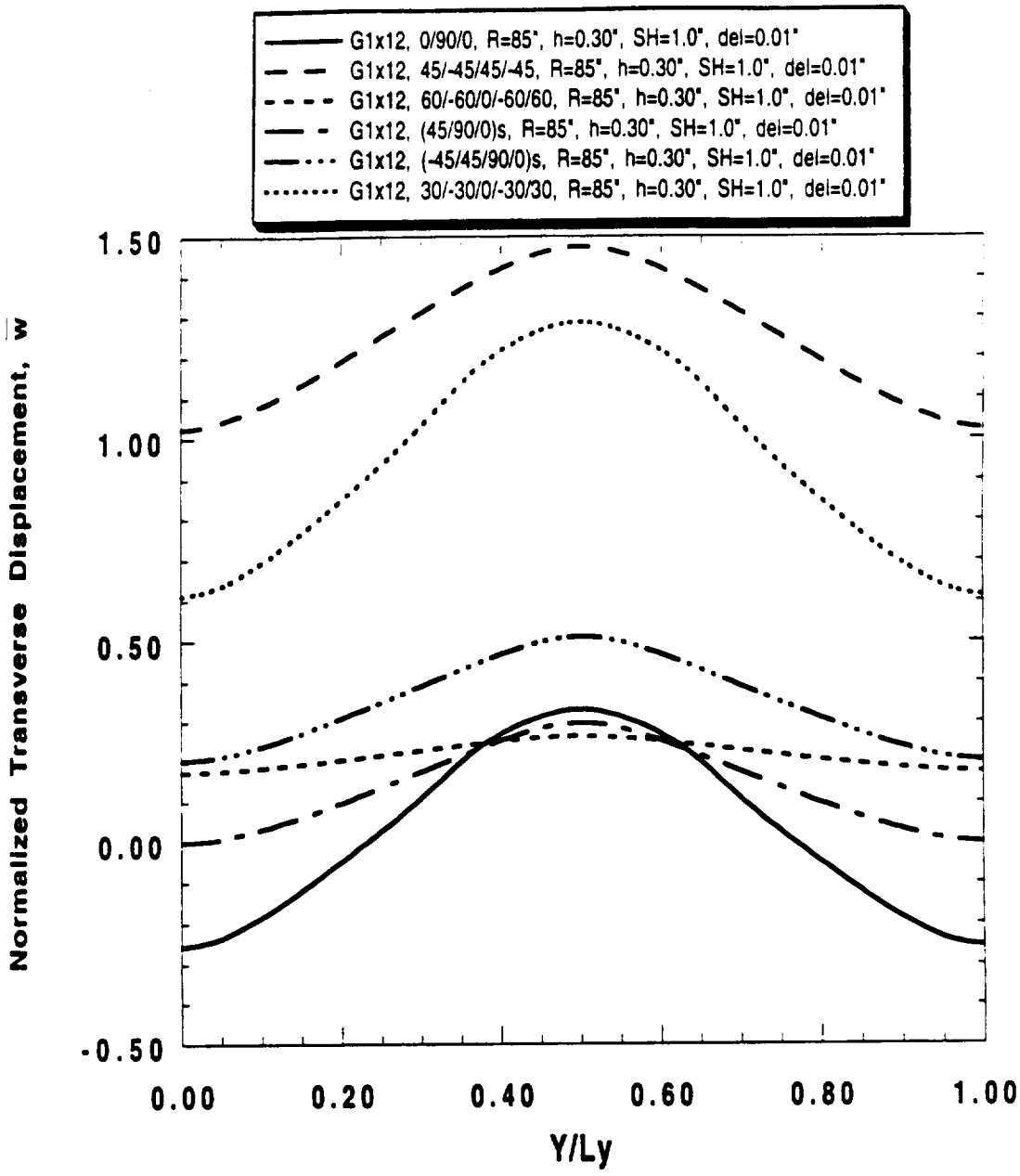

$$\overline{w} = \frac{w E_{11} h^2}{N_x R L} \times 100$$

Figure 50. Nondimensional transverse displacements for a 1x12 geodesically stiffened shell as a function of the laminate stacking sequence under compressive loading (R = 85", L = 100").

orientation angle, α, relative to the shell is shown in Figure 1 and Figure 14. Figure 51 shows the nondimensional transverse displacement as a function of the geodesic shell geometry and the subsequent stiffener orientation angle. The variation in the stiffener orientation angles were obtained by changing the cell geometry from G1x12 to G1x16 in Figure 51a and by changing the shell length from 50" to 200" in Figure 51b. The nondimensional transverse displacement field presented in Figure 51a shows that as the cell geometry is changed from G1x12 ($\alpha = 24^0$) to G1x16 ($\alpha = 18.5^0$) the maximum nondimensional transverse displacement decreases by 72%. The maximum transverse displacement shows the largest decrease, 41%, when the cell geometry is changed from G1x12 ($\alpha = 24^0$) to G1x13 ($\alpha = 22.3^0$). When the cell geometry is changed from G1x15 ($\alpha = 19.6^0$) to G1x16 ($\alpha = 18.5^0$) the change in maximum transverse displacement becomes less significant (2.5%). The results presented in Figure 51b show the transverse displacement as a function of the stiffener angle by changing the shell length. The trends predicted here indicate that as the shell length is decreased from 200" to 50" the maximum transverse displacement decreases by 52% even though the stiffener orientation angle is increased from 12.5^0 to 41.7^0. Thus, decreasing the shell length has a much greater effect on the shell stiffness than does increasing the stiffener orientation angle. The results presented in Figure 51 indicate that the response of geodesic shells is a stronger function of the shell geometry i.e. the number of cells around the circumference and the cell length and a weaker function of the stiffener orientation angle.

The effect of increasing the stiffener height on the nondimensional transverse displacement for both compressive loading and combined loading is shown in Figure 52. A [0/90/0] 1x12 geodesically stiffened shell is used in this analysis. Shown in Figure 52a is a plot of the nondimensional transverse displacement along the nondimensional shell circumference. As expected the nondimensional transverse displacements decrease as a

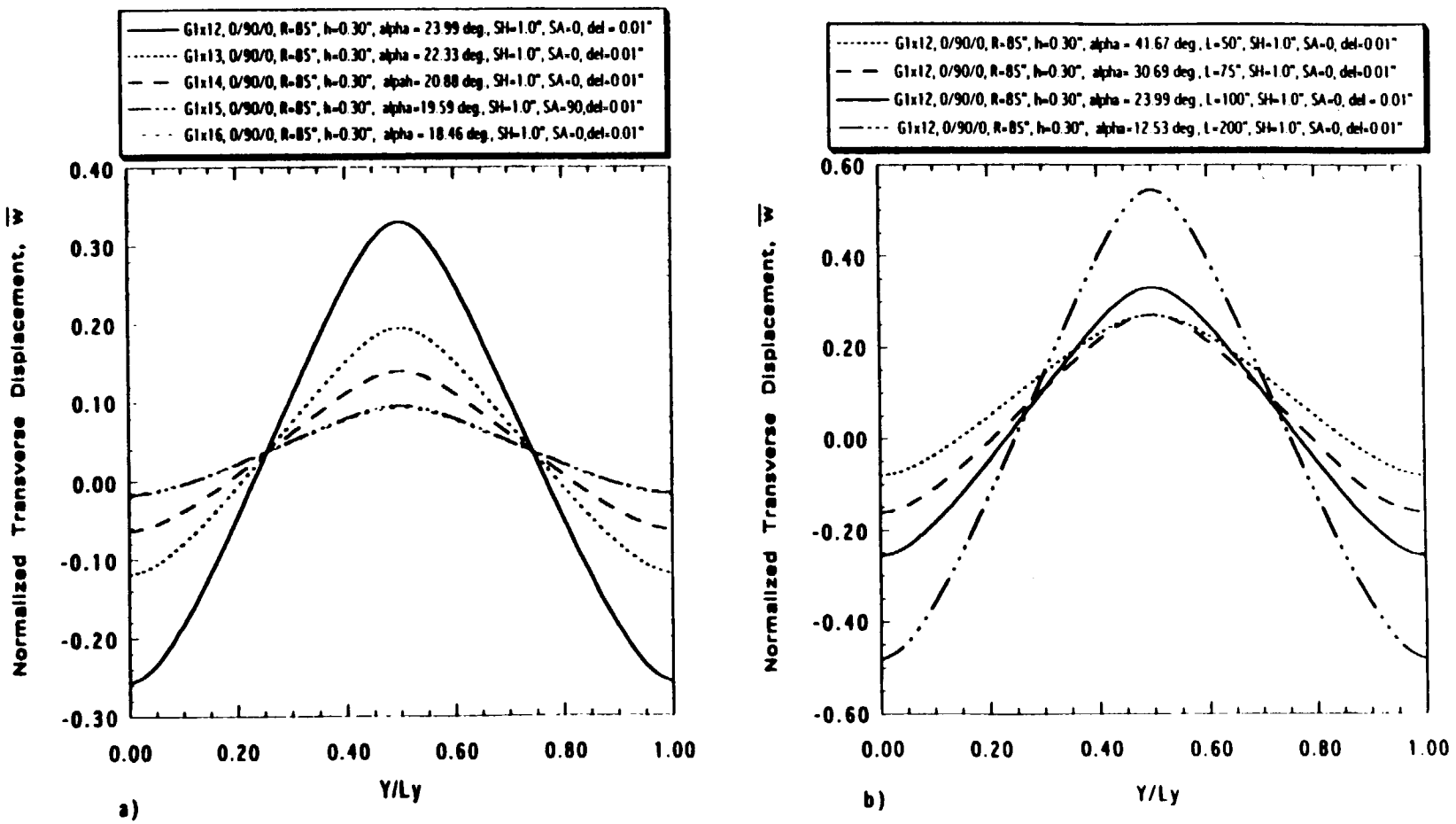

Figure 51. Nondimensional transverse displacements for geodesically stiffened shells as a function of the stiffener orientation: a) changing cell geometry; b) changing cell length.

function of the stiffener height. As the stiffener height is increased the area of the stiffeners is increased and consequently the applied load $\overline{N}_x$ increases because the load is a function of the applied displacements. In this study the applied displacement are constant and thus increasing the area increases the applied load. The transverse displacements are also a strong function of the stiffener bending stiffness and to some extent the axial stiffness of the stiffener. Thus, the transverse displacements are a function of the applied load, which increases as the stiffener height is increased, and the stiffness of the stiffeners. Shown in Figure 52b is the effect of the stiffener height on the nondimensional transverse displacements along the shell circumference when the shell is subjected to combined loads. The decrease in the nondimensional transverse displacement appears to be fairly uniform. In this case the applied load $\overline{N}_x$ is a function of the applied displacements, load area, and the internal pressure. The load area is a function of the increasing stiffener height. Therefore, the normalized transverse displacements will be a complex function of the stiffener height, stiffener stiffness, and the internal pressure.

The nondimensional transverse displacements as a function of the shell laminate thickness for a [0/90/0] 1x12 geodesically stiffened shell are shown in Figure 53. The laminate thicknesses studied here are 0.15", 0.30", 0.45", and 0.60". The results for compressive loading, shown in Figure 53b, reveals that the nondimensional transverse displacements decrease by 40.6% when increasing the shell thickness from 0.15" to 0.60". The maximum normalized transverse displacements for the 0.15" and 0.30" thicknesses are close together. This probably occurs because the nondimensional transverse displacement used in this study is a function of the shell thickness squared. The actual transverse displacements differ by 88%. The maximum difference in the actual transverse displacements is between the 0.15" and 0.60" shell thicknesses and is 558%. The results for the combined loading condition as a function of shell laminate thickness is shown in

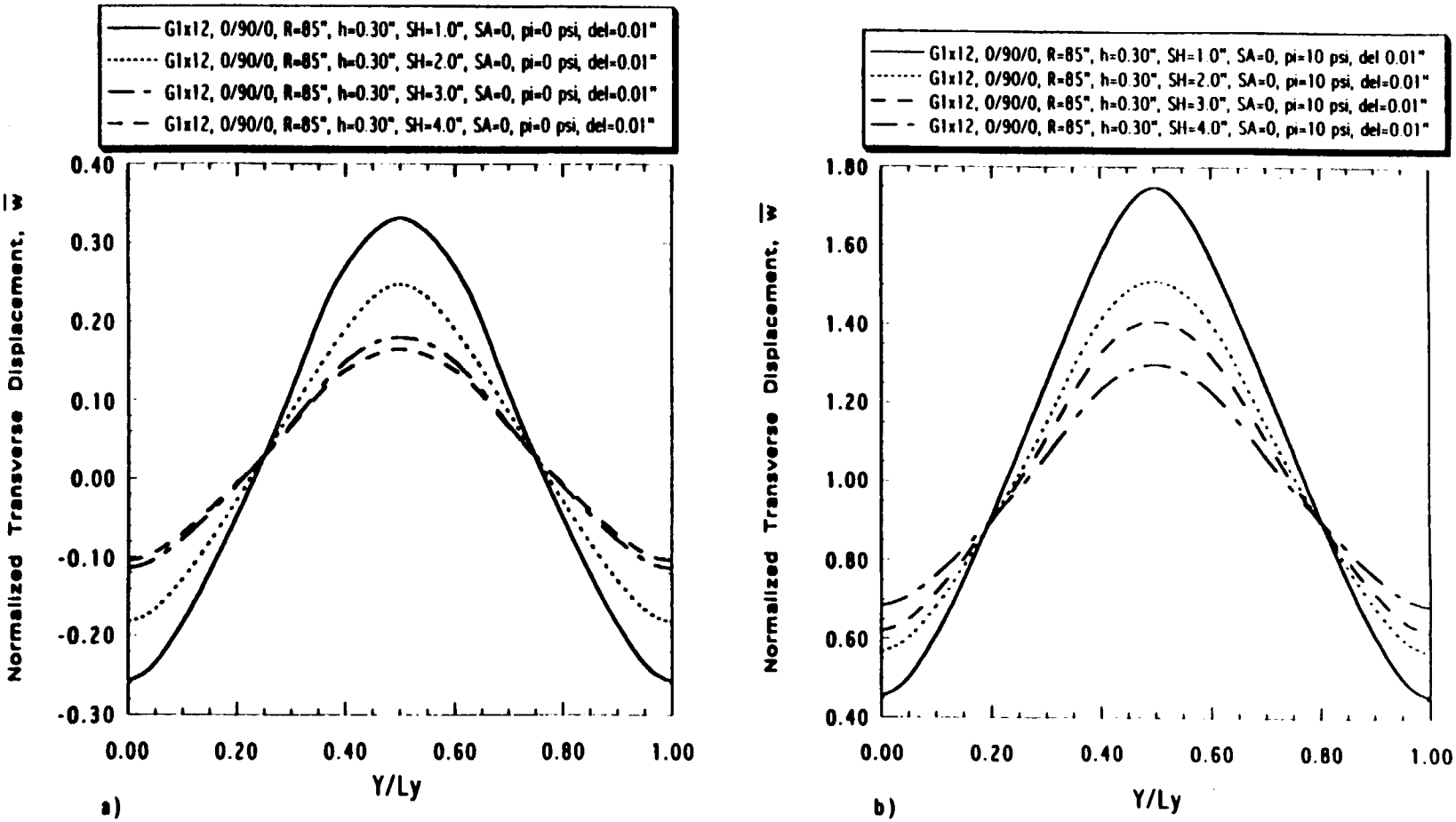

Figure 52. Nondimensional transverse displacements for geodesically stiffened shells as a function of the stiffener height: a) compressive loading; b) combined loading.

Figure 53b. As in the case for compressive loading, increasing the shell laminate thickness causes the nondimensional transverse displacement to decrease. The maximum difference in the nondimensional transverse displacement is 40.3% when increasing the shell thickness from 0.15" to 0.60". The actual transverse displacement difference between the 0.15" and 0.60" thicknesses is 386%. The transverse displacements are definitely a function of the shell laminate thickness.

Shown in Figure 54 are the nondimensional transverse displacement comparisons of linear and geometrically nonlinear analyses for [0/90/0] 1x12 geodesically stiffened shells. The results for the compressive loading load is found in Figure 54b. The nondimensional transverse displacement results indicate that using a geometrically nonlinear analysis does yield a stiffer structure and consequently slightly smaller transverse displacements than the linear analysis. The maximum difference in the nondimensional transverse displacements between the linear and nonlinear analysis is 8.9%. The results for a combined loading are shown in Figure 54b. The addition of internal pressure yields larger differences and variations in the nondimensional transverse displacements between the linear and nonlinear analyses than does the case of compressive loading only. As can be seen from Figure 54b the distribution and magnitude of the nonlinear results are much different than the linear results. The maximum difference in the displacements is 28.7% for the combined loading condition. Therefore, it can be concluded that the geometric nonlinearities become more significant with the addition of internal pressure.

The effect of increasing the shell radius is shown in Figure 55. The nondimensional transverse displacements for shell radii of 85", 170", and 255" subjected to an applied end compression developed through applied displacements for a [0/90/0] laminate are described in Figure 55a. As can be seen, as the shell radius is increased the maximum

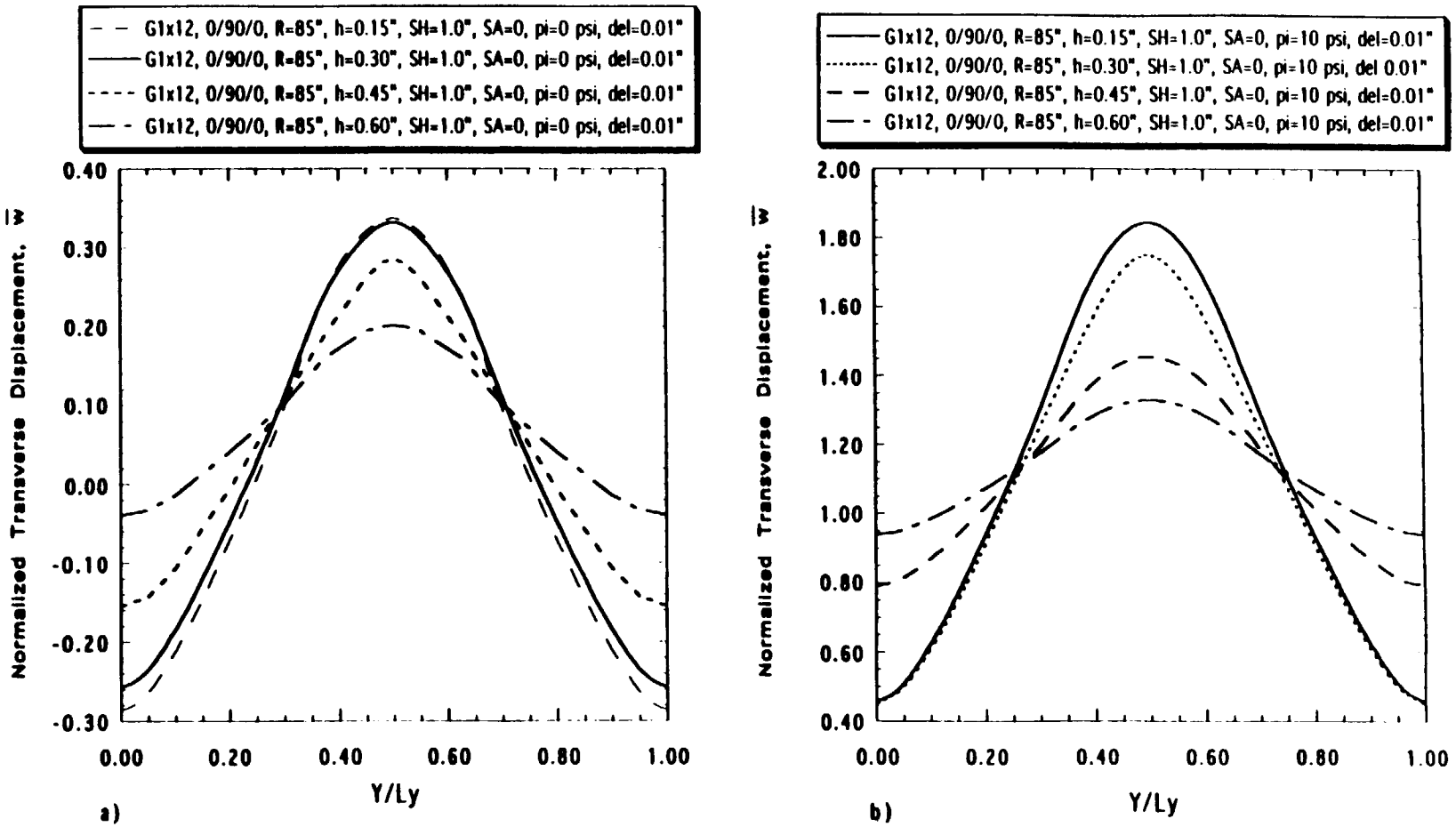

Figure 53. Nondimensional transverse displacements for geodesically stiffened shells as a function of the shell laminate thickness: a) compressive loading; b) combined loading.

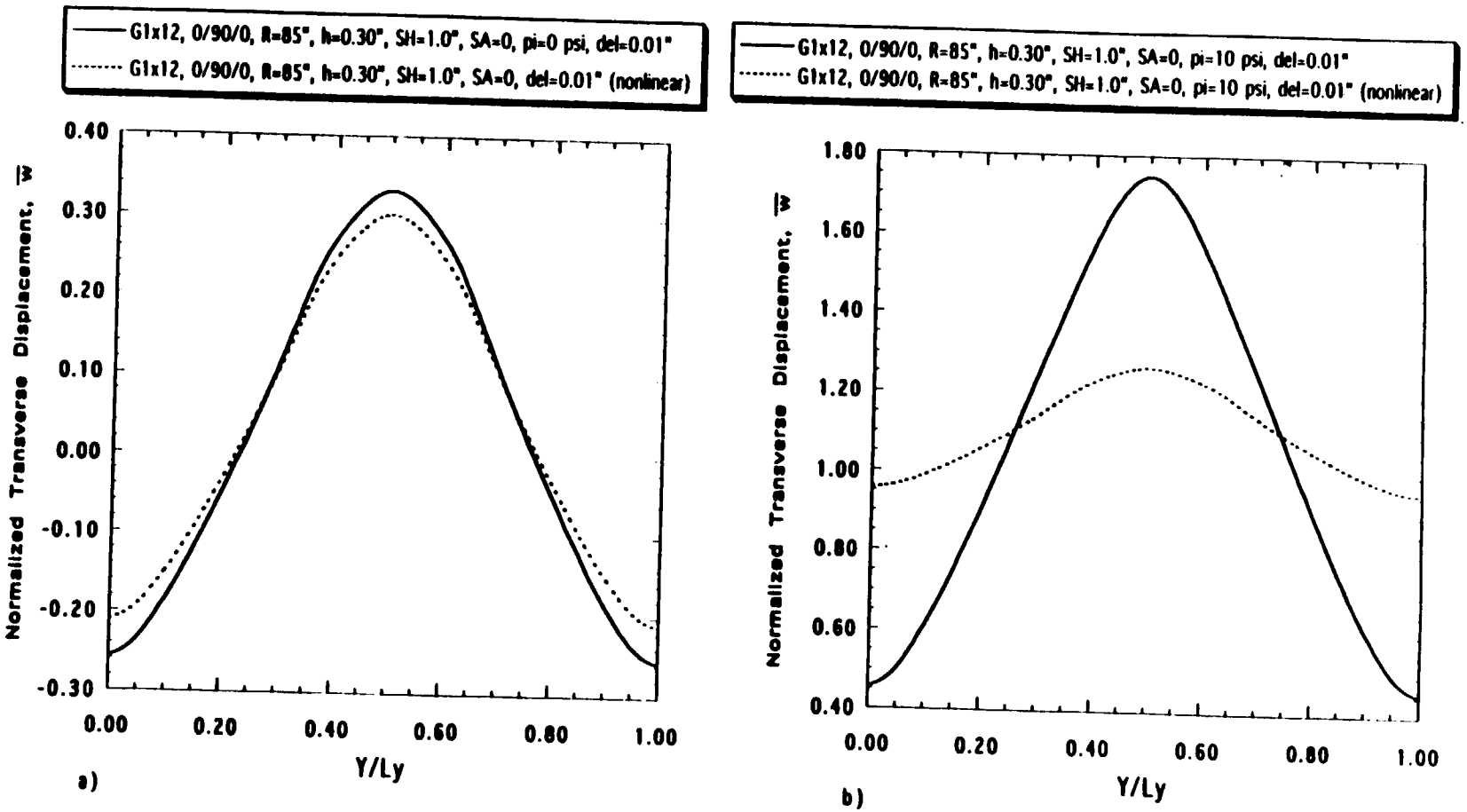

Figure 54. Nondimensional transverse displacements for geodesically stiffened shells for linear and geometrically nonlinear analyses: a) compressive loading; b) combined loading.

nondimensional transverse displacement is reduced by 52.8% when the shell radius is increased from 85" to 170". When the shell radius is increased from 85" to 255" the maximum nondimensional transverse displacements are reduced 73%. Figure 55b shows the nondimensional transverse displacements when an internal pressure of 10 psi is added to the applied end compression loading for varying shell radii. When the radius is increased from 85" to 170" the maximum transverse increases 47%. Increasing the shell radius from 85" to 255" increases the transverse displacement by 55.5%. The addition of internal pressure yields large differences and variations in the nondimensional transverse displacements as a function of the shell radius. As can be seen from Figure 55b, the distribution of the nondimensional transverse displacements yields a maximum displacement at the stiffener intersection for the 85" shell, almost a uniform variation of the displacements for the 170" shell, and a minimum displacement at the stiffener intersection for the 255" shell. A possible explanation for this phenomena is that for a constant shell thickness, as the shell radius is increased the ratio of the stiffener stiffness to the shell stiffness to resist pressure induced deflections increases. Moreover, as the shell radius is increased the load on the shell due to internal pressure increases and the stiffeners exert a larger influence on the structural response. This becomes evident with the addition of pressure loading. In this case the 85" shell has the smallest stiffness ratio and thus with the addition of pressure the stiffeners tend to deflect more. The 170" shell has an almost equal ratio and therefore a uniform displacement field is observed. The 255" shell has the largest stiffness ratio and thus with the addition of pressure the shell deflects more away from the stiffener intersection.

Shown in Figure 56 is a comparison of a [0/90/0] 1x12 geodesically stiffened shell, a [0/90/0] 1x12 axial/ring stiffened shell, and a [0/90/0] unstiffened shell. The axial/ring stiffened shell internal axial and ring stiffeners consisting of 1.0" orthotropic stiffeners.

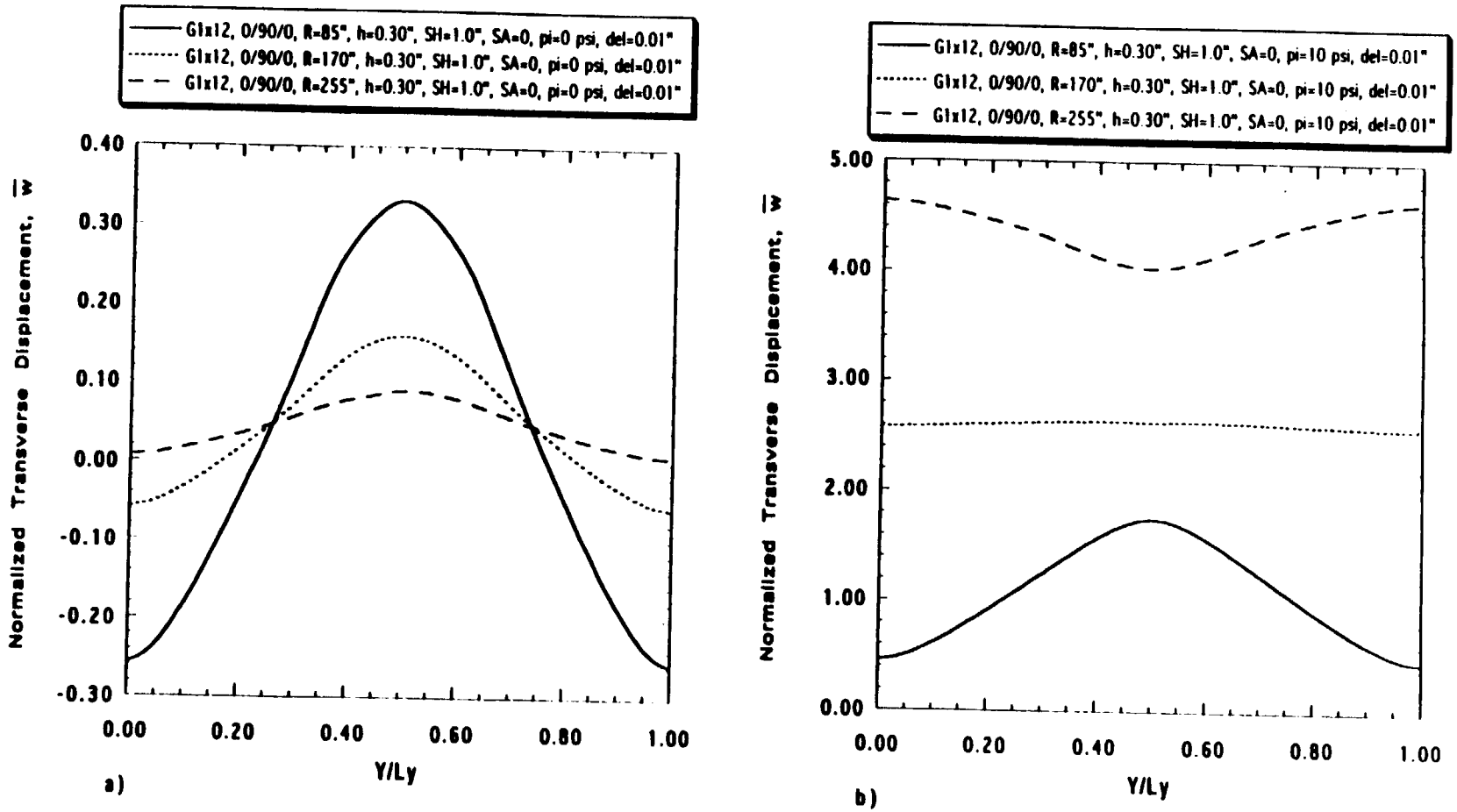

Figure 55. Nondimensional transverse displacements for geodesically stiffened shells as a function of the shell radius: a) compressive loading; b) combined loading.

The axial/ring stiffened finite element model with appropriate boundary conditions is shown in Figure 57. The results for compressive end loads are shown in Figure 56a. The geodesically stiffened shells show the largest transverse displacements of the shells studied here. The nondimensional transverse displacements for the geodesically stiffened shells are 91% greater than the displacements for axial/ring stiffened shells and are 90% greater than the displacements of unstiffened shells. The results for combined loading is shown in Figure 56b. The geodesically stiffened shells exhibit the largest nondimensional transverse displacements. The geodesically stiffened shells yield nondimensional transverse displacements 46.3% larger than the axial/ring stiffened shells and are 37.1% larger than the unstiffened shells. The axial/ring stiffened shells show that the shell stiffness at the stiffener intersection is much greater than that of the geodesically stiffened shell when internal pressure is applied. In this case the displacements away from the stiffener intersection are larger than those at the intersection in much the same way as the displacement field generated via the 255″ shell shown in Figure 55b.

The last displacement field analysis involves studying the effects of combined loading on geodesically stiffened shells. Figure 58 shows the results of these loadings on 0.075″, 0.15″, and 0.30″ [0/90/0] laminates with various stiffener heights. The results show that the maximum nondimensional transverse displacement occurs at the stiffener intersection until the stiffeners reach a critical height at which point the stiffeners are sufficiently stiff in bending to prevent large transverse displacements at the stiffener intersection. At this point the shell displacements away from the stiffener intersection becomes larger than the displacements at the stiffener intersection. The stiffener height at which this occurs is also a function of the laminate thickness. For example, the transverse displacement away from the stiffener intersection exceeds the transverse displacement at the stiffener intersection for a stiffener height of 2.0″ for a 0.075″ laminate,

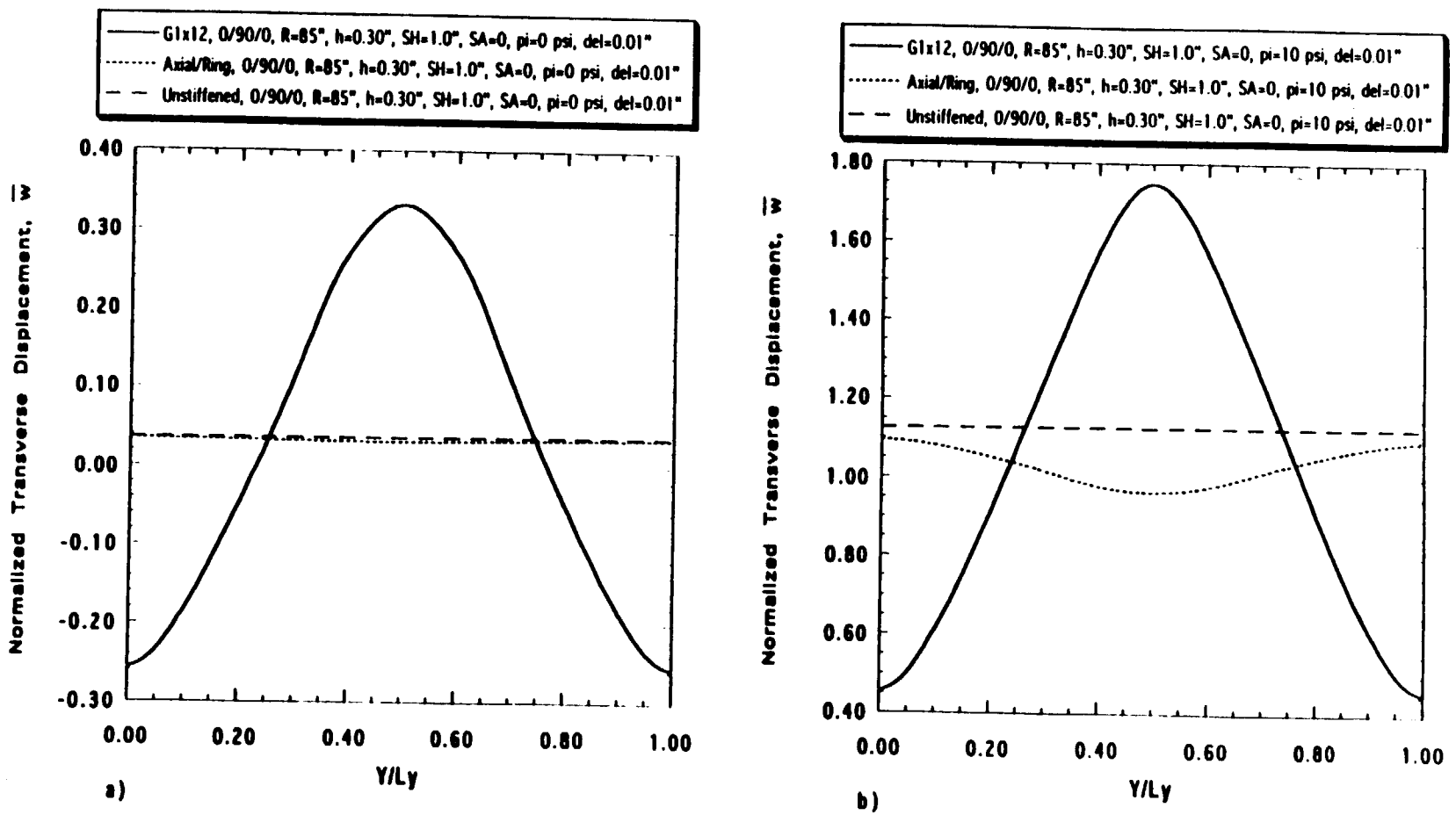

Figure 56. Nondimensional transverse displacements for geodesically stiffened, axial/ring stiffened, and unstiffened shells: a) compressive loading; b) combined loading.

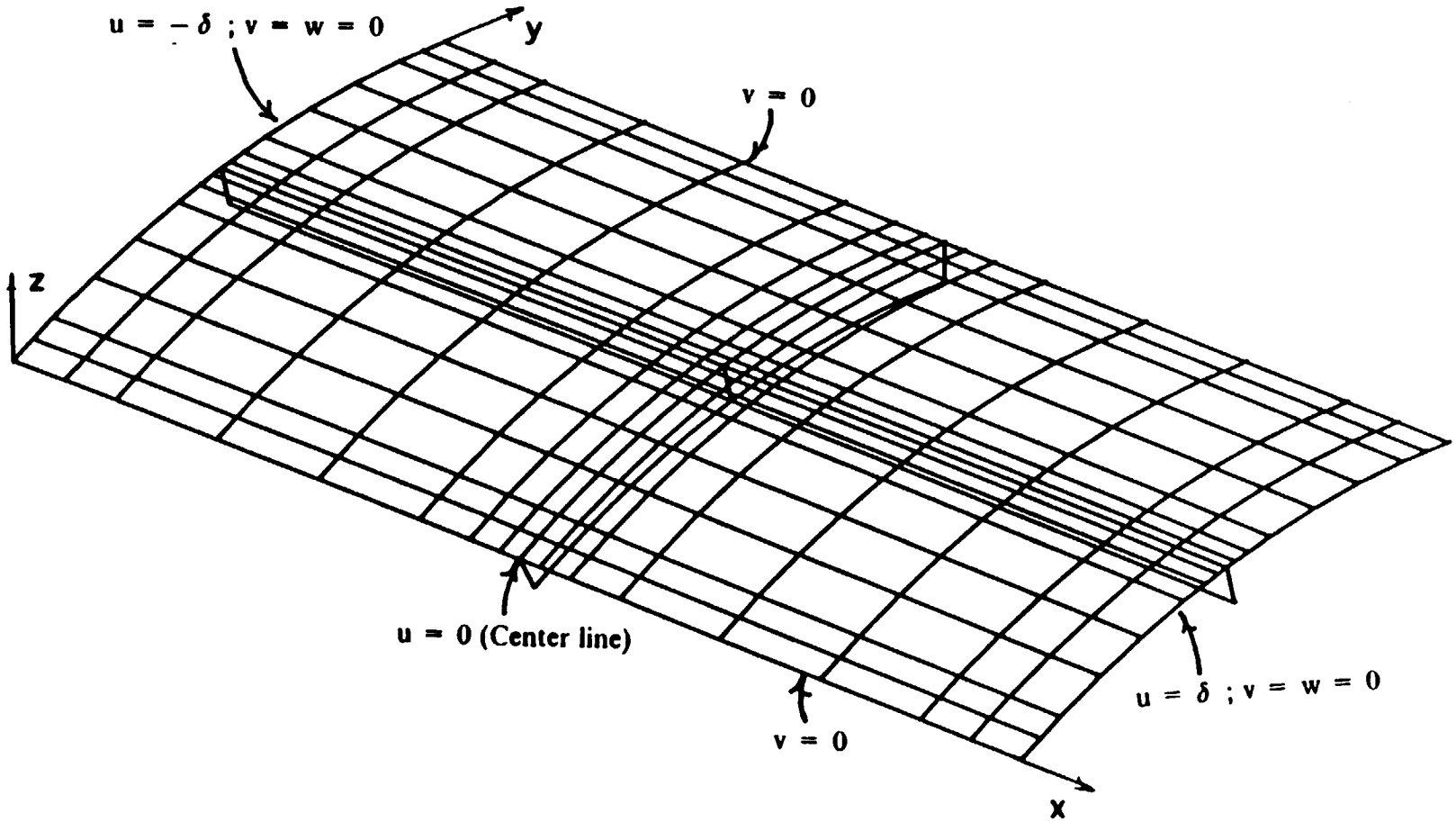

Figure 57. Unit cell finite element mesh and boundary conditions of the LWTR stress analysis of the axial and ring stiffened shell (256 elements).

4.0″ for a 0.15″ laminate, and 6.0″ for a 0.30″ laminate. Therefore, under the action of compressive load and internal pressure the stiffeners act to decrease the transverse displacements at the stiffener intersection, but only when the stiffeners are sufficiently deep compared to the laminate thickness do the shell transverse displacements away from the stiffener intersection exceed those at the stiffener intersection.

This study of the transverse displacement field trends has yielded some interesting results. The shell laminate layup will have a major factor on the transverse displacement field. Changing the stiffener height, shell geometry, shell radius, and shell laminate thickness all have a major impact on the structural response of the stiffened shells. A geometric nonlinear analysis does not yield major changes in the displacement field for compressive loading, but nonlinearity is significant when pressure is added to the loading. The geometry of the geodesically stiffened shell has a significant impact on the displacement field. When subjected to combined compression and internal pressure the transverse displacements of the shell away from the stiffener intersection do not exceed those at the stiffener intersection until deep stiffeners, a large radius, or an axial/ring stiffened structure are used. One of the nice features in using the LWTR finite element code to conduct this design analysis is that it is fairly simple and quick to generate new models by changing the cell geometry or the stiffener parameters. This is not true for the Testbed finite element code where a more time consuming effort is needed to generate models that change shell geometries and/or stiffener heights.

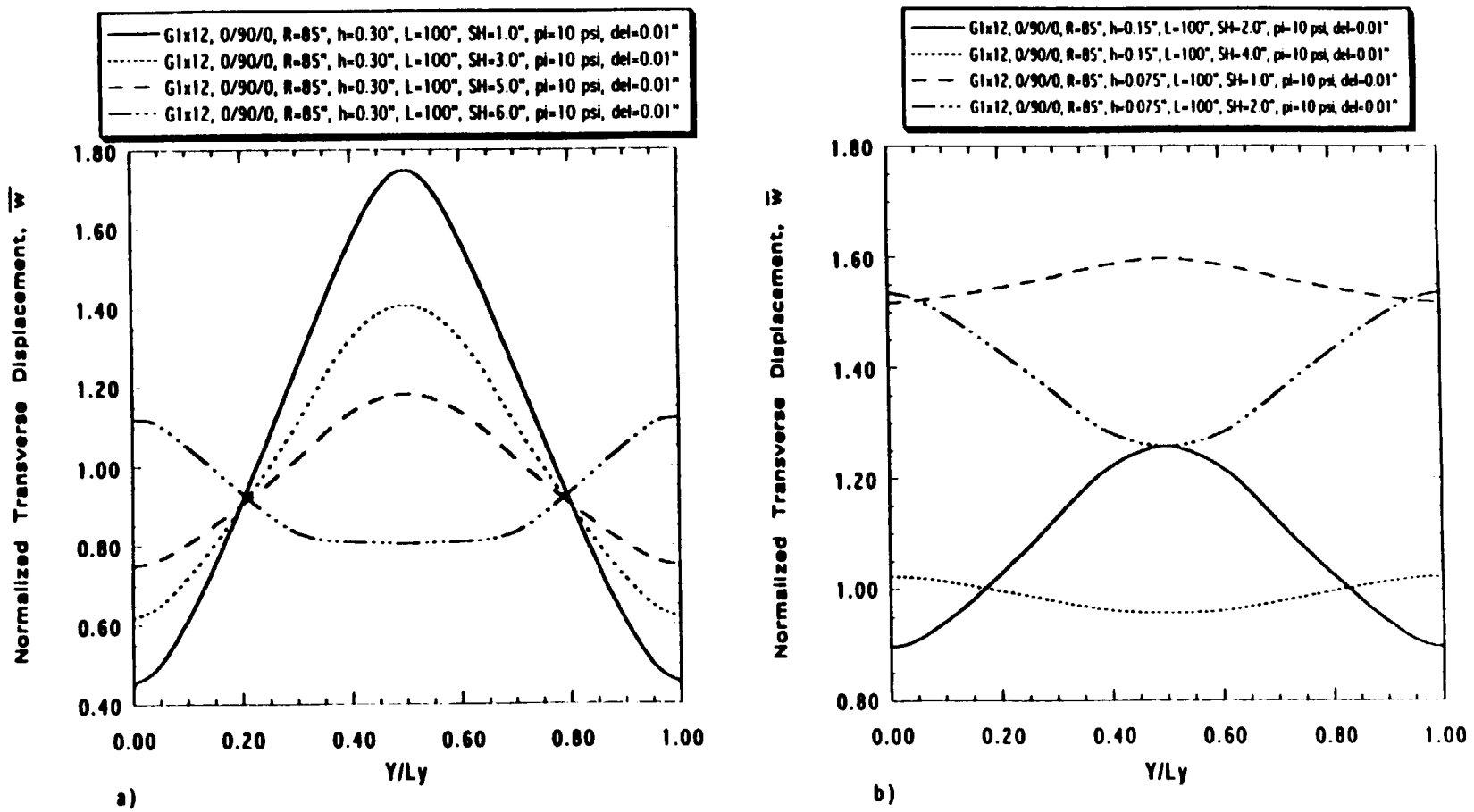

Figure 58. Nondimensional transverse displacements for geodesically stiffened shells under combined loading: a) laminate thickness = 0.30"; b) laminate thickness = 0.15" and 0.075".

5.5 Detailed Stress Study

The results presented in this section will focus on interlaminar stresses, but a few examples of the in-plane stresses σ_{xx} and σ_{xy} over the region of the entire shell will also be presented. Interlaminar stresses in the geodesic shells have never been studied in detail before. The interlaminar stresses over the entire shell structure for a few specific cases will be presented. This will help to determine the regions of peak interlaminar stresses and the nature of the stress distribution over the entire region. The interlaminar stresses at the critical regions, probably near the stiffener intersection, will be studied. The interlaminar stress distribution through the thickness at the critical regions will be studied. The effects of the shell laminate layups, laminate thickness, pressure loading, stiffener height, shell radii, cell geometry, and geometric nonlinearity on the interlaminar stresses will presented. The base line design used in this study is a [0/90/0] 1x12 geodesically stiffened shell with a shell radius of 85" and 1.0" internal orthotropic stiffeners. The base line laminate thickness used here is 0.30". The loadings considered in these analyses are applied compressive end loads generated through applied end displacements of 0.01" on each edge (x=0, Lx) and combined compressive loads and internal pressure (10 psi). Some of the more interesting interlaminar stress results are presented in this work. The stresses are nondimensionalized in this study using the following expression:

$$\bar{\sigma} = \frac{\sigma h L}{\bar{N}_x R} \tag{5.5}$$

Here $\bar{\sigma}$ is the nondimensional stress, σ is the generated stress, h is the total laminate thickness, $\bar{N}_x$ is the applied load, R is the shell radius, and L is the shell length.

5.5.1 In-Plane Stress Study

The nondimensional in-plane stresses, $\bar{\sigma}_{xx}$ and $\bar{\sigma}_{xy}$, will be discussed in this section. The in-plane stress, $\bar{\sigma}_{xx}$, of the inner layer for a [0/90/0] 1x12 geodesically stiffened shell with 1.0" internal stiffeners subjected to an applied end load of 0.01" is shown in Figure 59. The peak in-plane stresses, $\bar{\sigma}_{xx}$, occur at the boundaries x = 0, L_x and also at the stiffener intersection $x = \frac{L_x}{2}$, $y = \frac{L_y}{2}$. The in-plane stresses, $\bar{\sigma}_{xx}$, are the largest of the six stresses and thus are likely to be the primary contributing stresses to cause failure. By viewing Figure 59 it can be said that failure would most likely occur at the boundaries (x = 0, Lx) or at the stiffener intersection. Figure 60 is a plot of $\bar{\sigma}_{xx}$ over the stiffened shell structure for the outer layer of a [0/90/0] 1x12 geodesically stiffened shell with 1.0" internal orthotropic stiffeners subjected to a compressive end load. The stress distribution, $\bar{\sigma}_{xx}$, over the surface of the shell in the top layer as shown in Figure 60 yields a different stress field shape than that generated in the inner layer shown in Figure 61. The stresses in the outer layer peak at the boundary corners and at the stiffener intersection. As can be seen from Figures 59 and 60, the in-plane stresses, $\bar{\sigma}_{xx}$, for the inner layer are more uniformly distributed, particularly at the boundaries than the in-plane stresses for the outer layer. One possible explanation for this phenomena is that the stiffeners are attached to the inner layer and this reduces the bending of the inner layer and in addition some of the load is carried by the stiffeners. This results in more uniform stresses in the inner layer. The influence of the stiffeners on the outer layers are evidenced by the fact that the in-plane stresses are lower at the corners of the boundaries and at the stiffener intersection. However, at the center of the shell boundaries the influence of the stiffeners is not as pronounced and more bending occurs. This results in

the outer layer carrying more load at these locations which produces larger compressive stresses.

The in-plane stress results, $\bar{\sigma}_{xx}$, for a combined loading on a [0/90/0] 1x12 geodesically stiffened shell are shown in Figures 61 and 62. The addition of 10 psi internal pressure to the geodesically stiffened shell produces significant changes in the stress distribution, $\bar{\sigma}_{xx}$, in the inner layer shown in Figure 61 when compared with the inner layer for compressive loading shown in Figure 59. As the internal pressure is increased these differences between pure compression and combined loading will become much larger. The pressure produces a much wider variation of the in-plane stresses and also changes the peak stresses at the edges and the stiffener intersection. The in-plane stress at the stiffener intersection for the inner layer subjected to combined loading is reduced by 52% from the inner layer stress generated from compressive loading. Figure 62 shows the stress distribution, $\bar{\sigma}_{xx}$, for the outer layer for the base line design. The boundaries at x = 0, Lx are fairly stiff having v = w = 0 boundary conditions at these locations and thus the addition of internal pressure results in large compressive bending stresses at the x boundaries. Away from the boundaries the pressure tends to reduce the compressive stresses by as much as 84% at the stiffener interior. Thus, adding pressure has a significant influence on the in-plane stresses of the shell laminate.

A plot of the shear stress, $\bar{\sigma}_{xy}$, in the inner layer for the base line design subjected to combined loading is shown in Figure 63. The shear stresses, $\bar{\sigma}_{xy}$, yield a skew-symmetric nature with the value of the shear stress being 0 at the stiffener intersection. The results for the application of compressive loading yield the same general shape as the results for combined loading, but the values of the stresses are about a factor of 10 smaller. Those results are not included here.

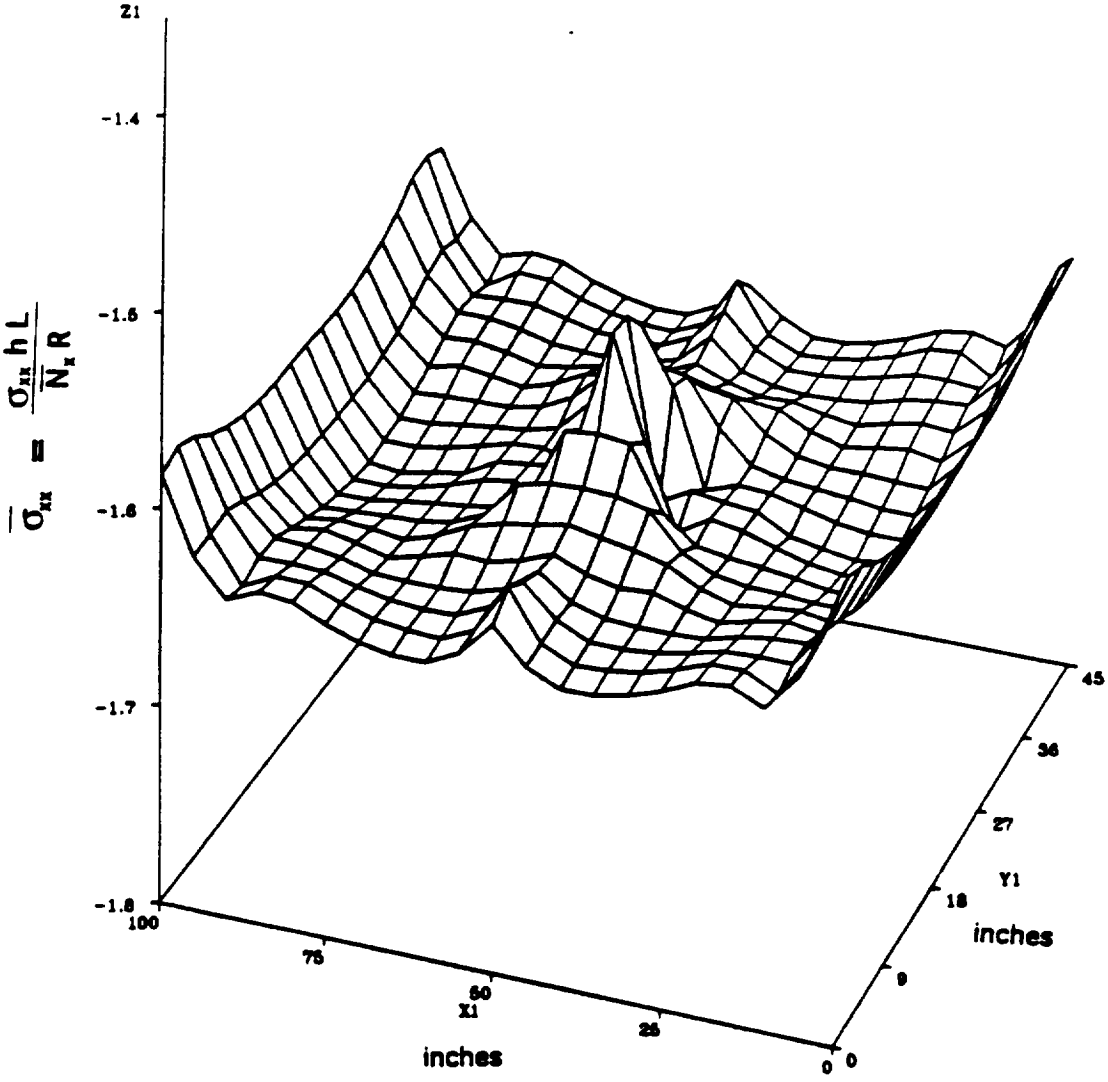

Figure 59. Surface plot of $\bar{\sigma}_{xx}$ for the inner layer of a [0/90/0] 1x12 geodesically stiffened shell under compressive loading.

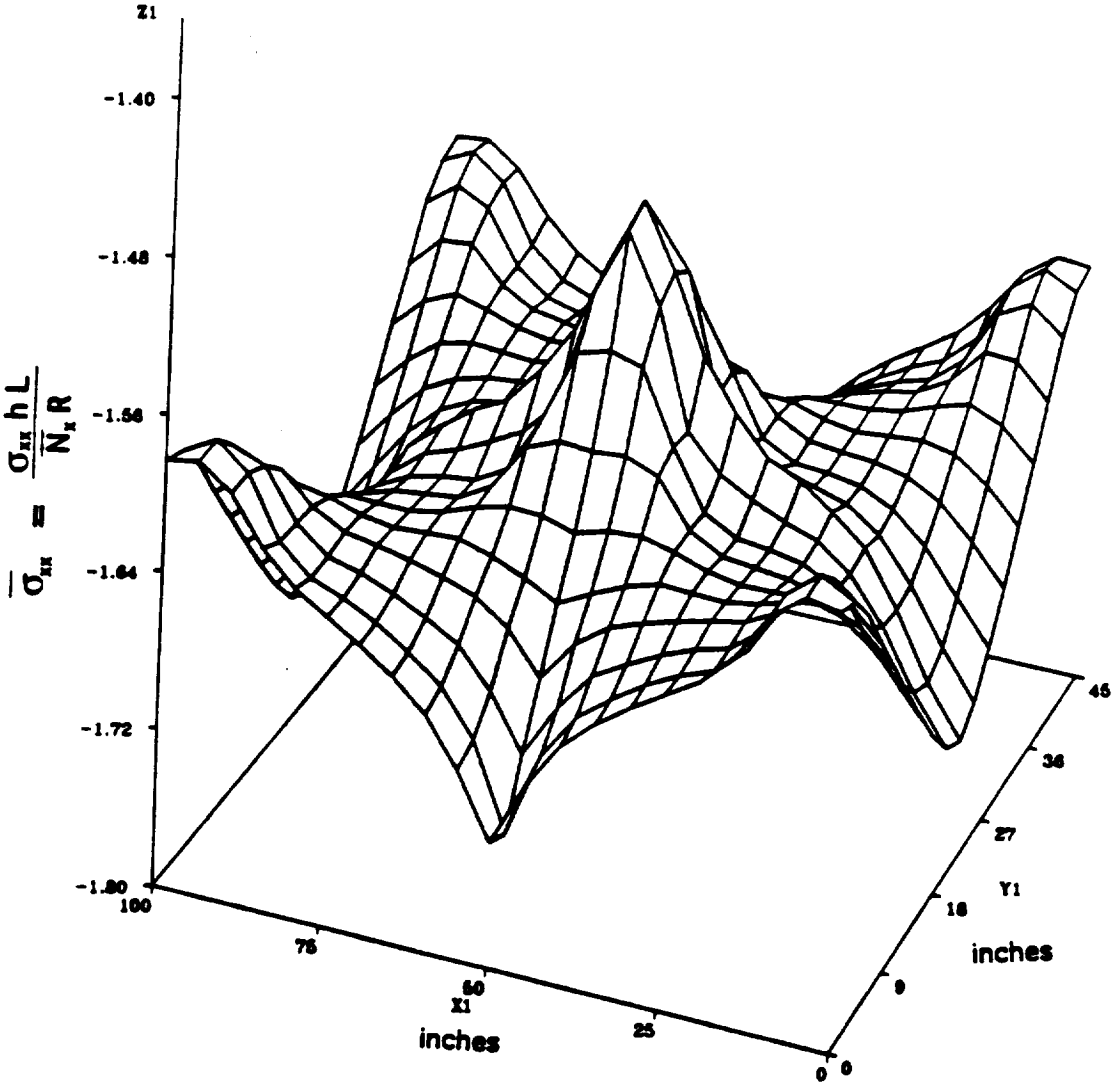

Figure 60. Surface plot of $\bar{\sigma}_{xx}$ for the outer layer of a [0/90/0] 1x12 geodesically stiffened shell under compressive loading.

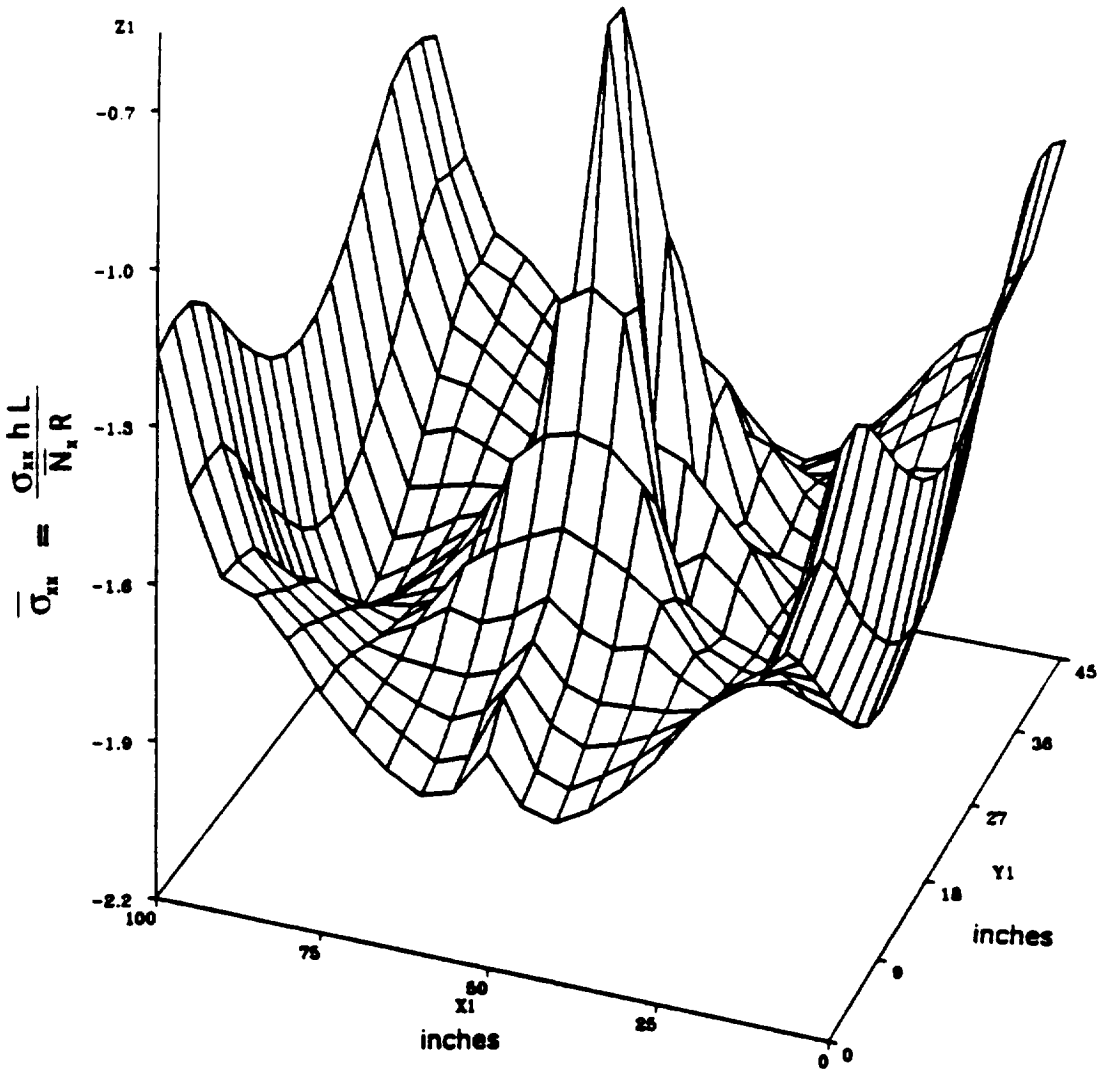

Figure 61. Surface plot of $\bar{\sigma}_{xx}$ for the inner layer of a [0/90/0] 1x12 geodesically stiffened shell under combined loading.

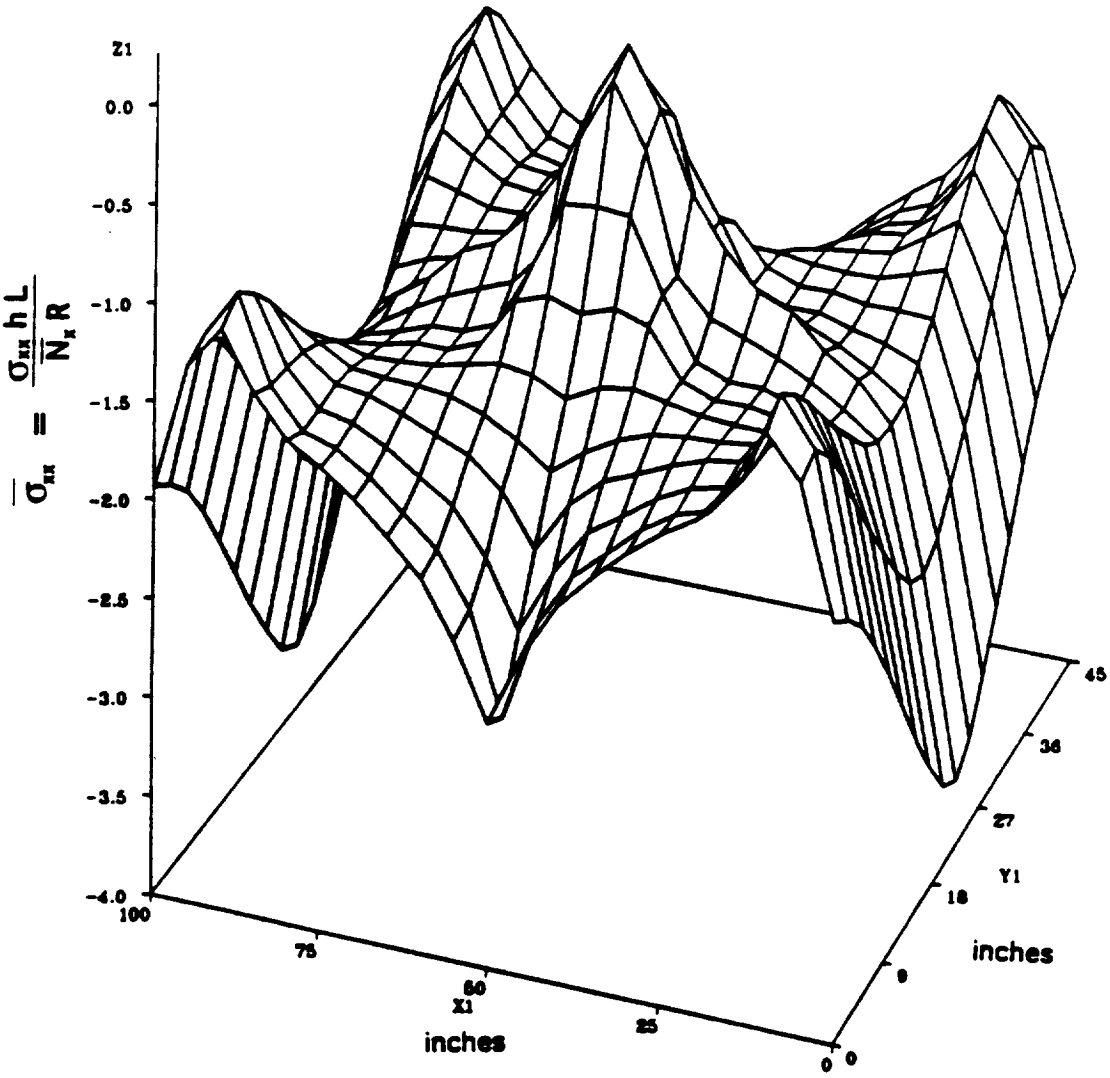

Figure 62. Surface plot of $\bar{\sigma}_{xx}$ for the outer layer of a [0/90/0] 1x12 geodesically stiffened shell under combined loading.

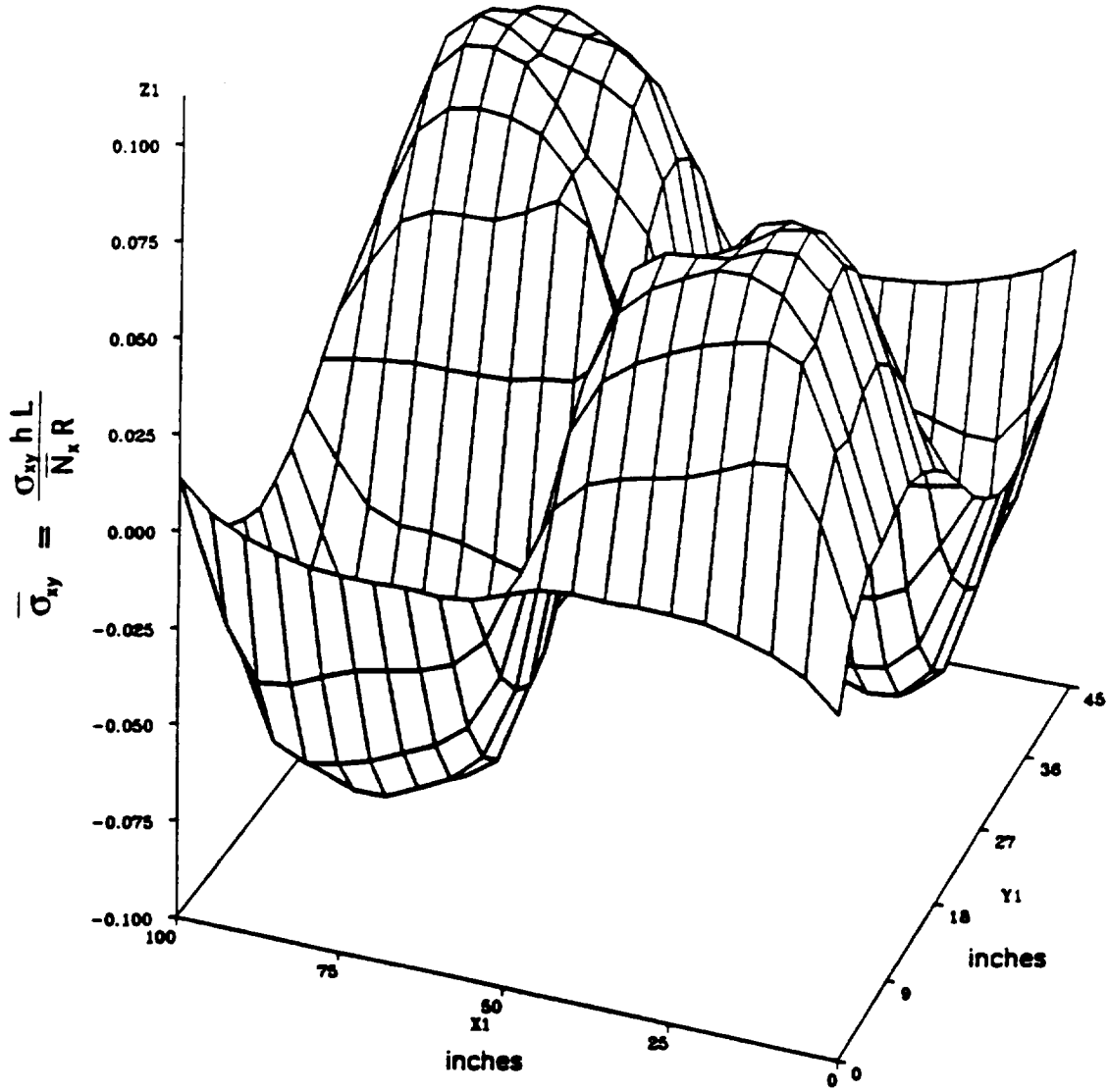

Figure 63. Surface plot of $\bar{\sigma}_{xy}$ for the inner layer of a [0/90/0] 1x12 geodesically stiffened shell under combined loading.

5.5.2 Interlaminar Normal Stress Study

The distribution of the interlaminar normal stress, $\bar{\sigma}_{zz}$, over the shell region for the outer layer of the base line design subjected to an applied compressive end load is shown in Figure 64. As can be seen, the interlaminar normal stresses peak at the x boundaries and also at the stiffener intersection. Along the center line $y = \frac{L_y}{2}$ away from the boundaries the interlaminar normal stresses are larger than those stresses over the remainder of the shell away from the surface. This indicates that the stiffener intersection has an influence on the interlaminar normal stresses along the line $y = \frac{L_y}{2}$. This could be due to the fact that the transverse displacements do peak at the stiffener intersection. Adding internal pressure to the preexisting compressive load yields an interlaminar normal stress distribution in the outer layer as described in Figure 65. Here the interlaminar normal stresses are significantly greater than for the case of end compression. The general pattern of the stress distribution is the same as that for compressive end loading only. The interlaminar normal stresses peak at the stiffener intersection and the interlaminar normal stresses being largest along the line $y = \frac{L_y}{2}$. Pressure does have a significant influence on the interlaminar normal stresses by increasing the interlaminar normal stresses by almost a factor of 4.

Nondimensional interlaminar normal stresses near the stiffener intersection through the thickness of the shell laminate for various geometries and loadings are presented in this section. The interlaminar normal stresses generated via combined loading are 400% larger than the interlaminar normal stresses generated from compressive loading and thus only combined loading conditions are studied in this section. Figure 66 is a plot of the interlaminar normal stresses, $\bar{\sigma}_{zz}$, near the stiffener intersection for 1x12 geodesically stiffened shells having 1.0" internal orthotropic stiffeners for various shell

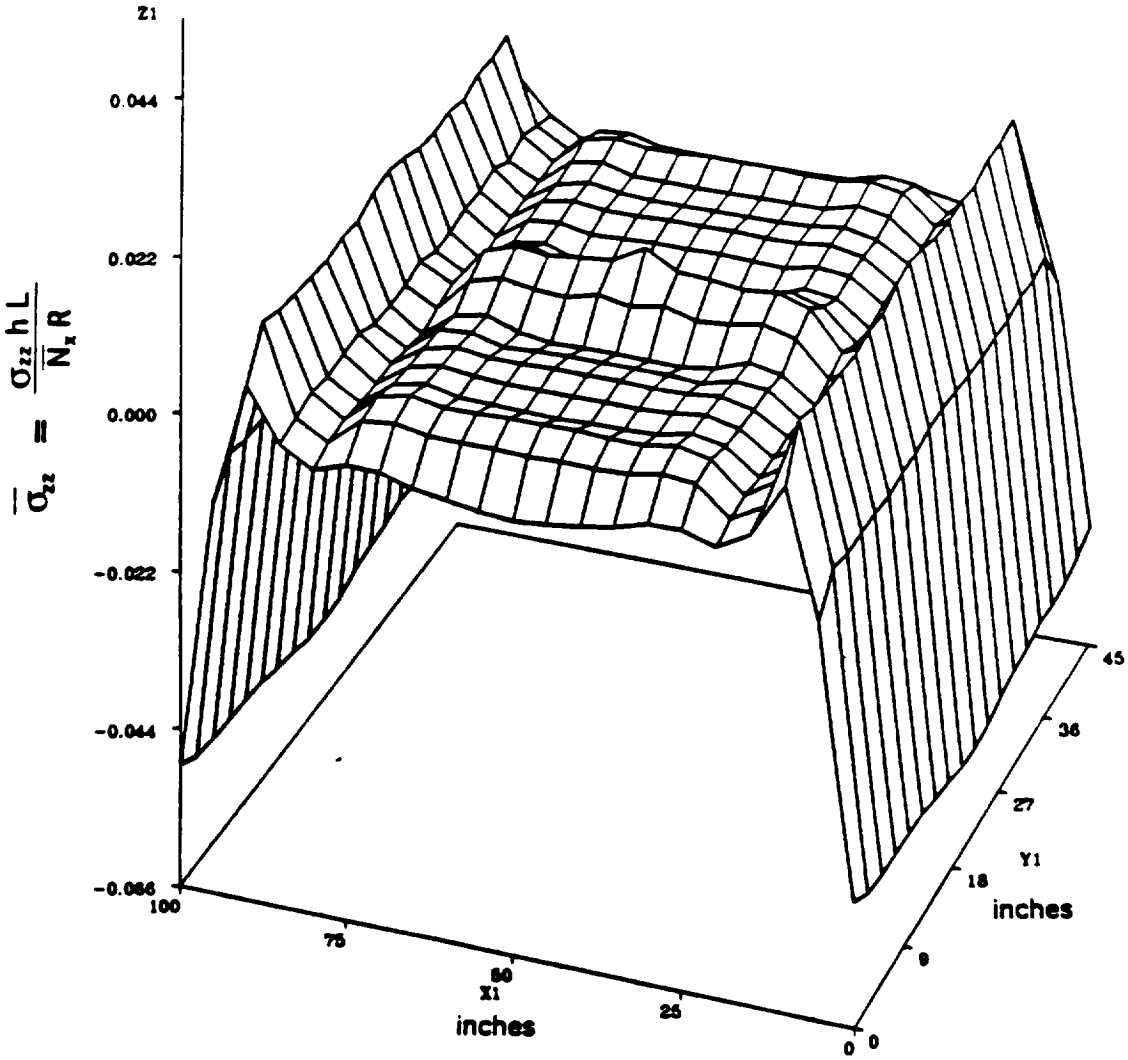

Figure 64. Surface plot of $\bar{\sigma}_{zz}$ for the outer layer of a [0/90/0] 1x12 geodesically stiffened shell under compressive loading.

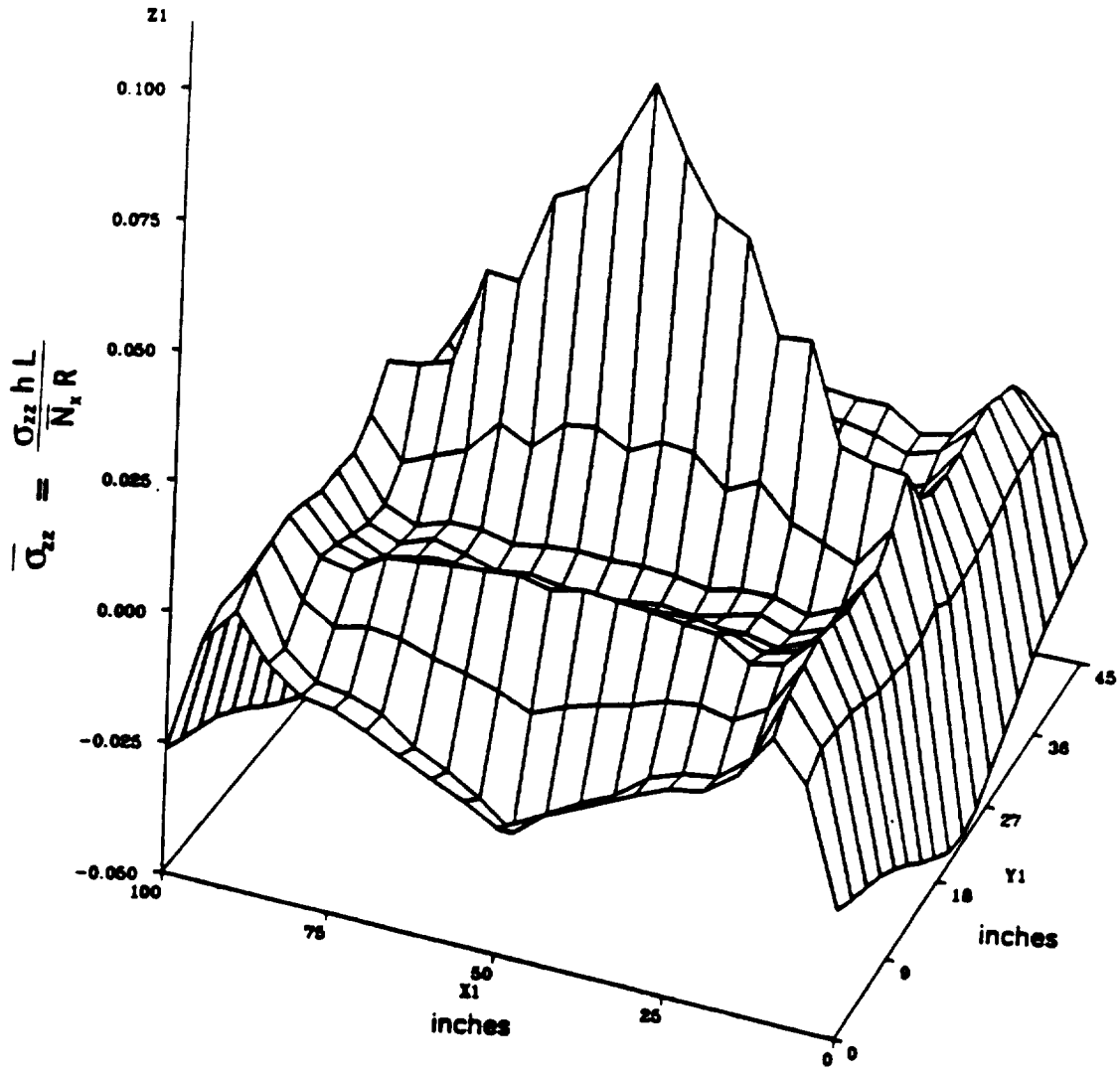

Figure 65. Surface plot of $\bar{\sigma}_{zz}$ for the outer layer of a [0/90/0] 1x12 geodesically stiffened shell under combined loading.

laminates subjected to combined loading. Figure 66 shows that the laminate stacking sequence has a large impact on the interlaminar normal stress. The $[60/-60/0/-60/60]$ and the $[-45/45/90/0]_S$ layups show the largest interlaminar normal stresses. For example, the maximum nondimensional interlaminar normal stresses in the $[60/-60/0/-60/60]$ layup is 66% larger than the maximum nondimensional interlaminar normal stress in the $[45/90/0]_S$. The order of decreasing maximum nondimensional interlaminar normal stress stresses in the laminates are $[30/-30/0/-30/30]$, $[-45/45/90/0]_S$, $[45/-45/45/-45]$, $[60/-60/0/-60/60]$, $[0/90/0]$, and $[45/90/0]_S$. Hence, laminates such as the $[45/90/0]_S$, $[0/90/0]$, and $[60/-60/0/-60/60]$ are preferable for use in keeping the $\bar{\sigma}_{zz}$ stresses from becoming significantly large.

The effects of conducting a geometrically nonlinear analysis on the stresses, $\bar{\sigma}_{zz}$, for a combined loading is shown in Figure 67. The nondimensional interlaminar normal stresses for the geometrically nonlinear analysis are 47.1% less than the stresses developed from the linear analysis. From the displacement field study shown in Figure 54b the nonlinear analysis generates smaller displacements than the linear analysis and obviously this results in lower strains and then subsequently lower stresses. Thus, when pressure loading is included on the structure a geometrically nonlinear analysis will yield significantly different nondimensional interlaminar normal stresses. The geometrically nonlinear analysis softens the structure and this reduces the displacements and subsequent stresses.

The effect of increasing the stiffener height on the nondimensional interlaminar normal stress for combined loading is shown in Figure 68. The nondimensional interlaminar normal stresses show a uniform decrease as the stiffener height is increased. The maxi-

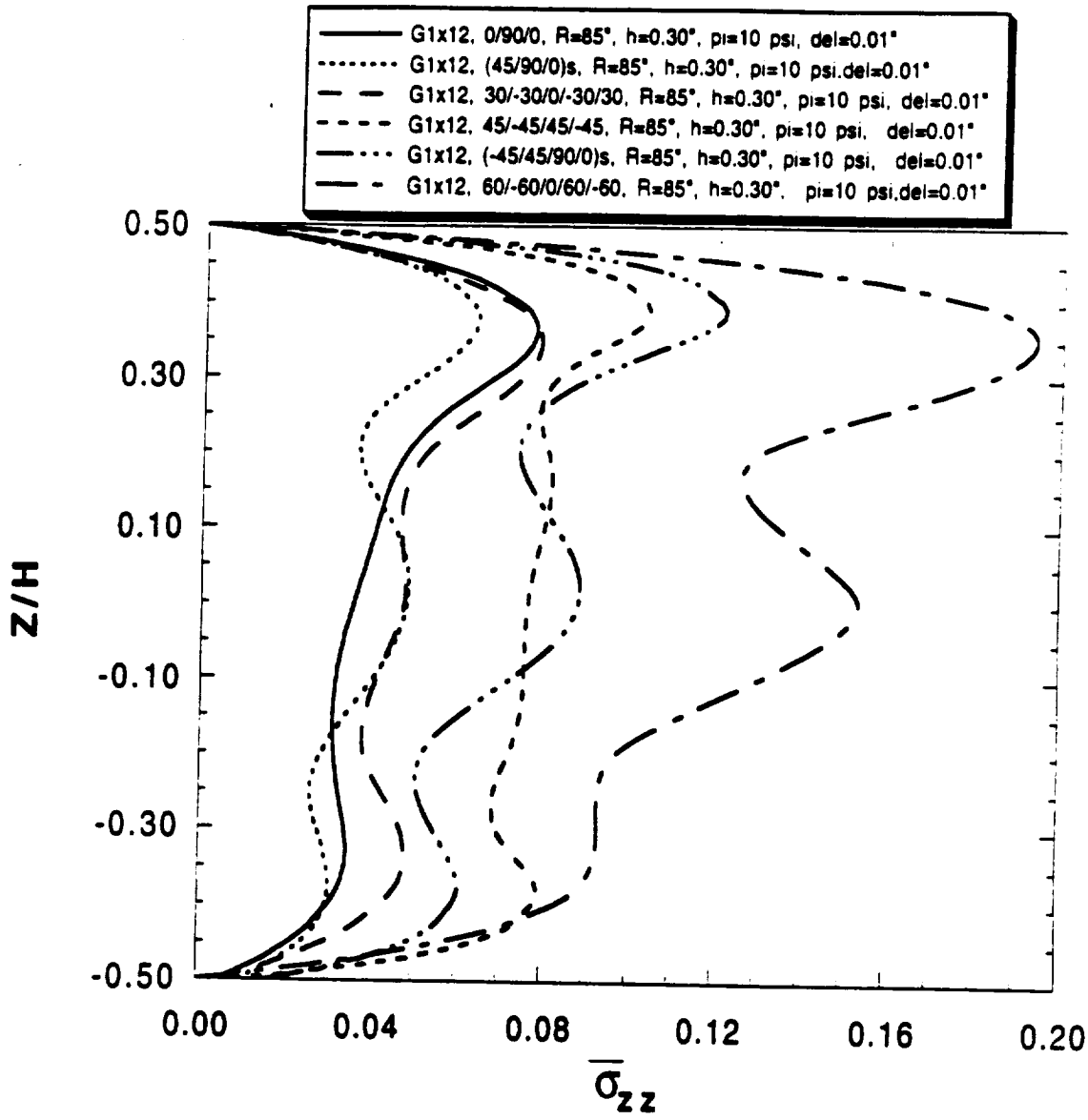

Figure 66. Through-the-thickness distribution of $\overline{\sigma}_{zz}$ for G1x12 shell near the stiffener intersection for various shell laminates under combined loading.

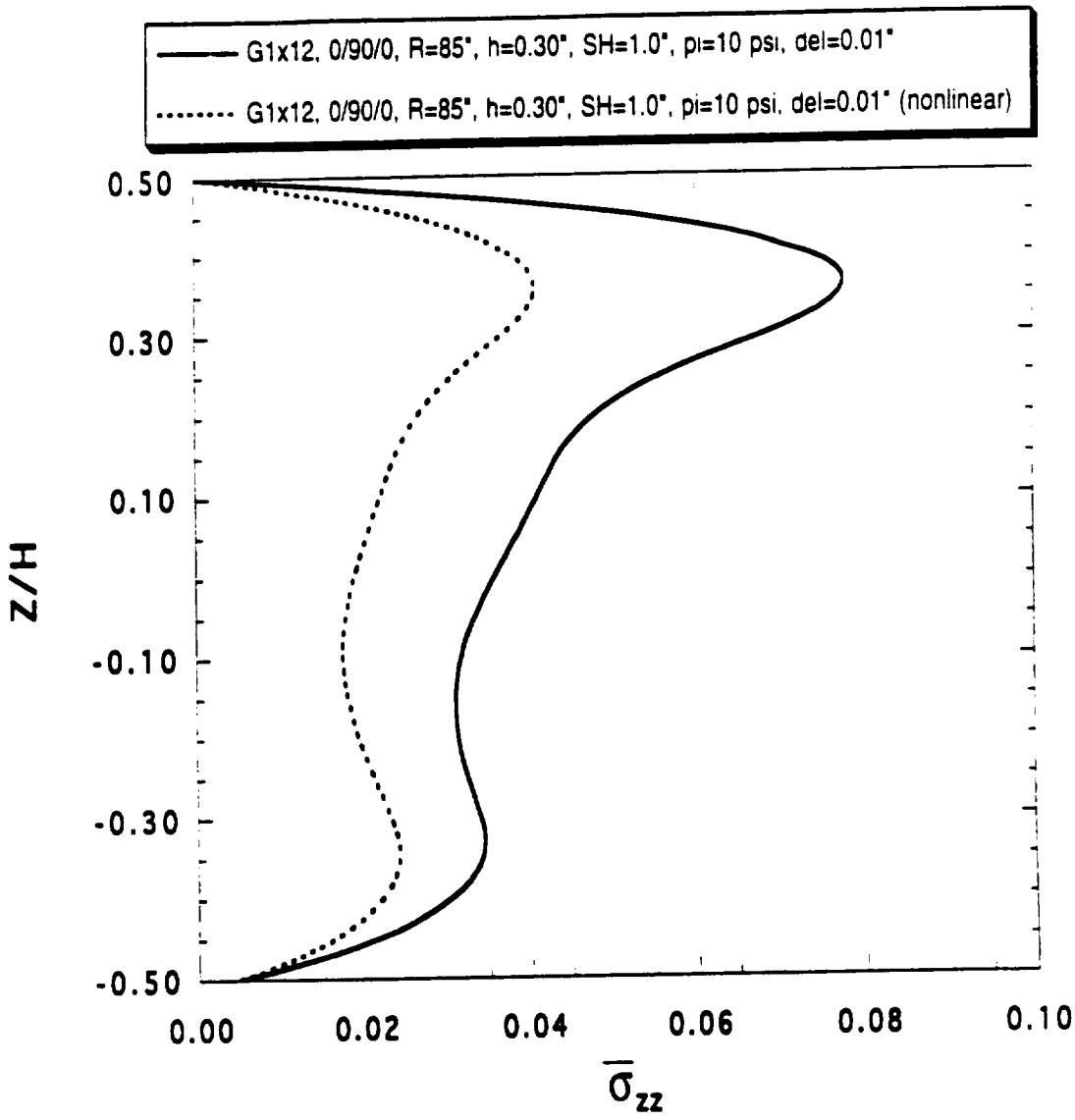

Figure 67. Through-the-thickness distribution of $\overline{\sigma}_{zz}$ for G1x12 shell near the stiffener intersection for linear and geometrically nonlinear analyses under combined loading.

mum differences in $\bar{\sigma}_{zz}$ between the 1″ and 2″, 3″, 4″, and 5″ stiffeners are 6.6%, 18.4%, 27.9%, and 37.5% respectively. The interlaminar normal stress decreases as the stiffener height increases as expected because the bending stiffness of the stiffeners increases as a function of the cube of the stiffener height. This increase in bending stiffness tends to decrease the transverse displacements and consequently the interlaminar normal stress. It is interesting to note that the height of the stiffener does not affect the overall shape of the stress through the thickness.

The effect of changing the cell geometry on the nondimensional interlaminar normal stress for [0/90/0] geodesically stiffened shells subjected to combined loading is shown in Figure 69. Geodesic cell geometries of 1x10, 1x12, 1x14, and 1x16 are considered in this analysis. As can be seen from Figure 69 and the displacement results shown in Figure 51, increasing the number of cells around the circumference causes the shells to become significantly stiffer because the number of stiffeners in the structure is increased. This lowers both the transverse displacements and the interlaminar normal stresses. For example, as the cell geometry is increased from 1x10 to 1x12, 1x14, and 1x16 the nondimensional interlaminar normal stresses are reduced 35%, 51%, and 85% respectively.

Shown in Figure 70 are the nondimensional interlaminar normal stress results for increasing the shell radius for [0/90/0] shells subjected to combined loading. The shell radii considered here are 85″, 170″, 255″. The maximum difference in nondimensional interlaminar normal stress is 56% when increasing the shell radius 2 times from 85″ to 170″ and the difference is 88% when increasing the shell radius 3 times from 85″ to 255″. As can be seen there are differences in the nondimensional interlaminar normal stress distribution. From the results shown in Figure 70 and the transverse displacement results of Figure 55b it is observed that as the shell radius is increased the influence of the

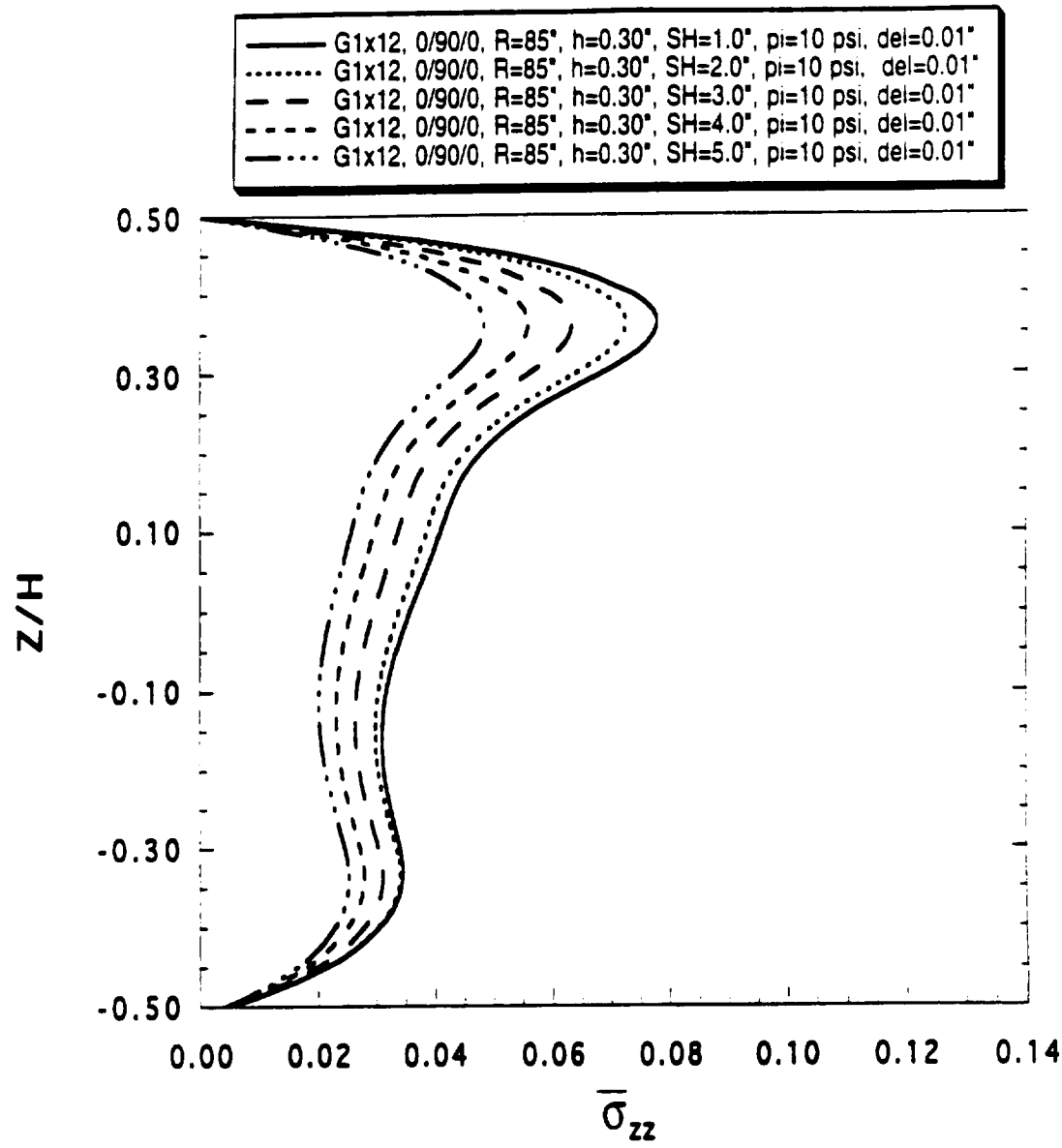

Figure 68. Through-the-thickness distribution of $\bar{\sigma}_{zz}$ for G1x12 shell near the stiffener intersection for *varying* stiffener heights under combined loading.

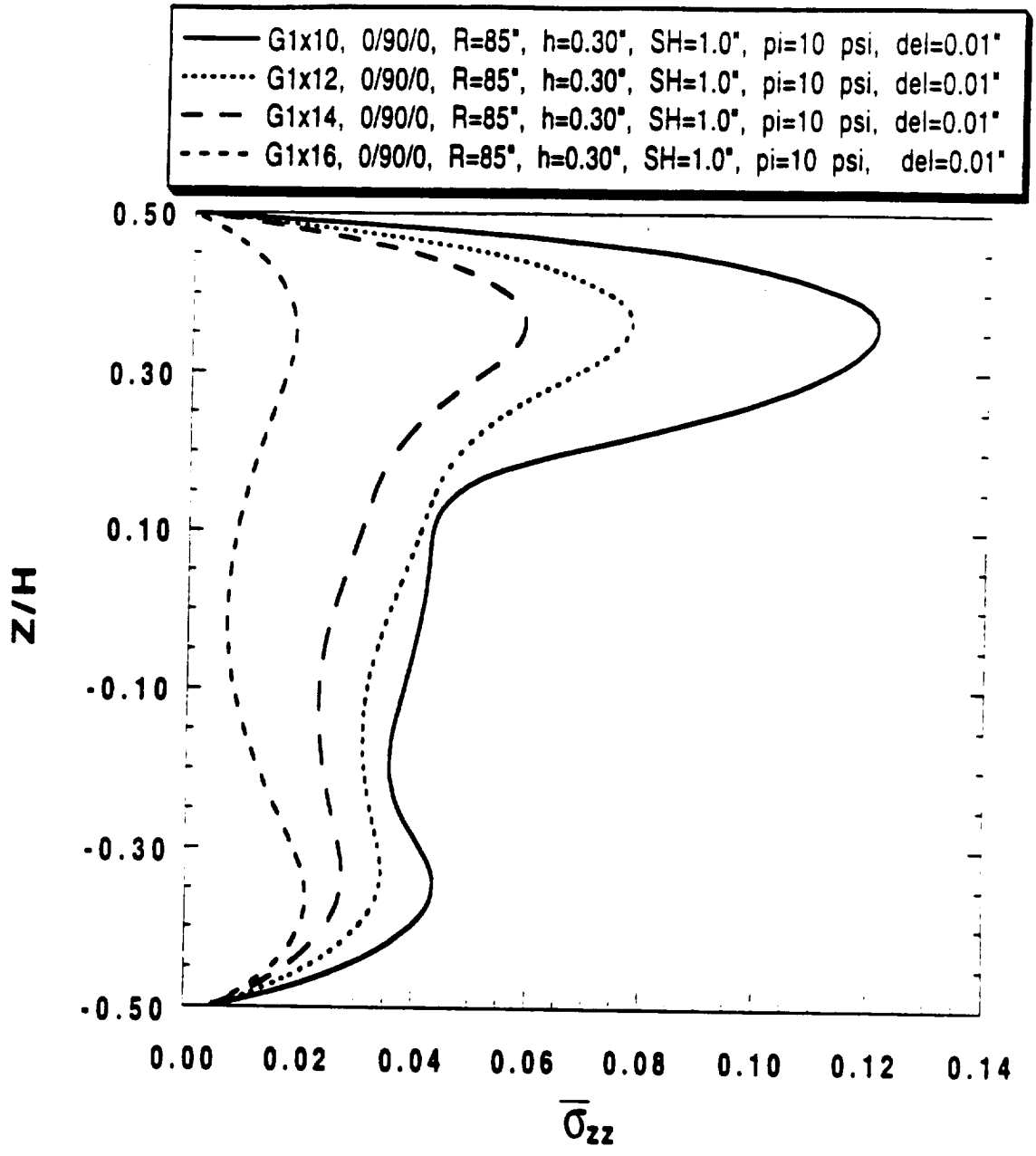

Figure 69. Through-the-thickness distribution of $\overline{\sigma}_{zz}$ for G1x12 shell near the stiffener intersection for varying the cell geometry under combined loading.

stiffener on the displacement and interlaminar normal stress fields increases. This is especially evident when pressure is applied to the shell structure. Moreover, as the shell and stiffener radius are increased and the shell thickness remains constant, the ratio of the stiffener stiffness to the shell stiffness increases and the stiffeners' influence on the response of the shell is increased.

The nondimensional interlaminar normal stresses for [0/90/0] 1x12 geodesically stiffened shells subjected to combined loading for variations in the shell laminate thickness are shown in Figure 71. As expected, changes in shell thickness have a direct effect upon the interlaminar normal stresses. The nondimensionalized interlaminar stresses are a strong function of the shell laminate thickness. The maximum differences in nondimensional interlaminar normal stresses between the 0.15" and the 0.30", 0.45", and 0.60" laminates are 78%, 89%, and 97% respectively. The bending stiffness of the shell is a function of the laminate thickness cubed. The smaller the laminate thickness the more the shell will deflect under pressure loading resulting in larger stresses.

The nondimensional interlaminar normal stresses for a 1x12 geodesically stiffened shell, 1x12 axial/ring stiffened shell, and an unstiffened shell are shown in Figure 72. The results presented here are for [0/90/0] shells with 1.0" internal orthotropic stiffeners subjected to combined loading. As can be seen the nondimensional interlaminar normal stresses generated in the geodesically stiffened shell is 67.8% larger than those generated in the axial/ring stiffened shell and 81.7% larger than those generated from the unstiffened shell. From Figures 56b and 72 it becomes apparent that the geodesic stiffeners tend to push the stiffener intersection outward which results in larger transverse displacements and stresses near the stiffener intersection than those generated by the axial/ring stiffened shell system or the unstiffened shells. Apparently, the geodesic

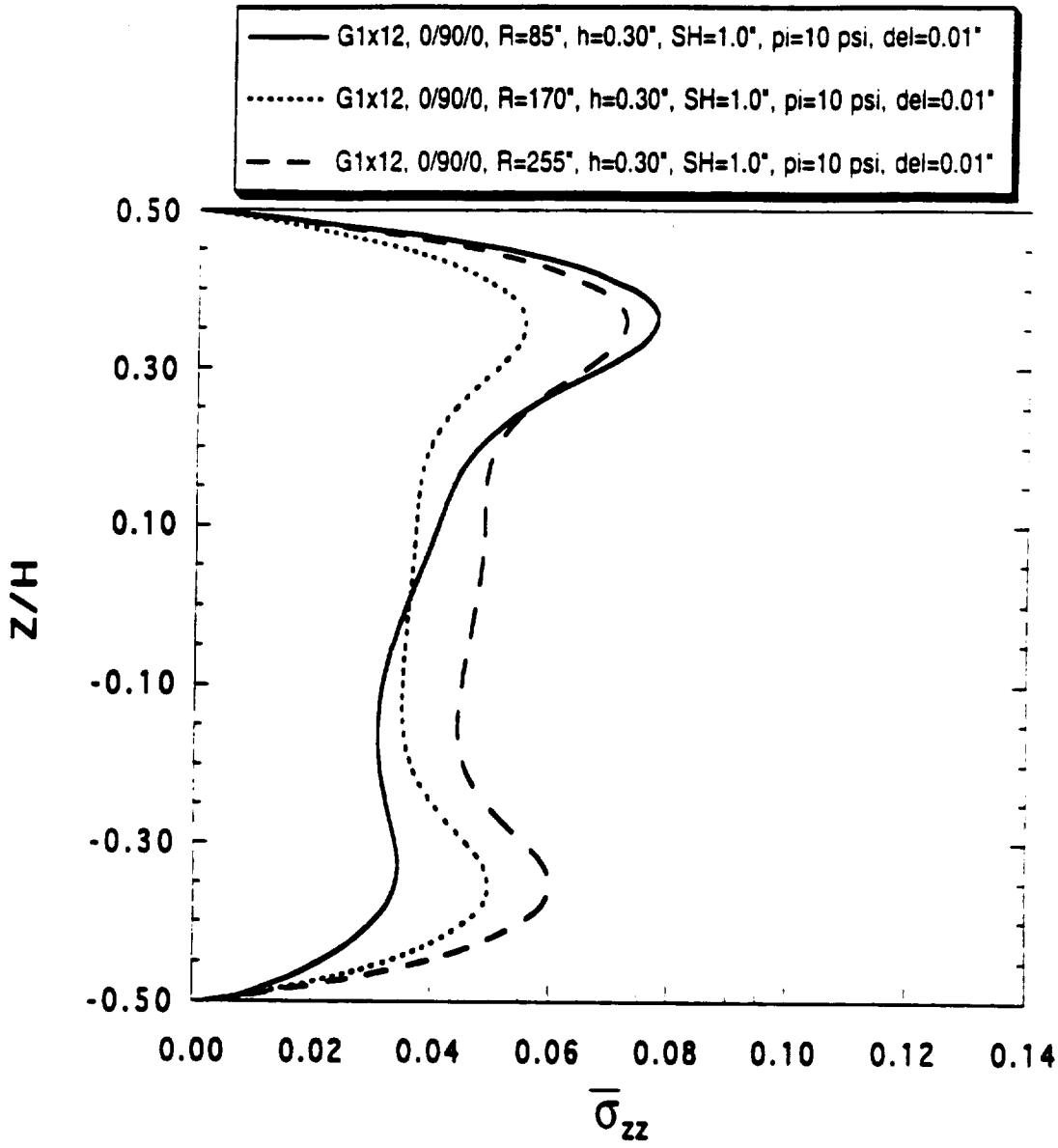

Figure 70. Through-the-thickness distribution of $\overline{\sigma}_{zz}$ for G1x12 shell near the stiffener intersection for increasing shell radii under combined loading.

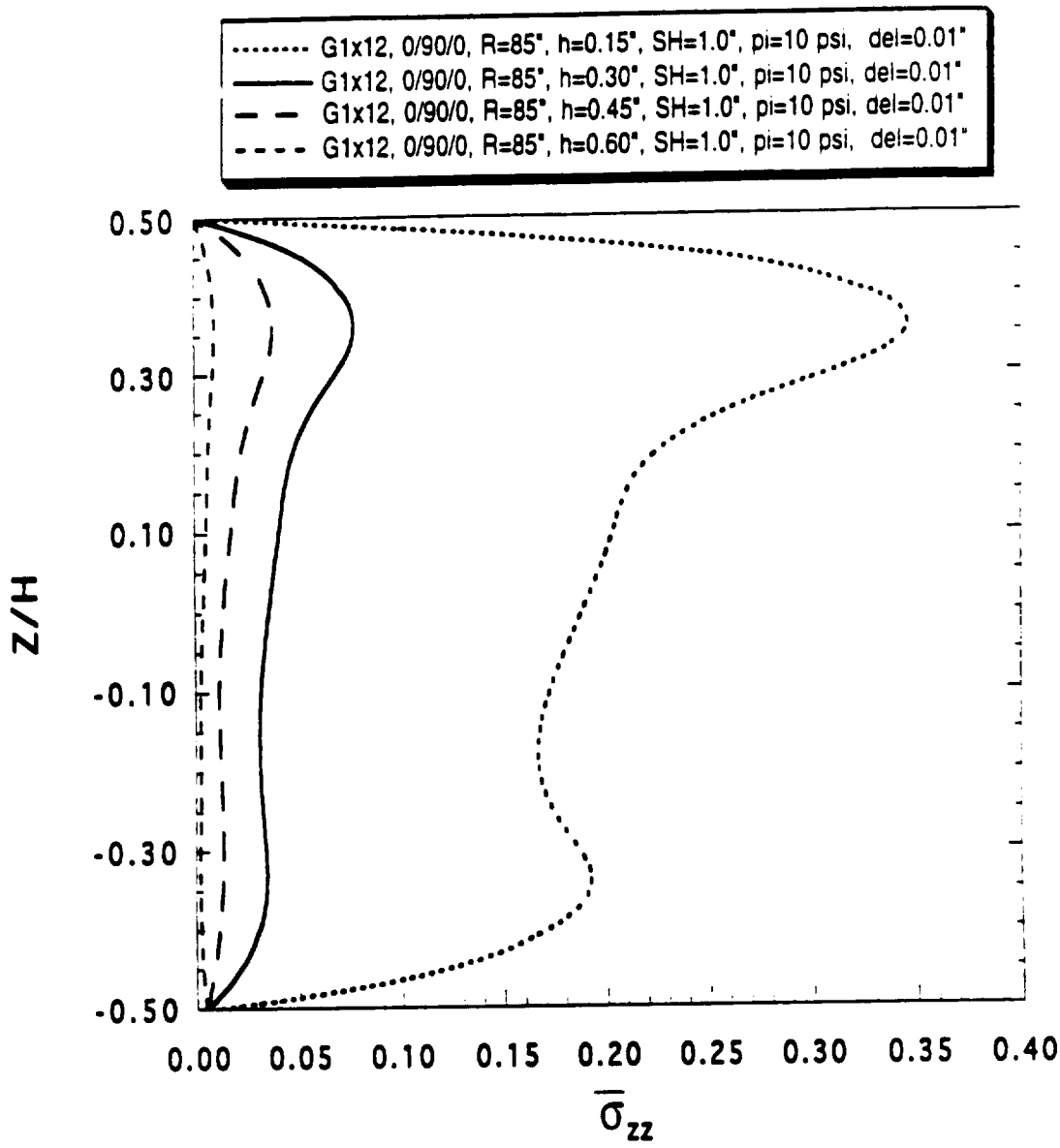

Figure 71. Through-the-thickness distribution of $\overline{\sigma}_{zz}$ for G1x12 shell near the stiffener intersection for increasing shell laminate thickness under combined loading.

stiffeners at the stiffener intersection are constrained so that the u and v displacements at that location are 0 because of symmetry and symmetric loading and boundary conditions. However, because of this constraint the stiffeners do exhibit large displacements in the transverse direction due to the compliance of the stiffener intersection. In addition, the distribution of the interlaminar normal stresses for the axial/ring stiffened shell and the geodesically stiffened shell are different. While both stiffened shells exhibit peak stresses in the bottom (inner) layers of the laminate where the stiffeners are attached, the axial/ring stiffened shell does not exhibit another peak in the interlaminar normal stress in the top (outer) layers as does the geodesically stiffened shells. Therefore, it can be concluded that because the geodesically stiffened shells produce significantly more displacements at the stiffener intersection than the axial/ring stiffened results as seen in Figure 56b this results in larger interlaminar normal stresses through the entire shell laminate for the geodesically stiffened shells. The axial/ring stiffened shells are very stiff at the stiffener intersection which results in smaller displacements at the stiffener intersection than away from the intersection (see Figure 56b). Therefore, the influence of the axial/ring stiffened structure is to cause peak interlaminar normal stresses in the inner layers of the shell, but because the transverse displacements away from the stiffener intersection are larger than at the stiffener joint the influence of the axial/ring stiffeners does not extend to the outer layers of the shell.

The interlaminar normal stresses are influenced by the laminate stacking sequence, geometric nonlinearity, stiffener height, cell geometry, shell radius, shell laminate thickness, and the type of shell structure (geodesic or axial/ring stiffened). The shape and magnitude of the nondimensional interlaminar normal stress is definitely influenced by the laminated stacking sequence. Changing the shell geometry, shell laminate thickness, shell radius, and conducting a geometrically nonlinear analysis all have an impact in the

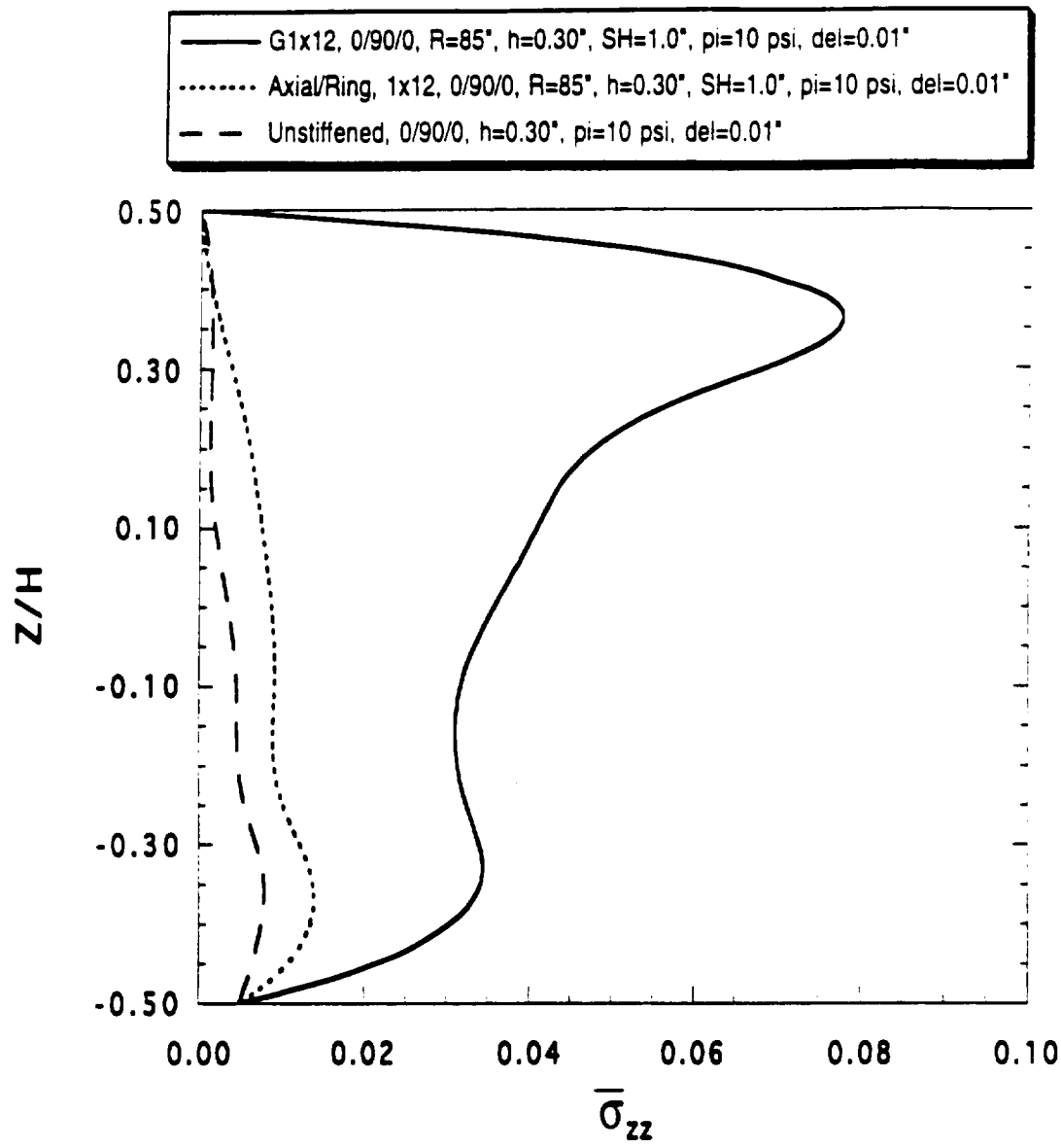

Figure 72. Through-the-thickness distribution of $\overline{\sigma}_{zz}$ for G1x12 stiffened, axial/ring stiffened, and unstiffened shells under combined loading.

structural response and the interlaminar normal stresses. Comparing a 1x12 geodesically stiffened shell, 1x12 axial/ring stiffened shell, and an unstiffened shell shows that the interlaminar normal stresses generated in a geodesically stiffened shell are much larger than those generated in other types of shells. However, the interlaminar normal stresses are still an order of magnitude less than the in-plane stresses. The addition of internal pressure increases the interlaminar normal stresses and therefore large increases in pressure may cause the interlaminar normal stresses to contribute to the failure of the geodesically stiffened shells.

5.5.3 Interlaminar Shear Stress Study

The interlaminar shear stresses, $\bar{\sigma}_{xz}$, are the interlaminar shear stresses having the largest magnitudes for geodesically stiffened shells and will be studied in this work. The interlaminar shear stress distribution, $\bar{\sigma}_{xz}$, for the outer layer base line design subjected to a compressive loading is shown in Figure 73. The interlaminar shear stress surface plot yields a skew-symmetric stress distribution. The shear stress do not peak at the stiffener intersection, but rather peak about 3.5" from the stiffener intersection. The interlaminar shear stress, $\bar{\sigma}_{xz}$, over the shell for a combined applied compressive load and an internal pressure of 10 psi is shown in Figure 74. This reveals that the interlaminar shear stresses yield similar type of behavior and peak at the same location as shown in Figure 73. The difference in nondimensional interlaminar shear stress between the compressive and combined loading is only 28.6%. Thus, a large portion of the interlaminar shear stresses, $\bar{\sigma}_{xz}$, are generated by the compressive rather than the pressure loads. The combined loading case does produce larger nondimensional interlaminar shear stresses by 40% at the x boundaries, x = 0, L_x. Combined loading will be used

to study the interlaminar shear stresses in order to be consistent with the interlaminar normal stress analyses.

Shown in Figure 75 are the nondimensional interlaminar shear stresses, $\bar{\sigma}_{xz}$, at the location of the peak stresses as indicated from the surface plots of Figures 73 and 74 for various shell laminates. The nondimensional interlaminar shear stresses for the geodesically stiffened shells shown in Figure 75 are developed via combined loading. Clearly due to the influence of the stiffeners and the stacking sequence there is no distinct pattern for the shear stresses $\bar{\sigma}_{xz}$. The [30/ − 30/0/ − 30/30], [0/90/0], and the [45/ − 45/45/ − 45] laminates yield the maximum values of the stresses $\bar{\sigma}_{xz}$. The $[45/90/0]_S$ laminated stiffened shell yields the smallest nondimensional interlaminar shear stresses. The difference in the nondimensional shear stresses between the [30/ − 30/0/ − 30/30] shell and the $[45/90/0]_S$ shell is 84.5%. Obviously the shell laminate has a definite influence on the interlaminar shear stresses. Laminates such as the $[-45/45/90/0]_S$, $[45/90/0]_S$, and [60/ − 60/0/ − 60/60] are preferable for use in keeping the $\bar{\sigma}_{xz}$ stresses from becoming significantly large.

In Figure 76, the interlaminar shear stresses, $\bar{\sigma}_{xz}$, are compared for a linear and a geometrically nonlinear analysis subjected to combined loading of the base line design. The results show that the nondimensional interlaminar shear stresses produced from the linear analysis are 80% larger than those generated from the geometrically nonlinear analysis. It is clear that a nonlinear analysis does tend to soften the structure, especially when pressure is applied, thus reducing the resulting displacements, strains, and stresses.

Next, the effect of changing the cell geometry upon the nondimensional interlaminar shear stresses for a [0/90/0] laminated shell subjected to combined loading is shown in Figure 77. The results presented here are for 1x10, 1x12, 1x14, and 1x16 geodesically

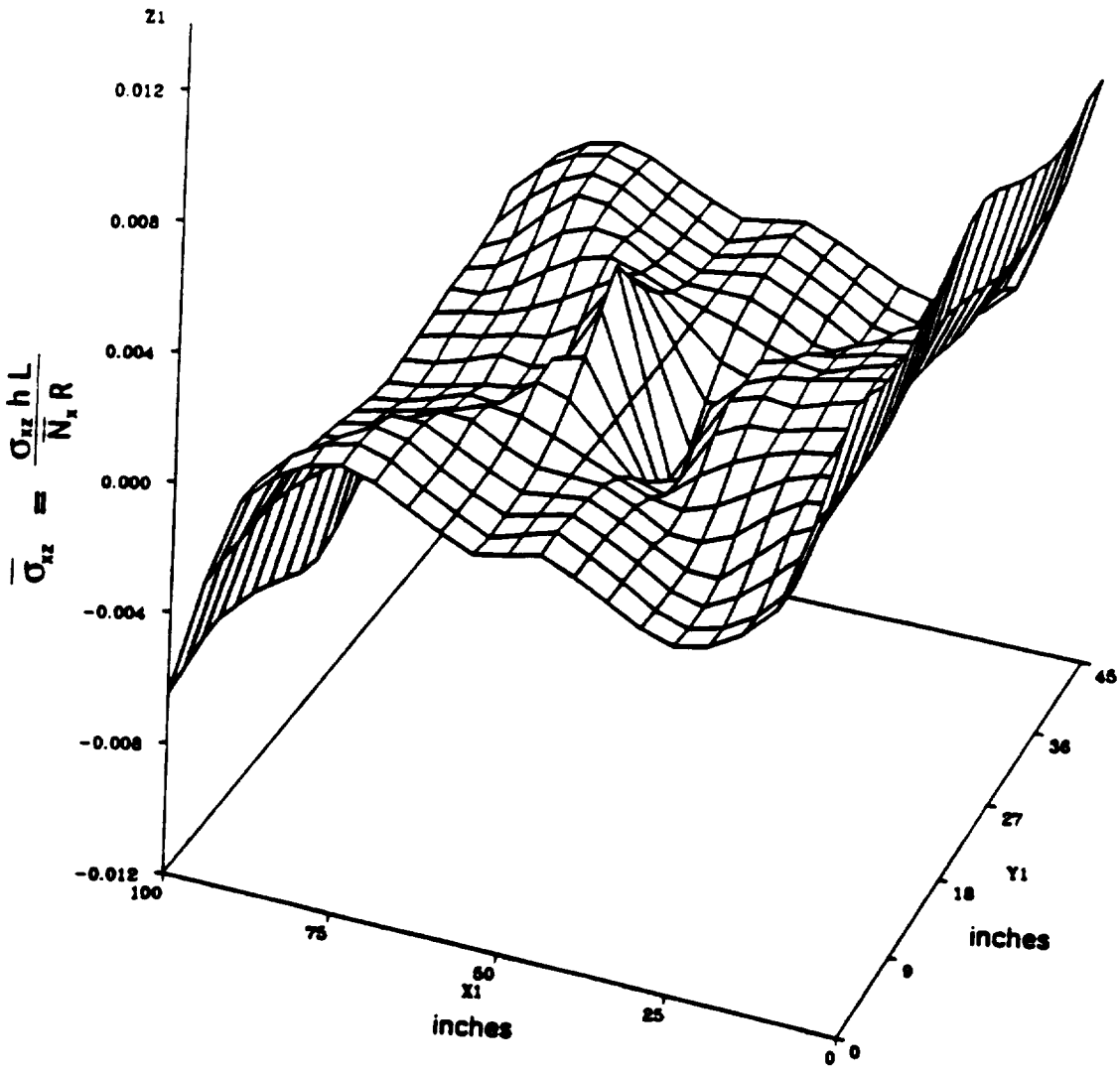

Figure 73. Surface plot of $\bar{\sigma}_{xz}$ for the outer layer of a [0/90/0] 1x12 geodesically stiffened shell under compressive loading.

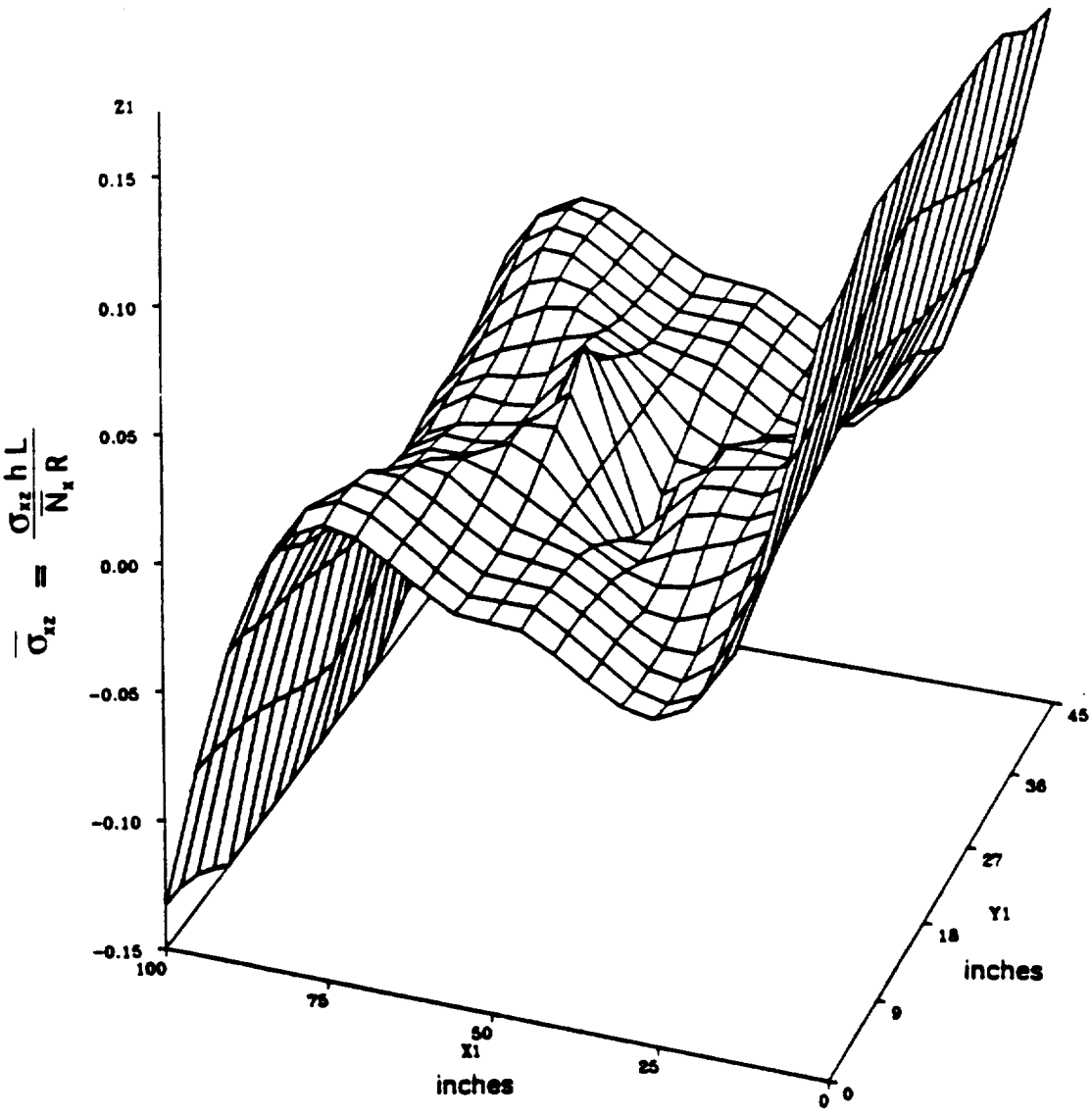

Figure 74. Surface plot of $\bar{\sigma}_{xz}$ for the outer layer of a [0/90/0] 1x12 geodesically stiffened shell under combined loading.

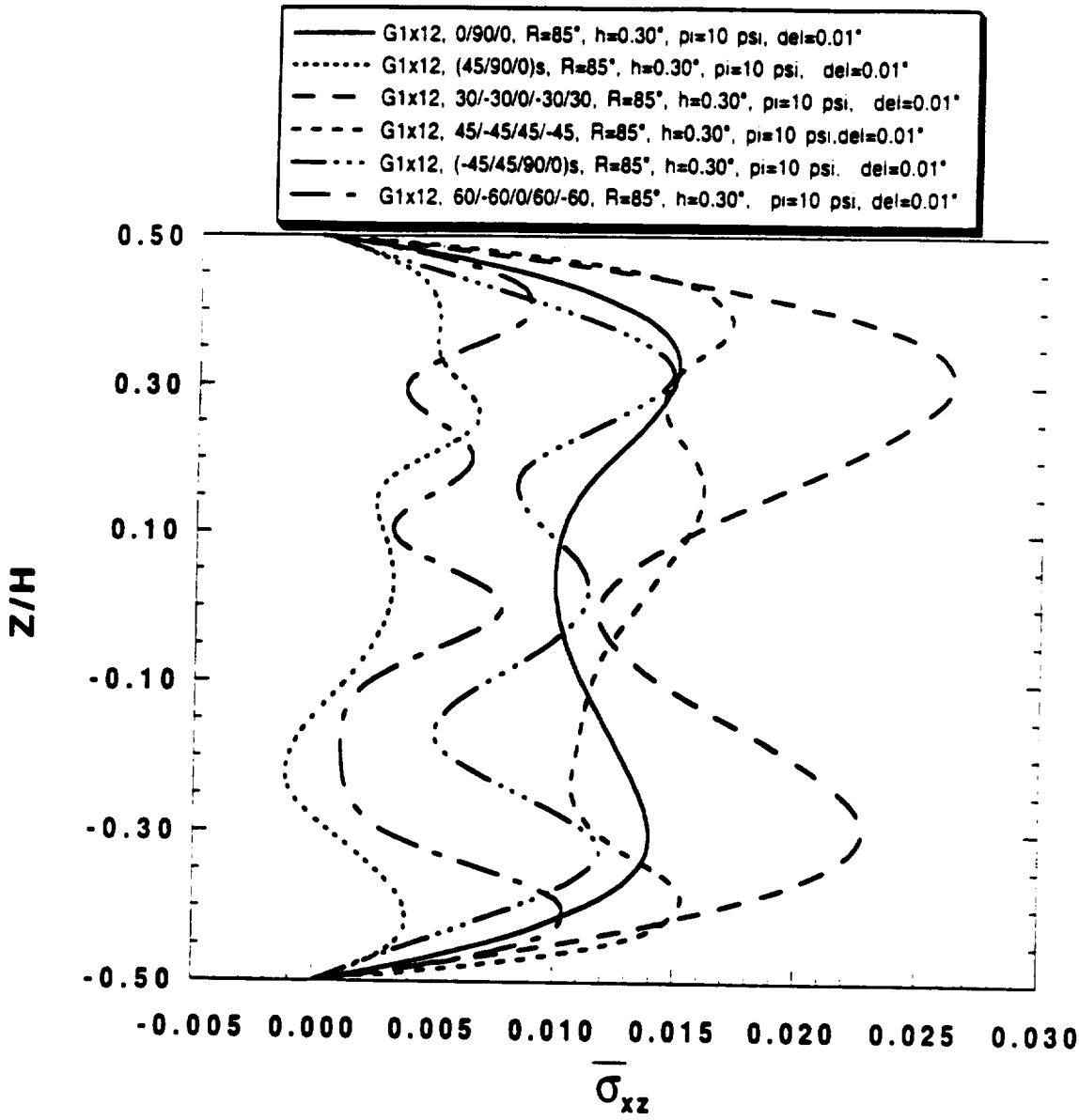

Figure 75. Through-the-thickness distribution of $\overline{\sigma}_{xz}$ for G1x12 shell at the critical region for various shell laminates under combined loading.

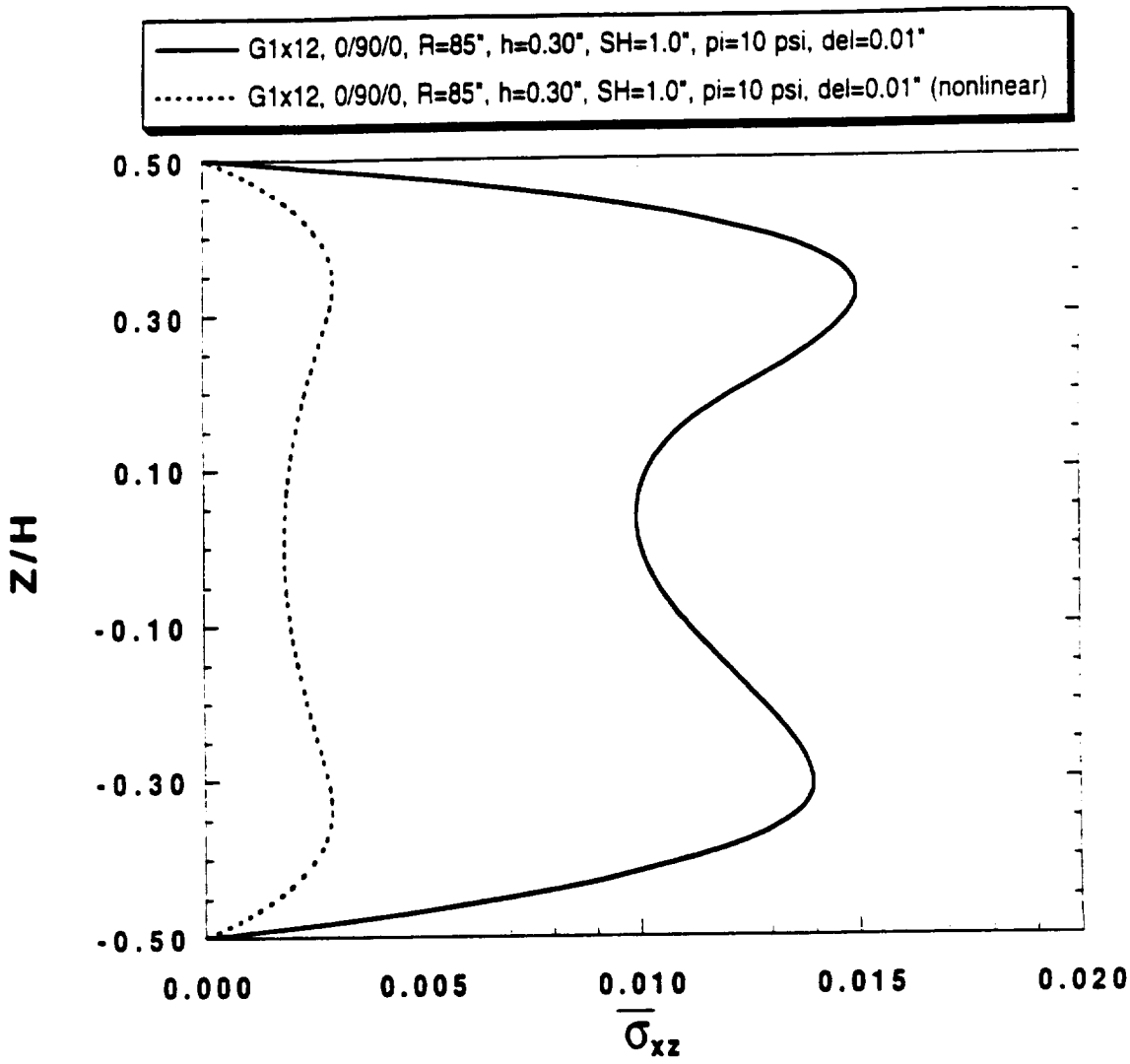

Figure 76. Through-the-thickness distribution of $\overline{\sigma}_{xz}$ for G1x12 shell at the critical region for linear and geometrically nonlinear analyses under combined loading.

stiffened shell models. Obviously as the number of cells around the circumference from 1x10 to 1x16 the shell becomes stiffer and thus lower interlaminar stresses result. The resulting differences in the maximum nondimensional interlaminar shear stresses between the 1x10 and 1x12, 1x14, and 1x16 models are 57%, 86%, and 93% respectively.

Changing the shell laminate thickness for the base line design under combined loading has a definite impact on the interlaminar stresses $\bar{\sigma}_{xz}$ as shown in Figure 78. The results presented in Figure 78 are for 0.15", 0.30", 0.45", and 0.60" shell laminate thicknesses. The nondimensional shear stress results for the 0.15" laminate shell thickness are 87% greater than those for the 0.30" laminate, 96.2% greater than those for the 0.45" laminate, and 98.2% greater than those for the 0.60" laminate. The bending stiffness of the shell is a function of the laminate thickness cubed. Under pressure loading the smaller laminate thicknesses will definitely deflect more and therefore larger interlaminar shear stresses are developed.

In Figure 79 the effects of increasing the shell radius on the nondimensional interlaminar shear stress $\bar{\sigma}_{xz}$ under combined loading is described. Shell radii of 85", 170", and 255" are considered in this analysis. The shell laminate thickness remains a constant 0.30". The results presented in Figure 79 clearly show that increasing the shell radius while holding the shell laminate thickness constant definitely has an impact on the interlaminar shear stresses. The addition of internal pressure is the loading which brings out the large variation in the interlaminar shear stress $\bar{\sigma}_{xz}$. As discussed in Section 5.4 concerning Figure 55b, increasing the shell radius while holding the laminate thickness constant increases the ratio of the stiffener stiffness to the shell stiffness to resist pressure loading. Thus, near the stiffener intersection for the 255" shell the geodesic stiffeners have a large influence on the displacement field when pressure is applied and therefore

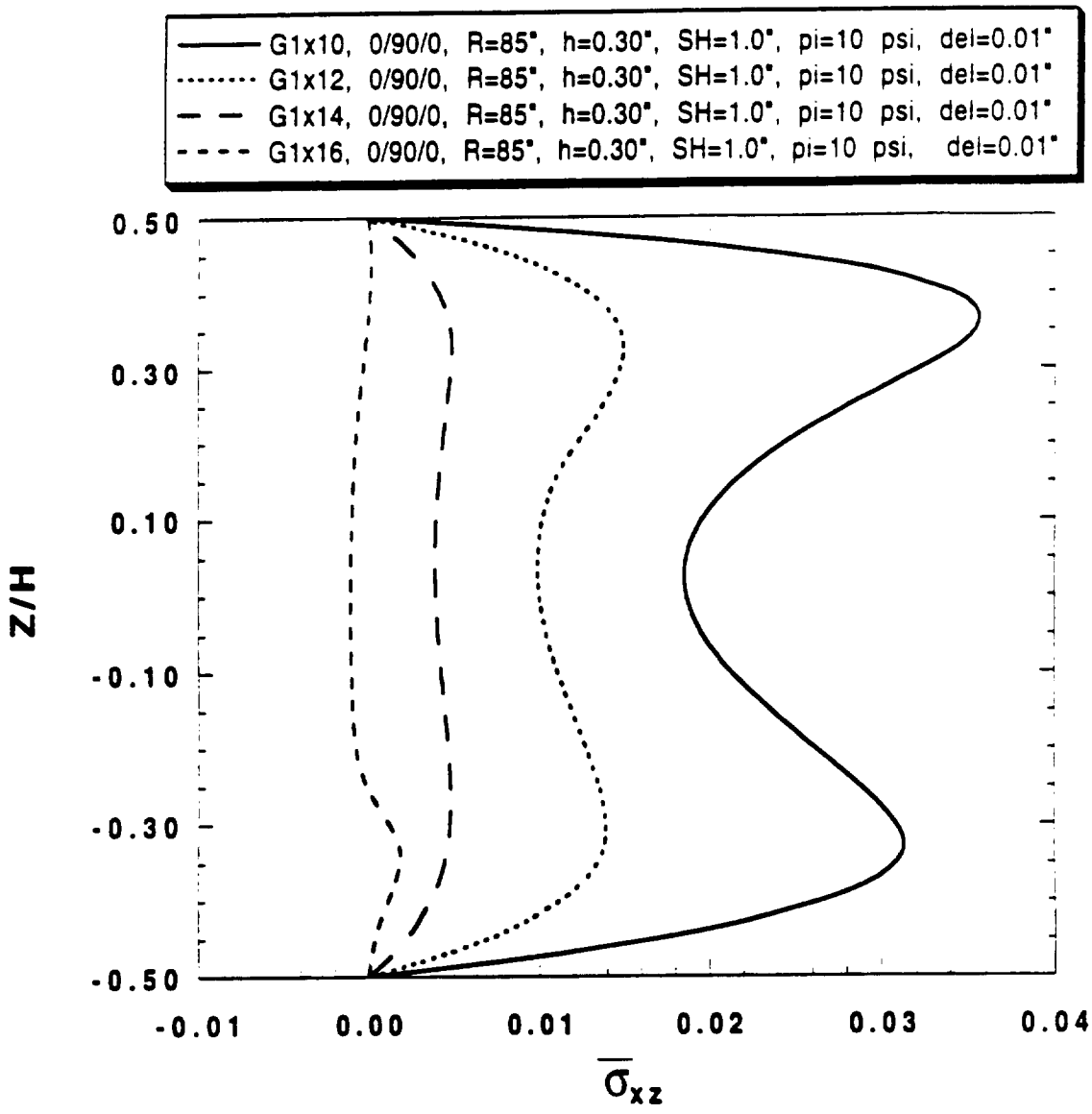

Figure 77. Through-the-thickness distribution of $\overline{\sigma}_{xz}$ for G1x12 shell at the critical region for changing cell geometry under combined loading.

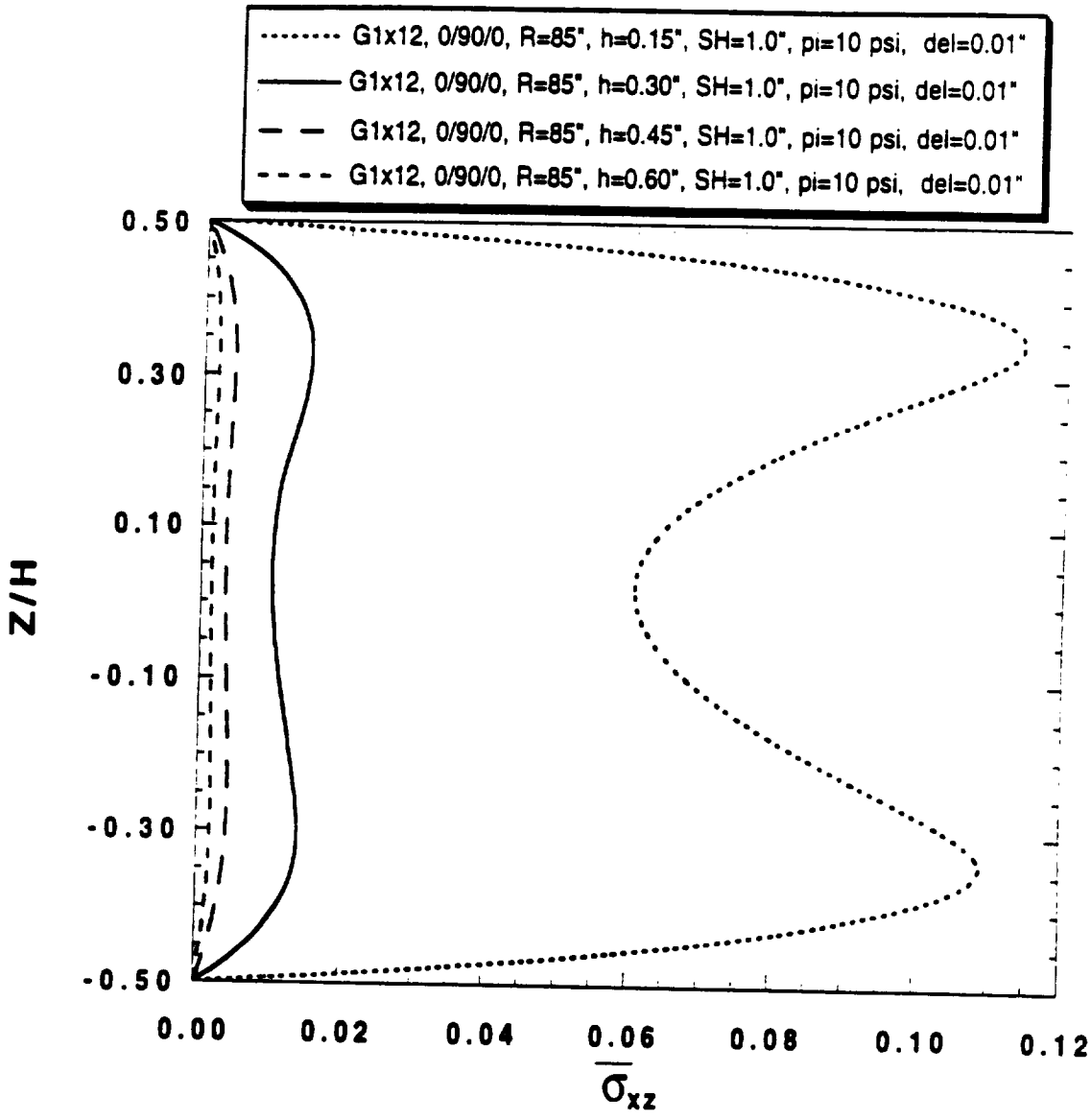

Figure 78. Through-the-thickness distribution of $\overline{\sigma}_{xz}$ for G1x12 shell at the critical region for varying shell laminate thickness under combined loading.

larger shear stresses result in the bottom laminate layers near the stiffener intersection. In fact, the shear stresses change sign through the laminate thickness for the 255″ shell. There appears to be a balance between the increased stiffness created when increasing the shell radius and the increased loading generated via internal pressure by increasing the shell radius. Thus, when the shell radius is increased from 85″ to 170″ the effect of the increased stiffness is not overcome by the increased loading from the internal pressure and thus the interlaminar stresses decrease. However, when the shell radius is increased from 85″ to 255″ the increase in loading from internal pressure exceeds the increase in shell stiffness and thus the interlaminar shear stresses exhibit a large variation through the laminate thickness.

The last interlaminar shear stress analysis considered here involves 1x12 geodesically stiffened shell, 1x12 axial/ring stiffened shell, and an unstiffened shell as shown in Figure 80. The results presented here are for [0/90/0] shells with 1.0″ internal orthotropic shells under combined loading. The results shown in Figure 80 clearly show that the influence of the stiffeners on the interlaminar shear stresses when compared with an analysis of an unstiffened shell. The maximum difference between the geodesically stiffened shell and the unstiffened shell is 93.3% while the maximum difference between the axial/ring stiffened shell and the unstiffened shell is 95.5%. Also, the distribution of the interlaminar shear stresses for the axial/ring stiffened shell and the geodesically stiffened shell are different. While both stiffened shells exhibit peak stresses in the bottom (inner) layers of the laminate where the stiffeners are attached, the axial/ring stiffened shell does not exhibit another peak in the interlaminar shear stress in the top (outer) layers as does the geodesically stiffened shells. Therefore, it can be concluded that because the geodesically stiffened shells produce significantly more displacements at the stiffener intersection than the axial/ring stiffened results as seen in Figure 56b this results in larger

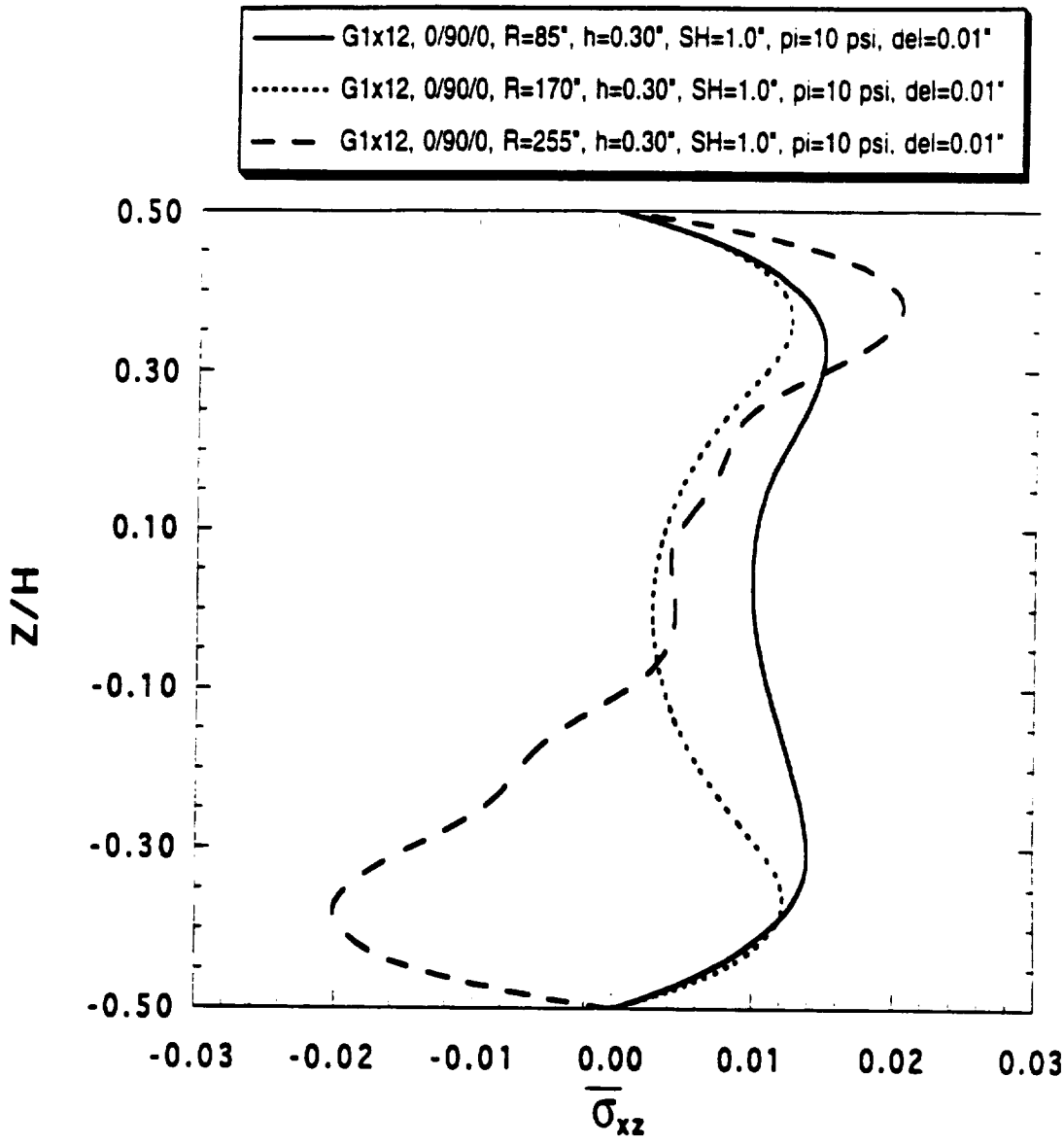

Figure 79. Through-the-thickness distribution of $\overline{\sigma}_{xz}$ for G1x12 shell at the critical region for increasing shell radii under combined loading.

interlaminar shear stresses through the entire shell laminate for the geodesically stiffened shells. The axial/ring stiffened shells are very stiff at the stiffener intersection which results in smaller displacements at the stiffener intersection than away from the intersection (see Figure 56b). Therefore, the influence of the axial/ring stiffened structure is to cause peak interlaminar shear stresses in the inner layers of the shell, but because the transverse displacements away from the stiffener intersection are larger than at the stiffener joint the influence of the axial/ring stiffeners does not extend to the outer layers of the shell.

The impact of laminate stacking sequence, geometric nonlinearity, cell geometry, shell laminate thickness, shell radius, and shell type (unstiffened, axial/ring stiffened, or geodesically stiffened) all influence the interlaminar shear stress. Changing any or many of these parameters will result in significant changes in the interlaminar shear stresses. However, these shear stresses are in many cases 2 orders of magnitude less than the in-plane stresses and these shear stresses' impact on the structural integrity is debatable.

5.6 First-Ply Failure Analysis

The purpose of this study is to determine the primary failure trends for geodesically stiffened shells. This work is not intended to be a detailed failure study similar to the research presented by Reddy and Pandey [159], but rather it should be viewed as a preliminary study of the failure of geodesically stiffened shells. The laminate strength values used in this analysis are given in Table 7. The Tsai-Wu failure criterion discussed in section 2.6 will be used to determine shell laminate material failure. Shown in Table 27 are a comparison of the results for linear material failure and buckling of [0/90/0] 1x12

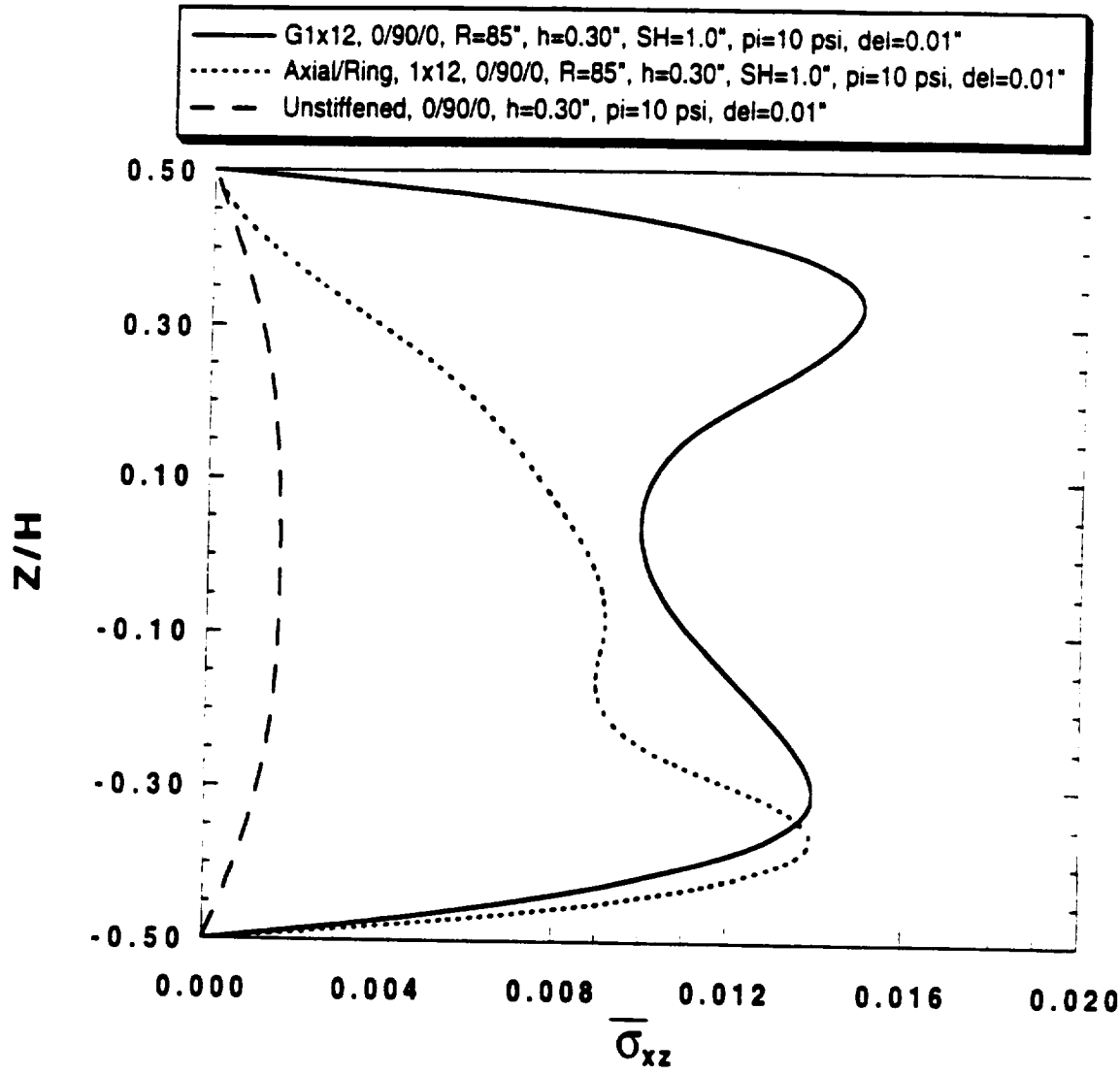

Figure 80. Through-the-thickness distribution of $\overline{\sigma}_{xz}$ for G1x12 stiffened, axial/ring stiffened, and unstiffened shells under combined loading.

geodesically stiffened shells with 1.0″ internal orthotropic stiffeners. Three shell laminate thicknesses, 0.15″, 0.30″, and 1.5″, were considered in this analysis. Results were obtained for pure compression and for shells subjected to combined loading with internal pressures of 10 psi and 25 psi. The end displacements were increased incrementally until failure occurred. The end loads, N_x, were calculated at first-ply failure. The results of Table 27 clearly show that for pure compression and combined loading with small to moderate internal pressures the shell will buckle before material failure occurs. It is also evident that as the pressure is increased from 0 psi to 25 psi the difference between the failure and buckling loads decreases rapidly. The buckling load increases as the pressure is increased due to the biaxial loading. Because the unit load in the circumferential (hoop) direction, N_y, is tensile when internal pressure is included, the buckling load, $\hat{N}_x$, increases due to this biaxial loading condition. The failure load decreases as the pressure is increased and thus it is concluded that for larger pressures material failure will occur.

The next study shown in Table 28 is for the analysis of [0/90/0] unstiffened shells, [0/90/0] 1x12 geodesically stiffened shells, and $[45/90/0]_S$ 1x12 geodesically stiffened shells. A constant shell thickness of 0.30″ is used. For these analyses the end displacement is held constant and the internal pressure is increased until material failure occurs. Applied end displacements of 0.0″, 0.10″, and 0.25″ were used as the constant end displacements. As can be seen material failure occurs at high pressures, (160 psi - 225 psi), and this depends upon the shell type and the applied displacements. The failure of the geodesically stiffened shells occurs at higher pressures than for the unstiffened shells primarily because of the stress concentrations at the stiffener intersection. As discussed in sections 5.2, 5.4, and 5.5 the maximum displacements, in-plane stresses, and interlaminar stresses occur at the stiffener intersection. Shown in Figure 81 is the finite element model and the location of first-ply failure marked with a circled X. The corners

of the shell and the stiffener intersection are the locations of first-ply failure for the geodesically stiffened shells as expected. However, some of the peak stresses at the corners may be artificially induced by the boundary conditions. The location of the first-ply failure depends upon the laminate layup and the applied end displacements. The [0/90/0] shells tend to fail at the stiffener intersection first and the $[45/90/0]_S$ shells tend to fail at the shell corners first. The differences in the failure pressures between the unstiffened and geodesically stiffened shells range from a minimum for 4.4% for the [0/90/0] geodesically stiffened shell with 0.0" end displacements to a maximum of 15.6% for the $[45/90/0]_S$ geodesically stiffened shell with 0.0" end displacements. The maximum difference in failure pressures between the [0/90/0] and the $[45/90/0]_S$ geodesically stiffened shells occurs for applied end displacements of 0.0". The failure pressures of the geodesically stiffened shells are the same for applied end displacements of 0.25". In all cases there is a large variation in the applied end load. It can be concluded that material failure of geodesically stiffened shells will occur for large internal pressures in the vicinity of the stiffener intersection or the corners of the shell section.

Table 27. Comparison of First-Ply Failure and Buckling Loads for Geodesically Stiffened [0/90/0] Shells.

Laminate Thickness (in.)	Applied Internal Pressure (psi)	Edge Load at Failure (lb/in)	Buckling Load (lb/in)	Percent Difference
0.15	0	18969	757	2406
0.30	0	37697	3291	1045
1.50	0	184025	67776	172
0.15	10	18890	888	2027
0.30	10	36030	3978	805
1.50	10	183972	72779	152
0.15	25	16724	2911	475
0.30	25	31738	5893	438
1.50	25	183898	80865	127

1x12 Geodesically Stiffened Shells with 1.0" Internal Orthotropic Stiffeners

Table 28. First-Ply Failure Results for Geodesically Stiffened and Unstiffened 0.3" Thick Shells Subjected to High Pressures.

Shell Type	Applied End Displacement (in)	Internal Pressure at Failure (psi)	End Load at Failure lb/in
US	0.0	225	-1197
G1x12X	0.0	215	-1348
G1x12Q	0.0	190	-2816
US	0.10	210	6662
G1x12X	0.10	195	6798
G1x12Q	0.10	180	2556
US	0.25	180	18491
G1x12X	0.25	160	19048
G1x12Q	0.25	160	10687

US = Unstiffened [0/90/0]

G1X12X = 1x12 [0/90/0] geodesically stiffened shell

G1X12Q = 1x12 $[45/90/0]_S$ geodesically stiffened shell

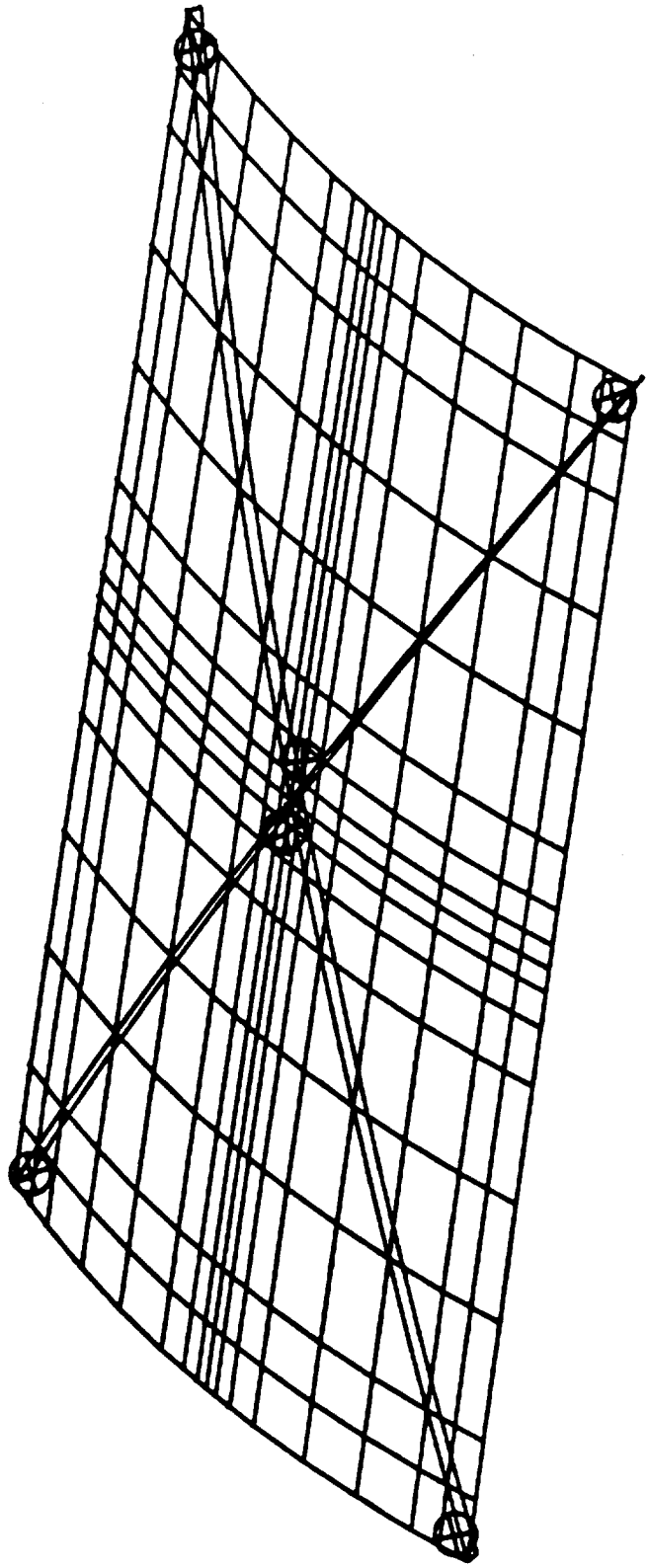

Figure 81. Location of the first-ply failure in the layerwise finite element model.

Chapter 6

Conclusions and Recommendations

6.1 Summary and Conclusions

The purpose of this research was to analyze geodesically stiffened shells using a layerwise approach. The literature review, theoretical developments, verifications of the analytical method and computer codes, and the analysis of the stiffened shells were all vital to the completion of this research. A summary of the major accomplishments of this work follow:

- Extensive literature review including shell theories, buckling of stiffened shells, finite element analysis of stiffened shells, failure theories, and calculation of interlaminar stresses.

- Theoretical and computational development of a layerwise discrete Ritz buckling procedure.

- Buckling analysis of geodesic, axial, and ring stiffened shells with smeared and finite element comparisons.

- Theoretical and computational development and subsequent verification of the layerwise shell and stiffener finite elements with applications to geodesically stiffened shells and interlaminar stresses.

The literature review provided the groundwork for this research and any subsequent work which naturally follows from this research. All of the analytical developments were derived because of a lack of study or knowledge about a particular area or because of an interest in expanding the database about a certain topic.

The layerwise discrete Ritz analytical buckling procedure was developed to prove the validity of the layerwise theory for use in the analysis of geodesically stiffened composite shells. Attachment of the discrete stiffeners was implemented by using the Lagrange multiplier technique. The layerwise analytical buckling results compare well with the smeared buckling results and the Testbed finite element results. The layerwise discrete analytical method yielded more conservative buckling results than the smeared results and the differences in results ranged from 0% to 70%. This is reasonable because discrete methods should yield more conservative buckling results than the smeared approaches. A comparison of the Testbed finite element buckling results with the layerwise discrete results shows that in general for quasi-isotropic and cross-ply laminates the layerwise theory yields more conservative results. The difference between the LWTR discrete method and the finite element method can be attributed to the fact that the LWTR method neglects the out-of-plane and the torsional stiffnesses of the stiffeners. The difference starts to become more pronounced as the stiffener heights increase. This is due to the fact that as the stiffener height increases the effects of the out-of-plane and

the torsional the stiffnesses on the global buckling results increase. The layerwise discrete method may be employed for axial, ring, or geodesically stiffened shells. This method is only directly applicable to specially orthotropic shells. Reasonable buckling results should be expected. The layerwise discrete buckling method provides design engineers with an optional tool in the design of stiffened shells based upon buckling. One of the drawbacks of this method is that it is restricted to shells which have boundary conditions that are analytically tractable. Run times for this method can be extreme if a sweep of the buckling modes must be made in order to determine the minimum eigenvalue. Also, this method is only directly applicable to specially orthotropic shells where $\overline{C}_{16} = \overline{C}_{26} = \overline{C}_{36} = \overline{C}_{45} = 0$. However, this method has provided good results for certain quasi-isotropic materials subjected to in-plane loads.

The layerwise finite element method for geodesically stiffened shells was developed primarily to study the displacement and stress fields in geodesically stiffened shells. Of particular interest were the interlaminar stresses. Both the layerwise shell and beam elements were developed for this research. The out-of-plane stiffness of the layerwise beam elements was included by using the ratio of the out-of-plane moment of inertia to the in-plane moment of inertia. Neglecting the out-of-plane beam stiffness has the greatest impact when angle ply laminates are used in the shell or beams. For these cases the finite element method does not yield good results unless the out-of-plane beam stiffness is included. Developing the beam elements in a layerwise fashion permits the beam element degrees of freedom to be assembled directly into the global stiffness matrix. Thus, no additional constraint equations are necessary. The layerwise finite element program was verified using 10 classical example problems. An additional comparison of the layerwise finite element method with the Testbed finite element method was conducted for geodesically stiffened shells and several shell lamination

schemes. A good correlation of stress results exists between the layerwise analyses and the Testbed analyses, less than 10%. The small differences occur at the stiffener intersection and are due to the different stiffener interaction responses measured by the two analyses.

A study of the displacements and the stresses for various geodesically stiffened shells was made using the layerwise finite element method. Varying the shell laminate layup, laminate thickness, stiffener height, stiffener orientation angle, cell geometry, shell radii, and shell length were all considered . All changes have an impact on the structural response, some more than others. The displacement field is most affected by changing the shell laminate layup and the cell geometry. Adding internal pressure to the shell has a major influence on the displacement response when compared with pure compression. This is most evident for the geometrically nonlinear case, when the shell radius is increased, and when axial and ring stiffened shells are considered. When subjected to combined compression and internal pressure the transverse displacements of the shell away from the stiffener intersection do not exceed those at the stiffener intersection until deep stiffeners, a large radius, or an axial/ring stiffened structure are used.

Interlaminar normal and shear stresses for geodesically stiffened shells are only significant when internal pressure is added. The interlaminar normal stresses are influenced by the laminate layup, geometric nonlinearity, stiffener height, cell geometry, shell radius, shell laminate thickness, and the type of shell structure. The shape and magnitude of interlaminar normal stress distribution through the thickness is influenced most by the laminate layup, shell laminate thickness, and shell type (unstiffened, axial and ring stiffened, or geodesically stiffened). However, the interlaminar normal stresses are an order of magnitude less than the in-plane compressive stresses. The interlaminar shear streses

are greatly influenced by the laminate layup, shell laminate thickness, and shell type. The interlaminar shear stresses are often two orders of magnitude less than the in-plane stresses. The influence of the interlaminar stresses on the structural integrity of stiffened shells is small for pure compression and combined loading when the internal pressure is small.

The failure analysis reveals that unless internal pressure is applied the geodesically stiffened shells will buckle before they experience material failure. Increasing the internal pressure can create a failure scenario. For large internal pressures failure of geodesically stiffened shells initiates at the stiffener intersection where the largest displacements and stresses occur.

The layerwise finite element method provides a useful analytical tool to study the structural response of geodesically stiffened shells. The layerwise method eliminates the finite element aspect ratio problem of traditional 3-D finite elements. Also, the layerwise finite element code was written so that a preprocessor is not needed to generate a large model and thus it is easier to change variables such as the shell radius, shell length, cell geometry, and stiffener height than for the Testbed models. However, for large problems the size of the bandwidth can hamper the solution by causing excessive run times and not converging to the correct solution.

6.2 Recommendations

The recommendations include expanding the existing analytical tools and augmenting the analyses. The layerwise Ritz method should be expanded to include calculation of the displacements, strains, and stresses for simply supported cylindrical shells. Including

the out-of-plane and torsional stiffnesses of the stiffeners used in the Ritz method can also be included in the future. Employment of layerwise beam elements in the Ritz method may also be useful. Also, perhaps the layerwise discrete approach could be extended to other tractable boundary conditions and linear vibration analyses. Development of robust postprocessors for both the analytical and finite element codes will provide the user with plots of the deformed shapes, eigenvectors, and stress contours. Including the torsional stiffnesses of the layerwise beam elements by assuming a displacement distribution through the thickness of the beam could improve finite element method. Improvement and/or additional finite element equation solvers could help circumvent the bandwidth problems for large models. Parallel processing is an option to consider for very large finite element problems.

A comparison of analytical data with any experimental data will provide useful information into the layerwise analyses' strengths and deficiencies. For example, work by Boitnott, Johnson, and Starnes [144] included a nonlinear failure analysis of pressurized composite panels. The work in Ref. [144] compared experimental failure results with analytical failure results. The analytical analyses were conducted in order to simulate the actual experimental conditions. The analyses utilized the measured radius, circumferential slip, and axial strain for each experimental specimen to model the response as accurately as possible. The failure analyses of the curved panels described in Ref. [144] could also be accomplished using a layerwise finite element model, but it will involve a great deal of work and therefore will be left for future study. A study of geodesically stiffened shells subjected to high pressures may provide interesting interlaminar stresses. Additional analyses that incorporate geometric nonlinearity should be considered. Also, a study of a variety of laminate layups as a function of various shell and stiffener parameters may provide some unique results and a good da-

tabase. Additional failure theories and post-ply failure could easily be implemented and studied. The aforementioned recommendations coupled with the work accomplished in this research should provide several additional research projects.

References

1. Starnes, J. H. Jr., Knight, N. F. Jr., and Rouse, M., "Postbuckling Behavior of Selected Flat Stiffened Graphite-Epoxy Panels Loaded in Compression," *AIAA Journal*, Vol. 23, No. 8, August 1985, pp. 1236-1246.

2. Knight, N. F. Jr. and Starnes, J. H. Jr., "Postbuckling Behavior of Selected Curved Stiffened Graphite-Epoxy Panels Loaded in Axial Compression," *AIAA Journal*, Vol. 26, No. 3, March 1988, pp. 344-352.

3. Love, A. E. H., "The Small Free Vibrations and Deformation of a Thin Elastic Shell," *Phil. Trans. Phys. Sci. Royal Society of London*, Vol. 199, 1888, pp. 491-546.

4. Sanders, J. L., "An Improved First-Approximation Theory for Thin Shells," *NASA Technical Report R-24*, 1959.

5. Donnell, L. H., "Stability of Thin-Walled Tubes Under Torsion," *NACA Report No. 479*, 1933.

6. Reissner, E., "The Effect of Transverse Shear Deformation on the Bending of Elastic Plates," *J. of Applied Mechanics*, Vol. 12, 1945, pp. A69-A77.

7. Mindlin, R. D., "Influence of Rotary Inertia and Shear on Flexural Motions of Isotropic Elastic Plates," *J. of Applied Mechanics* , Vol. 18, 1951, pp. 31-38.

8. Reissner, E., "A New Derivation of the Equations for the Deformation of Elastic Shells," *American Journal of Mathematics* , Vol. 63, 1941, pp. 177-184.

9. Reissner, E., "Stress Strain Relations in the Theory of Thin Elastic Shells," *J. of Mathematics and Physics*, Vol. 3, July 1952, pp. 109-119.

10. Reissner, E., "A Note on Generating Generalized Two-Dimensional Plate and Shell Theories," *J. of Applied Math. and Physics (ZAMP)*, Vol. 28, 1977, pp. 633-642.

11. Naghdi, P. M., "A Survey of Recent Progress in the Theory of Elastic Shells," *Appl. Mech. Reviews*, Vol. 9, No. 9, Sept. 1956, pp. 365-368.

12. Bert, C. W., "Analysis of Shells," *Composite Materials Volume 7, Structural Design and Analysis Part I*, C. C. Chamis, editor, Academic Press, 1975, pp. 207-258.

13. Krauss, H., *Thin Elastic Shells*, John Wiley and Sons, Inc., New York, N.Y., 1967.

14. Flügge, W., *Stresses in Shells*, Julius Springer, Berlin, Germany, 1960.

15. Ambartsumyan, S. A., *Theory of Anisotropic Shells*, Moscow, 1961, English Translation, NASA TT F118, May 1964.

16. Ambartsumyan, S. A., "Calculation of Laminated Anisotropic Shells ," *Izvestiia Akademiia Nauk Armenskoi SSR, Ser. Fiz. Mat. Est. Tekh. Nauk.*, Vol. 6, No. 3, 1953, p. 15.

17. Dong, S. B., Pister, K. S., and Taylor, R. L., "On the Theory of Laminated Anisotropic Shells and Plates," *J. of the Aerospace Sciences*, Vol. 29, No. 7, July 1962, pp. 969-975.

18. Reissner, E. and Stavsky, Y., "Bending and Stretching of Certain Types of Heterogeneous Aeolotropic Elastic Plates," *J. Appl. Mech.*, Paper No. 61-APM-21, 1961.

19. Cheng, S. and Ho, B. P. C., "Stability of Heterogeneous Aeolotropic Cylindrical Shells Under Combined Loading," *AIAA Journal*, Vol. 1, No. 4, April 1963, pp. 892-898.

20. Widera, G. E. O., "Asymptotic Theories for the Unsymmetric Vibrations of Cylindrical Shells," *J. of Appl. Math. and Physics (ZAMP)*, Vol. 21, 1970, pp. 378-399.

21. Widera, G. E. O. and Logan, D. L., "Refined Theories for Nonhomogeneous Anisotropic Cylindrical Shells : Part I - Derivation," *J. Eng. Mech. Div.*, 106 (EM6), 1980, pp. 1053-1074.

22. Logan, D. L. and Widera, G. E. O., "Refined Theories for Nonhomogeneous Anisotropic Cylindrical Shells : Part II - Application," *J. Eng. Mech. Div.*, 106 (EM6), 1980, pp. 1075-1090.

23. Reddy, J. N., "Exact Solutions of Moderately Thick Laminated Shells," *J. Eng. Mech.*, ASCE, Vol. 110, No. 5, May 1984, pp. 794-809.

24. Gulati, S. T. and Essenburg, F., " Effects of Anisotropy in Axisymmetric Cylindrical Shells," *J. Appl. Mech.*, Vol. 34, September 1967, pp. 659-666.

25. Hsu, T. M. and Wang, J. T. S., "A Theory of Laminated Cylindrical Shells Consisting of Layers of Orthotropic Laminae," *AIAA Journal*, Vol. 8, No. 12, December 1970, pp. 2141-2146.

26. Zukas, J. A. and Vinson, J. R., "Laminated Transversely Isotropic Cylindrical Shells," *J. Appl. Mech.*, Vol. 38, June 1971, pp. 400-407.

27. Dong, S. B. and Tso, F. K. W., "On a Laminated Orthotropic Shell Theory Including Transverse Shear Deformation," *J. Appl. Mech.*, Vol. 39, December 1972, pp. 1091-1097.

28. Naghdi, P. M., "On a Variational Theorem in Elasticity and Its Application to Shell Theory," *J. Appl. Mech.*, Vol. 31, No. 4, Trans. ASME, Vol. 86, Series E, Dec. 1964, pp. 647-653.

29. Naghdi, P. M., "On the Differential Equations of the Linear Theory of Elastic Shells," *Proceedings of the Eleventh International Congress of Applied Mechanics*, Munich, 1964.

30. Whitney, J. M. and Sun, C. T., "A Higher Order Theory for Extensional Motion of Laminated Composites," *J. of Sound and Vibration*, Vol. 30, 1973, pp. 85-97.

31. Whitney, J. M. and Sun, C. T., "A Refined Theory for Laminated Anisotropic Cylindrical Shells," *J. Appl. Mech.*, Vol. 41, 1974, pp. 471-476.

32. Reddy, J. N., "Bending of Laminated Anisotropic Shells by a Shear Deformable Finite Element," *Fibre Science and Tech.*, Vol. 17, 1982, pp. 9-24.

33. Reddy, J. N. and Liu, C. F., "A Higher-Order Shear Deformation Theory of Laminated Elastic Shells," *J. Eng. Sci.*, Vol. 23, No. 3, 1985, pp. 319-330.

34. Librescu, L., "Refined Geometrically Nonlinear Theories of Anisotropic Laminated Shells," *Quarterly of Appl. Math.*, April 1987, pp. 1-22.

35. Librescu, L., "Geometrically Non-Linear Theory of Shear Deformable Anisotropic Laminated Composite Shallow Shells," *Proceedings, 7th ASCE Engineering Mechanics Specialty Conference*, Blacksburg, VA, 1988, pp. 283-293.

36. Reddy, J. N., "A Generalization of Two-Dimensional Theories of Laminated Composite Plates," *Commun. Appl. Num. Meth.*, Vol. 3, 1987, pp. 173-180.

37. Reddy, J. N., *A Layer-Wise Shell Theory With Applications to Buckling and Vibration of Cross-Ply Laminated Stiffened Circular Cylindrical Shells*, Virginia Polytechnic Institute and State University, CCMS-92-01, January 1992.

38. Barbero, E. J., Reddy, J. N., and Teply, J. L., "General Two-Dimensional Theory of Laminated Cylindrical Shells," *AIAA Journal*, Vol. 28, No. 3, March 1990, pp. 544-553.

39. Bert, C. W. and Francis, P. H., "Composite Material Mechanics : Structural Mechanics," *AIAA Journal*, Vol. 12, No. 9, Sept. 1974, pp. 1173-1186.

40. Kapania, R. K., "Analysis of Laminated Shells," *Journal of Pressure Vessel Technology*, Vol. 111, May 1989, pp. 88-96.

41. Zienkiewicz, O. C., *The Finite Element Method*, McGraw-Hill, NY, 1976.

42. Gallagher, R. H., "Shell Elements," *Proceedings of World Congress on Finite Elements in Structural Mechanics*, Vol. 1, Bournemouth, England, 1975.

43. Irons, B. M., "Engineering Application of Numerical Integration in Stiffness Methods," *AIAA Journal*, Vol. 4, 1966, pp. 2035-2037.

44. Ergatoudis, I., Irons, B. M., and Zienkiewicz, O. C., "Curved Isoparametric Quadrilateral Element," *Int. J. Solids Struct.*, Vol. 4, 1968, pp. 31-42.

45. Ahmad, S., Irons, B. M., and Zienkiewicz, O. C., "Analysis of Thick and Thin Shell Structures by Curved Finite Elements," *Int. J. Num. Meth. Eng.*, Vol. 2, 1970, pp. 419-451.

46. Bathe, K. J., *Finite Element Proceedures in Engineering Analysis*, Prentice Hall, N.J., 1982.

47. Chao, W. C. and Reddy, J. N., "Analysis of Laminated Composite Shells Using a Degenerated 3-D Element," *Int. J. Num. Meth. Eng.*, Vol. 20, 1984, pp. 1991-2007.

48. Chang, T. Y. and Sawamiphakdi, K., "Large Deformation Analysis of Laminated Shells by Finite Element Method," *Computers and Structures*, Vol. 13, 1981, pp. 331-340.

49. Wung, P. M., *Large Deformation Analysis of Laminated Composite Structures by a Continuum-Based Shell Element with Transverse Deformation*, Ph.D. Dissertation, Virginia Polytechnic Institute and State University, June 1989.

50. Dong, S. B., "Analysis of Laminated Shells of Revolution," *J. Eng. Mech. Div.*, ASCE, (92) EM6, 1966.

51. Wilson, E. A. and Parsons, B., "The Finite Element Analysis of Filament-Reinforced Axisymmetric Bodies," *Fibre Sci. Tech.*, Vol. 2, 1969, pp. 155-166.

52. Schmit, L. A. Jr. and Monforton, G. R., "Finite Deflection Discrete Element Analysis of Sandwich Plates and Cylindrical Shells with Laminated Faces," *AIAA Journal*, Vol. 8, No. 8, August 1970, pp. 1454-1461.

53. Panda, S. C. and Natarajan, R., "Finite Element Analysis of Laminated Shells of Revolution," *Computers and Structures*, Vol. 6, 1976, pp. 61-64.

54. Rao, K. P., "A Rectangular Laminated Anisotopic Shallow Thin Shell Finite Element," *Comp. Meth. Appl. Mech. Eng.*, 15, 1978, pp. 13-33.

55. Noor, A. K. and Andersen, C. M., "Mixed Isoparametric Finite Element Models of Laminated Composite Shells," *Comp. Meth. Appl. Mech. Eng.*, 11, 1977, pp. 255-280.

56. Yaghmai, S. and Popov, E. P., "Incremental Analysis of Large Deflections of Shells of Revolution," *Int. J. Solids Struct.*, Vol. 7, 1971, pp. 1375-1393.

57. Bathe, K. J. and Bolourchi, S., "A Geometric and Material Nonlinear Plate and Shell Element," *Computers and Structures*, Vol. 11, 1980, pp. 23-48.

58. Saigal, S., Kapania, R. K., and Yang, T. Y., "Geometrically Nonlinear Finite Element Analysis of Imperfect Laminated Shells," *Journal of Composite Materials*, Vol. 20, No. 2, March, 1986, pp. 197-214.

59. Wagner, W. and Stein, E., "A New Finite Element Formulation For Cylindrical Shells of Composite Material," *Composites Engineering*, Vol. 3, No. 9, 1993, pp. 899-910.

60. Yamaki, N., *Elastic Stability of Circular Cylindrical Shells* , North-Holland Series in Applied Mathematics and Mechanics, 1984.

61. Timoshenko, S. and Woinowsky-Krieger, S., *Theory of Plates and Shells*, McGraw-Hill, NY, 1959.

62. Donnell, L. H., "A New Theory for the Buckling of Thin Cylinders Under Axial Compression and Bending," *Trans. Am Soc. Mech. Engrs.*, Vol. 56, 1934, pp. 795-806.

63. von Kármán, T. and Tsien, H. S., "The Buckling of Thin Cylindrical Shells Under Axial Compression," *Journal of the Aeronautical Sciences*, Vol. 8, No. 8, June 1941, pp. 303-312.

64. Tsien, H. S., "A Theory for the Buckling of Thin Shells," *Journal of the Aeronautical Sciences*, Vol. 9, No. 10, August 1942, pp. 373-384.

65. Batdorf, S. B., "A Simplified Method of Elastic-Stability of Axially Compressed Cylindrical Shells," NACA Report No. 874, 1947.

66. Stein, M., "The Influence of Prebuckling Deformations and Stresses on the Buckling of Perfect Cylinders," NASA TR R-190, Feb. 1964.

67. Almroth, B. O., "Influence of Edge Conditions on the Stability of Axially Compressed Cylindrical Shells," *AIAA Journal*, Vol. 4, No. 1, January 1966, pp. 134-140.

68. Leissa, A. W., "Buckling of Laminated Composite Plates and Shell Panels," Air Force Wright Aeronautical Lab., AFWAL-TR-85-3069, 1985, pp. 969-975.

69. Lei, M. M. and Cheng, S., "Buckling of Composite and Homogeneous Isotropic Cylindrical Shells Under Axial and Radial Loading," *J. Appl. Mech.*, Dec. 1969, pp. 791-798.

70. Tennyson, R. C. and Muggeridge, D. B., "Buckling of Laminated Anisotropic Imperfect Circular Cylinders Under Axial Compression," *J. Spacecraft*, Vol. 10, No. 2, Feb. 1973, pp. 143-148.

71. Jones, R. M. and Morgan, H. S., "Buckling and Vibration of Cross-Ply Laminated Circular Cylindrical Shells," *AIAA Journal*, Vol. 13, No. 5, May 1975, pp. 664-671.

72. Hirano, Y., "Buckling of Angle-Ply Laminated Circular Cylindrical Shells," *J. Appl. Mech.*, Vol. 46, March 1979, pp. 233-234.

73. Greenberg, J. B. and Stavsky, Y., "Stability and Vibrations of Compressed, Aeolotropic, Composite Cylindrical Shells," *J. Appl. Mech.*, Vol. 49, Dec. 1982, pp. 843-848.

74. Tennyson, R. C., "Buckling of Laminated Composite Cylinders : A Review," *Composites*, Jan. 1975, pp. 17-24.

75. Ho, B. P. C. and Cheng, S., "Some Problems in Stability of Heterogeneous Aeolotropic Cylindrical Shells Under Combined Loading," *AIAA Journal*, Vol. 1, No. 7, July 1963, pp. 1603-1607.

76. Tsai, J., "Effect of Heterogeneity on the Stability of Composite Cylindrical Shells Under Axial Compression," *AIAA Journal*, Vol. 4, No. 6, June 1966, pp. 1058-1062.

77. Perry, T. and Miller, Z., "A Study of the Jones' Equation for Buckling of Laminated Composite Cylinders Under External Hydrostatic Pressure," *Journal of Ship Research*, Vol. 37, No. 3, Sept. 1993, pp. 239-252.

78. Van der Neut, A., "The General Instability of Stiffened Cylindrical Shells Under Axial Compression," Report S-314, National Aeronautical Research Institute, Amsterdam, The Netherlands, 1947.

79. Baruch, M. and Singer, J., "Effect of Eccentricity of Stiffeners on the General Instability of Stiffened Cylindrical Shells Under Hydrostatic Pressure," *Journal of Mechanical Engineering Science*, Vol. 5, No. 1, 1963, pp. 23-27.

80. Hedgepeth, J. M. and Hall, D. B., "Stability of Stiffened Cylinders," *AIAA Journal*, Vol. 3, No. 12, Dec. 1965, pp. 2275-2286.

81. Singer, J., Baruch, M., and Harari, O., "Inversion of the Eccentricity Effect in Stiffened Cylindrical Shells Buckling Under External Pressure," *Journal of Mechanical Engineering Science*, Vol. 8, No. 4, 1966, pp. 363-373.

82. Singer, J., Baruch, M., and Harari, O., "On the Stability of Eccentrically Stiffened Cylindrical Shells Under Axial Compression," *Int. J. Solids Structures*, Vol. 3, 1967, pp. 445-470.

83. Block, D. L., Card, M. T., and Mikulas, M. M., Jr., "Buckling of Eccentrically Stiffened Orthotropic Cylinders," NASA TN D-2960, Aug. 1965.

84. McElman, J. A., Mikulas, M. M., Jr., and Stein, M., "Static and Dynamic Effects of Eccentric Stiffening of Plates and Cylindrical Shells," *AIAA Journal*, Vol. 4, No. 5, May 1966, pp. 887-894.

85. Card, M. F., "Preliminary Results of Compression Tests on Cylinders with Eccentric Stiffeners," NASA TM X-1004, September 1964.

86. Card, M. F. and Jones, R. M., "Experimental and Theoretical Results for Buckling of Eccentrically Stiffened Cylinders," NASA TN D-3639, Oct. 1966.

87. Simitses, G. J., "Instability of Orthotropic Cylindrical Shells Under Combined Torsion and Hydrostatic Pressure," *AIAA Journal*, Vol. 5, No. 8, August 1967, pp. 1463-1469.

88. Simitses, G. J., "A Note on the General Instability of Eccentrically Stiffened Cylinders," *J. Aircraft*, Vol. 4, No. 5, Sept.-Oct. 1967, pp. 473-475.

89. Simitses, G. J., "Buckling of Eccentrically Stiffened Cylinders Under Torsion," *AIAA Journal*, Vol. 6, No. 10, Oct. 1968, pp. 1856-1860.

90. Jones, R. M., "Buckling of Circular Cylindrical Shells with Multiple Orthotropic Layers and Eccentric Stiffeners," *AIAA Journal*, Vol. 6, No. 12, Dec. 1968, pp. 2301-2305.

91. Jones, R. M., "Buckling of Stiffened Multilayer Circular Cylindrical Shells with Different Orthotropic Moduli in Tension and Compression," *AIAA Journal*, Vol. 9, No. 5, May 1971, pp. 917-923.

92. Soong, T. C., "Buckling of Cylindrical Shells with Eccentric Spiral-Type Stiffeners," *AIAA Journal*, Vol. 7, No. 1, Jan. 1969, pp. 65-72.

93. Meyer, R. R., "Buckling of 45° Eccentric-Stiffened Waffle Cylinders," *J. of the Royal Aeronautical Society*, July 1967, pp. 516-520.

94. Rehfield, L. W., Deo, R. B., and Renieri, G. D., "Continuous Filament Advanced Composite Isogrid: A Promising Structural Concept," *Fibrous Composites in Structural Design*, Plenum Publishing Corp., 1980, pp. 215-239.

95. Reddy, A. D., Valisetty, R. R., and Rehfield, L. W., "Continuous Filament Wound Composite Concepts for Aircraft Fuselage Structures," *J. Aircraft*, Vol. 22, No. 3, March 1985, pp. 249-255.

96. Shaw, I. S. and Simitses, G. J., "Nonlinear Analysis of Axially-Loaded Laminated Cylindrical Shells," *Computers and Structures*, Vol. 16, No. 1-4, 1983, pp. 131-137.

97. Franklin, H. G., "Membrane Solution of the Spirally Corrugated Shell," *AIAA Journal*, Vol. 5, No. 2, Feb. 1967, pp. 295-300.

98. Pappas, M. and Amba-Rao, C. L., "Structural Synthesis of Thin Cylindrical Shells with Spiral-Type Stiffeners," *AIAA Journal*, Vol. 8, No. 8, Aug. 1970, pp. 1529-1530.

99. Karmakar, R. "Axially Compressed Optimum Cylinder-Comparison of Stiffener Configurations," *J. Spacecraft*, Vol. 17, No. 5, Sept.-Oct. 1980, pp. 477-479.

100. Egle, D. M. and Sewall, J. L., "An Analysis of Free Vibrations of Orthogonally Stiffened Cylindrical Shells with Stiffeners Treated as Discrete Elements," *AIAA Journal*, Vol. 6, No. 3, March 1968, pp. 518-526.

101. McDonald, D., "A Problem in the Free Vibration of Stiffened Cylindrical Shells," *AIAA Journals*, Vol. 8, No. 2, Feb. 1970, pp. 252-258.

102. Rinehart, S. A. and Wang, J. T. S., "Vibrations of Simply Supported Cylindrical Shells with Longitudinal Stiffeners," *J. of Sound and Vibration*, Vol. 24, No. 2, 1972, pp. 151-163.

103. Wang, J. T. S. and Rinehart, S. A., "Free Vibrations of Longitudinally Stiffened Cylindrical Shells," *J. Appl. Mech.*, Vol. 41, 1974, pp. 1087-1093.

104. Moe, J. "Stability of Rib-Reinforced Cylindrical Shells Under Lateral Pressure," *Publications*, Vol. 18, 1958, International Association for Bridge and Structural Engineering, pp. 113-136.

105. Van der Neut, A., "General Instability of Orthogonally Stiffened Cylindrical Shells," NASA TN D-1510, 1962, pp. 309-319.

106. MacNeal, K. H., Winemiller, A. F., and Baile, J. A., "Elastic Stability of Cylindrical Shells Reinforced by One or Two Frames and Subjected to External Radial Pressure," *AIAA Journal*, Vol. 4, No. 8, Aug. 1966, pp. 1431-1433.

107. Singer, J. and Haftka, R., "Buckling of Discretely Ring Stiffened Cylindrical Shells," TAE Rept. 67, Aug. 1967, Israel Inst. of Technology, Haifa.

108. Wang, J. T. S., "Orthogonally Stiffened Cylindrical Shells Subjected to Internal Pressure," *AIAA Journal*, Vol. 6, 1970, pp. 455-461.

109. Wang, J. T. S. and Lin, Y. J., "Stability of Discretely Stringer-Stiffened Cylindrical Shells," *AIAA Journal*, Vol. 11, No. 6, June 1973, pp. 810-814.

110. Wang, J. T. S. and Hsu, T. M., "Discrete Analysis of Stiffened Composite Cylindrical Shells," *AIAA Journal*, Vol. 23, No. 11, Nov. 1985, pp. 1753-1761.

111. Pochtman, Y. M. and Tugai, O. V., "Stability and Optimal Design of Multilayer Composite Cylindrical Shells Stiffened with a Polyregular System of Cross Ribs," *Mechanics of Composite Materials*, Vol. 15, No. 1, July 1979, pp. 77-83.

112. Chao, C. C., Kuo, W. S., and Lin, I. S., "Buckling of Unstiffened/Stiffened Orthotropic Foam Sandwich Cylindrical Shells," *Composite Structures 3*, 1985, pp. 452-467.

113. Birman, V., "Divergence Instability of Reinforced Composite Cylindrical Shells," *Recent Advances in the Marco- and Micro- Mechanics of Composite Materials and Structures. Proceedings of the Symposium*, ASME Winter Annual Meeting, Chicago, Il., Nov. 27 - Dec. 2, 1988, NY, ASME, pp. 169-175.

114. Lee, R. L. and Lu, S. Y., "General Instability of Inclined-Stiffened Cylinders Under Bending," *J. Appl. Mech.*, Sept. 1969, pp. 403-407.

115. Stephens, W. B., "Imperfection Sensitivity of Axially Compressed Stringer Reinforced Cylindrical Panels Under Internal Pressure," *AIAA Journal*, Vol. 9, No. 9, Sept. 1971, pp. 1713-1719.

116. Tvergaard, V., "Buckling of Elastic-Plastic Cylindrical Panel Under Axial Compression," *Int. J. Solids and Struct.*, Vol. 13, 1977, pp. 957-970.

117. Reddy, B. D., "Buckling of Elastic-Plastic Discretely Stiffened Cylinders in Axial Compression," *Int. J. Solids and Struct.*, Vol. 16, 1980, pp. 313-328.

118. Budiansky, B. and Hu, P. C., "The Lagrangian Multiplier Method of Finding Upper and Lower Limits to Critical Stresses of Clamped Plates," NACA TN No. 1103, 1946.

119. Budiansky, B., Hu, P. C., and Conor, R. W., "Notes on the Lagrangian Multiplier Method In Elastic-Stability Analysis," NACA, TN No. 1558, May 1948.

120. Al-Shareedah, E. M. and Seireg, A. A., "Use of Undetermined Multipliers in the Solution of Complex Plate Problems," *Computers in Mechanical Engineering*, Vol. 4, No. 3, Nov. 1985, pp. 59-68.

121. Al-Shareedah, E. M. and Seireg, A. A., "The Design of Slabs With Constraining Columns Using the Undetermined Multiplier Method," *Computers in Mechanical Engineering*, Vol. 4, No. 4, Jan. 1986, pp. 59-68.

122. Al-Shareedah, E. M. and Seireg, A. A., "Use of Undetermined Multipliers in the Design of Stiffened Plates," *Computers in Mechanical Engineering*, Vol. 4, No. 5, March 1986, pp. 57-64.

123. Phillips, J. L. and Gürdal, Z., *Structural Analysis and Optimum Design of Geodesically Stiffened Composite Panels*, Virginia Polytechnic Institute and State University, CCMS-90-05, July 1990.

124. Johnson, E. R. and Rastogi, N., "Interacting Loads in an Orthogonally Stiffened Composite Cylindrical Shell," *35th Structures, Structural Dynamics, and Materials Conference*, April 18-22, 1994, AIAA-94-1646, Part 5, pp. 2607-2620.

125. Mukhopadhyay, M., "Stiffened Plate Plane Stress Elements for the Analysis of Ships' Structures," *Comput. Struct.*, Vol. 13, 1981, pp. 563-573.

126. Mukhopadhyay, M. and Satsangi, S. K., "Isoparametric Stiffened Plate Bending Element for the Analysis of Ships' Structures," *Trans. R. Inst. Naval Arch.*, 1983, pp. 141-151.

127. Thompson, P. A., Bettess, P., and Caldwell, J. B., "An Isoparametric Eccentrically Stiffened Plate Bending Element," *Eng. Comput.*, Vol. 5, June 1988, pp. 110-116.

128. Deb, A. and Booton, M., "Finite Element Models for Stiffening Plates Under Transverse Loading," *Comput. Struct.*, Vol. 28, No. 3, 1988, pp. 361-372.

129. Yurkovich, R. N., Schmidt, J. H., and Zak, A. R., "Dynamic Analysis of Stiffened Panel Structures," *J. Aircraft*, Vol. 8, No. 3, March 1971, pp. 149-155.

130. Nair, P. S. and Rao, M. S., "On Vibration of Plates with Varying Stiffener Length," *J. Sound and Vibration*, Vol. 95, No. 1, 1984, pp. 19-29.

131. Kohnke, P. C. and Schnobrich, N. C., "Analysis of Eccentrically Stiffened Cylindrical Shells," *J. Struct. Div.*, ASCE, Vol. 98, St. 7, July 1972, pp. 1493-1510.

132. Venkatesh, A. and Rao, K. P., "A Laminated Anisotropic Curved Beam and Shell Stiffening Finite Element," *Computers and Structures*, Vol. 15, No. 2, 1982, pp. 197-201.

133. Venkatesh, A. and Rao, K. P., "Analysis of Laminated Shells With Laminated Stiffeners Using Rectangular Shell Finite Elements," *Comp. Meth. Appl. Mech.*, Vol. 38, 1983, pp. 255-272.

134. Venkatesh, A. and Rao, K. P., "Analysis of Laminated Shells of Revolution with Laminated Stiffeners Using a Doubly Curved Quadrilateral Finite Element," *Computers and Structures*, Vol. 20, No. 4, 1985, pp. 669-682.

135. Venkatesh, A., Ramana Murthy, P. V., and Rao, K. P., "Finite Element Analysis of Bimodulus Composite Stiffened Thin Shells of Revolution," *Computers and Structures*, Vol. 22, No. 1, 1986, pp. 13-24.

136. Bhimaraddi, A., Carr, A. J., and Moss, P. J., "Finite Element Analysis of Laminated Shells of Revolution With Laminated Stiffeners," *Computers and Structures*, Vol. 33, No. 1, 1989, pp. 295-305.

137. Ferguson, G. H. and Clark, R. D., "A Variable Thickness, Curved Beam and Shell Stiffening Element With Shear Deformation," *Int. J. Num. Meth. Eng.*, Vol. 14, 1979, pp. 581-592.

138. Liao, C. L. and Reddy, J. N., "Continuum-Based Stiffened Composite Shell Element for Geometrically Nonlinear Analysis," *AIAA Journal*, Vol. 27, No. 1, Jan. 1989, pp. 95-101.

139. Liao, C. L. and Reddy, J. N., "Analysis of Anisotropic, Stiffened Composite Laminates Using a Continuum-Based Shell Element," *Computers and Structures*, Vol. 34, No. 6, 1990, pp. 805-815.

140. Carr, A. J. and Clough, R. W., "Dynamic Earthquake Behaviour of Shell Roofs," *Fourth World Conf. on Earthquake Engineering* , Santiago, Chile, 1969, pp. 171-185.

141. Sandhu, J. S., Stevens, K. A., and Davies, G. A. O., "Torsional Buckling and Post-Buckling of Composite Geodetic Cylinders with Special Reference to Joint Flexibility," *Composite Structures*, 15, 1990, pp. 301-322.

142. Hansen, J. S. and Tennyson, R. C., "Study of the Dynamic Behaviour of Stiffened Composite Fuselage Shell Stuctures," *Energy Absorption of Aircraft Stuctures as an Aspect of Crashworthiness*, AGARD-CP-433, 1988, pp. 15-1 - 15-12.

143. Leissa, A. W. and Qatu, M., "Stress and Deflection Analysis of Composite Cantilevered Shallow Shells," *Journal of Engineering Mechanics*, Vol. 117, No. 4, April 1991, pp. 893-906.

144. Boitnott, R. L., Johnson, E. R., and Starnes, J. H., "Nonlinear Response and Failure Characteristics of Internally Pressurized Composite Cylindrical Panels," Virginia Polytechnic Institute and State University, CCMS-85-07, June 1985.

145. Spier, E. E., "Crippling/Column Buckling Analysis and Test of Graphite/Epoxy Stiffened Panels," *AIAA/ASME/SAE 16th Structures, Structural Dynamics and Materials Conference*, Denver, CO, May 27-29, 1975, pp. 1-16.

146. Sandhu, R. S., "A Survey of Failure Theories of Isotropic and Anisotropic Materials," Technical Report, AFFDL-TR-72-71.

147. Tsai, S. W., "A Survey of Macroscopic Failure Criteria for Composite Materials," Technical Report, AFWAL-TR-84-4025.

148. Tsai, S. W. and Hahn, H. T., "Failure Analysis of Composite Materials," *Inelastic Behavior of Composite Materials*, ASME, 1975, pp. 73-96.

149. Nahas, M. N., "Survey of Failure and Post-Failure Theories of Laminated Fibre-Reinforced Composites," *J. Composites Tech. and Research*, Vol. 8, 1986, pp. 138-153.

150. Hill, R., *The Mathematical Theory of Plasticity*, Oxford University Press, 1950.

151. Azzi, V. D. and Tsai, S. W., "Anisotropic Strength of Composites," *Experimental Mechanics*, Vol. 5, 1965, pp. 283-288.

152. Chamis, C. C., "Failure Criteria for Filamentary Composites," *Composite Materials: Testing and Design, STP 460*, ASTM, Philadelphia, PA, 1969, pp. 336-351.

153. Hoffman, O., "The Brittle Strength of Orthotropic Materials," *J. Composite Materials*, Vol. 1, 1967, pp. 200-206.

154. Tsai, S. W. and Wu, E. M., "A General Theory of Strength for Anisotropic Materials," *J. Composite Materials*, Vol. 5, Jan. 1971, pp. 58-80.

155. Hashin, Z., "Failure Criteria for Unidirectional Fiber Composites," *J. Appl. Mech.*, Vol. 47, June 1980, pp. 329-334.

156. Craddock, J. N. and Zak, A. R., "Nonlinear Response of Composite Material Structures," *J. Composite Materials*, Vol. 11, April 1977, pp. 204-221.

157. Sanders, R. C., Edge, E. C., and Grant, P., "Basic Failure Mechanisms of Laminated Composites and Related Aircraft Design Implications," *Composite Structures 2, Proceedings of the 2nd Int. Conf. on Composite Materials*, Scotland, 1983, pp. 467-484.

158. Cope, R. D. and Pipes, R. B., "Design of the Composite Spar-Wingskin Joint," *Composites*, Jan. 1982, pp. 47-53.

159. Reddy, J. N. and Pandey, A. K., "A First-Ply Failure Analysis of Composite Laminates," *Computers and Structures*, Vol. 25, No. 3, 1987, pp. 371-393.

160. Kim, R. Y. and Soni, S. R., "Experimental and Analytical Studies On the Onset of Delamination In Laminated Composites," *J. Composite Materials*, Vol. 18, Jan. 1984, pp. 70-80.

161. Kim, R. Y. and Soni, S. R., "Failure of Composite Laminates Due to Combined Interlaminar Normal and Shear Stresses," *Composites '86: Recent Advances in Japan and the United States*, K. Kawata, S. Umekawa, and A. Kobayashi (editors), Tokyo, 1986, pp. 341-350.

162. Brewer, J. C. and Lagace, P. A., "Quadratic Stress Criterion for Initiation of Delamination," *J. Composite Materials*, Vol. 22, Dec. 1988, pp. 1141-1155.

163. Reddy, J. N., *An Introduction to the Finite Element Method*, McGraw-Hill, NY, 1984.

164. Bhimaraddi, A. and Chandrashekhara, K., "Some Observations on the Modeling of Laminated Composite Beams with General Lay-ups," *Composite Struct.*, Vol. 19, 1991, pp. 371-380.

165. Kassegne, S. K., *Layerwise Theory for Discre[illegible] Stiffened Laminated Cylindrical Shells*, Virginia Polytechnic Institute and Sta[illegible] University, December 1992.

166. Jones, R. M., *Mechanics of Composite Materials*, Hemisphere Publishing Corp., NY, 1975.

167. Reddy, J. N., *Energy and Variational Methods in Applied Mechanics*, John-Wiley and Sons, Inc., 1984.

168. Ugural, A. C., *Stresses in Plates and Shells*, McGraw-Hill, NY, 1981.

169. Soedel, W., *Vibrations of Shells and Plates*, Marcel Dekker, Inc., 1981.

170. Cook, Robert D., *Concepts and Applications of Finite Element Analysis*, John Wiley and Sons, NY, 1981.

171. Chaudhuri, R. A. and Seide, P., "An Approximate Semi-Analytical Method for Prediction of Interlaminar Shear Stresses in an Arbitrarily Laminated Thick Plate," *Computers and Structures*, Vol. 25, No. 4, 1987, pp. 627-636.

172. Barbero, E. J. and Reddy, J. N., *On a Generalized Laminate Plate Theory with Application to Bending, Vibration, and Delamination Buckling in Composite Laminates*, Virginia Polytechnic Institute and State University, CCMS-89-20, Oct. 1989.

173. Chaudhuri, R. A., "An Equilibrium Method for Prediction of Transverse Shear Stresses in a Thick Laminated Plate," *Computers and Structures*, Vol. 23, No. 2, 1986, pp. 139-146.

174. Engblom, J. J. and Ozden, O. O., "Finite Element Formulation Including Interlaminar Stress Calculations," *Computers and Structures*, Vol. 23, No. 2, 1986, pp. 241-249.

175. Byun, C. and Kapania, R. K., "Prediction of Interlaminar Stresses in Laminated Plates Using Global Orthogonal Interpolation Polynomials," *AIAA Journal*, Vol. 30, No. 11, Nov. 1992, pp. 2740-2749.

176. Rao, K. P., "A Rectangular Laminated Anisotropic Shallow Thin Shell Finite Element," *Comput. Meth. Appl. Mech. Eng.*, Vol. 15, 1978, pp. 13-33.

177. Scordelis, A. C. and Lo, K. S, "Computer Analysis of Cylindrical Shells," *J. Am. Concr. Inst.*, Vol. 61, May 1964, pp. 539-561.

178. Zienkiewicz, O. C., Taylor, R. L., and Too, J. M., "Reduced Integration Techniques in General Analysis of Plates and Shells," *Int. J. Num. Meth. Eng.*, Vol. 3, 1971, pp. 275-290.

179. Pawsey, S. F. and Clough, R. W., "Improved Numerical Integration of Thick Shell Finite Elements," *Int. J. Num. Meth. Eng.*, Vol. 3, 1971, pp. 575-586.

180. Sander, G. and Idelsohn, S., "A Family of Conforming Finite Elements for Deep Shell Analysis," *Int. J. Num. Meth. Eng.*, Vol. 18, 1982, pp. 363-380.

181. Kiciman, O. K. and Popov, E. P., "A General Finite Element Model for Shells of Arbitrary Geometry," *Comput. Meth. Appl. Mech. Eng.*, Vol. 13, 1978, pp. 45-58.

182. Palmerio, A. F., *On a Moderate Rotation Theory for Anisotropic Shells*, Ph.D. Dissertation, Virginia Polytechnic Institute and State University, Blacksburg, VA, 1988.

183. Liao, C. L., *An Incremental Total Lagrangian Formulation for General Anisotropic Shell-Type Structures*, Ph.D. Dissertation, Virginia Polytechnic Institute and State University, Blacksburg, VA, 1987.

184. Roark, R. J. and Young, W. C., *Formulas for Stress and Strain*, Fifth Edition, McGraw-Hill, NY, 1961.

185. Khdeir, A. A., Reddy, J. N. and Frederick, D., "A Study of Bending, Vibration and Buckling of Cross-Ply Circular Cylindrical Shells," *Int. J. Engng. Sci.*, Vol. 27, No. 11, 1989, pp. 1337-1351.

186. Gendron, G. and Gürdal, Z., "Optimal Design of Geodesically Stiffened Composite Cylindrical Shells," *AIAA Conference 1992*, pp. 1 - 11.

187. Stewart, C. B. (compiler), "The Computational Structural Mechanics Testbed User's Manual," NASA TM-100644, 1989.

188. Knight, N. F., Jr., Gillian, R. E., McCleary, S. L., Lotts, C. G., Poole, E. L., Overman, A. L., and Macy, S. C., "CSM Testbed Development and Large-Scale Structural Applications," NASA TM-4072, 1989.

Appendix A

Nonlinear Variational Statement for Laminated Shells

Nonlinear Variational Statement

$$
\begin{aligned}
\delta\Pi = \int_\Omega \Bigg\{ & \Bigg[D_{11}^{ij}\frac{\partial u_j}{\partial x} + D_{12}^{ij}\left(\frac{\partial v_j}{\partial y} + \frac{w_j}{R}\right) + \overline{D}_{13}^{ij} w_j + D_{16}^{ij}\left(\frac{\partial u_j}{\partial y} + \frac{\partial v_j}{\partial x}\right) \\
& + \frac{1}{2} D_{11}^{ijk}\frac{\partial w_j}{\partial x}\frac{\partial w_k}{\partial x} + D_{16}^{ijk}\frac{\partial w_j}{\partial x}\frac{\partial w_k}{\partial y} + \frac{1}{2} D_{12}^{ijk}\frac{\partial w_j}{\partial y}\frac{\partial w_k}{\partial y} \Bigg]\left(\frac{\partial \delta u_i}{\partial x}\right) \\
& + \Bigg[D_{12}^{ij}\frac{\partial u_j}{\partial x} + D_{22}^{ij}\left(\frac{\partial v_j}{\partial y} + \frac{w_j}{R}\right) + \overline{D}_{23}^{ij} w_j + D_{26}^{ij}\left(\frac{\partial u_j}{\partial y} + \frac{\partial v_j}{\partial x}\right) \\
& + \frac{1}{2} D_{12}^{ijk}\frac{\partial w_j}{\partial x}\frac{\partial w_k}{\partial x} + D_{26}^{ijk}\frac{\partial w_j}{\partial x}\frac{\partial w_k}{\partial y} + \frac{1}{2} D_{22}^{ijk}\frac{\partial w_j}{\partial y}\frac{\partial w_k}{\partial y} \Bigg]\left(\frac{\partial \delta v_i}{\partial y} + \frac{\delta w_i}{R}\right) \\
& + \Bigg[D_{16}^{ij}\frac{\partial u_j}{\partial x} + D_{26}^{ij}\left(\frac{\partial v_j}{\partial y} + \frac{w_j}{R}\right) + \overline{D}_{36}^{ij} w_j + D_{66}^{ij}\left(\frac{\partial u_j}{\partial y} + \frac{\partial v_j}{\partial x}\right) \\
& + \frac{1}{2} D_{16}^{ijk}\frac{\partial w_j}{\partial x}\frac{\partial w_k}{\partial x} + D_{66}^{ijk}\frac{\partial w_j}{\partial x}\frac{\partial w_k}{\partial y} + \frac{1}{2} D_{26}^{ijk}\frac{\partial w_j}{\partial y}\frac{\partial w_k}{\partial y} \Bigg]\left(\frac{\partial \delta u_i}{\partial y} + \frac{\partial \delta v_i}{\partial x}\right) \\
& + \left[\overline{\overline{D}}_{55}^{ij} u_j + \overline{D}_{55}^{ji}\frac{\partial w_j}{\partial x} + \overline{\overline{D}}_{45}^{ij} v_j + \overline{D}_{45}^{ji}\left(\frac{\partial w_j}{\partial y} - \frac{v_j}{R}\right)\right](\delta u_i) \\
& + \left[\overline{\overline{D}}_{45}^{ij} u_j + \overline{D}_{45}^{ji}\frac{\partial w_j}{\partial x} + \overline{\overline{D}}_{44}^{ij} v_j + \overline{D}_{44}^{ji}\left(\frac{\partial w_j}{\partial y} - \frac{v_j}{R}\right)\right](\delta v_i) \\
& + \Bigg[\overline{D}_{13}^{ji}\frac{\partial u_j}{\partial x} + \overline{D}_{23}^{ji}\left(\frac{\partial v_j}{\partial y} + \frac{w_j}{R}\right) + \overline{\overline{D}}_{33}^{ij} w_j + \overline{D}_{36}^{ji}\left(\frac{\partial u_j}{\partial y} + \frac{\partial v_j}{\partial x}\right) \\
& + \frac{1}{2}\overline{D}_{13}^{jki}\frac{\partial w_j}{\partial x}\frac{\partial w_k}{\partial x} + \overline{D}_{36}^{jki}\frac{\partial w_j}{\partial x}\frac{\partial w_k}{\partial y} + \frac{1}{2}\overline{D}_{23}^{jki}\frac{\partial w_j}{\partial y}\frac{\partial w_k}{\partial y} \Bigg](\delta w_i) \\
& + \left[\overline{D}_{55}^{ij} u_j + D_{55}^{ij}\frac{\partial w_j}{\partial x} + \overline{D}_{45}^{ij} v_j + D_{45}^{ij}\left(\frac{\partial w_j}{\partial y} - \frac{v_j}{R}\right)\right]\left(\frac{\partial \delta w_i}{\partial x}\right) \\
& + \left[\overline{D}_{45}^{ij} u_j + D_{45}^{ij}\frac{\partial w_j}{\partial x} + \overline{D}_{44}^{ij} v_j + D_{44}^{ij}\left(\frac{\partial w_j}{\partial y} - \frac{v_j}{R}\right)\right]\left(\frac{\partial \delta w_i}{\partial y} - \frac{\delta v_i}{R}\right) \\
& + \Bigg[D_{11}^{ijk}\frac{\partial u_k}{\partial x} + D_{12}^{ijk}\left(\frac{\partial v_k}{\partial y} + \frac{w_k}{R}\right) + \overline{D}_{13}^{ijk} w_k + D_{16}^{ijk}\left(\frac{\partial u_k}{\partial y} + \frac{\partial v_k}{\partial x}\right)
\end{aligned}
$$

$$+\frac{1}{2}D_{11}^{ijkl}\frac{\partial w_k}{\partial x}\frac{\partial w_l}{\partial x}+D_{16}^{ijkl}\frac{\partial w_k}{\partial x}\frac{\partial w_l}{\partial y}+\frac{1}{2}D_{12}^{ijkl}\frac{\partial w_k}{\partial y}\frac{\partial w_l}{\partial y}\Bigg]\left(\frac{\partial \delta w_i}{\partial x}\frac{\partial w_j}{\partial x}\right)$$

$$+\left[D_{12}^{ijk}\frac{\partial u_k}{\partial x}+D_{22}^{ijk}\left(\frac{\partial v_k}{\partial y}+\frac{w_k}{R}\right)+\overline{D}_{23}^{ijk}w_k+D_{26}^{ijk}\left(\frac{\partial u_k}{\partial y}+\frac{\partial v_k}{\partial x}\right)\right.$$

$$\left.+\frac{1}{2}D_{12}^{ijkl}\frac{\partial w_k}{\partial x}\frac{\partial w_l}{\partial x}+D_{26}^{ijkl}\frac{\partial w_k}{\partial x}\frac{\partial w_l}{\partial y}+\frac{1}{2}D_{22}^{ijkl}\frac{\partial w_k}{\partial y}\frac{\partial w_l}{\partial y}\right]\left(\frac{\partial \delta w_i}{\partial y}\frac{\partial w_j}{\partial y}\right)$$

$$+\left[D_{16}^{ijk}\frac{\partial u_k}{\partial x}+D_{26}^{ijk}\left(\frac{\partial v_k}{\partial y}+\frac{w_k}{R}\right)+\overline{D}_{36}^{ijk}w_k+D_{66}^{ijk}\left(\frac{\partial u_k}{\partial y}+\frac{\partial v_k}{\partial x}\right)\right.$$

$$\left.+\frac{1}{2}D_{16}^{ijkl}\frac{\partial w_k}{\partial x}\frac{\partial w_l}{\partial x}+D_{66}^{ijkl}\frac{\partial w_k}{\partial x}\frac{\partial w_l}{\partial y}+\frac{1}{2}D_{26}^{ijkl}\frac{\partial w_k}{\partial y}\frac{\partial w_l}{\partial y}\right]\times$$

$$\left.\left(\frac{\partial \delta w_i}{\partial x}\frac{\partial w_j}{\partial y}+\frac{\partial w_i}{\partial x}\frac{\partial \delta w_j}{\partial y}\right)-q\delta w_i\right\}dx\,dy+\delta V$$

Appendix B

Ritz Stiffness and Mass Terms

Stiffness Terms

i = 1, 2, 3, ..., NINT (# of interfaces)

m = 1, 2, 3, ..., M (mode shape)

n = 1, 2, 3, ..., N (mode shape)

NS = # of stiffeners

NC = # of constraint points per stiffener

$$[K_{11}] = \sum_{j=1}^{NINT} \frac{LL_c}{4}\left[D_{11}^{ij}\alpha_m{}^2 + D_{66}^{ij}\beta_n{}^2 + \bar{\bar{D}}_{55}^{ij}\right]$$

$$[K_{12}] = \sum_{j=1}^{NINT} \frac{LL_c}{4}\left[-\alpha_m\beta_n\left(D_{12}^{ij} + D_{66}^{ij}\right)\right]$$

$$[K_{13}] = \sum_{j=1}^{NINT} \frac{LL_c}{4}\left[-\alpha_m\left(\frac{1}{R}D_{12}^{ij} + \bar{D}_{13}^{ij} - \bar{D}_{55}^{il}\right)\right]$$

$$[K_{1,8}] = \sum_{j=1}^{NS}\sum_{p=1}^{NC} \cos\alpha_m x_{jp} \cos\beta_n y_{jp}$$

$$[K_{21}] = \sum_{j=1}^{NINT} \frac{LL_c}{4}\left[-\alpha_m\beta_n\left(D_{12}^{ij} + D_{66}^{ij}\right)\right]$$

$$[K_{22}] = \sum_{j=1}^{NINT} \frac{LL_c}{4}\left[D_{66}^{ij}\alpha_m{}^2 + D_{22}^{ij}\beta_n{}^2 + \bar{\bar{D}}_{44}^{ij} - \frac{1}{R}\left(\bar{D}_{44}^{ij} + \bar{D}_{44}^{il}\right) + \frac{1}{R^2}D_{44}^{ij}\right]$$

$$[K_{23}] = \sum_{j=1}^{NINT} \frac{LL_c}{4}\left[\left(\beta_n\frac{1}{R}D_{22}^{ij} + \frac{1}{R}D_{44}^{ij} + \bar{D}_{23}^{ij} - \bar{D}_{44}^{il}\right)\right]$$

$$[K_{2,10}] = \sum_{j=1}^{NS}\sum_{p=1}^{NC} \sin\alpha_m x_{jp} \sin\beta_n y_{jp}$$

$$[K_{31}] = \sum_{j=1}^{NINT} \frac{LL_c}{4}\left[-\alpha_m\left(\frac{1}{R}D_{12}^{ij} + \bar{D}_{13}^{ij} - \bar{D}_{55}^{ij}\right)\right]$$

$$[K_{32}] = \sum_{j=1}^{NINT} \frac{LL_c}{4}\left[\beta_n\left(\frac{1}{R}D_{22}^{ij} + \frac{1}{R}D_{44}^{ij} + \overline{D}_{23}^{jl} - \overline{D}_{44}^{ij}\right)\right]$$

$$[K_{33}] = \sum_{j=1}^{NINT} \frac{LL_c}{4}\left[D_{55}^{ij}\alpha_m{}^2 + D_{44}^{ij}\beta_n{}^2 + \frac{1}{R^2}D_{22}^{ij} + \frac{1}{R}\overline{D}_{23}^{ij} + \frac{1}{R}\overline{D}_{23}^{jl} + \bar{\bar{D}}_{33}^{jl}\right]$$

$$[K_{39}] = \sum_{j=1}^{NS}\sum_{p=1}^{NC} \sin\alpha_m x_{jp} \cos\beta_n y_{jp}$$

$$[K_{3,11}] = \sum_{j=1}^{NS}\sum_{p=1}^{NC} \sin\alpha_m x_{jp} \cos\beta_n y_{jp}$$

$$[K_{44}] = \sum_{l=1}^{NS} \frac{L_s^l}{2}\left[E_s^l A_s^l \alpha_k{}^2\right]$$

$$[K_{45}] = \sum_{l=1}^{NS} \frac{L_s^l}{2}\left[E_s^l A_s^l\left(-\frac{\alpha_k}{R'} - \bar{\zeta}_s^l \alpha_k{}^3\right)\right]$$

$$[K_{48}] = -\sum_{j=1}^{NS}\sum_{p=1}^{NC} \cos\alpha_k \eta_{jp}$$

$$[K_{54}] = \sum_{l=1}^{NS} \frac{L_s^l}{2}\left[E_s^l A_s^l\left(-\frac{\alpha_k}{R'} - \bar{\zeta}_s^l \alpha_k{}^3\right)\right]$$

$$[K_{55}] = \sum_{l=1}^{NS} \frac{L_s^l}{2}\left[E_s^l I_s^l \alpha_k{}^4 + E_s^l A_s^l\left(\frac{2\bar{\zeta}_s^l}{R'}\alpha_k{}^2 + \frac{1}{R'^2}\right)\right]$$

$$[K_{59}] = -\sum_{j=1}^{NS}\sum_{p=1}^{NC} \sin\alpha_k \eta_{jp}$$

$$[K_{66}] = \sum_{l=1}^{NS} \frac{L_s^l}{2}\left[E_s^l A_s^l \beta_l{}^2\right]$$

$$[K_{67}] = \sum_{l=1}^{NS} \frac{L_s^l}{2}\left[E_s^l A_s^l\left(\frac{\beta_l}{R'} + \bar{\zeta}_s^l \beta_l{}^3\right)\right]$$

$$[K_{6,10}] = -\sum_{j=1}^{NS}\sum_{p=1}^{NC} \sin\beta_l \eta_{jp}$$

$$[K_{76}] = \sum_{l=1}^{NS} \frac{L_s^l}{2} \left[E_s^i A_s^i \left(\frac{\beta_l}{R'} + \bar{\zeta}_s^i \beta_l^3 \right) \right]$$

$$[K_{77}] = \sum_{l=1}^{NS} \frac{L_s^l}{2} \left[E_s^i I_s^i \beta_l^4 + E_s^i A_s^i \left(\frac{2\bar{\zeta}_s^i}{R'} \beta_l^2 + \frac{1}{R'^2} \right) \right]$$

$$[K_{7,11}] = -\sum_{j=1}^{NS} \sum_{p=1}^{NC} \cos \beta_l \eta_{jp}$$

$$[K_{81}] = \sum_{j=1}^{NS} \sum_{p=1}^{NC} \cos \alpha_m x_{jp} \cos \beta_n y_{jp}$$

$$[K_{84}] = -\sum_{j=1}^{NS} \sum_{p=1}^{NC} \cos \alpha_k \eta_{jp}$$

$$[K_{93}] = \sum_{j=1}^{NS} \sum_{p=1}^{NC} \sin \alpha_m x_{jp} \cos \beta_n y_{jp}$$

$$[K_{95}] = -\sum_{j=1}^{NS} \sum_{p=1}^{NC} \sin \alpha_k \eta_{jp}$$

$$[K_{10,2}] = \sum_{j=1}^{NS} \sum_{p=1}^{NC} \sin \alpha_m x_{jp} \sin \beta_n y_{jp}$$

$$[K_{10,6}] = -\sum_{j=1}^{NS} \sum_{p=1}^{NC} \sin \beta_l \eta_{jp}$$

$$[K_{11,3}] = \sum_{j=1}^{NS} \sum_{p=1}^{NC} \sin \alpha_m x_{jp} \cos \beta_n y_{jp}$$

$$[K_{11,7}] = -\sum_{j=1}^{NS} \sum_{p=1}^{NC} \cos \beta_l \eta_{jp}$$

Mass Terms

$$[M_{33}] = -\frac{LL_c}{4}\left[\hat{N}_1\alpha_m{}^2 + \hat{N}_2\beta_n{}^2\right]$$

$$[M_{55}] = -\sum_{l=1}^{NS}\frac{L_s^l}{2}\hat{F}_s^l\alpha_k{}^2$$

$$[M_{77}] = -\sum_{l=1}^{NS}\frac{L_s^l}{2}\hat{F}_s^l\beta_l{}^2$$

Appendix C

Finite Element Stiffness Terms

C.1 Layerwise Shell Element Direct Stiffness Terms

$$[K_{11}^{mn}] = \int_{\Omega_e} \left\{ \frac{\partial \psi^m}{\partial x} D_{11}^{ij} \frac{\partial \psi^n}{\partial x} + \frac{\partial \psi^m}{\partial x} D_{16}^{ij} \frac{\partial \psi^n}{\partial y} + \frac{\partial \psi^m}{\partial y} D_{16}^{ij} \frac{\partial \psi^n}{\partial x} + \frac{\partial \psi^m}{\partial y} D_{66}^{ij} \frac{\partial \psi^n}{\partial y} + \psi^m \bar{\bar{D}}_{55}^{ij} \psi^n \right\} dx\, dy$$

$$[K_{12}^{mn}] = \int_{\Omega_e} \left\{ \frac{\partial \psi^m}{\partial x} D_{12}^{ij} \frac{\partial \psi^n}{\partial y} + \frac{\partial \psi^m}{\partial x} D_{16}^{ij} \frac{\partial \psi^n}{\partial x} + \frac{\partial \psi^m}{\partial y} D_{26}^{ij} \frac{\partial \psi^n}{\partial y} + \frac{\partial \psi^m}{\partial y} D_{66}^{ij} \frac{\partial \psi^n}{\partial x} + \psi^m \bar{\bar{D}}_{45}^{ij} \psi^n - \psi^m \bar{D}_{45}^{ij} \frac{\psi^n}{R} \right\} dx\, dy$$

$$\begin{aligned}[K_{13}^{mn}] = \int_{\Omega_e} \Bigg\{ & \left[\frac{\partial \psi^m}{\partial x} D_{12}^{ij} \frac{\psi^n}{R} + \frac{\partial \psi^m}{\partial x} \bar{D}_{13}^{ij} \psi^n + \frac{\partial \psi^m}{\partial y} D_{26}^{ij} \frac{\psi^n}{R} + \frac{\partial \psi^m}{\partial y} \bar{D}_{36}^{ij} \psi^n \right. \\ & \left. + \psi^m \bar{D}_{55}^{ij} \frac{\partial \psi^n}{\partial x} + \psi^m \bar{D}_{45}^{ij} \frac{\partial \psi^n}{\partial y} \right] \\ & + \frac{\partial \psi^m}{\partial x} \left[\frac{1}{2} D_{11}^{ijk} \frac{\partial \psi^n}{\partial x} \frac{\partial w_k}{\partial x} + \frac{1}{2} D_{12}^{ijk} \frac{\partial \psi^n}{\partial y} \frac{\partial w_k}{\partial y} \right. \\ & \left. + \frac{1}{2} D_{16}^{ijk} \left(\frac{\partial \psi^n}{\partial x} \frac{\partial w_k}{\partial y} + \frac{\partial \psi^n}{\partial y} \frac{\partial w_k}{\partial x} \right) \right] \\ & + \frac{\partial \psi^m}{\partial y} \left[\frac{1}{2} D_{16}^{ijk} \frac{\partial \psi^n}{\partial x} \frac{\partial w_k}{\partial x} + \frac{1}{2} D_{26}^{ijk} \frac{\partial \psi^n}{\partial y} \frac{\partial w_k}{\partial y} \right. \\ & \left. + \frac{1}{2} D_{66}^{ijk} \left(\frac{\partial \psi^n}{\partial x} \frac{\partial w_k}{\partial y} + \frac{\partial \psi^n}{\partial y} \frac{\partial w_k}{\partial x} \right) \right] \Bigg\} dx\, dy \end{aligned}$$

$$[K_{21}^{mn}] = \int_{\Omega_e} \left\{ \frac{\partial \psi^m}{\partial y} D_{12}^{ij} \frac{\partial \psi^n}{\partial x} + \frac{\partial \psi^m}{\partial y} D_{26}^{ij} \frac{\partial \psi^n}{\partial y} + \frac{\partial \psi^m}{\partial x} D_{16}^{ij} \frac{\partial \psi^n}{\partial x} + \frac{\partial \psi^m}{\partial x} D_{66}^{ij} \frac{\partial \psi^n}{\partial y} + \psi^m \bar{\bar{D}}_{45}^{ij} \psi^n - \psi^m \bar{D}_{45}^{ij} \frac{\psi^n}{R} \right\} dx\, dy$$

$$[K_{22}^{mn}] = \int_{\Omega_e} \left\{ \frac{\partial \psi^m}{\partial y} D_{22}^{ij} \frac{\partial \psi^n}{\partial y} + \frac{\partial \psi^m}{\partial y} D_{26}^{ij} \frac{\partial \psi^n}{\partial x} + \frac{\partial \psi^m}{\partial x} D_{26}^{ij} \frac{\partial \psi^n}{\partial y} + \frac{\partial \psi^m}{\partial x} D_{66}^{ij} \frac{\partial \psi^n}{\partial x} + \psi^m \bar{\bar{D}}_{44}^{ij} \psi^n - \psi^m \bar{D}_{44}^{ij} \frac{\psi^n}{R} - \psi^m \bar{D}_{44}^{ij} \frac{\psi^n}{R} + \psi^m D_{44}^{ij} \frac{\psi^n}{R^2} \right\} dx\, dy$$

$$\begin{aligned}[K_{23}^{mn}] = \int_{\Omega_e} \Bigg\{ & \left[\frac{\partial \psi^m}{\partial y} D_{22}^{ij} \frac{\psi^n}{R} + \frac{\partial \psi^m}{\partial y} \bar{D}_{23}^{ij} \psi^n + \frac{\partial \psi^m}{\partial x} D_{26}^{ij} \frac{\psi^n}{R} + \frac{\partial \psi^m}{\partial x} \bar{D}_{36}^{ij} \psi^n \right. \\ & \left. + \psi^m \bar{D}_{45}^{ij} \frac{\partial \psi^n}{\partial x} + \psi^m \bar{D}_{44}^{ij} \frac{\partial \psi^n}{\partial y} - \frac{\psi^m}{R} D_{45}^{ij} \frac{\partial \psi^n}{\partial x} - \frac{\psi^m}{R} D_{44}^{ij} \frac{\partial \psi^n}{\partial y} \right] \\ & + \frac{\partial \psi^m}{\partial y} \left[\frac{1}{2} D_{12}^{ijk} \frac{\partial \psi^n}{\partial x} \frac{\partial w_k}{\partial x} + \frac{1}{2} D_{22}^{ijk} \frac{\partial \psi^n}{\partial y} \frac{\partial w_k}{\partial y} \right. \\ & \left. + \frac{1}{2} D_{26}^{ijk} \left(\frac{\partial \psi^n}{\partial x} \frac{\partial w_k}{\partial y} + \frac{\partial \psi^n}{\partial y} \frac{\partial w_k}{\partial x} \right) \right] \\ & + \frac{\partial \psi^m}{\partial x} \left[\frac{1}{2} D_{16}^{ijk} \frac{\partial \psi^n}{\partial x} \frac{\partial w_k}{\partial x} + \frac{1}{2} D_{26}^{ijk} \frac{\partial \psi^n}{\partial y} \frac{\partial w_k}{\partial y} \right. \\ & \left. + \frac{1}{2} D_{66}^{ijk} \left(\frac{\partial \psi^n}{\partial x} \frac{\partial w_k}{\partial y} + \frac{\partial \psi^n}{\partial y} \frac{\partial w_k}{\partial x} \right) \right] \Bigg\} dx\, dy \end{aligned}$$

$$
\begin{aligned}
[K_{31}^{mn}] = \int_{\Omega_e} \Bigg\{ \Bigg[& \frac{\psi^m}{R} D_{12}^{ij} \frac{\partial \psi^n}{\partial x} + \psi^m \overline{D}_{13}^{jl} \frac{\partial \psi^n}{\partial x} + \frac{\psi^m}{R} D_{26}^{ij} \frac{\partial \psi^n}{\partial y} + \psi^m \overline{D}_{36}^{jl} \frac{\partial \psi^n}{\partial y} \\
& + \frac{\partial \psi^m}{\partial x} \overline{D}_{55}^{ij} \psi^n + \frac{\partial \psi^m}{\partial y} \overline{D}_{45}^{ij} \psi^n \Bigg] \\
& + \frac{\partial \psi^m}{\partial x} \left[D_{11}^{ijk} \frac{\partial \psi^n}{\partial x} \frac{\partial w_j}{\partial x} + D_{16}^{ijk} \frac{\partial \psi^n}{\partial y} \frac{\partial w_j}{\partial x} \right] \\
& + \frac{\partial \psi^m}{\partial y} \left[D_{12}^{ijk} \frac{\partial \psi^n}{\partial x} \frac{\partial w_j}{\partial y} + D_{26}^{ijk} \frac{\partial \psi^n}{\partial y} \frac{\partial w_j}{\partial y} \right] \\
& + \left(\frac{\partial \psi^m}{\partial x} \frac{\partial w_j}{\partial y} + \frac{\partial \psi^m}{\partial y} \frac{\partial w_j}{\partial x} \right) \left[D_{16}^{ijk} \frac{\partial \psi^n}{\partial x} + D_{66}^{ijk} \frac{\partial \psi^n}{\partial y} \right] \Bigg\} dx\, dy
\end{aligned}
$$

$$
\begin{aligned}
[K_{32}^{mn}] = \int_{\Omega_e} \Bigg\{ \Bigg[& \frac{\psi^m}{R} D_{22}^{ij} \frac{\partial \psi^n}{\partial y} + \psi^m \overline{D}_{23}^{jl} \frac{\partial \psi^n}{\partial y} + \frac{\psi^m}{R} D_{26}^{ij} \frac{\partial \psi^n}{\partial x} + \psi^m \overline{D}_{36}^{jl} \frac{\partial \psi^n}{\partial x} \\
& + \frac{\partial \psi^m}{\partial x} \overline{D}_{45}^{ij} \psi^n - \frac{\partial \psi^m}{\partial x} D_{45}^{ij} \frac{\psi^n}{R} + \frac{\partial \psi^m}{\partial y} \overline{D}_{44}^{ij} \psi^n - \frac{\partial \psi^m}{\partial y} D_{44}^{ij} \frac{\psi^n}{R} \Bigg] \\
& + \frac{\partial \psi^m}{\partial x} \left[D_{16}^{ijk} \frac{\partial \psi^n}{\partial x} \frac{\partial w_j}{\partial x} + D_{12}^{ijk} \frac{\partial \psi^n}{\partial y} \frac{\partial w_j}{\partial x} \right] \\
& + \frac{\partial \psi^m}{\partial y} \left[D_{26}^{ijk} \frac{\partial \psi^n}{\partial x} \frac{\partial w_j}{\partial y} + D_{22}^{ijk} \frac{\partial \psi^n}{\partial y} \frac{\partial w_j}{\partial y} \right] \\
& + \left(\frac{\partial \psi^m}{\partial x} \frac{\partial w_j}{\partial y} + \frac{\partial \psi^m}{\partial y} \frac{\partial w_j}{\partial x} \right) \left[D_{66}^{ijk} \frac{\partial \psi^n}{\partial x} + D_{26}^{ijk} \frac{\partial \psi^n}{\partial y} \right] \Bigg\} dx\, dy
\end{aligned}
$$

$$
\begin{aligned}
[K_{33}^{mn}] = \int_{\Omega_e} \Bigg\{ \Bigg[& \frac{\psi^m}{R} D_{22}^{ij} \frac{\psi^n}{R} + \frac{\psi^m}{R} \overline{D}_{23}^{ij} \psi^n + \psi^m \overline{D}_{23}^{ji} \frac{\psi^n}{R} + \psi^m \overline{\overline{D}}_{33}^{ij} \psi^n \\
& + \frac{\partial \psi^m}{\partial x} D_{55}^{ij} \frac{\partial \psi^n}{\partial x} + \frac{\partial \psi^m}{\partial x} D_{45}^{ij} \frac{\partial \psi^n}{\partial y} + \frac{\partial \psi^m}{\partial y} D_{45}^{ij} \frac{\partial \psi^n}{\partial x} + \frac{\partial \psi^m}{\partial y} D_{44}^{ij} \frac{\partial \psi^n}{\partial y} \Bigg] \\
& + \frac{\psi^m}{R} \Bigg[\frac{1}{2} D_{12}^{ijk} \frac{\partial \psi^n}{\partial x} \frac{\partial w_k}{\partial x} + \frac{1}{2} D_{22}^{ijk} \frac{\partial \psi^n}{\partial y} \frac{\partial w_k}{\partial y} \\
& + \frac{1}{2} D_{16}^{ijk} \left(\frac{\partial \psi^n}{\partial x} \frac{\partial w_k}{\partial y} + \frac{\partial \psi^n}{\partial y} \frac{\partial w_k}{\partial x} \right) \Bigg] \\
& + \psi^m \Bigg[\frac{1}{2} \overline{D}_{13}^{jki} \frac{\partial \psi^n}{\partial x} \frac{\partial w_k}{\partial x} + \frac{1}{2} \overline{D}_{23}^{jki} \frac{\partial \psi^n}{\partial y} \frac{\partial w_k}{\partial y} \\
& + \frac{1}{2} \overline{D}_{36}^{jki} \left(\frac{\partial \psi^n}{\partial x} \frac{\partial w_k}{\partial y} + \frac{\partial \psi^n}{\partial y} \frac{\partial w_k}{\partial x} \right) \Bigg] \\
& + \left(\frac{\partial \psi^m}{\partial x} \frac{\partial w_j}{\partial x} \right) \Bigg[D_{12}^{ijk} \frac{\psi^n}{R} + \overline{D}_{13}^{ijk} \psi^n + \frac{1}{2} D_{11}^{ijkl} \frac{\partial \psi^n}{\partial x} \frac{\partial w_l}{\partial x} \\
& + \frac{1}{2} D_{12}^{ijkl} \frac{\partial \psi^n}{\partial y} \frac{\partial w_l}{\partial y} + \frac{1}{2} D_{16}^{ijkl} \left(\frac{\partial \psi^n}{\partial x} \frac{\partial w_l}{\partial y} + \frac{\partial \psi^n}{\partial y} \frac{\partial w_l}{\partial x} \right) \Bigg] \\
& + \left(\frac{\partial \psi^m}{\partial y} \frac{\partial w_j}{\partial y} \right) \Bigg[D_{22}^{ijk} \frac{\psi^n}{R} + \overline{D}_{23}^{ijk} \psi^n + \frac{1}{2} D_{12}^{ijkl} \frac{\partial \psi^n}{\partial x} \frac{\partial w_l}{\partial x} \\
& + \frac{1}{2} D_{22}^{ijkl} \frac{\partial \psi^n}{\partial y} \frac{\partial w_l}{\partial y} + \frac{1}{2} D_{26}^{ijkl} \left(\frac{\partial \psi^n}{\partial x} \frac{\partial w_l}{\partial y} + \frac{\partial \psi^n}{\partial y} \frac{\partial w_l}{\partial x} \right) \Bigg] \\
& + \left(\frac{\partial \psi^m}{\partial x} \frac{\partial w_j}{\partial y} + \frac{\partial \psi^m}{\partial y} \frac{\partial w_j}{\partial x} \right) + \Bigg[D_{26}^{ijk} \frac{\psi^n}{R} + \overline{D}_{36}^{ijk} \psi^n \\
& + \frac{1}{2} D_{16}^{ijkl} \frac{\partial \psi^n}{\partial x} \frac{\partial w_l}{\partial x} + \frac{1}{2} D_{26}^{ijkl} \frac{\partial \psi^n}{\partial y} \frac{\partial w_l}{\partial y} \\
& + \frac{1}{2} D_{66}^{ijkl} \left(\frac{\partial \psi^n}{\partial x} \frac{\partial w_l}{\partial y} + \frac{\partial \psi^n}{\partial y} \frac{\partial w_l}{\partial x} \right) \Bigg] \Bigg\} dx\, dy
\end{aligned}
$$

C.2 Layerwise Shell Element Tangent Stiffness Terms

$$[K_{11}^{mn}]^T = [K_{11}^{mn}]$$

$$[K_{12}^{mn}]^T = [K_{12}^{mn}]$$

$$[K_{13}^{mn}]^T = [K_{13}^{mn}] + \int_{\Omega_e} \left\{ \frac{\partial \psi^m}{\partial x} \left[\frac{1}{2} D_{11}^{ijk} \frac{\partial \psi^n}{\partial x} \frac{\partial w_j}{\partial x} + \frac{1}{2} D_{12}^{ijk} \frac{\partial \psi^n}{\partial y} \frac{\partial w_j}{\partial y} + \frac{1}{2} D_{12}^{ijk} \left(\frac{\partial \psi^n}{\partial y} \frac{\partial w_j}{\partial x} + \frac{\partial \psi^n}{\partial x} \frac{\partial w_j}{\partial y} \right) \right] + \frac{\partial \psi^m}{\partial y} \left[\frac{1}{2} D_{16}^{ijk} \frac{\partial \psi^n}{\partial x} \frac{\partial w_j}{\partial x} + \frac{1}{2} D_{26}^{ijk} \frac{\partial \psi^n}{\partial y} \frac{\partial w_j}{\partial y} + \frac{1}{2} D_{66}^{ijk} \left(\frac{\partial \psi^n}{\partial y} \frac{\partial w_j}{\partial x} + \frac{\partial \psi^n}{\partial x} \frac{\partial w_j}{\partial y} \right) \right] \right\} dx\, dy$$

$$[K_{21}^{mn}]^T = [K_{21}^{mn}]$$

$$[K_{22}^{mn}]^T = [K_{22}^{mn}]$$

$$[K_{23}^{mn}]^T = [K_{23}^{mn}] + \int_{\Omega_e} \left\{ \frac{\partial \psi^m}{\partial y} \left[\frac{1}{2} D_{12}^{ijk} \frac{\partial \psi^n}{\partial x} \frac{\partial w_j}{\partial x} + \frac{1}{2} D_{22}^{ijk} \frac{\partial \psi^n}{\partial y} \frac{\partial w_j}{\partial y} + \frac{1}{2} D_{26}^{ijk} \left(\frac{\partial \psi^n}{\partial y} \frac{\partial w_j}{\partial x} + \frac{\partial \psi^n}{\partial x} \frac{\partial w_j}{\partial y} \right) \right] + \frac{\partial \psi^m}{\partial x} \left[\frac{1}{2} D_{16}^{ijk} \frac{\partial \psi^n}{\partial x} \frac{\partial w_j}{\partial x} + \frac{1}{2} D_{26}^{ijk} \frac{\partial \psi^n}{\partial y} \frac{\partial w_j}{\partial y} + \frac{1}{2} D_{66}^{ijk} \left(\frac{\partial \psi^n}{\partial y} \frac{\partial w_j}{\partial x} + \frac{\partial \psi^n}{\partial x} \frac{\partial w_j}{\partial y} \right) \right] \right\} dx\, dy$$

$$[K_{31}^{mn}]^T = [K_{31}^{mn}]$$

$$[K_{32}^{mn}]^T = [K_{32}^{mn}]$$

$$\begin{aligned}
[K_{33}^{mn}]^T = [K_{33}^{mn}] + \int_{\Omega_e} \Bigg\{ & \frac{\partial \psi^m}{\partial x}\frac{\partial \psi^n}{\partial x}\left(D_{11}^{ijk}\frac{\partial u_j}{\partial x} + D_{16}^{ijk}\frac{\partial u_j}{\partial y}\right) \\
& + \frac{\partial \psi^m}{\partial y}\frac{\partial \psi^n}{\partial y}\left(D_{12}^{ijk}\frac{\partial u_j}{\partial x} + D_{26}^{ijk}\frac{\partial u_j}{\partial y}\right) \\
& + \left(\frac{\partial \psi^m}{\partial x}\frac{\partial \psi^n}{\partial y} + \frac{\partial \psi^m}{\partial y}\frac{\partial \psi^n}{\partial x}\right)\left(D_{16}^{ijk}\frac{\partial u_j}{\partial x} + D_{66}^{ijk}\frac{\partial u_j}{\partial y}\right) \\
& + \frac{\partial \psi^m}{\partial x}\frac{\partial \psi^n}{\partial x}\left(D_{12}^{ijk}\frac{\partial v_j}{\partial y} + D_{16}^{ijk}\frac{\partial v_j}{\partial x}\right) \\
& + \frac{\partial \psi^m}{\partial y}\frac{\partial \psi^n}{\partial y}\left(D_{22}^{ijk}\frac{\partial v_j}{\partial y} + D_{26}^{ijk}\frac{\partial v_j}{\partial x}\right) \\
& + \left(\frac{\partial \psi^m}{\partial x}\frac{\partial \psi^n}{\partial y} + \frac{\partial \psi^m}{\partial y}\frac{\partial \psi^n}{\partial x}\right)\left(D_{26}^{ijk}\frac{\partial v_j}{\partial y} + D_{66}^{ijk}\frac{\partial v_j}{\partial x}\right) \\
& + \frac{\psi^m}{R}\Bigg[\frac{1}{2} D_{12}^{ijk}\frac{\partial \psi^n}{\partial x}\frac{\partial w_j}{\partial x} + \frac{1}{2} D_{22}^{ijk}\frac{\partial \psi^n}{\partial y}\frac{\partial w_j}{\partial y} \\
& + \frac{1}{2} D_{26}^{ijk}\left(\frac{\partial \psi^n}{\partial x}\frac{\partial w_j}{\partial y} + \frac{\partial \psi^n}{\partial y}\frac{\partial w_j}{\partial x}\right)\Bigg] \\
& + \psi^m\Bigg[\frac{1}{2} \overline{D}_{13}^{kjl}\frac{\partial \psi^n}{\partial x}\frac{\partial w_j}{\partial x} + \frac{1}{2} \overline{D}_{23}^{kjl}\frac{\partial \psi^n}{\partial y}\frac{\partial w_j}{\partial y} \\
& + \frac{1}{2} \overline{D}_{36}^{kjl}\left(\frac{\partial \psi^n}{\partial x}\frac{\partial w_j}{\partial y} + \frac{\partial \psi^n}{\partial y}\frac{\partial w_j}{\partial x}\right)\Bigg] \\
& + \left(\frac{\partial \psi^m}{\partial x}\frac{\partial \psi^n}{\partial x}\right)\Bigg[D_{12}^{ijk}\frac{w_j}{R} + \overline{D}_{13}^{ikj} w_j + \frac{1}{2} D_{11}^{ijkl}\frac{\partial w_j}{\partial x}\frac{\partial w_l}{\partial x} \\
& + \frac{1}{2} D_{12}^{ijkl}\frac{\partial w_j}{\partial y}\frac{\partial w_l}{\partial y} + \frac{1}{2} D_{16}^{ijkl}\left(\frac{\partial w_l}{\partial x}\frac{\partial w_j}{\partial y} + \frac{\partial w_l}{\partial y}\frac{\partial w_j}{\partial x}\right)\Bigg]
\end{aligned}$$

$$
+\left(\frac{\partial\psi^m}{\partial x}\frac{\partial w_j}{\partial x}\right)\left[\frac{1}{2}D_{11}^{ijkl}\frac{\partial\psi^n}{\partial x}\frac{\partial w_l}{\partial x}+\frac{1}{2}D_{12}^{ijkl}\frac{\partial\psi^n}{\partial y}\frac{\partial w_l}{\partial y}\right.
$$

$$
\left.+\frac{1}{2}D_{16}^{ijkl}\left(\frac{\partial w_l}{\partial x}\frac{\partial\psi^n}{\partial y}+\frac{\partial w_l}{\partial y}\frac{\partial\psi^n}{\partial x}\right)\right]
$$

$$
+\left(\frac{\partial\psi^m}{\partial y}\frac{\partial\psi^n}{\partial y}\right)\left[D_{22}^{ijk}\frac{w_j}{R}+\overline{D}_{23}^{lkj}w_j+\frac{1}{2}D_{12}^{ijkl}\frac{\partial w_j}{\partial x}\frac{\partial w_l}{\partial x}\right.
$$

$$
\left.+\frac{1}{2}D_{22}^{ijkl}\frac{\partial w_j}{\partial y}\frac{\partial w_l}{\partial y}+\frac{1}{2}D_{26}^{ijkl}\left(\frac{\partial w_j}{\partial x}\frac{\partial w_l}{\partial y}+\frac{\partial w_j}{\partial y}\frac{\partial w_l}{\partial x}\right)\right]
$$

$$
+\left(\frac{\partial\psi^m}{\partial y}\frac{\partial w_j}{\partial y}\right)\left[\frac{1}{2}D_{12}^{ijkl}\frac{\partial\psi^n}{\partial x}\frac{\partial w_l}{\partial x}+\frac{1}{2}D_{22}^{ijkl}\frac{\partial\psi^n}{\partial y}\frac{\partial w_l}{\partial y}\right.
$$

$$
\left.+\frac{1}{2}D_{26}^{ijkl}\left(\frac{\partial w_l}{\partial x}\frac{\partial\psi^n}{\partial y}+\frac{\partial w_l}{\partial y}\frac{\partial\psi^n}{\partial x}\right)\right]
$$

$$
+\left(\frac{\partial\psi^m}{\partial x}\frac{\partial\psi^n}{\partial y}+\frac{\partial\psi^m}{\partial y}\frac{\partial\psi^n}{\partial x}\right)\left[D_{26}^{ijk}\frac{w_j}{R}+\overline{D}_{36}^{lkj}w_j\right.
$$

$$
+\frac{1}{2}D_{16}^{ijkl}\frac{\partial w_j}{\partial x}\frac{\partial w_l}{\partial x}+\frac{1}{2}D_{26}^{ijkl}\frac{\partial w_j}{\partial y}\frac{\partial w_l}{\partial y}
$$

$$
\left.+\frac{1}{2}D_{66}^{ijkl}\left(\frac{\partial w_j}{\partial x}\frac{\partial w_l}{\partial y}+\frac{\partial w_j}{\partial y}\frac{\partial w_l}{\partial x}\right)\right]
$$

$$
+\left(\frac{\partial\psi^m}{\partial x}\frac{\partial w_j}{\partial y}+\frac{\partial\psi^m}{\partial y}\frac{\partial w_j}{\partial x}\right)\left[\frac{1}{2}D_{16}^{ijkl}\frac{\partial\psi^n}{\partial x}\frac{\partial w_l}{\partial x}+\frac{1}{2}D_{26}^{ijkl}\frac{\partial\psi^n}{\partial y}\frac{\partial w_l}{\partial y}\right.
$$

$$
\left.\left.+\frac{1}{2}D_{66}^{ijkl}\left(\frac{\partial w_l}{\partial x}\frac{\partial\psi^n}{\partial y}+\frac{\partial w_l}{\partial y}\frac{\partial\psi^n}{\partial x}\right)\right]\right\}dx\,dy
$$

C.3 Layerwise Beam Element Direct Stiffness Terms

$$[\overset{s}{K}{}^{mn}_{11}] = \int_0^{L_s} \left\{ \frac{\partial \psi^m}{\partial \eta} B^{ij}_{11} \frac{\partial \psi^n}{\partial \eta} + \psi^m \overline{\overline{B}}^{ij}_{44} \psi^n - \psi^m \overline{B}^{ji}_{44} \frac{\psi^n}{R'} - \psi^m \overline{B}^{ij}_{44} \frac{\psi^n}{R'} + \frac{\psi^m}{R'} B^{ij}_{44} \frac{\psi^n}{R'} \right\} d\eta$$

$$[\overset{s}{K}{}^{mn}_{12}] = \int_0^{L_s} \left\{ \frac{\partial \psi^m}{\partial \eta} B^{ij}_{11} \frac{\psi^n}{R'} + \frac{\partial \psi^m}{\partial \eta} \overline{B}^{ij}_{13} \psi^n + \psi^m \overline{B}^{ji}_{44} \frac{\partial \psi^n}{\partial \eta} - \frac{\psi^m}{R'} B^{ij}_{44} \frac{\partial \psi^n}{\partial \eta} + \frac{1}{2} \frac{\partial \psi^m}{\partial \eta} B^{ijk}_{11} \frac{\partial \psi^n}{\partial \eta} \frac{\partial w_k}{\partial \eta} \right\} d\eta$$

$$[\overset{s}{K}{}^{mn}_{21}] = \int_0^{L_s} \left\{ \frac{\psi^m}{R'} B^{ij}_{11} \frac{\partial \psi^n}{\partial \eta} + \psi^m \overline{B}^{ji}_{13} \frac{\partial \psi^n}{\partial \eta} + \frac{\partial \psi^m}{\partial \eta} \overline{B}^{ij}_{44} \psi^n - \frac{\partial \psi^m}{\partial \eta} B^{ij}_{44} \frac{\psi^n}{R'} + \frac{\partial \psi^m}{\partial \eta} B^{ijk}_{11} \frac{\partial \psi^n}{\partial \eta} \frac{\partial w_j}{\partial \eta} \right\} d\eta$$

$$\begin{aligned}[\overset{s}{K}{}^{mn}_{22}] = \int_0^{L_s} \Bigg\{ & \left[\frac{\psi^m}{R'} B^{ij}_{11} \frac{\psi^n}{R'} + \psi^m \overline{B}^{ij}_{13} \frac{\psi^n}{R'} + \psi^m \overline{B}^{ji}_{13} \frac{\psi^n}{R'} + \psi^m \overline{\overline{B}}^{ij}_{33} \psi^n + \frac{\partial \psi^m}{\partial \eta} B^{ij}_{44} \frac{\partial \psi^n}{\partial \eta} \right] \\ & + \left[\frac{\partial \psi^m}{\partial \eta} B^{ijk}_{11} \frac{\psi^n}{R'} \frac{\partial w_j}{\partial \eta} + \frac{1}{2} \frac{\psi^m}{R'} B^{ijk}_{11} \frac{\partial \psi^n}{\partial \eta} \frac{\partial w_k}{\partial \eta} \right. \\ & \left. + \frac{\partial \psi^m}{\partial \eta} \overline{B}^{ijk}_{13} \psi^n \frac{\partial w_j}{\partial \eta} + \frac{1}{2} \psi^m \overline{B}^{jkl}_{13} \frac{\partial \psi^n}{\partial \eta} \frac{\partial w_k}{\partial \eta} \right] \\ & + \left[\frac{1}{2} \frac{\partial \psi^m}{\partial \eta} B^{ijkl}_{11} \frac{\partial \psi^n}{\partial \eta} \frac{\partial w_j}{\partial \eta} \frac{\partial w_l}{\partial \eta} \right] \Bigg\} d\eta \end{aligned}$$

C.4 Layerwise Beam Element Tangent Stiffness Terms

$$[\overset{s}{K}{}^{mn}_{11}]^T = [\overset{s}{K}{}^{mn}_{11}]$$

$$[\overset{s}{K}{}^{mn}_{12}]^T = [\overset{s}{K}{}^{mn}_{12}] + \int_0^{L_s} \left\{ \frac{1}{2} B_{11}^{ijk} \frac{\partial \psi^m}{\partial \eta} \frac{\partial \psi^n}{\partial \eta} \frac{\partial w_j}{\partial \eta} \right\} d\eta$$

$$[\overset{s}{K}{}^{mn}_{21}]^T = [\overset{s}{K}{}^{mn}_{21}]$$

$$[\overset{s}{K}{}^{mn}_{22}]^T = [\overset{s}{K}{}^{mn}_{22}] + \int_0^{L_s} \left\{ \frac{1}{2} B_{11}^{ijkl} \frac{\partial \psi^m}{\partial \eta} \frac{\partial \psi^n}{\partial \eta} \frac{\partial w_i}{\partial \eta} \frac{\partial w_j}{\partial \eta} + B_{11}^{ijk} \frac{\partial \psi^m}{\partial \eta} \frac{\partial \psi^n}{\partial \eta} \frac{w_j}{R'} \right.$$
$$+ \frac{1}{2} B_{11}^{ijkl} \frac{\partial \psi^m}{\partial \eta} \frac{\partial \psi^n}{\partial \eta} \frac{\partial w_i}{\partial \eta} \frac{\partial w_j}{\partial \eta} + \overline{B}_{13}^{ikj} \frac{\partial \psi^m}{\partial \eta} w_j \frac{\partial \psi^n}{\partial \eta}$$
$$\left. + \frac{1}{2} B_{11}^{ijk} \frac{\psi^m}{R'} \frac{\partial w_j}{\partial \eta} \frac{\partial \psi^n}{\partial \eta} + \frac{1}{2} \overline{B}_{13}^{kji} \psi^m \frac{\partial \psi^n}{\partial \eta} \frac{\partial w_j}{\partial \eta} \right\} d\eta$$

C.5 Computation of Higher Order Derivatives

The computation of the second and higher order derivatives of the interpolation functions with respect to the global coordinates involves additional computations.

The first order derivatives with respect to the global coordinates are related to those with respect to the local (or element) coordinates according to

$$\begin{Bmatrix} \frac{\partial \psi^n}{\partial x} \\ \frac{\partial \psi^n}{\partial y} \end{Bmatrix} = \begin{bmatrix} \frac{\partial x}{\partial \xi} & \frac{\partial y}{\partial \xi} \\ \frac{\partial x}{\partial \eta} & \frac{\partial y}{\partial \eta} \end{bmatrix}^{-1} \begin{Bmatrix} \frac{\partial \psi^n}{\partial \xi} \\ \frac{\partial \psi^n}{\partial \eta} \end{Bmatrix} \equiv [J]^{-1} \begin{Bmatrix} \frac{\partial \psi^n}{\partial \xi} \\ \frac{\partial \psi^n}{\partial \eta} \end{Bmatrix} \qquad (C.5.1)$$

where the Jacobian matrix [J] is evaluated using the approximation of the geometry:

$$\begin{aligned} x &= \sum_{j=1}^{r} x_j \phi^j(\xi, \eta) \\ y &= \sum_{j=1}^{r} y_j \phi^j(\xi, \eta) \end{aligned} \qquad (C.5.2)$$

where ϕ^j are the interpolation functions used for the geometry and (ξ, η) are the element natural coordinates. For the isoparametric formulation r = NDS and $\phi^j = \psi^j$. The second order derivatives of ψ^n with respect to the global coordinates (x, y) are given by

$$\begin{Bmatrix} \frac{\partial^2 \psi^n}{\partial x^2} \\ \frac{\partial^2 \psi^n}{\partial y^2} \\ \frac{\partial^2 \psi^n}{\partial x \partial y} \end{Bmatrix} = [J_1]^{-1} \begin{Bmatrix} \frac{\partial^2 \psi^n}{\partial \xi^2} \\ \frac{\partial^2 \psi^n}{\partial \eta^2} \\ \frac{\partial^2 \psi^n}{\partial \xi \partial \eta} \end{Bmatrix} - [J_2] \begin{Bmatrix} \frac{\partial \psi^n}{\partial x} \\ \frac{\partial \psi^n}{\partial y} \end{Bmatrix} \qquad (C.5.3)$$

where

$$[J_1] = \begin{bmatrix} \left(\frac{\partial x}{\partial \xi}\right)^2 & \left(\frac{\partial y}{\partial \xi}\right)^2 & 2\frac{\partial y}{\partial \xi}\frac{\partial x}{\partial \xi} \\ \left(\frac{\partial x}{\partial \eta}\right)^2 & \left(\frac{\partial y}{\partial \eta}\right)^2 & 2\frac{\partial x}{\partial \eta}\frac{\partial y}{\partial \eta} \\ \frac{\partial x}{\partial \eta}\frac{\partial x}{\partial \xi} & \frac{\partial y}{\partial \eta}\frac{\partial y}{\partial \xi} & \frac{\partial x}{\partial \eta}\frac{\partial y}{\partial \xi} + \frac{\partial y}{\partial \eta}\frac{\partial x}{\partial \xi} \end{bmatrix} \qquad (C.5.4)$$

$$[J_2] = \begin{bmatrix} \frac{\partial^2 x}{\partial \xi^2} & \frac{\partial^2 y}{\partial \xi^2} \\ \frac{\partial^2 x}{\partial \eta^2} & \frac{\partial^2 y}{\partial \eta^2} \\ \frac{\partial^2 x}{\partial \xi \partial \eta} & \frac{\partial^2 y}{\partial \xi \partial \eta} \end{bmatrix} \qquad (C.5.5)$$

The matrices [J_1] and [J_2] are computed using Eq. (C.5.2).